Theoretical Investigations into Adsorption and Co-adsorption on Transition-Metal Surfaces as Models to Heterogeneous Catalysis

von
M. Sc. Ari Paavo Seitsonen
aus Janakkala (Finnland)

Vom Fachbereich 4 (Physik)
der Technischen Universität Berlin
zur Verleihung des akademischen Grades
Doktor der Naturwissenschaften
genehmigte Dissertation

Berlin 2002
D 83

Tag der mündlichen Prüfung: 28. November 2000

Promotionsausschuß:

Vorsitzender:	Prof. Dr. Richter
Berichter:	Prof. Dr. Schöll
	Prof. Dr. Scheffler
	Prof. Dr. Scherz

Contents

1 Introduction **3**

2 Theory, Methods, . . . **7**
2.1 Electronic structure methods . . . 7
2.2 Density Functional Theory – DFT . . . 8
2.3 Methods . . . 16
2.4 Implementation . . . 22
2.5 Output from the calculations . . . 29

3 Results **35**
3.1 Bulk properties of ruthenium . . . 35
3.2 Clean Ru(0001) surface . . . 36
3.3 Adsorption on Ru(0001) . . . 40
3.4 Co-adsorption on Ru(0001) . . . 75
3.5 Discussion . . . 91

4 Conclusions **95**

5 References **97**

A Methodological aspects **105**
A.1 **k** point generation schemes . . . 105
A.2 Parallelisation of a plane wave code . . . 111
A.3 Evaluation of exchange-correlation energy and potential on a discrete grid . . . 112
A.4 Test calculations . . . 114

Chapter 1

Introduction

The human life in its present form is governed by various processes in different circumstances. Familiar examples are *e. g.* the photosynthesis, burning of fossil fuels, corrosion, metabolism and energy consumption of the body in general *etc*. Many of these processes have their origins at the microscopic level, in reactions which occur at the atomic scale via the chemical interaction between the active groups of materials. Thus the macroscopic outcome of the initial products is ultimately settled by the interaction of the microscopic intermediate reactants.

In the chemical industry the goal is often to transfer materials into different materials to obtain the wanted end product or products. Often the reactions needed are far too slow or even energetically unfavourable without external influence. A common practise to direct and assist the wanted reaction is via *catalysis i. e.* using a material – catalyst – which does not actively take part in the reaction but provides a bedding for the reactants and shifts the balance or energetics of the reaction controllably. Please notice however that this traditional definition of a catalyst is reshaping as evidence has been appearing of an active participation of the catalyst during the interaction of the reacting materials with the catalyst. Thus a reformulation of the definition of a catalyst is to call as such the solid which does not wear, or get consumed, during the reactions. For an excellent overview of catalysis please refer to the books by Ertl, Knözinger and Weitkamp (1997).

The real catalysts used in the industrial processes are subjected to many economical and practical requirements: The active area of the catalyst must be large but the catalytically active material can be costly and thus a minimal volume or mass must provide as large an active surface as possible – as the catalytic processes occur at the surfaces of the catalyst – and the active material is thus located on the catalyst support, which usually is inactive for the reactions but cheaper and available in large quantities; the reactions are usually driven at high temperatures and gas or liquid pressures, and the catalyst must remain operative for long operation times. Therefore the impurities in the intake materials, already in extremely low concentrations *e. g.* 10^{-10} impurities per reactant, will, at a pressure equal to that of the atmosphere, try to attack the surface area of 1 centimetre $\times$ 1 centimetre approximately at the temperature of 600 K, and so roughly 100 000 impurities would adsorb in one second assuming a probability for sticking of 10^{-8} per trial, and soon the catalytically active surface would be covered with the impurities unless the catalyst is unreactive towards the typical impurities, *e. g.* in residual gases the carbon monoxide, water *etc*, or has an efficient way to remove the impurities via desorption, reaction to side products or other means. The catalyst must also stand demanding mechanic conditions like the wear, cracking and heat convection; these must be taken into account when theoretically modelling the real catalyst.

Typical catalytically active materials are the transition metals – they are the elements located centrally in the Periodic Table – as they have a partially filled *d* shell as the outer-most electronic orbitals; thus they are chemically reactive with these rather localised and directed *d* states, but are still strongly bound and closely packed in larger solid particles like clusters, thin films and bulk materials, and due to the directional bonds geometrical modifications like phase transitions between different lattice structures do not occur easily despite the multiple energetically close phases. The chemically significant electronic structure can furthermore be fine-tuned by the variety of the transition metal elements with a slightly differing filling of the *d* shell.

In addition to the basic catalytic material the reactivity and selectivity for the wanted end products can be improved with additives called promoters, which modify either the electronic or geometrical structure of the surface of the catalyst. Often used promoters are the alkali metals and rare earth elements, placed at the two left-most columns in the Periodic Table. They have rather loosely bound *s* electrons as the active valence, making bonds to other atoms, outside a closed and inter shell. Therefore these elements have high electropositivity as seen also in the low ionisation energy of them, and with other materials they form easily bonds or hybrids where the charge of the *s* state is partially moved to the more electro-negative substance.

The other group of additives with the opposite tendency are the electro-negative ad-species; they often prevent the desired reaction or the sticking of the reactants by either electronic modification or geometric site blocking, the latter making otherwise feasible sites at the surface inaccessible to the reactants. The atomic oxygen and sulphur are examples of such inhibitors since they form strong bonds with most metallic elements and are always present as impurities in residual gases. Yet often the oxygen is one of the reactants for a wanted reaction and thus its presence is even preferential like serving as the reservoir of atomic oxygen in the process of oxidation of the carbon monoxide (Böttcher *et al*, 1997) or stabilising the alkali promoter against wearing by oxygen in the iron-based catalysts for the synthesis of ammonia (Paál, Ertl & Lee, 1981; Altenburg *et al*, 1980).

From the considerations above and the large amount of different possible materials and reaction conditions it is evident that the optimisation of the catalytic output is a demanding and complicated task. The efficiency is

eventually measured as the macroscopic output, but a guide and an implication for the choice of the conditions would be gained from the knowledge of the microscopic steps of the reactions, including the intermediate phases, reaction barriers and potential energy surfaces, effect of the promoters and inhibitors *etc*.

However at the industrial scale, or even down-scaling the catalysts to smaller length scale, there are few and even they not very detailed methods which can provide information on the different steps during the reaction, or *in situ*. Thus simplifications are called for, and they are often done in two different ways: *i*) measuring the catalyst properties either before or after the reaction in an ultra-high vacuum where impurities, which are not present during the reaction either, do not cover the catalytic surface, or in a low pressure of the reaction gases, and *ii*) simplifying the composition of the catalyst. These categories are not exclusive, for example high-pressure studies can be performed on the simplified catalysts. The limitations lead to the famous questions about the validity of the conclusions derived from the simplified studies to the real catalysis across the *pressure* and *material gaps*. Recently there have appeared sophisticated studies *e.g.* from the groups of Gerhard Ertl and D Wayne Goodman which link the low-pressure, simplified measurements to the high-pressure, realistic catalysts and demonstrate the transferability of the results from the model to the practical conditions, thus bridging the material and pressure gaps; an example is also the simple model of Stoltze and Nørskov (1985) who showed a direct relationship between the results from measurements on the clean iron surfaces in the ultra-high vacuum and the iron-based industrial catalysts in the synthesis of ammonia. However there are examples where the connection between the two extremes is not that simple: For example the promoter potassium is believed to form facets of the highly reactive (111) orientation of iron during the reaction conditions of the synthesis of ammonia on the iron-based catalysts, and the high on- and sub-surface coverage of oxygen during the oxidation of the carbon monoxide is achieved by the continuous high-pressure dosing of oxygen to the catalyst during the reaction. Thus the relevance of the results obtained at the simplified conditions is not necessarily straight-forward or even possible.

The ways of analysing the catalysts becomes easier with the simplifications above, and if the optimisation of catalysts in the industry itself is labelled as development the research done at academic institutions can basically be divided into two categories of applied and basic research, whose border-line however is weakly defined. The level of the simplifications is higher in the basic research approach and thus the relevance of the basic research is mainly in improving the understanding of the microscopic mechanism of the catalyst, and the applied research links the basic research and the industrial catalytic plants. The field of basic research which can provide the details of the processes occurring at the catalyst is the surface science. Please notice that the surface science of course covers also many other fields beyond the catalysis, *e.g.* the growth of thin films and high-purity lattices. The characteristic length scale of phenomena at the surfaces goes down to the size of atoms which is less than one millionth of a milli-meter, and the typical times are as fast as pico- to femtoseconds *i.e.* $10^{-12} \ldots 10^{-15}$ seconds. The methodological arsenal of the surface science can capture the finesse of even these high demands; however most of them require a very good, the ultra-high vacuum – *UHV* – in order to avoid impurities from gathering to the surface under study and to avoid the test particles – usually photons, electrons, light atoms or atoms desorbing from the surface – either when approaching or emerging from the surface from interacting with the residual gases. Typical methods include vibrational and electronic spectroscopies, diffractive methods, scattering of light atoms, microscopies *etc*. Several of these approaches are usually needed to form a unique picture of the microscopic structure and dynamics of a system, but even then there remain deficiencies. This is because in few cases the methods listed above can provide a direct and unique outcome of the target but methods by themselves require modelling of the interaction and information carried by the appearing test particle, the methods need a statistics from often an ordered phase of the atoms on the target, or the probe might cause modification of the target.

Therefore comparisons to results from theoretical studies which require as little or preferentially no input from measurement can reliably help further to pin-point and explain the atomic-scale details of the reaction channels, inter-mediate species, interaction of reactants with the different inhibitors and promoters *etc*. Such methods exist but they are in general very tedious as the interactions among the reactants, substrate and additive species are mostly due to chemical bonds formed by the electrons which are distributed between the atoms, and treating the electrons explicitly results in a complicated many-body problem although all the interactions at these length scales are due to the electro-static force, simple in its form. The increase in the computer power in the last decades has however made possible the numerical simulations of configurations of atoms where the electronic structure is solved from the Schrödinger equation or its derivative, and the methods which can yield also accurate forces on the atoms can easily in addition to the electronic structure provide either the static, ground state atomic positions or the realistic dynamics according to the equations of motion. The methods, which can provide accurate energies and electron structures for ensembles of many electrons, include the various approaches in quantum chemistry, the density functional theory and the quantum Monte Carlo method. However even the least costly method for large systems in terms of the computational time required, the density functional theory, can nowadays routinely be used for systems reaching up to tens, in the easiest cases hundreds, of atoms on the most powerful present-day computers. Thus clearly these methods are restricted to only small regions of the potential energy surface, which gives the energy as a function of the atomic coordinates and possibly must include also the electronic excitations and other complex phenomena, of the adsorbate structures and reactions on surfaces, and the achieved microscopic parameters can then be used *e.g.* to model the reaction dynamics or to explain and to some extent predict the experimental results. It is necessary to study the accuracy of the methods, since for example even when the strict density functional theory is in principle exact, the practical formulations are forced to include some approximation, in addition to the numerical inaccuracies involved. The electronic structure calculations on surfaces have so far concentrated on the atomically flat, highly ordered surfaces or clusters modelling them, but recently also *e.g.* the properties of zeolites, which have hollow structures and thus provide a wide surface area to reactions, have been accessed

also.

This work belongs to the category of the basic research. Our main purpose is to expand the knowledge of the mutual adsorbate-adsorbate and the adsorbate-substrate interactions via realistic calculations employing the density functional theory on structures modelling the flat, high-index surfaces of transition metals. The main classes of adsorbates in our studies contain the important molecule namely carbon monoxide, the promoter cesium, which belongs to the alkali metals, and to some extent also the oxygen, which is an inhibitor. The present work will also incorporate several previously unexplored entries to the forming database in the literature which gives the community of surface scientists an impression of the accuracy attainable with the present density functional methods.

The present work first includes a short introduction to the density functional theory in the minimal extent in order to understand the computational approach used to obtain the results presented in the following Chapter; a longer and more thorough presentation is unfortunately not feasible within the restrictions on the length of the present form. Some details of the developments achieved by the author are included in the Appendix. We also give a list of the quantities which have been extracted from our calculations. The results are classified into two groups according to phases of single adsorbates and co-adsorbed structures; at the end the results shall be discussed in light of the present knowledge of the systems under study. Regrettably also the Chapter on the results can contain only a part of the results acquired during the course of the activities for the present work. A short summary will out-look the importance the present work. Atomic units are used in the equations unless otherwise mentioned.

Chapter 2

Theory, Methods, . . .

Contents

2.1 Electronic structure methods . . . 7
2.2 Density Functional Theory – DFT . . . 8
2.2.1 Foundations of DFT – Thomas-Fermi theories and Hohenberg-Kohn theorems . . . 9
2.2.2 Kohn-Sham scheme . . . 9
2.2.3 Exchange-correlation functional . . . 11
2.2.4 Generalised gradient approximation – GGA . . . 13
2.2.5 Other approaches to the exchange-correlation term . . . 15
2.3 Methods . . . 16
2.3.1 Super-cell and Brillouin zone . . . 16
2.3.2 Brillouin zone summation . . . 18
2.3.3 Fractional occupation numbers . . . 18
2.3.4 Pseudo potentials . . . 19
2.4 Implementation . . . 22
2.4.1 Basis sets — plane waves . . . 22
2.4.2 The Car-Parrinello method – iterative schemes . . . 26
2.4.3 An implementation – Fauſt . . . 28
2.5 Output from the calculations . . . 29
2.5.1 Lattice parameter, bulk modulus and the cohesive energy . . . 29
2.5.2 Adsorption energies . . . 29
2.5.3 Density of States – DOS . . . 30
2.5.4 Projected or Local Density of States – PDOS or LDOS . . . 31
2.5.5 Work function . . . 31
2.5.6 Blyholder model for adsorption of carbon monoxide . . . 31
2.5.7 Iso-electronic reactivity function . . . 32
2.5.8 Density differences / induced density . . . 33
2.5.9 Interaction density / energy . . . 34
2.5.10 Electro-static potential / electric field . . . 34
2.5.11 Pseudo scanning tunnelling microscope image . . . 34

2.1 Electronic structure methods

The interactions which govern a system consisting of electrons and atomic nuclei are of electrostatic nature. The Coulomb interaction, although simple in its form, becomes very complicated to handle already for a few particle ensembles and soon impossible to treat exactly with the current computational resources; thus approximations are called for. The ionic and electronic masses differ by a factor over three orders of magnitude so the ionic movement is much slower than the electronic and the nuclei are much more localised than the electronic wave function; therefore the nuclei move slowly in the instantaneous potential created by surrounding, more de-localised electrons. The electronic and ionic degrees of freedom can be de-coupled using the Born-Oppenheimer approximation which states that the electrons sense the instantaneous positions of the ions and adapt to these before the ions have moved significantly; thereby the total many-body wave function $\Psi\left[\{\mathbf{r}_i\},\{\mathbf{R}_I\}\right]$ can be factorised into an ionic $\Phi\left[\{\mathbf{R}_I\}\right]$ and electronic $\chi\left[\{\mathbf{r}_i\},\{\mathbf{R}_I\}\right]$ wave functions; $\mathbf{r}_i$ are the electronic and $\mathbf{R}_I$ the ionic coordinates:

$$\Psi\left[\{\mathbf{r}_i\},\{\mathbf{R}_I\}\right] = \Phi\left[\{\mathbf{R}_I\}\right]\chi\left[\{\mathbf{r}_i\},\{\mathbf{R}_I\}\right] \ . \tag{2.1}$$

Now the electronic degrees of freedom can be solved with the nuclei held fixed and the ions can be regarded as classical point charges:

$$\left[-\frac{1}{2}\nabla^2 + V\right]\chi = E_{\mathrm{tot}}\chi \tag{2.2}$$

$$\ddot{\mathbf{R}}_I = \mathbf{F}/M_I \ , \tag{2.3}$$

where the forces on the ions are obtained as

$$\mathbf{F}_I = -\frac{dE}{d\mathbf{R}_I} = -\frac{\partial E}{\partial \mathbf{R}_I} \; ; \tag{2.4}$$

the total energy E contains also the ion-ion repulsion in addition to the electronic total energy $E_{\rm tot}$. The potential for the electrons, V, includes the electron-electron repulsion and the ion-electron attraction. The Born-Oppenheimer approximation is often a precise treatment but sometimes it notorously fails for the nuclei of the light atoms, especially hydrogen.

Despite these simplification the electron structure is a many-body problem, and thus still not exactly solvable in a reasonable time. Computational procedures exist which approach the exact result but are too demanding for all except few-atom systems; in physics community the Quantum Monte Carlo – *QMC* – (Ceperley & Alder, 1986; Hammond, Lester & Reynolds, 1994; Ceperley & Mitas, 1996; Mitas, 1996) and in quantum chemistry community the Configuration Interaction – *CI* – (Fulde, 1991; Szabo & Ostlund, 1989) have existed already for decades but still have their limitations. In the quantum Monte Carlo method the many-body electron wave function is probed stochastically and the physical observables are obtained as statistical averages. Different algorithms exist, of different accuracy: the Variational Monte Carlo – *VMC* –, the Diffusion Monte Carlo – *DMC* – and the Green's Function Monte Carlo – *GFMC*. The so-called sign problem (Schmidt & Kalos, 1984; Anderson, 1995) arises from the fermionic exclusion principle and makes the methodology much more difficult than for bosons. The quantum Monte Carlo algorithms have progressed in the recent years in the speed for calculation (Umrigar, 1993; Umrigar, Nightingale & Runge, 1993; Harju *et al*, 1997), but still the quantum Monte Carlo calculations are not broadly used for studies of realistic materials due to the higher complexity in the practical implementation than *e.g.* in the density functional calculations.

The methods in quantum chemistry tackle the problem of interacting particles from a different perspective; in them instead of the many-body wave function $\Phi(\mathbf{r}_1, \mathbf{r}_2, \ldots \mathbf{r}_N)$ single-particle wave functions $\Phi(\mathbf{r})$ are employed; a single-particle wave function depends only on the coordinates of a single electron, and is thus much more straight-forward to treat than the many-body wave function which depends explicitly on all the particle coordinates. The total many-body wave function can be regarded to consist of combinations of the single-particle orbitals, usually of determinants or a determinant of them like in the Hartree-Fock method (Ashcroft & Mermin, 1976); the determinant is convenient because it automatically fulfils the Pauli exclusion principle. The Hartree-Fock method is variational because the Hamiltonian is the exact many-body operator and a trial function is assigned for the total wave function which minimises the total energy and thus the approximate wave functions can only yield an energy higher than the exact energy. The Hartree-Fock – or Hartree-Fock-Slater – determinant leads to the single-particle equations

$$-\frac{1}{2}\nabla^2\psi_i(\mathbf{r}) + \sum_I \frac{Z_I}{|\mathbf{r}-\mathbf{R}_I|}\,\psi_i(\mathbf{r}) + \int_{\mathbf{r}'} \frac{n(\mathbf{r}')}{|\mathbf{r}-\mathbf{r}'|}\,d\mathbf{r}'\;\psi_i(\mathbf{r}) + \sum_j \int_{\mathbf{r}'} \frac{\psi_i(\mathbf{r}')\,\psi_j^*(\mathbf{r}')}{|\mathbf{r}-\mathbf{r}'|}\,d\mathbf{r}'\,\psi_j(\mathbf{r}) = \varepsilon_i\psi_i(\mathbf{r}) \;\; , \tag{2.5}$$

where $\mathbf{R}_I$ are the nuclear positions, $n(\mathbf{r})$ is the electron density $n(\mathbf{r}) = \sum_i |\psi_i(\mathbf{r})|^2$ and ε_i the eigenvalue of orbital i. The fact which makes these equations time-consuming to solve is that the potential of orbital i contains explicitly a contribution from orbital j, and the integral operator in the last term – called the *exchange* – on the left hand sign. What is still missing from the Hartree-Fock equations is the *correlation* (please see *e.g.* Fulde, 1991) which describes the dependence in the movement of an electron on the movement of all the other electrons. The correlation is usually of a smaller magnitude than the other terms but significant for a reliable and qualitative analysis; unfortunately it's analytic form is not known and therefore cannot be exactly implemented numerically. In the configuration interaction method the variational Hartree-Fock wave functions – the ground and excited states – are mixed and the result is still guaranteed to be limited from below with the exact energy. A very accurate method of this approach is the Full Configuration Interaction – *FCI* – which includes all the configurations in the given basis set.

The mostly used approach in physics and physical chemistry nowadays is the density functional theory which will be shortly introduced in the following Section.

2.2 Density Functional Theory – DFT

Density Functional Theory – *DFT* – has been the cornerstone of realistic, atomic-scale condensed matter investigations since mid-1960's. It is currently the only method which can be applied to problems of moderate size ($\approx 10 - 1000$ atoms) still explicitly accounting for the electronic degrees of freedom. The density functional theory originates as a continuation of the earlier work on approximate density-only theories – Thomas-Fermi, Thomas-Fermi-Dirac – and quantum-chemical approaches – Hartree, Hartree-Fock – yet unlike them it is not approximate *per se* but exact by construction. The theoretical foundations of the density functional theory were introduced by Hohenberg and Kohn (1964), and it was soon thereafter given a practically tractable form by Kohn and Sham – *KS* – (1965). Since then a lot of work has been done to improve on the still currently necessary approximations to the many-body terms in the density functional theory but the basic principles of the Hohenberg-Kohn-Sham formalism are unchanged since their introduction.

As there exist many good textbooks (Lundqvist & March, 1983; Parr & Yang, 1989; Dreizler & Gross, 1990) and reviews (Callaway & March, 1984; Jones & Gunnarsson, 1989) about the density functional theory in the literature we shall here discuss only the aspects which are necessary to understand the practical scheme applied in the present work.

2.2.1 Foundations of DFT – Thomas-Fermi theories and Hohenberg-Kohn theorems

The density functional theory treats the many-body problem by employing the electronic charge density as its basic variable. In this respect it closely resembles the Thomas-Fermi theories which were constructed approximating the kinetic energy contribution E_{kin} to the Coulomb-interacting many-body total energy expression,

$$E_{\text{tot}} = E_{\text{kin}} + E_{\text{ext}} + E_{\text{e-e}} \ , \tag{2.6}$$

by its correspondent for the local, non-interacting energy gas. Here $E_{\text{ext}} = \int_{\mathbf{r}} n(\mathbf{r}) V_{\text{ext}}(\mathbf{r}) \, d\mathbf{r}$ is the energy arising from an external potential $V_{\text{ext}}(\mathbf{r})$, usually the attractive Coulomb interaction with ionic cores; $E_{\text{e-e}}$ is the electron-electron interaction, which for convenience is usually split into two parts, the classical Hartree energy

$$E_{\text{Hartree}} = \frac{1}{2} \int_{\mathbf{r}} \int_{\mathbf{r}'} \frac{n(\mathbf{r}) \, n(\mathbf{r}')}{|\mathbf{r} - \mathbf{r}'|} \, d\mathbf{r}' \, d\mathbf{r} \tag{2.7}$$

and the so-called *exchange-correlation* functional $E_{\text{xc}}[n]$, which will be discussed below.

The density functional theory and the Kohn-Sham method as its application is theoretically well justified. The basis for the density functional theory is constituted by the two mathematical theorems of Hohenberg and Kohn (1964) for a system with non-degenerate electronic ground state:

1. The potential V_{ext} is – to within a constant shift – a unique functional of the density $n(\mathbf{r})$; especially the ground state density $n_0(\mathbf{r})$ corresponding to an external potential V_{ext} cannot be reproduced using any other potential V'_{ext} and thus, since the density is uniquely related to the external potential it also is sufficient to determine the ground state and all other electronic properties or observables of the system.

2. The correct ground state density $n_0(\mathbf{r})$ minimises the total energy functional

$$E_{\text{tot},V}[n] = E_{\text{kin}}[n] + E_{\text{e-e}}[n] + E_{\text{ext}}[n] = F_{\text{HK}}[n] + E_{\text{ext}}[n] \ , \tag{2.8}$$

   now written using the universal – *i.e.* independent of any particular external potential – functional $F_{\text{HK}}[n]$ defined by Hohenberg and Kohn; the sub-script V reminds here that the energy is defined for a given external potential.

The essential content of the Hohenberg-Kohn theorems is that to find the electronic properties of the system, defined by V_{ext}, it is enough to minimise the total energy expression with respect to all the densities $n(\mathbf{r})$. The one giving the lowest energy is the ground state density and it can then be used to evaluate the wanted observables. However, this still remains a formidable task due to its many-body nature and a practical scheme is highly welcome. Such was described by Kohn and Sham (1965) and will be shortly introduced below.

We stress here that the density functional theory is thus a theory for the ground state. It can, however, in particular cases be used to extract properties of excited states; please see *e.g.* Dreizler and Gross (1990). For extensions of Hohenberg-Kohn theorems for systems with degenerate ground states, spin-polarised, magnetic, time-dependent systems *etc* please see the textbooks mentioned above and references therein.

2.2.2 Kohn-Sham scheme

Kohn and Sham (1965) conducted a scheme which employs single-particle wave functions, similarly to the Hartree and Hartree-Fock methods. However, the following remarks are in order:

- The single-particle Kohn-Sham orbitals serve only as an auxiliary basis for the calculation, they are not guaranteed to bear any resemblance to any observable quantity.
- The same comment holds for the single-particle eigenvalues, except the eigenvalue of the highest occupied orbital and ionisation energy (Perdew *et al*, 1982). This point cannot be over-emphasised, in particular in the semi-conductor community, where for example the "gap problem" has received lots of concern.
- The Kohn-Sham formalism is still exact – for physically sensible densities – by construction. In practice an approximation is necessary to account for the many-particle exchange-correlation effects but this approximation is well understood and many exact properties for them are known.

Nowadays the Kohn-Sham scheme constitutes the main-stream of the applications of the density functional theory to real-world systems, and even a limited list of systems where Kohn-Sham formalism has been applied would be overwhelming. The explanation behind the success of Kohn-Sham method lies in its simplicity and relatively low computational cost needed to access moderately accurate results.

The Kohn-Sham scheme can be thought as a mapping of the many-body problem of fully-interacting particles in an external potential V_{ext} to a system of non-interacting particles in an effective potential V_{eff} giving the same ground state density. The effective potential must be local and it is the same for all the orbitals, leading to a mean-field kind of description of the interactions.

In the framework of one-particle orbitals $\psi_i(\mathbf{r})$ the kinetic energy of non-interacting particles can easily be calculated exactly:

$$E_{\text{kin},s}[n] = \sum_i^N \int_{\mathbf{r}} \psi_i(\mathbf{r})^* \left(-\frac{1}{2} \nabla^2 \right) \psi_i(\mathbf{r}) \, d\mathbf{r} \ , \tag{2.9}$$

where the sum runs over the occupied states up to the N electrons. That a density functional formalism contains explicitly orbital-dependent terms is not a conceptual problem since if one first assumes the existence of the effective potential V_{eff} generating the ground state density n, then according to the first Hohenberg-Kohn theorem it is unique and thus the single-particle orbitals, being a property of the ground state, are functionals of the density: $\psi_i(\mathbf{r}) = \psi_i([n];\mathbf{r})$. The improved accuracy of the Kohn-Sham method over the Thomas-Fermi approaches lies just at the exact description of the kinetic energy; thus the large extra cost due to the single-particle orbital treatment compared to the density-only schemes is justified.

The single-particle equations of the Kohn-Sham method can be derived from the total energy expression. The functional $F_{\text{HK}}[n]$ is first divided into $E_{\text{kin},s}[n]$ and a new universal functional $G[n]$:

$$\begin{aligned} E_{\text{tot}}[n] &= F_{\text{HK}}[n] + E_{\text{ext}}[n] \\ &= E_{\text{kin},s} + G[n] + E_{\text{ext}}[n] \ . \end{aligned} \tag{2.10}$$

The functional $G[n]$ is further split into the classical Hartree electron-electron interaction term $E_{\text{Hartree}}[n]$ of the Equation 2.7 and a term containing the many-body interactions, $E_{\text{xc}}[n]$, the exchange-correlation energy which was mentioned above. Formally $E_{\text{xc}}[n]$ is thus defined as

$$E_{\text{xc}}[n] = F_{\text{HK}}[n] - E_{\text{Hartree}} - E_{\text{kin},s} \ . \tag{2.11}$$

The final total energy functional reads now

$$E_{\text{tot}}[n] = E_{\text{kin},s}[n] + E_{\text{Hartree}}[n] + E_{\text{xc}}[n] + E_{\text{ext}}[n] \ . \tag{2.12}$$

Note that once a practical scheme for obtaining the single-particle orbitals $\psi_i(\mathbf{r})$ (for $E_{\text{kin},s}$) exists and the form of $E_{\text{xc}}[n]$ is known the exact ground state energy can be easily obtained from the expression 2.12. However, as will be discussed below, although the first part – finding $\psi_i(\mathbf{r})$ – is straight-forward the exchange-correlation part remains a challenge and currently requires an approximation.

When the single-particle orbitals are employed they are in principle functionals of the density as just mentioned. The density is obtained using the orbitals as

$$n(\mathbf{r}) = \sum_i^N \psi_i(\mathbf{r})^* \, \psi_i(\mathbf{r}) = \sum_i^N |\psi_i(\mathbf{r})|^2 \ . \tag{2.13}$$

The requirement of the minimisation of the energy with respect to a change in the wave function lead into a set of single-particle equations known as the Kohn-Sham equations:

$$\left(-\frac{1}{2}\nabla^2 + V_{\text{Hartree}} + V_{\text{xc}} + V_{\text{ext}} \right) \psi_i = \varepsilon_i \psi_i(\mathbf{r}) \ . \tag{2.14}$$

This corresponds to a partial differential equation with a Hamiltonian

$$H_s = -\frac{1}{2}\nabla^2 + V_{\text{Hartree}} + V_{\text{xc}} + V_{\text{ext}} = -\frac{1}{2}\nabla^2 + V_{\text{eff}}[n] \ . \tag{2.15}$$

The effective potential depends on the density, the Kohn-Sham orbitals ψ_i on the effective potential, and the density on the orbitals due to its definition 2.13; thus this set of equations form a loop which has to be solved self-consistently: One starts *e.g.* with an approximate density, constructs the effective potential and solves the Kohn-Sham equations to obtain the orbitals which are then used to calculate the new density *etc*. This procedure is continued until the density, orbitals, total energy and so on no longer change from the previous iteration.

As each of the Kohn-Sham equations is of the same form as the Schrödinger equation the same methods can be used to solve the Kohn-Sham orbitals. However, because the Kohn-Sham scheme consists of the self-consistent loop this may cause different algorithms which do not perform the full solution of the Kohn-Sham equations at each iteration to become more efficient than the traditional, straight-forward matrix diagonalisation. We shall shortly discuss some different algorithms when discussing the practical implementation of the Kohn-Sham method.

Studying the form of the Kohn-Sham equations 2.14 one can easily derive an alternative expression to the Equation 2.12 at self-consistency for the total energy,

$$E_{\text{tot}} = \sum_i^{\text{occ}} \varepsilon_i - E_{\text{Hartree}} + E_{\text{xc}} - \int n(\mathbf{r}) \, V_{\text{xc}}(\mathbf{r}) \, d\mathbf{r} \ . \tag{2.16}$$

The terms additional to the sum over the occupied eigenvalues are called the double-counting correction terms and are caused by the non-linearity of the total energy expression 2.12 with respect to the density – *e.g.* the Hartree energy contains the square of the density – so that the sum over eigenvalues

$$\sum_i^N \langle \psi_i | \, H \, | \psi_i \rangle \neq E_{\text{tot}} \ . \tag{2.17}$$

Above we have discussed only the spin-polarised, integer-occupied formulation of the Kohn-Sham scheme; more general discussion will follow, but to introduce the theoretical background a simplified framework was chosen. For the detailed derivation of the more general Kohn-Sham formalism please see *e.g.* Dreizler and Gross (1990).

2.2.3 Exchange-correlation functional

The term of exchange and correlation functional was introduced into the Kohn-Sham theory when the kinetic energy of non-interacting particles $E_{\mathrm{kin,s}}$ was inserted to replace the true kinetic energy, and the classical Hartree interaction 2.7 was extracted from the full electron-electron interaction in order to enable an exact evaluation of these terms, hoping that the remaining terms are small in magnitude or can be approximated sufficiently accurately. Therefore it might first be surprising that the exchange and correlation constituents have clear physical origins: The exchange arises from the Pauli principle that two electrons with parallel spins cannot occupy the same region in space, and correlation because the motion of an electrons is correlated, *i.e.* the instantaneous position of an electron depends on all the other electronic positions as well. While the exchange energy is known exactly and used in the Hartree-Fock method, correlation is analytically only moderately known; it can, however, be obtained in some limiting cases and calculated to a very high accuracy using the quantum chemistry (Fulde, 1991) or quantum Monte Carlo (Ceperley & Alder, 1980) methods. Note that the definition of correlation associated with the Hartree-Fock scheme is somewhat different from the definition within density functional theory: in Hartree-Fock-correlated schemes the correlation energy is a correction to the Hartree-Fock energy, *i.e.* the wave functions are calculated to self-consistency without a correlation potential, but in density functional theory it is included in the self-consistent effective potential.

We shall briefly discuss some approximative exchange and correlation functional schemes. The main emphasis will, however, be on the generalised gradient approximation as the main bulk of the result of the present work was produced with it. Local density approximation is discussed in length due to its simplicity and wide use. Due to restrictions in the length we shall discuss only the spin-unpolarised case below unless otherwise mentioned; the generalisation to spin-polarised case is straight-forward – please see *e.g.* Parr and Yang (1989).

Local density approximation – LDA

The most straight-forward and frequently used approximation is the Local Density Approximation – *LDA* – (Kohn & Sham, 1965), or its spin-polarised version Local Spin Density Approximation – *LSDA* or *LSD* –, where the exchange-correlation energy and potential at each point of space are replaced by their correspondents for the homogeneous electron gas, *i.e.* as if at each point separately there was a constant density, independent of all the other points. The exact expression for exchange energy of homogeneous electron gas is easily derivable analytically (Dirac, 1930; Gáspár, 1954) and highly accurate quantum Monte Carlo calculations can be done for the correlation energy (Ceperley & Alder, 1980) in addition to some exact analytical limits (Wigner, 1934; Carr, 1961; Nozieres & Pines 1966; Gell-Mann & Brueckner, 1957; Carr & Maradudin, 1964) – please see *e.g.* Mahan (1981). The local density approximation is expected to give good results only when the variations of homogeneity are small or slow; slow means the density changes are small within the Fermi wave momentum $k_F = \left[3\pi^2 n\left(\mathbf{r}\right)\right]^{1/3}$. However, neither of these requirements are ful-filled in real systems. Thus the high level of accuracy in calculations employing local density approximation – reviewed *e.g.* by Jones and Gunnarsson (1989) and Parr and Yang (1989) – is really surprising. Part of this success can be explained by the exact properties obeyed by the local density approximation, like the sum rule that the exchange-correlation hole around an electron contains exactly minus one electron – *i.e.* one hole –

$$\int_{\mathbf{r}'} n_{\mathrm{xc}}\left(\mathbf{r},\mathbf{r}'\right)\, d\mathbf{r}' = -1 \;\forall \mathbf{r} \tag{2.18}$$

and correct scaling behaviours, and partially by error cancellation; for example the errors in exchange have partially different sign than errors in correlation. Also helpful is that the region where typically most of the electrons reside, the core electrons close to the nuclei, are chemically inert and thus the error *e.g.* in total energy between two similar systems – like a molecule and its atoms separated infinitely far apart – is smaller than the errors in total energies. The amount of correlation, whose characteristics are least known, is also smallest; the accuracy of exchange energy and potential can at least be tested using exact functional like the Hartree-Fock method or the exact-exchange methods in the density functional theory (Talman & Shadwick, 1976; Aashamar, Luke & Talman, 1978).

The exchange-correlation energy in the local density approximation is given by

$$E_{\mathrm{xc}}^{\mathrm{LDA}}\left[n\right] = \int_{\mathbf{r}} n\left(\mathbf{r}\right) \varepsilon_{\mathrm{xc}}^{\mathrm{hom}}\left(n\left(\mathbf{r}\right)\right)\, d\mathbf{r} \tag{2.19}$$

and the potential by

$$V_{\mathrm{xc}}^{\mathrm{LDA}}\left(\mathbf{r}\right) = \frac{\partial\left(n\varepsilon_{\mathrm{xc}}^{\mathrm{hom}}\right)}{\partial n} = \varepsilon_{\mathrm{xc}}^{\mathrm{hom}} + \frac{n\partial\varepsilon_{\mathrm{xc}}^{\mathrm{hom}}}{\partial n}\ , \tag{2.20}$$

where $\varepsilon_{\mathrm{xc}}^{\mathrm{hom}}\left(n\left(\mathbf{r}\right)\right)$ is the energy density of homogeneous electron gas *per particle*. There exist several parametrisations of the correlation energy of the homogeneous electron gas. The most accurate and famous ones by Perdew and Zunger (1981), Vosko, Wilk and Nusair (1980) and Perdew and Wang (1992a) are fits to the quantum Monte Carlo results of Ceperley and Alder (1980). Recent accurate parametrisation of $\varepsilon_{\mathrm{xc}}^{\mathrm{LDA}}\left(n\right)$is given in the Figure 2.1.

One clear case where the local density approximation fails qualitatively is the asymptotic decay of potential away from a density distribution; one can derive that the exact energy falls off like $\propto \frac{1}{r}$ outside the density distribution $n\left(\mathbf{r}\right)$ (Almbladh & von Barth, 1985) whereas in the local density approximation it decays exponentially

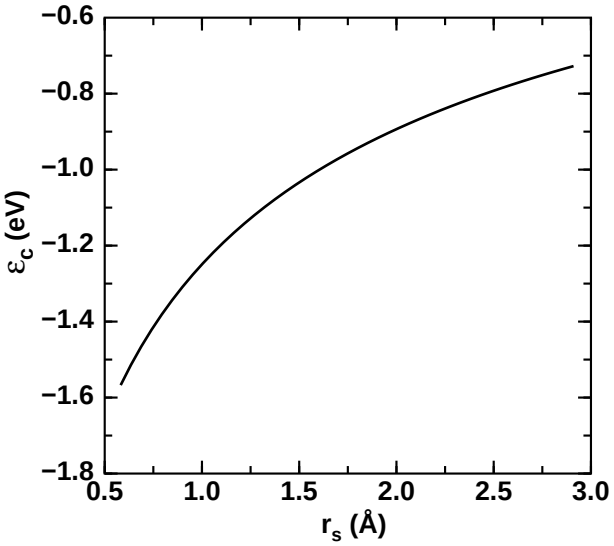

Figure 2.1: The parametrisation of the form $\varepsilon_c^{\mathrm{LDA}}(n) = -2A(1+\alpha_1 r_s)\log\left[1+\frac{1}{2a\left(\beta_1 r_s^{1/2}+\beta_2 r_s+\beta_3 r_s^{3/2}+\beta_4 r_s^2\right)}\right]$, with constants a, α_1, β_1, β_2, β_3, β_4, of the correlation energy for the homogeneous electron gas by Perdew and Wang (1992); $r_s = \left[\frac{3}{4\pi n(\mathbf{r})}\right]^{1/3}$ is the local Wigner-Seitz radius. Thus the correlation energy is obtained like in the local exchange: one inserts at a point the density and obtains from the functions the exchange and correlation energy density and potential, independently of the other points

away from n (Tong & Sham, 1966; Lang & Kohn, 1970; Lang & Kohn, 1971) due to the exponential decay of the density. Although the tail of the potential is essential in determining the ionisation energies of atoms and molecules or the work function in the case of a surface, the local density approximation often provides good results for these quantities. However, *e.g.* the negatively charged atoms are incorrectly not stable within the local density approximation due to this shortcoming in the asymptotic potential.

In overview general features of local density approximation are:

- binding energies, cohesion in case of solids, are usually overestimated, *i.e.* too much binding is given, often as much as 30 % – please see *e.g.* Parr and Yang (1989) or Dreizler and Gross (1990) – but in systems of weakly bound such as by hydrogen bonds – please see *e.g.* Laasonen, Csajka and Parrinello (1992) – or van der Waals forces even five times too large binding energies are obtained (Pérez-Jordá & Becke, 1995; Montanari, Ballone & Jones, 1998; Zhang, Pan & Yang, 1997), for example in dimers of rare gas atoms
- lattice constants of solids are mostly too small due to under-binding of the core electrons and thus too diffuse cores seen by the valence electrons (Kresse, Furthmüller & Hafner, 1994)
- vibrational frequencies, phonons in solids, are well given; the bulk compressibility or bulk modulus is usually too large as a consequence of the too small a lattice constant
- the magnetic or spin-polarised properties are often non-satisfactorily predicted; for example the ground state of iron is erroneously not the ferromagnetic body-centred cubic phase but the non-magnetic hexagonal close-packed lattice
- reaction barriers are often underestimated *e.g.* for H+H_2 →H_2+H (Johnson *et al*, 1994) and H_2 dissociation on transition metal surfaces like Cu(111) (Hammer *et al*, 1994) and Al(110) (Hammer, Jacobsen & Nørskov, 1993); this was concluded to arise from incomplete Pauli repulsion between the states of the anti-bonding orbital of hydrogen, whose filling leads to the dissociation, and the states of the substrate
- *sd* transfer energies are too low (Gunnarsson & Jones, 1985)
- some negative ions are not bound although they are stable in experiments (Schwarz, 1978; Shore, Rose & Zaremba, 1977); this deficiency originates from the wrong asymptotic behaviour of the exchange and correlation as discussed above

The local density approximation has been the backbone of applications of density functional theory since the beginning. The straight-forward implementation of it and superior accuracy over the Hartree method with the same and comparable accuracy with Hartree-Fock method with a smaller computational cost have resulted in a vast amount of calculations using it. Much work has been devoted to go beyond the local density approximation but despite progress no method with overall, systematic improvement has been found yet. Moreover, the delicate error cancellation between exchange and correlation in the local density approximation aggravates the simultaneous testing and especially application of new exchange and correlation functionals difficult.

2.2.4 Generalised gradient approximation – GGA

The most obvious method to extend the local density approximation to inhomogeneous systems is to include also the changes or gradients of the density. The straight-forward attempt is to try a first-order Taylor expansion around the constant density and hope for the inhomogeneities to be either small or at least slowly varying, thus justifying the low-order Taylor expansion. The expansion has been derived for the kinetic, exchange and correlation energies, the former to be used in the density-only like Thomas-Fermi methods. For correlation, even though the analytical formula for the homogeneous density is missing, a gradient expansion is known. The expansion is expected to work only when (Hohenberg & Kohn, 1964)

$$\frac{|\nabla n(\mathbf{r})|}{2n(\mathbf{r})} << k_F(\mathbf{r}) \quad \frac{\left|\nabla^2 n(\mathbf{r})\right|}{2|\nabla n(\mathbf{r})|} << k_F(\mathbf{r}) \ . \tag{2.21}$$

In this approach, called the Gradient Expansion Approximation – *GEA* – (Hohenberg and Kohn, 1964), the terms with odd powers of the gradient of density, ∇n, must vanish due to rotational invariance. Thus the lowest-order gradient expansion approximation for the exchange reads as (Sham, 1971; Gross & Dreizler, 1981)

$$\begin{aligned} E_{\mathrm{x}}^{\mathrm{GEA}}(n,\nabla n) &= \underbrace{E_{\mathrm{x}}^{(0)}}_{=E_{\mathrm{x}}^{\mathrm{LDA}}} + E_{\mathrm{x}}^{(2)} = d_0 \int_{\mathbf{r}} n^{4/3}\, d\mathbf{r} + d_2 \int_{\mathbf{r}} \frac{|\nabla n|^2}{n^{4/3}}\, d\mathbf{r} \ , \\ & d_0 = -\frac{3}{4}\left(\frac{3}{\pi}\right)^{1/3} \ , \ d_2 = -\frac{7}{432}\left(3\pi^5\right)^{-1/3} \ . \end{aligned} \tag{2.22}$$

Please note the orders of $|\nabla n|$ and n in this expression; it can be shown that the exact functional has the order $|\nabla n|/n^{4/3}$ in all the orders of the expansion. The zeroth order term is the local density approximation as expected.

Practical tests with the gradient expansion approximation applied have shown that many properties are less accurately produced than in the local density approximation. For example the correlation energy in helium and neon atoms has even a wrong sign (Burke, Perdew & Levy, 1995), the second-order exchange potential diverges in atoms both at large and small radii (Herman, van Dyke & Ortenburger, 1969) and the energy terms of the fourth or higher order also diverge for finite systems. One of the reasons for the shortcomings of the gradient expansion approximation is that the sum rule 2.18 is not obeyed, and the value of scaled gradient does not meet the expectations 2.21 set for the convergence of a Taylor series. Thus the gradient expansion does not converge after the first, lowest-order terms, invalidating the low-order Taylor expansion. Furthermore since the computation of higher gradients and gradients with increasing order of the expansion are finer and thus need higher a convergence with respect to the basis set this approach is not satisfactory and an alternative method has to be searched for.

A different way to include the gradient of the density is to construct a functional which still depends only on the local density $n(\mathbf{r})$ and the magnitude of the gradient $|\nabla n(\mathbf{r})|$ but whose functional form is no longer chosen to be the one of the exact gradient expansion. Therefore this approach is called the Generalised Gradient Approximation – *GGA* –, generalised because of the increased freedom in the choice of the form and approximation because the chosen function usually does not follow the exact lowest-order properties of the electron gas, whereas the gradient expansion approximation can be called a gradient correction – although the "correction" terms do not necessarily improve the results as discussed above. In the literature the term "gradient corrections" has often been misused to mean also generalised gradient approximations.

The choice of the functional form for the generalised gradient approximation is not unique and many different functions have been proposed. Here we shall follow the formalism of Perdew *et al* since their forms are the most *ab initio* in nature and they have also been used for the calculations of the present work. By the years they have proposed several parametrisations of which the so-called Perdew-Wang 1991 or GGA-II (Perdew, 1991; Perdew *et al*, 1992; Perdew, Burke & Wang, 1996) has been used most; it has lately been slightly modified in the newer Perdew-Burke-Ernzerhof (1996) parametrisation. This parametrisation is mostly just a simplification of the Perdew-Wang 1991 functional, sacrifying some exact properties for the sake of simplicity of the resulting functional. Although the parametrisation Perdew-Wang 1991 was used for the majority of the calculations in the present work we shall describe here the Perdew-Burke-Ernzerhof parametrisation because of the simpler form it possesses. They write the exchange and correlation energies somewhat differently due to the different spin dependence, as the correct exchange scales as (Oliver & Perdew, 1979)

$$E_{\mathrm{x}}[n_{\pm}] = \frac{1}{2}\left(E_x[2n_+] + E_x[2n_-]\right) \ , \tag{2.23}$$

where n_+, n_- are the spin up and down densities, respectively. In exchange an enhancement factor F^{PBE} over the local density approximation energy density is used, whereas in correlation the gradient-dependent part is an additive to the correlation of homogeneous density distribution:

$$\begin{aligned} E_{\mathrm{x}}^{\mathrm{PBE}}(n(\mathbf{r}), |\nabla n(\mathbf{r})|) &= \int_{\mathbf{r}} n(\mathbf{r})\, \varepsilon_{\mathrm{x}}^{\mathrm{LDA}}(n(\mathbf{r}))\, F_{\mathrm{x}}^{\mathrm{PBE}}(s)\, d\mathbf{r} \ , \\ F_{\mathrm{x}}^{\mathrm{PBE}}(s) &= 1 + \kappa - \frac{\kappa}{1 + \frac{\mu s^2}{\kappa}} \end{aligned}$$

$$
\begin{aligned}
\mu &= \beta\left(\frac{\pi^2}{3}\right) \\
E_{\mathrm{c}}^{\mathrm{PBE}}\left(n\left(\mathbf{r}\right),\left|\nabla n\left(\mathbf{r}\right)\right|\right) &= \int_{\mathbf{r}} n\left(\mathbf{r}\right)\left[\varepsilon_{\mathrm{xc}}^{\mathrm{LDA}}\left(n\left(\mathbf{r}\right)\right)+H_{\mathrm{c}}^{\mathrm{PBE}}\left(r_s,\eta,t\right)\right]\,d\mathbf{r}\ , \\
H_{\mathrm{c}}^{\mathrm{PBE}}\left(r_s,\eta,t\right) &= \gamma\phi^3\ln\left[1+\frac{\beta}{\gamma}t^2\left(\frac{1+At^2}{1+At^2+A^2t^4}\right)\right]\ , \\
A\left(r_s,\eta\right) &= \frac{\beta}{\gamma}\frac{1}{e^{-\varepsilon_{\mathrm{c}}^{\mathrm{LDA}}/\gamma\phi^3}-1}\ , \\
\phi\left(\eta\right) &= \frac{1}{2}\left[\left(1+\eta\right)^{2/3}+\left(1-\eta\right)^{2/3}\right]\ , \\
\gamma &= \frac{1-\ln 2}{\pi^2}\ .
\end{aligned}
\tag{2.24}
$$

Here $s\left(\mathbf{r}\right)=\frac{\left|\nabla n\right|}{2k_F n}$ and $t\left(\mathbf{r}\right)=\frac{\left|\nabla n\right|}{2\phi k_s n}$, $k_s=\sqrt{4k_F/\pi}$, are dimensionless density gradients – of the correct form discussed above – and β comes from the generalised gradient expansion for the correlation (Perdew *et al*, 1992) and is $\approx 0.066\,725$ (Wang & Perdew, 1991). κ is formally set by the Lieb-Oxford bound (1981) for the exchange energy

$$
E_{\mathrm{x}}\left[n_{\pm}\right]\geq E_{\mathrm{xc}}\left[n_{\pm}\right]\geq -1.679\int_{\mathbf{r}} n\left(\mathbf{r}\right)^{4/3}\,d\mathbf{r}\ . \tag{2.25}
$$

However it has been lately suggested (Zhang & Yang, 1998; Perdew, Burke & Ernzerhof, 1996; Mortensen, 1998; Hammer, Hansen & Nørskov, 1999) that choosing a different, larger value of κ than 0.804 derived by Perdew, Burke and Ernzerhof leads to improved energetics and thus has been used semi-empirically in calculations; however, the geometric properties like the lattice constant would be worsened.

Requirements in the construction of $F_{\mathrm{x}}^{\mathrm{PBE}}$ and $H_{\mathrm{c}}^{\mathrm{PBE}}$ are

- they exactly reduce to the homogeneous limit, the local density approximation, for constant density *i. e.* then $F\equiv 1$ and $H\equiv 0$; in the slowly varying limit the correlation is given by its second order gradient expansion whereas the exchange is set to cancel the correlation in this limit to recover the good linear response of the local spin density approximation
- the exchange-correlation hole integrates up exactly to minus one to satisfy the sum rule 2.18; this is achieved by a real-space cut-off construction (Perdew, Burke & Wang, 1996) where the exchange-correlation hole of the second-order gradient expansion is set to zero beyond a radius where the sum rule is obeyed. The Perdew-Wang 1991 and Perdew-Burke-Ernzerhof 1996 functionals are analytic fits to the obtained function
- in the rapidly varying limit $t\to\infty$ the correlation vanishes
- under uniform coordinate scaling $n\left(\mathbf{r}\right)\to\lambda^3 n\left(\lambda\mathbf{r}\right)$ the exchange energy must scale like λ (Levy & Perdew, 1985) and the correlation scales to a constant when $\lambda\to\infty$ (Levy, 1989)

From the enhancement factor $F_{\mathrm{xc}}^{\mathrm{PBE}}$, defined by

$$
E_{\mathrm{xc}}^{\mathrm{PBE}}\left(n\left(\mathbf{r}\right),\left|\nabla n\left(\mathbf{r}\right)\right|\right)=\int_{\mathbf{r}} n\left(\mathbf{r}\right)\varepsilon_{\mathrm{x}}^{\mathrm{LDA}}\left(n\left(\mathbf{r}\right)\right)F_{\mathrm{xc}}^{\mathrm{PBE}}\left(r_s,\eta,s\right)\,d\mathbf{r} \tag{2.26}
$$

or

$$
F_{\mathrm{xc}}^{\mathrm{PBE}}\left(r_s,\eta,s\right)=\frac{\varepsilon_{\mathrm{xc}}\left(n\left(\mathbf{r}\right)\right)}{\varepsilon_{\mathrm{x}}^{\mathrm{LDA}}\left(n\left(\mathbf{r}\right)\right)}\ , \tag{2.27}
$$

it can be seen that the gradient terms deepen the exchange-correlation energy because the exchange energy of the homogeneous electron gas is negative and the enhancement factor is larger than one; thus inhomogeneities are preferred.

Other popular parametrisations within the generalised gradient approximation are the exchange functional of Becke (1988) and the correlation functional functional of Lee, Yang and Parr (1988) which start from the Colle-Salvetti (1975; 1979) formula to be discussed below. The combination of these two – commonly denoted as *BLYP* – has been used widely in the computational chemistry although they both contain a fit parameter and the correlation energy does not reduce to the local density approximation for the homogeneous electron gas; yet the results are often pretty good (Johnson, Gill & Pople, 1993) for the light elements.

The generalised gradient approximations and especially the parametrisations of Perdew-Wang 1991 and Perdew, Burke and Ernzerhof 1996 have the following general properties:

- the core electrons are bound more strongly, thus the valence electrons see a better screened nucleus and are less bound than in local density approximation
- as a consequence the bond lengths in molecules, lattice constants of solids, tend to come out too large, with some exceptions like aluminium
- the bulk moduli of solids are usually too low, most probably due to the too large a lattice constant

- the accuracy of vibrational frequencies is similar to local density approximation
- reaction barriers are higher than in local density approximation but still often too low, *e.g.* for dissociation of H_2 on Cu(111) (Hammer *et al*, 1994) and $H+H_2 \Leftrightarrow H_2+H$ (Johnson *et al*, 1994)
- the work function of surfaces is usually too low whereas they are much closer to the experimental values within the local density approximation; the reason for this is still unknown (Martin Fuchs, personal communication)
- the surface energies are often lower than those from local density approximation or experiments; this has been suggested to be due to the too weak bonding in generalised gradient approximation so when the coordination is reduced by cutting the surface it does not cost as much energy, thus giving too low a surface energy
- the ground state of iron is correctly reproduced by the generalised gradient approximations
- the binding energy of rare gas dimers are in good agreement with experiments within the Perdew-Burke-Ernzerhof 1996 functional (Pérez-Jordá & Becke, 1995; Zhang, Pan & Yang, 1997) whereas they were even unbound with the older parametrisations of the exchange energy by Perdew and Wang (1986) and Becke (1988)

Thus generalised gradient approximation often does better than the local density approximation but has its pitfalls too. The interest is now shifting towards a generalised gradient approximation with second order gradients, and suggestions for such have been given by Engel and Vosko (1994), Proynov, Vela and Salahub (1994), Neumann and Handy (1997). Becke (1993; 1996) has introduced a functional where exact exchange from a Hartree-Fock-operator is mixed with the generalised gradient approximation for the exchange, and with the correlation functional of Lee, Yang and Parr this *B3LYP* approximation has become widely used in computational chemistry.

For the systems studied in the present work the generalised gradient approximation is more advantageous than harmful, and since the computational cost is only minimally higher than in local density approximation we preferred the generalised gradient approximation and used it for most of our calculations. However, the calculation of gradients and more complicated form of the exchange-correlation functional set a slightly higher convergence requirement for the basis set size.

2.2.5 Other approaches to the exchange-correlation term

There has naturally been a long-standing effort to find exchange-correlation functionals which would perform better than the local density or generalised gradient approximations. All of them lead to improved properties in some quantity, but no general improvement in the comparison to experiments has been achieved; only the method of exact exchange provides, as the name suggests, an over-all up-grade in the accuracy. However, it is computationally demanding and a correlation functional accurate enough has not been found yet.

- The correct potential acting on an electron does not explicitly depend on itself but only indirectly via the other electrons. However, the exchange-correlation potentials from *e.g.* local density and generalised gradient approximations do not cancel the contribution of the electron in the Hartree term. The method of the self-interaction correction – *SIC* – (Perdew & Zunger, 1981) corrects for this shortcoming explicitly, but leads to a more complicated set of single-particle equations, with orbital-dependent potentials so the eigenfunctions are no longer invariant with respect to an orthonormal rotation of the orbitals. Furthermore the correction from this scheme vanishes for Bloch waves so that alternative basis sets, *e.g.* Wannier functions, should be employed. These complications explain why the method has been seldomly used
- A truly non-local exchange-correlation scheme is the weighted density approximation – *WDA* – (Gunnarsson, Jonson & Lundqvist, 1977; 1979; Alonso & Girifalco, 1977; 1978) which is obtained from the exact expression for the exchange-correlation energy by replacing the pair correlation functional of the non-homogeneous electron distribution by its correspondent for the homogeneous electron gas, but the correct, non-local density pre-factor is remained unlike in the local density approximation. This leads to the improved asymptotic behaviour of the exchange-correlation term, although with the wrong proportionality factor. The scheme is computationally somewhat more involved and not as straight-forward to implement as the local density and generalised gradient approximations, and the original results were not too encouraging but recently Singh (1993) has reported newer calculations with good accuracy
- The Hartree-Fock contains the correct exchange energy, the Fock term. It can be used also in the Kohn-Sham method but the potential will be derived in a different manner, *e.g.* using the method of optimised effective potential – *OEP* –, also called optimised potential method – *OPM*. This leads to a local effective potential which is the same for all the orbitals, as required to remain in the framework of the Kohn-Sham scheme. This calculation is non-trivial and an approximation, which however still requires a large amount of computation, was derived by Krieger, Li and Iafrate – *KLI* – (1992). The exact exchange leads to energies very close to the Hartree-Fock method when used without the correlation functional, but the poor knowledge of the exact correlation functional makes the very accurate calculations using the Kohn-Sham scheme difficult. However, now that the accuracy provided by the first orbital-dependent correlation functional of Colle and Salvetti (1975; 1979) has been found to be inadequate the rather new functional

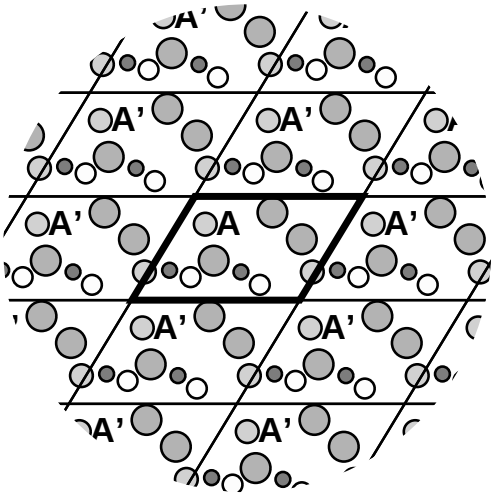

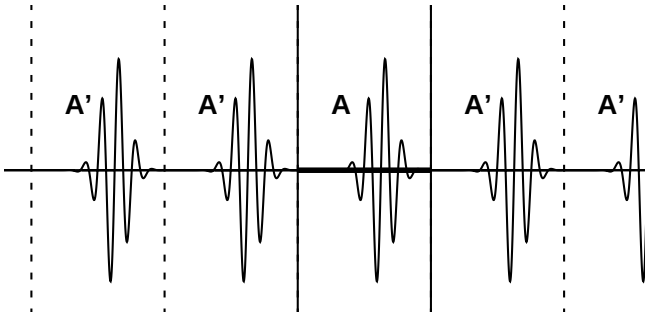

Figure 2.2: An illustration of two-dimensional periodic boundary conditions for atoms. The atom **A** and its periodic replicas **A'** are shown for one atom, and the super-cell has been emphasised

Figure 2.3: An illustration of one-dimensional periodic boundary conditions for a wave function. The super-cell is shown with the vertical solid lines, and the replicas of the wave function **A** with **A'**

(Görling & Levy, 1994; Engel *et al*, 1998) based on the perturbation theory similar to the MP2 correlation in the case of the Hartree-Fock method might provide improved results. However, the computational effort of this functional is even larger than that of the exact exchange

- Two methods, the screened exchange (Bylander & Kleinman, 1990; Seidl, 1995; Seidl *et al*, 1996) and local mass approximations (Engel & Pickett, 1996), which were recently proposed try to approximate the correct exchange-correlation term by splitting it into two parts which are known at the limiting cases of a non-homogeneous and a homogeneous electron system, and the sum of the two exchange-correlation contributions is known more accurately than the total term. The screened exchange method is computationally very demanding, whereas the local mass approximation needs less than twice the computational time of *e.g.* the corresponding calculation employing the local density approximation. The number of applications of these approximations is still scarse and has mainly concentrated on the gap problem in the semi-conductors

2.3 Methods

2.3.1 Super-cell and Brillouin zone

When calculating the electronic structure atoms, molecules or clusters the object is isolated and does not interact with other particles. However, when studying crystals in one – *e.g.* wires, chains – two – surfaces, planes – or three dimensions the number of atoms is to be considered macroscopic along the continuous direction, leading to atom densities of 10^{23} 1/cm^3. Simulating this amount of particles is, a formidable task and a simplification needs to be applied. If the system is fully periodic an obvious choice is to use the periodic boundary conditions, *i.e.* the atomic and electronic structure is repeated along the three basis vectors $\mathbf{a}_{1,2,3}$ so that if there is an atom at position $\mathbf{R}_\mathrm{I}$ there are atoms also at $\mathbf{R}_\mathrm{I} + i\mathbf{a}_1 + j\mathbf{a}_2 + k\mathbf{a}_3$ where i, j and k are integers like shown in the Figure 2.2; likewise for the electronic wave functions, in the Figure 2.3 in a one-dimensional case.

The calculational saving comes if only the atoms and electrons inside the unit cell of the calculation – called the super-cell and shown in the Figure 2.2 with the emphasised line – needs to be explicitly considered and the replicas of these objects are incorporated implicitly. In the current calculations up to hundreds of atoms in the super-cell can be treated in the density functional theory and up to millions of atoms in classical molecular dynamics calculations where the electronic degrees of freedom are not explicitly included.

If non-homogeneities are introduced to the system the periodicity is often lost; this is the case *e.g.* for point defects in crystals, perpendicular to a surface, line defects *etc.* One way of modelling such systems is still to use the periodic boundary conditions but the super-cell is chosen to be so large that the defects do not interact An example of this approach is the slab geometry – sketched in the left-most panel of the Figure 2.4 – which is used in most of the calculations of surfaces nowadays: the system is treated periodically in all the three directions but perpendicular to the surface the replicas of the slab are isolated with a large enough region of vacuum in between them; also the thickness of the slab has to be carefully chosen to prevent artificial interactions between the two surfaces. The quality of the approximation depends on the system under study: if it is *e.g.* a periodic structure of adsorbates like in the middle panel of the Figure 2.4 the lateral ordering is correctly taken into account but if an isolated molecule or a reaction as in the right-most panel of the Figure 2.4 needs to be studied a large unit cell is required.

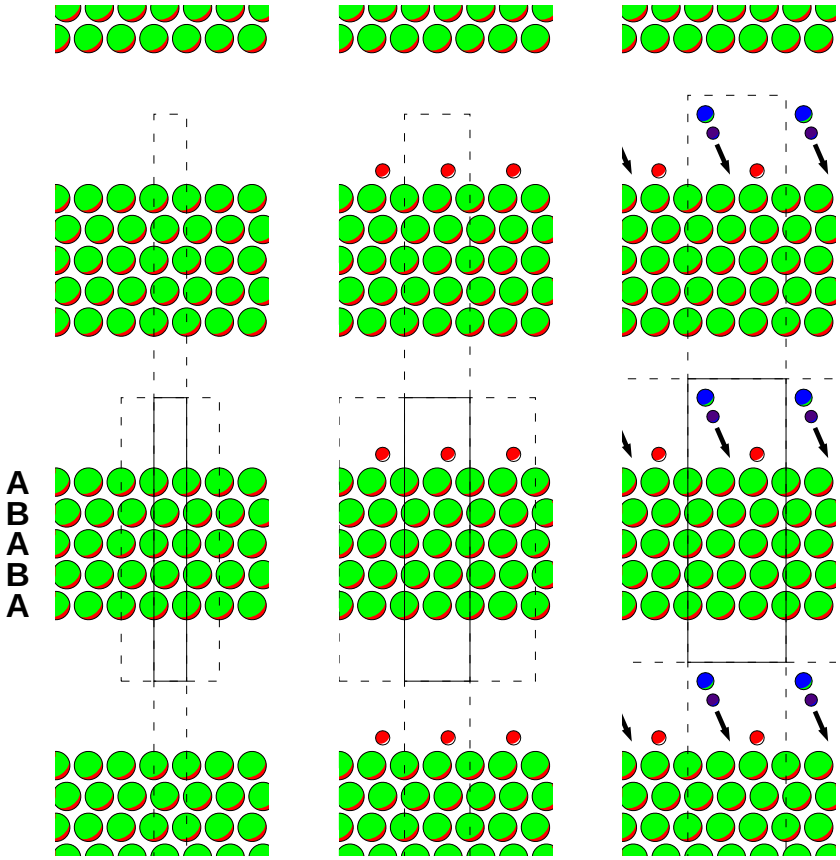

Figure 2.4: *Left* Side view of a slab geometry for a five-layer hcp slab; *Middle* The slab with adsorbates; *Right* Modelling surface reactions in the slab geometry

The reciprocal lattice of a periodic real space lattice with the three basis vectors $\mathbf{a}_{1,2,3}$ consists of the points $\mathbf{G}$ which yield

$$e^{i\mathbf{G}\cdot\mathbf{R}} = 1 \; ; \tag{2.28}$$

$\mathbf{R} = n_1\mathbf{a}_1 + n_2\mathbf{a}_2 + n_3\mathbf{a}_3$ is a point in the real space lattice with integer coefficients $n_{1,2,3}$. Bloch's Theorem – please see *e.g.* Tinkham (1964) – states that the solutions of the one-electron Hamiltonian H can be chosen as

$$\psi_{i\mathbf{k}}(\mathbf{r}) = e^{i\mathbf{k}\cdot\mathbf{r}} u_{i\mathbf{k}}(\mathbf{r}) \;\; , \tag{2.29}$$

where i is the band index, $\mathbf{k}$ is a point in the first Brillouin zone *i.e.* in the region of the reciprocal lattice closer to $\mathbf{k} = \mathbf{0}$ than any integer multiple $\mathbf{G} = m_1\mathbf{b}_1 + m_2\mathbf{b}_2 + m_3\mathbf{b}_3$ of the reciprocal lattice vectors and $u_{i\mathbf{k}}(\mathbf{r})$ is a function with the periodicity of the real space lattice so that

$$u_{i\mathbf{k}}(\mathbf{r}+\mathbf{R}) = u_{i\mathbf{k}}(\mathbf{r}) \;\; , \;\; \mathbf{R} = n_1\mathbf{a}_1 + n_2\mathbf{a}_2 + n_3\mathbf{a}_3 \; . \tag{2.30}$$

From this form it follows that

$$\psi_{i\mathbf{k}}(\mathbf{r}+\mathbf{R}) = e^{i\mathbf{k}\cdot\mathbf{R}} \psi_{i\mathbf{k}}(\mathbf{r}) \;\; , \tag{2.31}$$

or that the translation by a multiple of a lattice vector introduces a modulation of the phase of the wave function with the periodicity of the real space lattice, with equivalent densities:

$$|\psi_{i\mathbf{k}}(\mathbf{r}+\mathbf{R})|^2 = |\psi_{i\mathbf{k}}(\mathbf{r})|^2 \;\; . \tag{2.32}$$

The attractivity of Bloch's Theorem can be understood as if the sum of all wave functions extending in the whole crystal is transformed into a – still infinite – set of wave functions of a plane wave times a periodic function; the quantities containing the full set of wave functions are transformed into integrals over the $\mathbf{k}$ points in the first Brillouin zone and for example the kinetic energy and density can thus be regarded as integrals

$$E_{\mathrm{kin,s}}[\{\psi\}] = \sum_i \int_{\mathbf{k}\in 1^{\mathrm{st}}\,\mathrm{BZ}} \int_{\mathbf{r}} \psi^*_{i\mathbf{k}}(\mathbf{r}) \left(-\frac{1}{2}\nabla^2\right) \psi_{i\mathbf{k}}(\mathbf{r}) \; d\mathbf{r}\, d\mathbf{k} \tag{2.33}$$

$$n[\{\psi\}](\mathbf{r}) = \sum_i \int_{\mathbf{k}\in 1^{\mathrm{st}}\,\mathrm{BZ}} \psi^*_{i\mathbf{k}}(\mathbf{r})\, \psi_{i\mathbf{k}}(\mathbf{r}) \; d\mathbf{k} \; . \tag{2.34}$$

The advantage comes from the smooth behaviour of the integrands in these equations and thus the integrals can be transformed into sums over a finite set of $\mathbf{k}$ points like discussed in the next Section.

2.3.2 Brillouin zone summation

The sums in the Equations 2.33 and 2.34 contain an integral over the first Brillouin zone. In the general case this cannot be evaluated exactly but has to be approximated. Two approaches have been widely used:

1. The Brillouin zone is divided into sub-volumes and the energy dependence of the bands is approximated by Taylor expansion at the corner points. The mostly used approach is the linear tetrahedron method (Jepsen & Andersen, 1971; Lehmann & Taut, 1972), where the sub-volumes are tetrahedra with one **k** point at each corner of them and the energy is expanded to linear order around these points. It turns out that the weights on the points depend only on the volume of the tetrahedra, not their shape. Recently Blöchl (1989; Blöchl, Jepsen & Andersen, 1994) introduced the second-order tetrahedron method

2. Special **k** point scheme; the integral is replaced with a finite, weighted sum over a set of discrete, sometimes called "representative" points. This method is simpler than the tetrahedron method; the latter is especially well suited for the calculation of the density of states. Earlier metals constituted a problem within the special point scheme due to the abrupt step in occupation numbers between occupied and unoccupied states and thus the approach was mainly used for semi-conductors and insulators only, but the introduction of the broadening of the occupation numbers – please see the Section 2.3.3 – has enabled also the treatment of metals within the special **k** point scheme. It has been used throughout the current work and will be described below

In the special **k** point scheme a finite, weighted sum substitutes the original, continuous integral, *i.e.*

$$\frac{1}{(2\pi)^3}\int_{\mathbf{k}} f(\mathbf{k})\; d\mathbf{k} \approx \frac{1}{\Omega}\sum_{\mathbf{k}_i} w_{\mathbf{k}_i} f(\mathbf{k}_i)\;, \tag{2.35}$$

where Ω the size of the super-cell, $\mathbf{k}_i$ form the set of **k** points and $w_{\mathbf{k}_i}$ are the corresponding weights chosen to weighten the contribution from the different **k** points correctly; the **k** points are chosen to span only the irreducible part of the Brillouin zone, defined as the smallest wedge of the first Brillouin zone which can be reduced with the symmetry operations, and the sum is normalised

$$\sum_{\mathbf{k}_i} w_{\mathbf{k}_i} = 1\;. \tag{2.36}$$

Please note that for isolated systems like atoms in three, lines or chains in two and surfaces in one directions the electron system does not interact over the periodicity – provided the vacuum separating the systems is large enough – and therefore in these directions there cannot be any hybridisation of the wave functions and thus no dispersion. Thereby the integration 2.35 is exact already with a sampling of a single point, and *e.g.* the Γ point $(0,0,0)$ alone is enough for the summation over the Brillouin zone for an atom or molecule; in the case of surfaces the so-called surface Brillouin zone is two-dimensional with the periodicity corresponding the directions along the surface plane in the real space.

We shall explore the special **k** point scheme more thoroughly in the Appendix, where especially the case of Brillouin zone summation in the two-dimensional hexagonal cell, for which we have generalised a previous scheme, will be discussed.

2.3.3 Fractional occupation numbers

In defect-free insulators and semi-conductors there is an energy gap separating the occupied and unoccupied single-electron states; however, in metals the density of states is continuous across the Fermi energy and there are plenty of states above and below the Fermi energy. At zero temperature, where most of the calculations are performed, the occupation of the states would be a step function, and an excitation of infinitesimal energy would change the occupation numbers. Thus during the self-consistent iterations, when the wave functions and subsequently the density are not yet converged, the occupation numbers would change abruptly leading to instability, which is not present in the calculations for insulators and semi-conductors; also more **k** points are usually needed when calculating metals in order to approximate the integral over the Brillouin zone because of the accurate mapping of the Fermi surface, which is the iso-surface in the reciprocal space where the bands cross the Fermi energy. Traditionally two approaches have been used to prevent the oscillations:

- Interpolation of the density of states between the **k** points with the linear or quadratic tetrahedron method; please see also the Section 2.3.2

- Using fractional occupation numbers; the occupation numbers vary smoothly near the Fermi energy, thus smoothing the changes in the density and leading to a stabilised convergence to self-consistency

The tetrahedron method is still used sometimes nowadays for the densities of states, but in the self-consistent procedure the broadening schemes are employed more often. In the following we shall explain the broadening schemes used in the present work.

The use of fractional occupation numbers is an artificial method to improve the convergence of the self-consistent calculation; only the Fermi broadening scheme has any real counterpart, being the physical occupation at finite temperatures. This property has been used to generalise the density functional theory to non-zero electronic temperature by Mermin (1965). Usually the broadening is, however, much larger than the

physical temperature and the ions are at zero temperature anyway; thereby the broadening introduces an approximations which has to be subsequently corrected if possible. The corrections are called *extrapolation to zero temperature* and exist explicitly for the energy (Gillan, 1989; Kresse & Furthmüller, 1996a) in the first order but no straight-forward method exist for the forces. In the case of the Fermi broadening the occupation number of the state i at the **k** point **k** is given by

$$f_{i\mathbf{k}}(x) = \frac{1}{e^x + 1} \ , \tag{2.37}$$

where $x = (\varepsilon_{i\mathbf{k}} - \varepsilon_{\mathrm{F}})/\sigma$; ε_{F} is the Fermi energy, determined by requiring the correct amount of electrons, and σ is the width or temperature in the broadening. The free energy, which includes the artificial entropy from the electronic degrees of freedom

$$S(f_{i\mathbf{k}}) = -\left[f_{i\mathbf{k}} \ln f_{i\mathbf{k}} + (1 - f_{i\mathbf{k}}) \ln (1 - f_{i\mathbf{k}})\right] \ , \tag{2.38}$$

is

$$F = E + \sum_{i\mathbf{k}} \sigma S(x) \ . \tag{2.39}$$

The energy extrapolated to zero temperature is in the case of the Fermi broadening given by

$$E_{\sigma=0} \approx \frac{1}{2}\left[F(\sigma) + E(\sigma)\right] \ . \tag{2.40}$$

Other methods for the broadening are the Gaussian and Methfessel-Paxton (1989) broadenings. The scheme of Gaussian broadening is a special case – the zeroth order function – of the Methfessel-Paxton scheme; these two usually need no correction to the forces. The latter leads, however, to occupation number slightly larger than one and less than zero.

The stability in the initial phase of the calculation or after an ionic movement is often rather poor since the electronic structure changes still remarkably and thus too large variations in the density need to be avoided. If the eigenvalues near the Fermi energy vary a lot the changes in the occupation numbers can be limited using the damping of the eigenvalues introduced by Stumpf (1993; Stumpf & Scheffler, 1994); as the self-consistent solution is approached the occupation numbers approach their non-damped values and this scheme leads to no additional error.

2.3.4 Pseudo potentials

Because deep in energy, highly localised and thus not available for bonding, the core electrons do not usually contribute significantly to the changes in the total energy or density in different chemical environments. Therefore their inclusion explicitly in a calculation is not necessary if the potential screening the nuclear contribution $-Z/r$ arising from the core electrons and the orthogonalisation of valence electrons against the core orbitals can be arranged implicitly. This is the goal of pseudo potentials; an excellent review about the pseudo potential concept and its development has been given by Pickett (1989). The modern pseudo potentials, created usually using the neutral, free atom as the reference state, are able to reproduce accurately the valence orbitals in the chemically significant region close to the states in an all-electron calculation, *i. e.* they are *transferable* into different chemical environments.

An example of a pseudo potential is shown in the Figure 2.5: it shows a pseudo potential for a silicon atom, whose valence configuration is $3s^2 4p^2$. The potentials for different l components are different, but all approach the asymptotic limit $-Z_v/r = -4/r$ beyond the core radii inside which the potentials and pseudo wave functions are allowed to differ from their all-electron counterparts. The pseudo wave functions of the valence orbitals, *i. e.* the ground state of the Kohn-Sham equation of that angular momentum channel l with the pseudo potential as the external potential, are node-less by construction in order to make them as smooth as possible; therefore a smaller basis set is sufficient to represent the valence orbitals, which will be close to the pseudo wave function at the core region.

The break-through in transferable pseudo potentials for the density functional calculations came with the scheme of Hamann, Schlüter and Chiang (1979): they devised a straight-forward procedure to generate transferable pseudo potentials which was followed by Bachelet, Hamann and Schlüter (1982) to generate a list of pseudo potentials going through most of the Periodic Table. In their scheme Hamann, Schlüter and Chiang required the following properties:

- The ground state eigenvalues of the pseudo and all-electron potentials shall be equivalent in the reference configuration
- The pseudo and all-electron wave functions match out-side the core radius
- The norm of the corresponding wave functions

  $$4\pi \int_{r=0}^{r_c} |\phi(r)|^2 r^2 \, dr \tag{2.41}$$

  is the same for the pseudo and all-electron orbital inside the core radius r_c; this norm-conservation guarantees that the electro-static potential felt by the pseudo valence function out-side the core radius is identical to the all-electron one. The norm-conservation further ensures that the logarithmic derivative of the pseudo and all-electron wave function and their first energy derivatives agree out-side the core radius; this is important for the scattering properties of the electrons and thus for the over-all transferability of the pseudo potential.

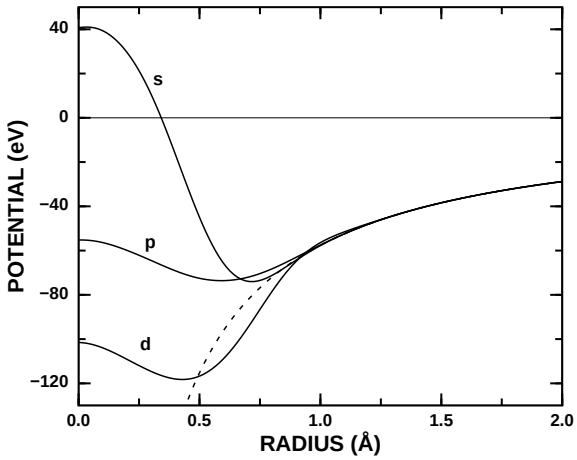

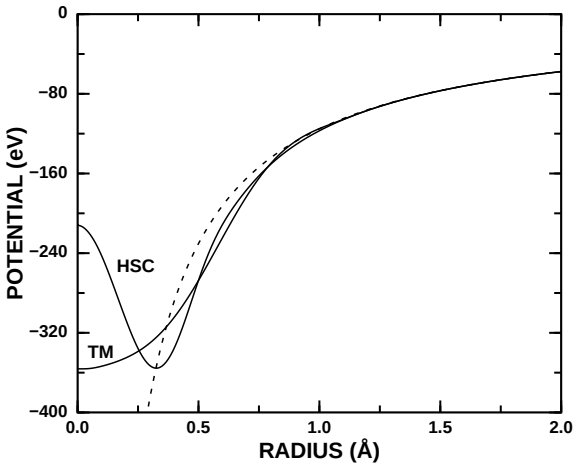

Figure 2.5: An example of a pseudo potential: A pseudo potential for silicon; the dashed line is the hard-core potential -Z_v/r

Figure 2.6: An example of a hard Hamann-Schlüter-Chiang and a soft Troullier-Martins pseudo potential for the 4*d* state of ruthenium; the dashed line is the hard-core potential -Z_v/r

Additionally the pseudo wave function and potential are constructed to be continuous up to some given derivative over the core radius. Hamann, Schlüter and Chiang used functions inside the core radii which decayed smoothly towards the all-electron counterparts and thus are not yet identical at the core radius; this might lead to errors in some cases (Martin Fuchs, personal communication).

The scheme of Hamann, Schlüter and Chiang was generalised by Hamann (1989) to allow the construction of a pseudo potential for the un-occupied or un-bound channels; Bachelet, Hamann and Schlüter used in their list of pseudo potentials an excited atom or a positively ionised ion as the configuration state for the potentials corresponding to those channels and neutral for the occupied ones, but Hamann's scheme allows one to generate a pseudo potential for all the channels in the neutral ground state.

The pseudo potentials generated using the concepts of Hamann, Schlüter and Chiang have the unpleasant feature that they are often very *hard*, *i.e.* they have rather steep maxima like in the Figure 2.6 which shows the pseudo potential for ruthenium. This sets higher requirements for the basis set used in the calculation for the solid; especially for the plane wave basis which will be introduced later this means a large increase in basis set size. The hard pseudo potentials occur mostly for the right-most second row and transition metal elements, where the 2*p* and 3*d*, 4*d* or 5*d* orbitals are very localised, especially the 2*p* and 3*d* where there is no orbital lower in energy with the same angular momentum to against which the orbital should be orthogonal and thus the orbital can remain more localised. To overcome the problem with too hard pseudo potentials new schemes were devised of which the ones by Kerker (1980), Vanderbilt (1985), Rappe *et al* (1990) and Troullier and Martins (1991) are examples; the Figure 2.6 shows also the 4*d* pseudo orbital of ruthenium generated with the scheme of Troullier and Martins, and the dip in the Hamann-Schlüter-Chiang is smoothed away. The smoother, *soft* pseudo potential are achieved by increasing the core radii, thus allowing for a larger freedom in the generation – however, the pseudo potential and wave function match now exactly the all-electron counterparts at the core radius without a decaying difference function –, by choosing a form which leads to a softer potential and in some cases setting a *penalty function* which affects the generation of the pseudo potential, trying to maximise the smoothness. The result is a large reduction in the plane wave basis set as shown in the Figure 2.7, but usually the transferability of the pseudo potentials generated according to Hamann, Schlüter and Chiang is better due to the smaller core radii used.

A more radical approach to increase the smoothness was invented by Vanderbilt (1990) and first implemented by Kari Laasonen (Laasonen *et al*, 1993). The Vanderbilt pseudo potentials are not norm-conserving in the sense that the pseudo wave function does not have to have the same norm inside the core radius as the all-electron wave function as seen in the Figure 2.8; the pseudo wave function may thus avoid the peak in the orbital – in this case the 4*d* – and thus a much softer pseudo wave function results. The charge missing from the square of the wave functions is later augmented with the missing charge. The complications arising from the charge augmentation partially diminishes the advantage gained from the lower basis set size needed as evidenced in the Figure 2.7 but still in most cases with very localised orbitals the Vanderbilt construction would save computational cost; the main obstacle for using it is the additional programming required.

The pseudo potential concept relies on the frozen-core approximation, *i.e.* that the core orbitals do not change significantly in different chemical environments. On the other hand the pseudo potential must ensure that the valence orbitals and in the reference state unoccupied orbitals are at least reasonably well reproduced since in a bonding situation these might become partially occupied or the orbitals gain some character with their angular momentum. If there are, however, energetically not much more bound states than the valence orbitals – called *semi-core* states – they may easily at least polarise and should thus be regarded as valence states; thus the same pseudo potential angular momentum channel should describe both the semi-core and unoccupied state although they are energetically rather far separated. A problematic example is cesium where the 4*f* states affect the screening of 5*s* and 5*p* electrons, and the originally unoccupied 6*p* is not much higher

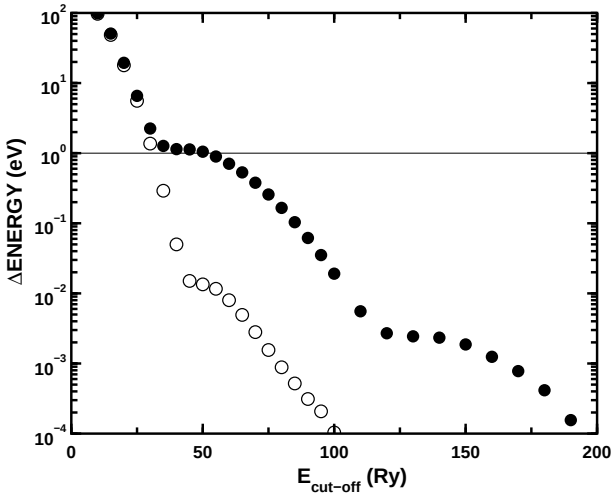

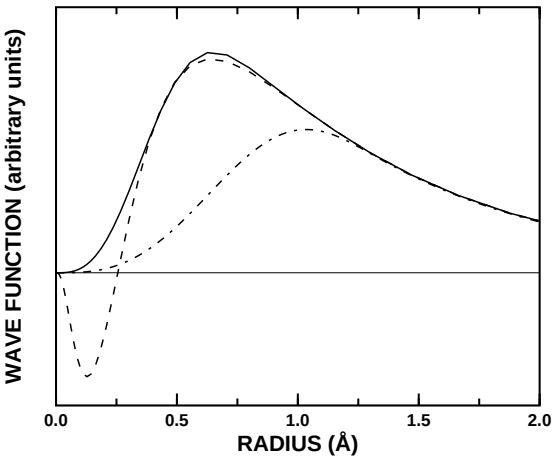

Figure 2.7: The convergence of the total energy with the plane wave basis size for different pseudo potentials in bulk platinium; a Hamann – filled circles – and a Troullier-Martins – empty circles – pseudo potential was used

Figure 2.8: An example of the pseudo wave function – times radius r – of the Troullier-Martins – solid line – and Vanderbilt ultra-soft – dot-dashed line – pseudo potential for the $4d$ orbital of ruthenium. The all-electron wave function is shown with a dashed line

in energy and becomes thus partially occupied in the calculation for the solid.

A convenient form to calculate the action of the pseudo potential to the orbitals $\psi_{i\mathbf{k}}$ would be fully *non-local* around the atom I:

$$V_{\mathrm{ps}}^{I}(\mathbf{r}) = V_{\mathrm{local}}(\mathbf{r}-\mathbf{R}_I) + \sum_{lm} |\eta_l(|\mathbf{r}-\mathbf{R}_I|)\rangle \left| lm\left(\widehat{\mathbf{r}-\mathbf{R}_I}\right)\right\rangle \left\langle lm\left(\widehat{\mathbf{r}'-\mathbf{R}_I}\right)\right| \langle \eta_l(|\mathbf{r}'-\mathbf{R}_I|)| \ , \tag{2.42}$$

since then the matrix elements become – the ionic coordinate $\mathbf{R}_I$ has been shifted to the origin for clarity –

$$\begin{aligned} \langle\chi_1(\mathbf{r})|\, V_{\mathrm{ps,nl}}\, |\chi_2(\mathbf{r}')\rangle &= \langle\chi_1(\mathbf{r})|V_{\mathrm{local}}(\mathbf{r})\delta(\mathbf{r}-\mathbf{r}')|\chi_2(\mathbf{r}')\rangle \\ &+ \sum_{lm} [\langle\chi_1(\mathbf{r})|\eta_l(|\mathbf{r}|)\rangle|lm(\widehat{\mathbf{r}})\rangle] \left[\langle lm(\widehat{\mathbf{r}'})|\langle\eta_l(|\mathbf{r}'|)|\chi_2(\mathbf{r}')\rangle\right] \end{aligned} \tag{2.43}$$

now the inner products $\langle\chi_1(\mathbf{r})|\eta_l(|\mathbf{r}|)\rangle|lm(\widehat{\mathbf{r}})\rangle$ can be calculated independently from $\langle lm(\widehat{\mathbf{r}'})|\langle\eta_l(|\mathbf{r}'|)|\chi_2(\mathbf{r}')\rangle$ – they are naturally the complex conjugates of each other – and thus the calculation scales only linearly with the number of basis functions. This is in contrast to the so-called semi-local form, where a matrix element involve integrals over both χ_1 and χ_2. This kind of construction was achieved by Kleinman and Bylander (1982) and is in use in most of the pseudo potential calculations. The pseudo potential term of Kleinman and Bylander reads as

$$\begin{aligned} V_{\mathrm{ps}}(\mathbf{r}) &= V_{\mathrm{local}}(\mathbf{r}) + \sum_{lm} \left|\Delta V_{\mathrm{ps}}^{l}(r)\,\phi_l(r)\right\rangle |lm\rangle\, E_{\mathrm{KB}}^{l}\, \langle lm| \left\langle \Delta V_{\mathrm{ps}}^{l}(r')\,\phi_l(r')\right| \\ E_{\mathrm{KB}} &= \frac{1}{\left\langle \phi_l(r)\,\Delta V_{\mathrm{ps}}^{l}(r)\,\phi_l(r)\right\rangle} \ . \end{aligned} \tag{2.44}$$

In addition to the calculational saving the Kleinman-Bylander construction unfortunately brings a disadvantage: it can lead to wrong ordering of the eigensolutions of the pseudo potential, *i.e.* there is a state – called a *ghost* state – lower in energy than the node-less wave function of reference state; this has to have nodes in order to be orthogonal to the wave function of the reference state. The origin of and ways to avoid the ghost states has been studied by Gonze and co-workers (Gonze, Käckell & Scheffler, 1990; Gonze, Stumpf & Scheffler, 1991), and generalised to the pseudo potentials with multiple projectors with the same angular quantum number by Khein (1995). In the semi-local form a corollary of the Wronskian theorem (Messiah, 1974) prevents the ghost states but this theorem is not valid in the fully separable Kleinman-Bylander form. The existence of a ghost state is disastrous in the calculation for a solid and therefore they must not exist in the pseudo potentials; a careful construction of the pseudo potential and choice of the local component enable the use of the Kleinman-Bylander construction free of ghost states for about all the elements of the Periodic Table (Stumpf, Gonze & Scheffler, 1990). Furthermore, there are now straight-forward tests which indicate the existence of ghost states already before the pseudo potential has been used in a calculation for a solid. However, the fully non-local form has always a worse quality than the semi-local form and although there would not exist any real ghost states sometimes a state with node is in energy close above the reference state, called a *pseudo* ghost state, so although it is not classified as a real ghost it affects the properties calculated using the pseudo potential.

A good transferability for a pseudo potential is achieved if the pseudo potential reproduces well the results which would be obtained from an all-electron calculation. A failure in the logarithmic derivatives, which were

earlier used to justify the quality of a pseudo potential, is indicative of serious problems but not a real test for the transferability. As another indicator of the transferability the change of the properties of the pseudo potential and an all-electron atom can be compared when the system is perturbed from its reference state. Such a test – called the *hardness* test due to its similarity to the hardness/softness concept in chemistry – is to follow the change in total energy and Kohn-Sham eigenvalues when the occupation numbers are changed. Teter (1993; Filippetti *et al*, 1997) suggested using the hardness as an ingredient in the process of creating the pseudo potential in order to guarantee a high transferability. The traditional definition of hardness does consider only spherical perturbations and therefore does not fully probe the transferability of a pseudo potential; an extension to non-spherical perturbations was discussed by Filippetti *et al* (1995).

In summary, the pseudo potential concept consists of the following approximations:

- Frozen-core approximation: the core electrons are not allowed to change in different environments
- Pseudisation: the potential seen by the valence electrons has been modified, and they no longer contain the correct radial nodes and are not explicitly orthogonalised against the core electrons
- Linearisation: the exchange-correlation functional is not linear in the un-screening process; the error arising from this can, however, be partially or fully avoided by using the pseudo core or true core electron density (Louie, Froyen & Cohen, 1982)
- Separation to non-local form: this is not always done but in most calculations the Kleinman-Bylander construction is used

In the current work we have used the Troullier-Martins pseudo potentials since we are mainly investigating solids with $4d$ and $2p$ elements. The potentials were generated using the fully relativistic generator written by José-Luis Martins (Troullier & Martins, 1991) and the program `psgen` in the package `gncpp` – for *Generalised Norm-Conserving Pseudo Potentials* – maintained by Martin Fuchs (Martin Fuchs, personal communication; Fuchs & Scheffler, 1998) based on the code by Hamann (1989). The potentials were tested against ghost states with the program `pswatch` in `gncpp`, and the transferability tests were performed in different atomic electronic states with the scripts provided in `gncpp`. Kleinman-Bylander form was used for all the atoms except the few Vanderbilt pseudo potentials employed during this work.

2.4 Implementation

Before the Kohn-Sham equations can be solved numerically a few approximations must be introduced. We will in the following discuss some of the major issues used to achieve the computationally attainable approach of the present work. Unfortunately due to limitation of space and to preserve compactness other methods like the full-potential linearised augmented plane wave – *FLAPW*, please see *e.g.* Singh (1994) –, projected augmented wave – *PAW*, Blöchl (1994) –, full-potential linearised muffin-tin orbital – *FP-LMTO*, please see *e.g.* Dietrich (1988) –, real space multi-grid methods – please see *e.g.* Arias, (1999) – and linear scaling methods – Goedecker (1999) – cannot be described here.

2.4.1 Basis sets — plane waves

Whereas the Kohn-Sham equations are continuous the computers work with a discrete and finite set of numbers, a task which is achieved employing a limited set of basis functions, called the basis set. Thus the ith state at the point $\mathbf{k}$ in the Brillouin zone is represented as

$$\psi_{i\mathbf{k}}(\mathbf{r}) = \sum_{n=1}^{N_{\text{basis}}} c_{i\mathbf{k},n}\,\chi_n(\mathbf{r}) \ , \tag{2.45}$$

where n goes through the basis functions $\chi_n(\mathbf{r})$ up to a finite count N_{basis}, and $c_{i\mathbf{k},n}$ are the expansion coefficient, *i.e.* plain numbers. The idea is that the operations acting on χ_n needed to solve the Kohn-Sham equations can be calculated, either analytically or numerically, and thus a straight-forward implementation leads to the equations

$$\sum_n c_{i\mathbf{k},n} H \chi_n(\mathbf{r}) = \varepsilon_i \sum_n c_{i\mathbf{k},n} \chi_n(\mathbf{r}) \ . \tag{2.46}$$

Multiplying with χ_m^* from the left and integrating over the space these equations become

$$\sum_n c_{i\mathbf{k},n} H_{mn} = \varepsilon_i \sum_n c_{i\mathbf{k},n} \mathcal{O}_{mn} \ , \qquad H_{mn} = \langle \chi_m | H | \chi_n \rangle \ , \qquad \mathcal{O}_{mn} = \langle \chi_m | \chi_n \rangle \ . \tag{2.47}$$

These equations can be expressed in a matrix form, noting that the $\mathbf{k}$ points are independent, as

$$\underline{\mathbf{H}}\mathbf{c} = \underline{\varepsilon}\mathcal{O}\mathbf{c} \ , \qquad \underline{\mathbf{H}}_{mn} = H_{mn} \ , \qquad \underline{\mathbf{c}}_{ni} = c_{i\mathbf{k},n} \ , \qquad \underline{\mathbf{O}}_{mn} = \mathcal{O}_{mn} \ . \tag{2.48}$$

This is a generalised – due to the over-lap matrix $\mathcal{O}$ – matrix eigenvalue problem which can be solved by a direct diagonalisation of the matrix $\underline{\mathbf{H}}$. However, the diagonalisation scales in the third power and the storage needed

in the square of the matrix size – in this case the matrix size is given by the number of basis functions N_{basis} – and an iterative method avoiding the direct diagonalisation will become advantageous in large systems; we will return to this later when discussing the Car-Parrinello method.

The following list governs some of the different kind of basis set functions in use nowadays.

- "Basis-set free" methods: logarithmic meshes, an equidistance grid; these can, however, also be regarded as basis sets with δ-functions as the basis functions
- Atom-centred functions: Gaussians, atomic orbitals, mixed basis, ...
- Equidistance mesh and adaptions: wavelets, plane waves, ...

The choice of the optimal basis set for the system at hand depends on the system and problem at hand.

One of the most widely used basis set is the plane wave basis. This is because of its simplicity and high efficiency, although the latter advantage is diminished by the large number of plane waves needed. The plane wave is a periodic function and is as such suitable as $u(\mathbf{r})$ in the Bloch theorem; thereby the Kohn-Sham state can be expressed as

$$\psi_{i\mathbf{k}}(\mathbf{r}) = \sum_{\mathbf{G}}^{\mathbf{G}_{\max}} c_{i\mathbf{k}}(\mathbf{G})\, e^{\mathrm{i}(\mathbf{k}+\mathbf{G})\cdot\mathbf{r}} \ , \tag{2.49}$$

where the set of $\mathbf{G}$ vectors is limited to those which have the periodicity of the real space unit cell; thus

$$\mathbf{G} = i\mathbf{b}_1 + j\mathbf{b}_2 + k\mathbf{b}_3 \tag{2.50}$$

with $\mathbf{b}$'s being the reciprocal lattice vectors, *i. e.* the $\mathbf{G}$ vectors are simply integer multiples of the $\mathbf{b}$'s. The plane waves are also often written in the bra-ket notation as

$$e^{\mathrm{i}(\mathbf{k}+\mathbf{G})\cdot\mathbf{r}} = |\mathbf{k}+\mathbf{G}\rangle \quad , \qquad \left[e^{\mathrm{i}(\mathbf{k}+\mathbf{G})\cdot\mathbf{r}}\right]^* = e^{-\mathrm{i}(\mathbf{k}+\mathbf{G})\cdot\mathbf{r}} = \langle\mathbf{k}+\mathbf{G}| \ . \tag{2.51}$$

The plane waves have the following useful properties:

- They are orthogonal,[1] *i. e.*

$$\langle\mathbf{g}|\,\mathbf{g}'\rangle = \int_{\mathbf{r}} e^{-\mathrm{i}\mathbf{g}\cdot\mathbf{r}} e^{\mathrm{i}\mathbf{g}'\cdot\mathbf{r}}\, d\mathbf{r} = \delta_{\mathbf{g}\mathbf{g}'} \ , \tag{2.52}$$

  where the integration is over the unit cell volume; thereby the overlap matrix in the Equation 2.47 becomes diagonal unit matrix and therefore vanishes from the eigenvalue problem.
- The plane wave set is complete, *i. e.* any function can be unambiguously represented using them
- The discrete Fourier transform can be used to transfer functions from real to reciprocal space; especially beneficial is the Fast Fourier Transform – FFT – variant of the discrete Fourier transform; this will be discussed below

Some terms of the Kohn-Sham energy and potential are easily evaluated using the plane wave basis in the reciprocal space – one example is the kinetic energy

$$E_{\text{kin}} = \sum_{i\mathbf{k}} f_{i\mathbf{k}} w_{\mathbf{k}} \int_{\mathbf{r}} \psi^*_{i\mathbf{k}}(\mathbf{r}) \left(-\frac{1}{2}\nabla^2\right) \psi_{i\mathbf{k}}(\mathbf{r})\ d\mathbf{r} = \frac{1}{2}\sum_{i\mathbf{k}} f_{i\mathbf{k}} w_{\mathbf{k}} \sum_{\mathbf{G}}^{N_{\mathbf{G}}} |\mathbf{k}+\mathbf{G}|^2 \left|c_{i\mathbf{k}}(\mathbf{G})\right|^2 \tag{2.53}$$

– since the expression is *diagonal* in the reciprocal space like the matrix element of the Hamiltonian,

$$\langle\mathbf{k}+\mathbf{G}|\,\hat{T}\,|\mathbf{k}+\mathbf{G}'\rangle = \underbrace{\left.\begin{pmatrix} |\mathbf{k}+\mathbf{G}_0|^2 & 0 & 0 & \dots & 0 \\ 0 & |\mathbf{k}+\mathbf{G}_1|^2 & 0 & \dots & 0 \\ 0 & 0 & \ddots & & \vdots \\ \vdots & \vdots & & \ddots & 0 \\ 0 & 0 & \dots & 0 & |\mathbf{k}+\mathbf{G}_{N_{\mathbf{G}}}|^2 \end{pmatrix}\right\}\mathbf{G}}_{\mathbf{G}'} \ , \tag{2.54}$$

i. e. it contains only a single summation over $\mathbf{G}$ and not over both $\mathbf{G}$ and $\mathbf{G}'$; it could be also written as include the sum

$$\sum_{\mathbf{G}\mathbf{G}'} \delta_{\mathbf{G}\mathbf{G}'} \ . \tag{2.55}$$

The early approach until the early 1980's was to calculate all the terms in the reciprocal space but *e. g.* the energy from the local part of the pseudo potential becomes a convolution

$$E_{\text{ps,local}} = \int_{\mathbf{r}} n(\mathbf{r})\, V_{\text{ps,local}}(\mathbf{r})\ d\mathbf{r} = \sum_{\mathbf{G}\mathbf{G}'} n^*(\mathbf{G})\, V_{\text{ps,local}}(\mathbf{G}-\mathbf{G}') \ , \tag{2.56}$$

[1] It is common to leave out the index $\mathbf{k}$ from $\mathbf{k}+\mathbf{G}$ and think of $\mathbf{G}$ as a generalised wave vector index no longer as discrete multiples of the reciprocal lattice vectors; in such context we shall use lowercase $\mathbf{g}$ to denote them

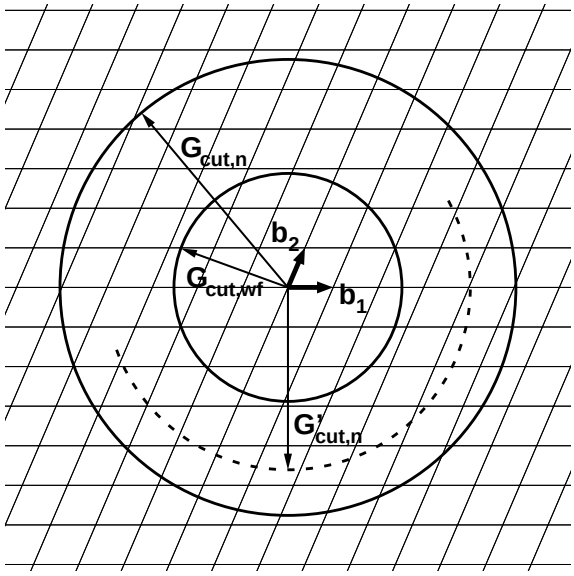

Figure 2.9: The construction of $\mathbf{G}$ vectors in two-dimensions. $\mathbf{b}_1$ and $\mathbf{b}_2$ are the reciprocal lattice vectors and all the crossings of the line give a $\mathbf{G}$ vector. The cut-off spheres for the wave functions $G_{\mathrm{cut,wf}}$ and density $G_{\mathrm{cut,n}} = 2\,G_{\mathrm{cut,wf}}$ as well as for density with duelling $G_{\mathrm{cut,n}} < 2\,G_{\mathrm{cut,wf}}$ are shown, the latter partially, with a dashed line. Please note that $\mathbf{k} = 0$ was used for the cut-off sphere of the wave functions

where $n(\mathbf{G})$ and $V_{\mathrm{ps,local}}(\mathbf{G})$ are the Fourier transforms of the density and local part of the pseudo potential into the reciprocal space, respectively. Now this term contains a double sum and is very costly to calculate, and furthermore scales in the square power of the number of the plane waves whereas in the real space the operation scales linearly. It is advantageous to take benefit of the FFT in this context; namely, the convolutions in the reciprocal space are diagonal in the real space and vice versa. Thus one calculates the terms diagonal in the space where the term is diagonal and uses FFT to transform between the two spaces when needed. The FFT scales only as $N_{\mathbf{G}} \ln(N_{\mathbf{G}})$ with the number of plane waves and thus quickly leads to large savings in the computational time.

It is interesting to further notice that an inner product can be calculated as easily in the real as in the reciprocal space since

$$\begin{aligned} \langle f(\mathbf{r}) \,|g(\mathbf{r})\rangle_{\mathbf{r}} &= \int_{\mathbf{r}} f^*(\mathbf{r})\, g(\mathbf{r})\, d\mathbf{r} = \int_{\mathbf{r}'}\int_{\mathbf{r}} f^*(\mathbf{r}) \underbrace{\int_{\mathbf{g}} e^{-\mathbf{i}\mathbf{g}\cdot\mathbf{r}} e^{\mathbf{i}\mathbf{g}\cdot\mathbf{r}'}\, d\mathbf{g}}_{\delta(\mathbf{r}-\mathbf{r}')}\, g(\mathbf{r}')\, d\mathbf{r}'\, d\mathbf{r} \\ &= \int_{\mathbf{g}} f^*(\mathbf{g})\, g(\mathbf{g})\, d\mathbf{g} = \langle f(\mathbf{g}) \,|g(\mathbf{g})\rangle_{\mathbf{g}} \end{aligned} \tag{2.57}$$

The number of plane waves is typically limited in the calculations using a so-called cut-off energy E_{cut}, which is defined as the kinetic energy of the largest frequency or longest $\mathbf{G}$ vector in the expansion:

$$\frac{1}{2}\left|\mathbf{k}+\mathbf{G}\right|^2 \leq E_{\mathrm{cut}} \tag{2.58}$$

at each $\mathbf{k}$. Thus the cut-off energy defines a sphere – illustrated in the Figure 2.9 in two dimensions – in the reciprocal space which contains all the $\mathbf{G}$ vectors. The cut-off energy is mainly set by the density close to the nuclei even when employing pseudo potentials, and thus depends on the material in use: the more localised states it contains, the higher the cut-off required. Especially demanding for a high cut-off are hydrogen, the $2p$, $3d$ materials, and always the materials where semi-core states have to be included in the plane wave expansion. Thus especially the materials where a new l channel is only partially occupied are difficult since it is more localised than in the elements below them in the Periodic Table where the orthogonalisation against the lower-lying orbital with the same l quantum number forces the orbital to be more de-localised. The cut-off energy is traditionally expressed in Rydberg units; this is convenient since the square of the maximum length of the $\mathbf{G}$ vectors is the same number in Hartree's.

As can be deduced from the definition of the cut-off energy the number of plane waves inside the cut-off sphere scales linearly with the volume of the system as for example doubling the volume would correspond to halving one of the reciprocal lattice vectors $\mathbf{b}$ and thus doubling the density of $\mathbf{G}$ vectors within the cut-off sphere. This holds also for increasing the empty vacuum in *e.g.* cluster or surface systems; this is not the case for the basis sets whose basis functions are localised at the atoms. This is one of the main reasons which lead Francois Gygi (1992) to apply the method of adaptive coordinates to the electronic structure calculations; there the problem is largely intervened by having grid points only in the physically relevant area. Another often appearing disadvantage of plane waves is that they always have the periodicity of the super cell used, even for

clusters and surfaces parallel to the surface; then the only chance to avoid artificial interactions is to separate the objects with enough space to decouple the electron densities.

The density from the Kohn-Sham orbitals is easily calculated real space, and it is diagonal in the $\mathbf{k}$ space:

$$n(\mathbf{r}) = \sum_{i\mathbf{k}} f_{i\mathbf{k}} w_{\mathbf{k}} |\psi_{i\mathbf{k}}(\mathbf{r})|^2 \quad . \tag{2.59}$$

Because the density no longer contains the $\mathbf{k}$ points the Fourier transform of the density contains only reciprocal vectors $\mathbf{G}$ but now to two times larger wave vectors as easily demonstrated by investigating the square of function $\cos x + \sin x$:

$$(\cos x + \sin x)^2 = 1 + \sin(2x) \quad , \tag{2.60}$$

i.e. the oscillations of a square of a function can contain frequencies twice higher than the function itself. Similarly to the density all the potential terms except the non-local part of the pseudo potential contain wave vectors on up to $|\mathbf{G}_{\mathrm{cut,n}}| = 2|\mathbf{G}_{\mathrm{cut,wf}}|$, and thus $E_{\mathrm{cut,n}} = 4E_{\mathrm{cut,wf}}$. The factor 4 can usually be reduced from its ideal value to about 2.5...3 – a trick to save some computer time called dualling (Remler & Madden, 1990) and depicted in the Figure 2.9 – when employing the local density approximation but should be not reduced at least as much when using more complicated exchange-correlation functionals like *e.g.* the generalised gradient approximation because these require a higher precision due to their higher non-linearity. Since all the operations on wave functions involve also the density or local potential all the FFT's have to performed in the grid which comprises all the $\mathbf{G}$ vectors of the density, *i.e.* up to $G_{\mathrm{cut,n}}$. Therefore the duelling is very efficient way to save computational time with small loss of accuracy: the wave functions are stored accurately, only the length of the FFT's is reduced; the errors are in the density and potentials.

An interesting property of the FFT is that it is exact on the grid points, *i.e.* a function in the reciprocal space is correctly transformed to the real space grid points and vice versa – the finite cut-off causes errors only in between the grid points in real space and in wave vectors beyond the cut-off energy. In principle one can use a finer FFT grid than required by the cut-off energy but as soon as the back-transformed functions are used in the reciprocal space the advantage is lost. A similar trick of "double grid", when executed consistently – like often done when employing the Vanderbilt pseudo potentials (Laasonen *et al*, 1993) – , leads to an improved accuracy, though.

A three-dimensional FFT consists of three subsequent one-dimensional FFT's along each of the lattice vectors; this is visualised in the Figure 2.10. It is easy to understand this if one looks at the definition of the discrete Fourier transform:

$$\begin{aligned} \mathcal{F}[f(\mathbf{r})](\mathbf{g}) &= f(\mathbf{g}) = \sum_{\mathbf{r}} f(\mathbf{r}) e^{\mathrm{i}\mathbf{g}\cdot\mathbf{r}} \\ &= \sum_{x,y,z} f(x,y,z) e^{\mathrm{i}(g_x x + g_y y + g_z z)} = \sum_z \left\{ \sum_y \left[\sum_x f(x,y,z) e^{\mathrm{i}g_x x} \right] e^{\mathrm{i}g_y y} \right\} e^{\mathrm{i}g_z z} \end{aligned} \tag{2.61}$$

and similarly for a non-rectangular case. This can be made use of in the parallelisation of the FFT as will be discussed below.

Because the radius of the cut-off sphere for the wave functions is only half of the radius for the density and the FFT's are three-dimensional the computational time can be slightly reduced by in the first two dimensions neglecting the transforms which contain only regions with zeroes; this is illustrated in the Figure 2.11.

One very useful benefit from working in the reciprocal space is that the calculation of atom-centred properties becomes very efficient and continuous with respect to a move of the atoms. This is because if a function f depends on the position $\mathbf{R}_{\mathrm{I}}$ of the ion I then

$$\begin{aligned} \mathcal{F}[f(\mathbf{r} - \mathbf{R}_{\mathrm{I}})](\mathbf{g}) &= \int_{\mathbf{r}} f(\mathbf{r} - \mathbf{R}_{\mathrm{I}}) e^{\mathrm{i}\mathbf{g}\cdot\mathbf{r}} d\mathbf{r} = \int_{\mathbf{r}'} f(\mathbf{r}') e^{\mathrm{i}\mathbf{g}\cdot(\mathbf{r}' + \mathbf{R}_{\mathrm{I}})} d\mathbf{r}' \\ &= e^{\mathrm{i}\mathbf{g}\cdot\mathbf{R}_{\mathrm{I}}} \int_{\mathbf{r}'} f(\mathbf{r}') e^{\mathrm{i}\mathbf{g}\cdot\mathbf{r}'} d\mathbf{r}' = e^{\mathrm{i}\mathbf{g}\cdot\mathbf{R}_{\mathrm{I}}} \mathcal{F}[f(\mathbf{r})] \quad , \end{aligned} \tag{2.62}$$

i.e. the atomic position enters only as a phase factor; in the real space an interpolation to the grid points would be necessary. Also the gradients with respect to $\mathbf{r}$ and ionic positions $\mathbf{R}_{\mathrm{I}}$ are trivial:

$$\begin{aligned} \frac{\partial}{\partial \mathbf{r}} f(\mathbf{r}) &= \sum_{\mathbf{g}} \mathrm{i}\mathbf{g} f(\mathbf{g}) e^{\mathrm{i}\mathbf{g}\cdot\mathbf{r}} = \mathcal{F}^{-1}[\mathrm{i}\mathbf{g} f(\mathbf{g})] \\ \frac{\partial}{\partial \mathbf{R}_{\mathrm{I}}} f(\mathbf{r} - \mathbf{R}_{\mathrm{I}}) &= \sum_{\mathbf{g}} \mathrm{i}\mathbf{g} e^{\mathrm{i}\mathbf{g}\cdot\mathbf{R}_{\mathrm{I}}} f(\mathbf{g}) e^{\mathrm{i}\mathbf{g}\cdot\mathbf{r}} = \mathcal{F}^{-1}\left[\mathrm{i}\mathbf{g} e^{\mathrm{i}\mathbf{g}\cdot\mathbf{R}_{\mathrm{I}}} f(\mathbf{g})\right] \quad . \end{aligned} \tag{2.63}$$

The latter equation guarantees also a very convenient way of calculating the forces acting on the ions. The evaluation of the forces is extremely trivial because the basis set does not depend on the atomic positions and is complete; therefore the forces are obtained from the formulation

$$\mathbf{F}_{\mathrm{I}} = -\frac{\partial E_{\mathrm{tot}}}{\partial \mathbf{R}_{\mathrm{I}}} \tag{2.64}$$

where no Pulay corrections (Pulay, 1969), which are often difficult to evaluate, are necessary.

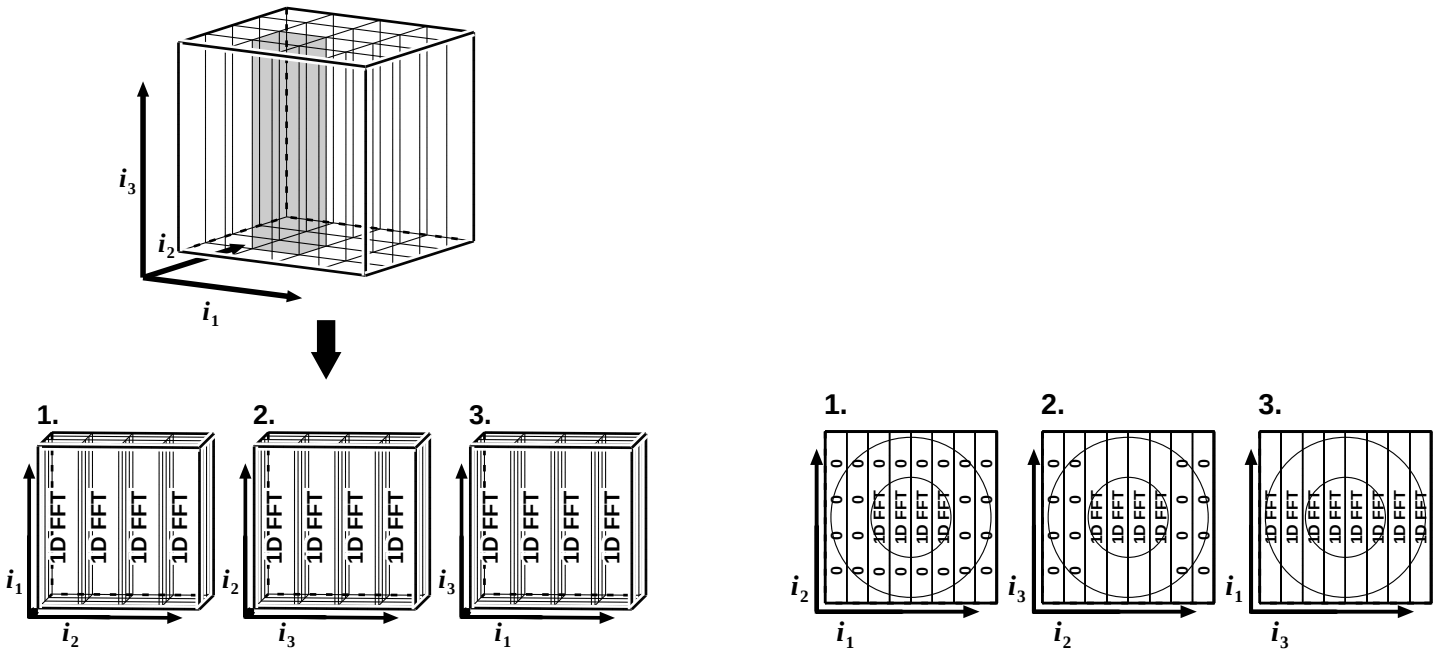

Figure 2.10: The three-dimensional fast Fourier transform as three subsequent one-dimensional transforms. The directions i are aligned along the three directions of the fast Fourier transform, and they are always orthogonal

Figure 2.11: The savings in the 3D FFT for a wave function which are possible to achieve in passing from the reciprocal space to real space thanks to the zeroes outside the cut-off sphere for the wave function; the transfer from real to reciprocal space would proceed in the same manner from right to the left

2.4.2 The Car-Parrinello method – iterative schemes

A major breakthrough for the realistic simulation of materials using electronic structure calculations was achieved in 1985 when Roberto Car and Michele Parrinello introduced a scheme which iteratively solved the electron structure while the ions were moved according to molecular dynamics; iteratively means that the Hamiltonian matrix is not diagonalised exactly at each electronic iteration. The iterative approach is natural also because the problem is self-consistent, therefore many exact diagonalisations are required, and the scheme of Car and Parrinello was able to make very efficient use of the Fast Fourier Transform – *FFT*. In the framework of the iterative procedure the wave functions are up-dated using information of the current wave function and possibly the previous iterations. Most of the algorithms proposed after the original work of Car and Parrinello are designed to optimise the electron structure – *i.e.* minimise the total energy with respect to the electronic degrees of freedom; they include the Williams-Soler algorithm (1987), second-order equations of motion (Payne *et al*, 1992; Tassone, Mauri & Car, 1994), conjugate gradient method (Gillan, 1989; Arias, Payne & Joannopoulos, 1992; Kresse, 1993; Kresse & Furthmüller, 1996a,b) and direct inversion in iterative subspace or the residual minimisation (Pulay, 1980; Wood & Zunger, 1985; Hutter, Lüthi & Parrinello, 1994; Kresse & Furthmüller, 1996a). The original Car-Parrinello dynamics has also been enhanced (Tassone, Mauri & Car, 1994; Tuckerman & Parrinello, 1994a,b; Hutter, Tuckerman & Parrinello, 1995) and it has been extended into path integrals (Marx & Parrinello, 1994; 1996; Tuckerman *et al*, 1996). Here we shall describe mainly only the approach based on equations of motion to up-date the wave functions but many features are transferable to the case of the other schemes also; further details of them can be found *e.g.* in the work of Kresse *et al* (1993; Kresse & Furthmüller, 1996a,b).

In the iterative methods using "equations of motion" – this should not be confused with the real dynamics of the electrons – the wave function of the next iteration is a linear combination of the present wave function, possibly the wave functions of the previous iterations and the residual $R(\mathbf{r})$ acting on the current state, *e.g.*

$$\begin{aligned} \psi^{n+1}(\mathbf{r}) &= \psi^{n}(\mathbf{r}) + f(\mathbf{r})\, R(\mathbf{r}) \\ \psi^{n+1}(\mathbf{r}) &= -\psi^{n-1}(\mathbf{r}) + \psi^{n}(\mathbf{r}) + \alpha\dot{\psi}(\mathbf{r}) + f(\mathbf{r})\, R(\mathbf{r}) \ , \quad \dot{\psi}(\mathbf{r}) = \psi^{n}(\mathbf{r}) - \psi^{n-1}(\mathbf{r}) \end{aligned} \tag{2.65}$$

for a first- and second-order equation of motion, respectively; n is the index for the iteration, α a coefficient equivalent to friction and $f(\mathbf{r})$ is a function whose magnitude controls the amount of change and shape the weighting in different parts of the cell; its form is in principle arbitrary and can be chosen to deliver fastest rate of convergence. Ideally it would resemble the inverse of the residual since then the wave functions would change approximately with the same amount everywhere and the magnitude of f is not limited by fast changing regions; this is called *pre-conditioning* and will be discussed below.

The residual is the difference between the current state $\psi_{i\mathbf{k}}(\mathbf{r})$ and the true eigen-state of the present Hamiltonian; however, as the latter is not known it is approximated by the product

$$R_{i\mathbf{k}}(\mathbf{r}) = -\left[H(\mathbf{r}) - \varepsilon_{i\mathbf{k}}\mathcal{S}\right]\psi_{i\mathbf{k}}(\mathbf{r}) \ . \tag{2.66}$$

$$\text{Input: } \psi_{i\mathbf{k}}(\mathbf{G}) = c_{i\mathbf{k}}(\mathbf{G}),\ V_{\text{loc}}(\mathbf{r}),\ B^I_{lm,i},\ \beta^I_{l'm'}(\mathbf{G})$$

Reciprocal space		Real space
$c_{i\mathbf{k}}(\mathbf{G})$	$\text{FFT}^{-1} \Longrightarrow$	$\psi_{i\mathbf{k}}(\mathbf{r})$
		$\Downarrow$
$H_{\text{kin+loc}}\psi_{i\mathbf{k}} = \lvert\mathbf{k}+\mathbf{G}\rvert^2 c_{i\mathbf{k}}(\mathbf{G}) + [V_{\text{loc}}\psi_{i\mathbf{k}}](\mathbf{G})$	$\Longleftarrow \text{FFT}$	$V_{\text{loc}}(\mathbf{r})\,\psi_{i\mathbf{k}}(\mathbf{r})$

$$H_{\text{pp}_{\text{non-loc}}}\psi_{i\mathbf{k}}(\mathbf{G}) = \sum_I \sum_{l'm',lm} D^{\mathcal{I}}_{l'm',lm}\beta^I_{l'm'}(\mathbf{G})\,B^I_{lm,i}$$

$$H\psi_{i\mathbf{k}} = H_{\text{kin+loc}}\psi_{i\mathbf{k}} + H_{\text{pp}_{\text{non-loc}}}\psi_{i\mathbf{k}}$$

Figure 2.12: The schematic illustration of the Hamiltonian operating on the wave function in the Car-Parrinello method implemented in the Kohn-Sham framework

$\mathcal{S}$ comes from the Vanderbilt construction and is a consequence of the generalised ortho-normalisation constraint (Laasonen *et al*, 1993). The residual can also be viewed as the force, or the partial derivative of the total energy with respect to the present orbital, acting on this orbital

$$R_{i\mathbf{k}}(\mathbf{r}) = \frac{\delta E_{\text{tot}}}{\delta\psi^*_{i\mathbf{k}}(\mathbf{r})}\ ; \tag{2.67}$$

the eigenvalue $\varepsilon_{i\mathbf{k}} = \langle\psi_{i\mathbf{k}}|H|\psi_{i\mathbf{k}}\rangle$ in the Equation 2.66 comes from the constraint of ortho-normalisation. Clearly in the ground state the inner product of the residual $R_{i\mathbf{k}}$ with the all eigenstates ψ_j vanishes since $\langle\psi_{j\mathbf{k}}|H|\psi_{i\mathbf{k}}\rangle$ is diagonal and equal to $\varepsilon_{i\mathbf{k}}$.

The operation of the Hamiltonian on the state can be performed easiest employing the fast Fourier transform since some of the terms in the product $H\psi_{i\mathbf{k}}$ are diagonal, *i.e.* depend only either on $\mathbf{G}$ or $\mathbf{r}$ and not on pairs $\mathbf{G}, \mathbf{G}'$ or $\mathbf{r}, \mathbf{r}'$, in real and some in reciprocal space; the product in case of the fully non-local form of the pseudo potential is

$$H(\mathbf{r})\,\psi_{i\mathbf{k}}(\mathbf{r}) = -\frac{1}{2}\nabla^2\psi_{i\mathbf{k}}(\mathbf{r}) + \sum_I \sum_{l'm',lm} D^{\mathcal{I}}_{l'm',lm}\left|\beta^I_{l'm'}\right\rangle B^I_{lm,i} + V_{\text{local}}(\mathbf{r})\,\psi_{i\mathbf{k}}(\mathbf{r})\ , \tag{2.68}$$

where $D^{\mathcal{I}}_{l'm',lm}$ are scalars arising from the Vanderbilt construction,

$$\beta^I_{l'm'}(\mathbf{r}-\mathbf{R}_I) = \mathrm{i}^l\beta^{\mathcal{I}}_{l'}(|\mathbf{r}-\mathbf{R}_I|)\,Y_{l'm'}\left(\widehat{\mathbf{r}-\mathbf{R}_I}\right)\ ,$$

$B^I_{lm,i} = \left\langle\beta^I_{lm}|\psi_{i\mathbf{k}}\right\rangle$ and $V_{\text{local}}(\mathbf{r}) = V^{\text{loc}}_{\text{pp}}(\mathbf{r}) + V_{\text{Hartree}}(\mathbf{r}) + V_{\text{xc}}(\mathbf{r})$; for norm-conserving Hamann or Troullier-Martins type of pseudo potentials $D^{\mathcal{I}}_{l'm',lm} = \delta_{ll'}\delta_{mm'}E_{\text{KB},l}$. As described in Section 2.4.1 the kinetic energy term is calculated most conveniently in the reciprocal space; the wave functions are also most efficiently stored in the reciprocal space since less coefficients need to be stored there – in the reciprocal space the number of points inside the cut-off sphere is smaller than the number of points on the corresponding real-space grid – and for the operations with the local potential it should be transformed to the larger fast Fourier transform grid anyway. The inner products $B^I_{lm,i}$ have been calculated beforehand, either in the real or reciprocal space: in the real space the operations are localised and this can be used to reduce the calculational burden, on the other hand in the reciprocal space the implementation is straight-forward. Thus the operation of the Hamiltonian on the current state is eventually

$$\begin{aligned}[H\psi_{i\mathbf{k}}](\mathbf{G}) &= \lvert\mathbf{k}+\mathbf{G}\rvert^2\psi_{i\mathbf{k}}(\mathbf{G}) + \sum_I\sum_{l'm',lm} D^{\mathcal{I}}_{l'm',lm}\beta^I_{l'm'}(\mathbf{G})\,B^I_{lm,i} \\ &\quad + \text{FFT}\left\{V_{\text{local}}(\mathbf{r})\,\text{FFT}^{-1}[\psi_{i\mathbf{k}}(\mathbf{G})](\mathbf{r})\right\}(\mathbf{G})\end{aligned} \tag{2.69}$$

or

$$\begin{aligned}[H\psi_{i\mathbf{k}}](\mathbf{G}) &= \lvert\mathbf{k}+\mathbf{G}\rvert^2\psi_{i\mathbf{k}}(\mathbf{G}) \\ &\quad + \text{FFT}\left\{\sum_I\sum_{l'm',lm} D^{\mathcal{I}}_{l'm',lm}\beta^I_{l'm'}(\mathbf{r})\,B^I_{lm,i} + V_{\text{local}}(\mathbf{r})\,\text{FFT}^{-1}[\psi_{i\mathbf{k}}(\mathbf{G}')](\mathbf{r})\right\}(\mathbf{G})\end{aligned} \tag{2.70}$$

with the fast Fourier transforms the calculation is arranged as shown in the Figure 2.12.

The density is the absolute value of the wave function squared in the real space, thus

$$n(\mathbf{r}) = \sum_{\mathbf{k}} w_{\mathbf{k}} \sum_i f_{i\mathbf{k}}\left|\text{FFT}^{-1}[\psi_{i\mathbf{k}}(\mathbf{G})](\mathbf{r})\right|^2\ . \tag{2.71}$$

The other fast Fourier transforms during one self-consistent cycle – with exchange-correlation functionals not explicitly dependent on single states – do not involve single states and therefore one iteration takes three fast

Input: Initial $\psi_{i\mathbf{k}}(\mathbf{G})$

$$\psi_{i\mathbf{k}}(\mathbf{G}) \overset{\text{FFT}^{-1}}{\Longrightarrow} \psi_{i\mathbf{k}}(\mathbf{r})$$
$$n(\mathbf{r}) = \sum_{\mathbf{k}} w_{\mathbf{k}} \sum_i \left|\psi_{i\mathbf{k}}(\mathbf{r})\right|^2$$
$$V_{\text{xc}}(\mathbf{r}) = V_{\text{xc}}[n(\mathbf{r})]$$
$$n(\mathbf{r}) \overset{\text{FFT}}{\Longrightarrow} n(\mathbf{G})$$
$$V_{\text{H}}(\mathbf{G}) = V_{\text{H}}[n(\mathbf{G})]$$
$$V_{\text{ps}_{\text{local}}}(\mathbf{G}) = V_{\text{ps}_{\text{local}}}[n(\mathbf{G})]$$
$$V_{\text{H}}(\mathbf{G}) + V_{\text{ps}_{\text{local}}}(\mathbf{G}) \overset{\text{FFT}^{-1}}{\Longrightarrow} [V_{\text{H}} + V_{\text{ps}_{\text{local}}}](\mathbf{r})$$
$$V_{\text{local}}(\mathbf{r}) = V_{\text{xc}}(\mathbf{r}) + [V_{\text{H}} + V_{\text{ps}_{\text{local}}}](\mathbf{r})$$
`foreach k`
`foreach i`
Calculate $R_{i\mathbf{k}} = -[H - \varepsilon_{i\mathbf{k}} S]\psi_{i\mathbf{k}}$
Up − date $\psi_{i\mathbf{k}}(t + \Delta t) = a\psi_{i\mathbf{k}}(t - \Delta t) + b\psi_{i\mathbf{k}}(t) + \mathtt{f}[R_{i\mathbf{k}}]$
`end loop i`
Ortho − normalise $\psi_{i\mathbf{k}}$
Calculate new $B^I_{lm,i}$
`end loop k`

Output: New $\psi_{i\mathbf{k}}(\mathbf{G})$

Figure 2.13: The schematic illustration of the self-consistent cycle in the equation-of-motion-based, iterative Car-Parrinello method implemented in the Kohn-Sham framework

Fourier transforms per electronic state, or two if the wave function Fourier transformed into the real space can be stored in the memory when calculating the density because the wave function is not changed before the first Fourier transform in $H\psi_{i\mathbf{k}}$. The density needs to be transformed into the reciprocal space for the Hartree and the local part of the pseudo potential, and its gradients when employing the generalised gradient approximations; the local potentials calculated in the reciprocal space are back-transformed and added to the exchange-correlation potential. Thereby the self-consistent cycle looks like shown in the Figure 2.13.

In the schemes not based on an equation of motion – *e. g.* the conjugate gradient or the residual minimisation – the basic iteration loop is very similar, only the details of the up-date of the wave functions have changed but the same gradient or residual of the Equation 2.66 is used. These methods are more similar in spirit to the original exact diagonalisation as they up-date the wave functions closer to a diagonal Hamiltonian and the density and potential are calculated less often. In the calculational effort both approaches are probably rather equal.

2.4.3 An implementation – Fauſt

The calculations of the present work were originally started using the `fhi93cp` code (Stumpf & Scheffler, 1994) and shortly the `fhi94md` version[2] until the author shifted to a program code obtained from Kari Laasonen (personal communication; please see also Laasonen *et al*, 1993); the code includes the possibility to use the Vanderbilt ultra-soft pseudo potentials. It has been actively maintained and developed by the author, and the working name for the code is "Fauſt" (Seitsonen, Boisvert & Laasonen, unpublished). The main goal was to achieve a code which is easily readable, portable and editable without sacrifying too much of the performance, and personally to obtain further experience in programming and electronic structure methods. Some features from other codes CASTEP/CETEP, da Capo (Bjørk Hammer/Denmark) `fhi94md`and preliminary versions of FINGER (Laboratory of Physics, Helsinki University of Technology, Finland) have been adapted to Fauſt, and $\mathbf{k}$ and $\mathbf{G}$ vector parallel versions have been written, the latter mainly with the help from Sami Pöykkö (personal communication). Recently the code was adapted from FORTRAN77 to FORTRAN90, with some modifications still to be done.

Some of the features in Fauſt include:

- Alternative compilation in fully double or partially single precision
- Dynamic memory allocation
- Compiles and runs at IBM, SGI, DEC, Cray T3E, HP, linux and other architectures
- Conjugate gradient algorithm/sub-space rotation
- Run-time control of many of the calculational parameters
- The numerical and White-Bird evaluation of gradient approximations
- Weighted-density approximation, local mass approximation, "Meta-GGA" (Perdew *et al*, 1999) as more "exotic" exchange-correlation functionals
- Fermi/Gaussian/Methfessel-Paxton/"cold" smearing of occupation numbers

[2]The newest version of the code, `fhi96md`, has been documented by Bockstedte *et al* (1997)

- Molecular dynamics for the ions
- Surface dipole correction (Neugebauer & Scheffler, 1992; Bengtsson, 1999)
- Semi-local form of the pseudo potential

2.5 Output from the calculations

Here we shall shortly explain the interpretation of the calculations, that is, what information can be won from the resulting output.

2.5.1 Lattice parameter, bulk modulus and the cohesive energy

The lattice constant is in principle the value which minimises the Gibbs's free energy but due to the approximation to the exchange-correlation term the theoretical lattice constant is not the same as from the experiments. Usually the temperature and zero-point effects are also not included; these would increase the lattice constant somewhat, typically less than one per cent.

The lattice constant is usually determined by calculating the total energy of the bulk material at several values of the lattice constant and performing a fit to the resulting points. We have used the Murnaghan (1944) fit, which also yields a value for the bulk modulus. The minimum of the total energy can be used to determine the cohesive energy, but this has seldom been calculated since for it the energy of an isolated atom is needed with an equivalent accuracy, and in the methods employing the atom has to be located in a large unit cell to avoid the interaction with its periodic replicas, and the calculation has to be performed with spin-polarisation, the occupation numbers are not necessarily integers and the charge density even not spherical (Kutzler & Painter, 1987).

We have checked the effect of the zero-point vibrations using the formulas of Moruzzi, Janak and Williams (1978). In metals like aluminium, rhodium and silver the change in the lattice constant due to the zero-point vibrations was found to be less than one per cent and we thus neglected this effect from the determination of the lattice properties for ruthenium.

2.5.2 Adsorption energies

The binding energy of an adsorbate to a surface is not always uniquely defined, as its value depends on the energy reference: For example atoms which form strongly bound molecules can overcome the repulsion which reigns between the adsorbed atoms *e.g.* when the surface is progressively heated but before the atoms would desorb they recombine. Also part of the energy gained in the recombination process might be partially adsorbed to the degrees of freedom of the surface. Thus the value of binding energy derived from the thermal desorption spectroscopy needs an accurate analysis of the spectra, and the value obtained from calculations should take into account a larger portion of the potential energy surface than only at the immediate vicinity of the adsorption sites. We usually refer the values to dimers in the case of atomic adsorbates of the $2p$ row, which are in gaseous form at normal conditions, but in the case of cesium the reference is a single atom. The binding energy in the case of with respect to an atom and to a dimer is respectively

$$\begin{aligned} E_{\mathrm{bind}}^{A/S} &= E\left(\mathrm{A/S}\right) - \left[E\left(\mathrm{S}\right) + E\left(A_{\mathrm{atom}}\right)\right] \\ E_{\mathrm{bind}}^{A/S} &= E\left(\mathrm{A/S}\right) - \left[E\left(\mathrm{S}\right) + \frac{1}{2}E\left(A_2\right)\right] \ , \end{aligned} \tag{2.72}$$

where A stands for the adsorbate and S the substrate and E is the total energy of the system; please note that then negative values indicate an energy gain upon adsorption and positive repulsion.

Furthermore if the adsorbate-adsorbate interaction is repulsive then desorbing one adsorbate reduces the repulsion and this energy will increase the binding energy of the remaining adsorbates. As an example let us consider the adsorption of cesium, which is repulsive at all coverages: if the ordered structures formed are $(\sqrt{3}\times\sqrt{3})$R30°, (2×2), $(\sqrt{7}\times\sqrt{7})$R19.1° and (3×3) at the coverages 1/3, 1/4, 1/7 and 1/9, the binding energy at the different coverages is obtained as

$$\begin{aligned} E_{\mathrm{bind},1/3} &= \left[E_{1/3} - 3E_{\mathrm{clean}}\right] - \left[E_{1/4} - 4E_{\mathrm{clean}}\right] = E_{1/3} - E_{1/4} + E_{\mathrm{clean}} \\ E_{\mathrm{bind},1/4} &= \left[E_{1/4} - 4E_{\mathrm{clean}}\right] - \left[E_{1/7} - 7E_{\mathrm{clean}}\right] = E_{1/4} - E_{1/7} + 3E_{\mathrm{clean}} \\ E_{\mathrm{bind},1/7} &= \left[E_{1/7} - 7E_{\mathrm{clean}}\right] - \left[E_{1/9} - 9E_{\mathrm{clean}}\right] = E_{1/7} - E_{1/9} + 2E_{\mathrm{clean}} \ ; \end{aligned} \tag{2.73}$$

E_{clean} is the total energy of the clean surface in a 1×1 unit cell. Please note that if the binding energy for adding one further adsorbate to the structure is defined in the same manner the value can be different, as the repulsion in this case might increase by a different amount than it decreases when an atom is desorbed.

The coverage dependence of the interaction between the adsorbates can easily be characterised using the lattice gas model where the interaction energy E_{int} is decomposed into a sum of parameters which are independent of the coverage. Kreuzer and Payne (1997) write the energy as a sum of the binding energy of an isolated adsorbate E_0, nearest neighbour pairs of the adsorbates V_2, second nearest neighbour pairs V_2', third nearest

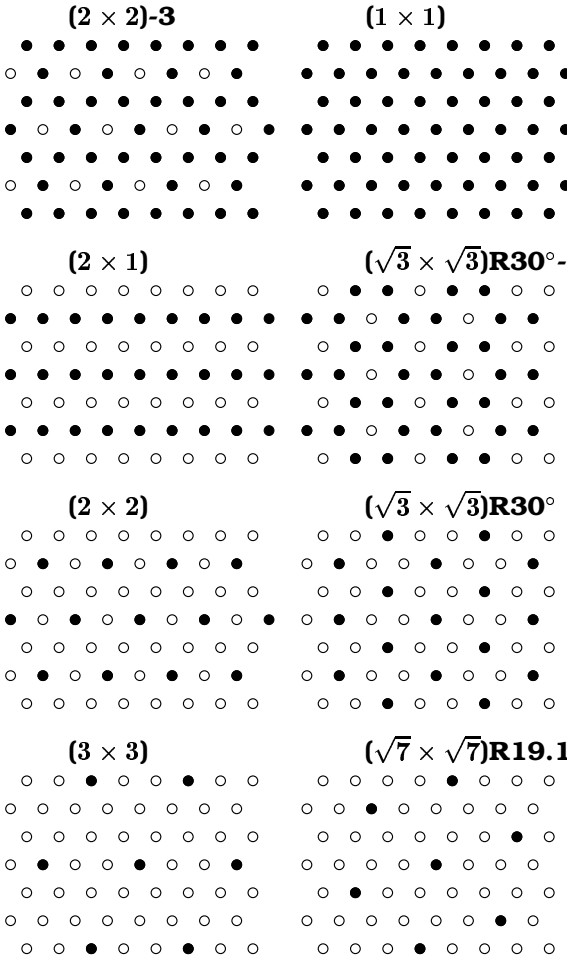

Structure	E_0	V_2	V_2'	V_2''	V_2'''	V_t	V_t'	V_t''
(1 × 1)	1	3	3	3	6	3	6	6
(2 × 2)-3	1	2	2	3	4	2	2	2
$(\sqrt{3} \times \sqrt{3})$R30°-2	1	3/2	3	3/2	3	0	3	0
(2 × 1)	1	1	1	3	2	1	0	0
$(\sqrt{3} \times \sqrt{3})$R30°	1	0	3	0	0	0	0	0
(2 × 2)	1	0	0	3	0	0	0	0
$(\sqrt{7} \times \sqrt{7})$R19.1°	1	0	0	0	3	0	0	0
(3 × 3)	1	0	0	0	0	0	0	0

Figure 2.14: The number of different interactions per atom in the lattice gas model on a hexagonal lattice at different coverages. All the different configurations up to the fourth nearest neighbour and the trio interactions have been treated as separate

pairs V_2'' *etc*, and triplets of atoms at the nearest neighbour sites V_t, V_t' and V_t'' depending on the angle between them, and so on:

$$\begin{aligned} E_{\text{int}} &= \sum_i n_i E_0 \\ &+ \sum_{i,j=\text{NN}} n_i n_j V_2 + \sum_{i,j=\text{NNN}} n_i n_j V_2' + \sum_{i,j=3\text{rdNN}} n_i n_j V_2'' + \ldots \\ &+ \sum_{i,j=\text{NN},\angle=180°} n_i n_j V_t + \sum_{i,j=\text{NN},\angle=120°} n_i n_j V_t' + \sum_{i,j=\text{NN},\angle=60°} n_i n_j V_t'' + \ldots \ , \end{aligned} \tag{2.74}$$

where $n_i = 0, 1$ is the occupation of the site i. Only one adsorption site is assumed at all configurations. The sums have to be truncated after some terms, and care must be taken that the same interaction is not counted twice; the Figure 2.14 shows as an example the number of different interactions on a hexagonal lattice, like has been studied in the present work. We obtain values for the parameters by calculating the binding energy of the adsorbate at different coverage and then inverting the Equation 2.74 to obtain the parameters.

2.5.3 Density of States – DOS

The density of states, or the total density of states, describes how many electronic states are located at inside an infinitesimally small region $d\varepsilon$ around a given energy ε. In practice this is usually calculated from the Kohn-Sham eigenvalues $\varepsilon_{i\mathbf{k}}$ from the weighted sum

$$g(\varepsilon) = \sum_{\mathbf{k}} w_{\mathbf{k}} \sum_i \mathcal{B}(\varepsilon - \varepsilon_{i\mathbf{k}}) \ . \tag{2.75}$$

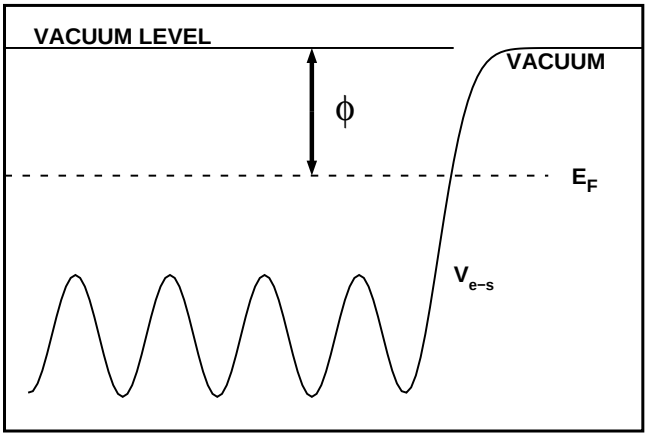

Figure 2.15: The definition of the work function $\phi = V_{\mathrm{e-s,vac}} - \varepsilon_F$; ε_F is the Fermi energy and $V_{\mathrm{e-s}}$ the electro-static potential

$\mathcal{B}$ is a broadening function necessary due to the discreteness of the eigenvalues; sometimes the tetrahedron method is used to interpolate the energies. We have used the Gaussian broadening in the present work; $w_{\mathbf{k}}$ is the weight associated with the $\mathbf{k}$ point as explained in the Section 2.3.2. The density of states is usually normalised to the Fermi energy in the case of metals and maximum of the valence band in semi-conductors; furthermore if the vacuum level of the potential or energy is known the energy can be normalised with respect to it. In the present work the energies are always referred to the Fermi energy if not explicitly mentioned.

The total density of states provides no direct information on the spatial location of the electronic states. Indirectly some of the states can often be associated to specific atoms if the energy range is well isolated from other features, *e.g.* the semi-core or deeply bound valence states and well-resolved peaks. A convenient quantity is obtained by subtracting from the density of states of the substrate with the adsorbate the density of states of the clean substrate; thereby the difference is only due to the adsorption. Subtracting also the density of states of the adsorbate only is usually not useful since it has only localised peaks which shift to different energies upon the adsorption.

2.5.4 Projected or Local Density of States – PDOS or LDOS

The local density of states is similar to the total density of states but it contains also spatial information; this is achieved by projecting or calculating the overlap of localised orbitals centred on the atoms with the Kohn-Sham states of the system under study:

$$g_{lm,I}(\varepsilon) = \sum_{\mathbf{k}} w_{\mathbf{k}} \sum_i f_{i\mathbf{k}} \mathcal{B}(\varepsilon - \varepsilon_{i\mathbf{k}}) \left| \left\langle \phi(|\mathbf{r}-\mathbf{R}|) Y_{lm}\left(\widehat{\mathbf{r}-\mathbf{R}}\right) \middle| \psi_{i\mathbf{k}}(\mathbf{r}) \right\rangle \right|^2 \tag{2.76}$$

Here $\phi(r)$ is a radial projection function, usually the atomic pseudo wave function; its use is unpleasant but unavoidable because the logical definition where the Kohn-Sham orbitals are projected only onto the angular functions would lead to semi-local expressions, which are computationally very demanding in large systems. Furthermore the radial function need to be cut off at a distance since its extent is very large and would otherwise over-lap the neighbouring atoms, leading to artificial contribution to the density of states. We have used a radial cut-off which is slightly smaller than half of the distance to the nearest atom.

The analysis of the local density of states is similar to the total density of states but it is now decomposed at each atom and to the angular momentum channels *l,m*.

2.5.5 Work function

The work function of a surface is defined as the minimum energy required to move an electron from the bulk to the vacuum outside the surface. In practice the value for the work function is obtained as illustrated in the Figure 2.15:

$$\phi = V_{\mathrm{e-s,vac}} - \varepsilon_F \ , \tag{2.77}$$

where $V_{\mathrm{e-s,vac}}$ is the value of the electro-static potential in the vacuum, *i.e.* far away from the slab.

2.5.6 Blyholder model for adsorption of carbon monoxide

The frontier orbitals – the highest occupied and the lowest unoccupied molecular orbitals – of carbon monoxide are the 5σ and $2\pi^*$ in the Figure 2.16; the energy levels of the molecule are listed as well. In 1964 George Blyholder introduced a model according to which the bonding of CO onto surfaces happens via the emptying of the 5σ orbital and filling of the $2\pi^*$ orbitals as shown in the Figure 2.17. The electrons are redistributed to the hybrids with the states of the substrate; the interaction with the electrons of *s* and *p* character is weak – CO is

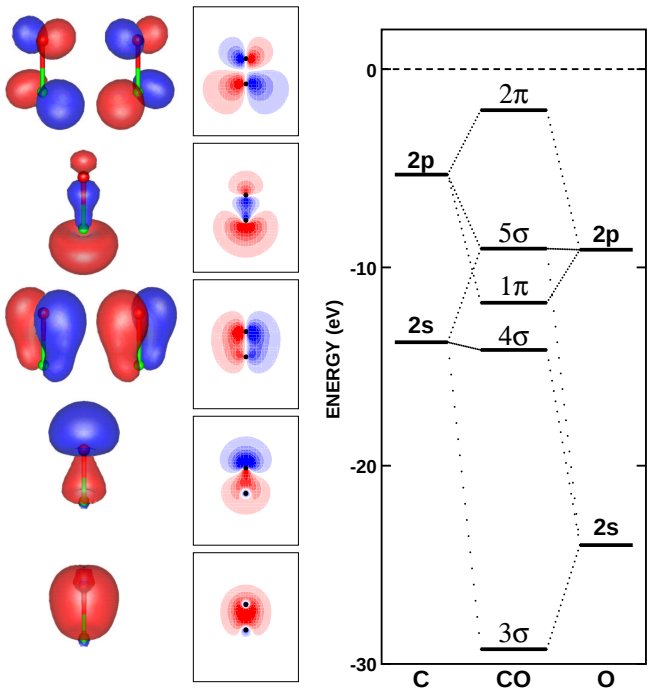

Figure 2.16: The significant Kohn-Sham single particle states of the carbon monoxide; right are the Kohn-Sham energy levels of the orbitals from our density functional calculation employing the generalised gradient approximation

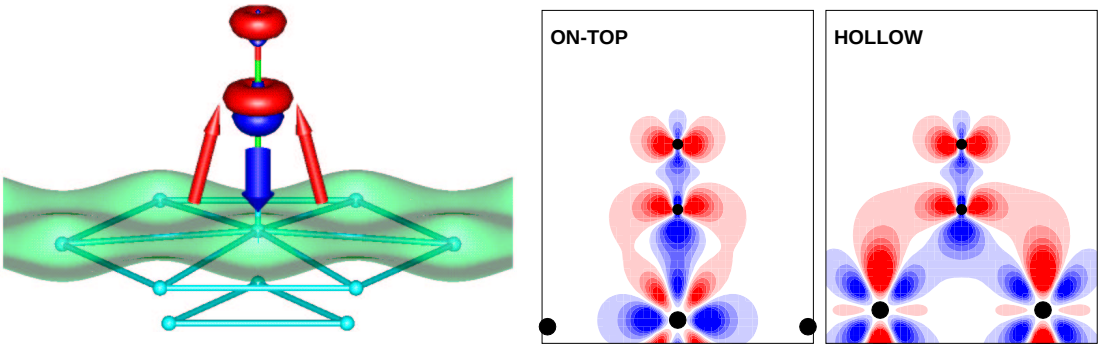

Figure 2.17: The Blyholder mechanism: The 5σ orbital is emptied and the $2\pi^*$ filled in the formation of hybrids with the substrate; right is the interaction mechanism with the different d like states on the on-top and hollow adsorption sites

only very weakly bound on the surfaces of aluminium – and thus the main ingredient is the hybridisation with the d orbitals, and the bond is strongest on the surfaces of the transition metals which have an open d shell. On the contrary the interaction with the noble metals gold, silver and copper is weaker as there are no free – mainly only polarisable – d electrons, and thus the back-bonding channel to the $2\pi^*$ orbitals is not efficient. The adsorption site for CO depends on the nature of the d hybrids: On the on-top site the 5σ orbital overlaps with the d_{z^2} like states and the back-bonding occurs via the $d_{xz,yz}$ orbitals, whereas on the three-fold – and two-follow bridge site – sites this is vice versa.

Recently the Blyholder model has been criticised as over-simplified and thus improper. However, although we have also found a strong mixing of the 4σ and 5σ orbitals and the Kohn-Sham energy level of the orbital with mainly 5σ character moves below the level of the 1π orbital, thus making the 5σ no longer the highest occupied "molecular" orbital – however the 1π does not take part into the bonding as its overlap is small due to little overlap with the substrate states –, the main features of the CO adsorption are still described well by the Blyholder model: a model is only a model, and the details of the bonding go beyond the Blyholder model.

2.5.7 Iso-electronic reactivity function

The straight-forward study of surface reactions by direct mapping of the related multi-dimensional potential energy surface is not feasible with the current methods and computer capacity. Therefore it would be advantageous to find a measure which could predict the response of a substrate to adsorbates without the actual, complicated calculation. These reactivity theories have been put forward especially in the community of quantum chemistry, where the concept of frontier orbitals – using the concepts like the highest occupied and lowest unoccupied molecular orbital, HOMO and LUMO – has emerged. However, this does not directly generalise

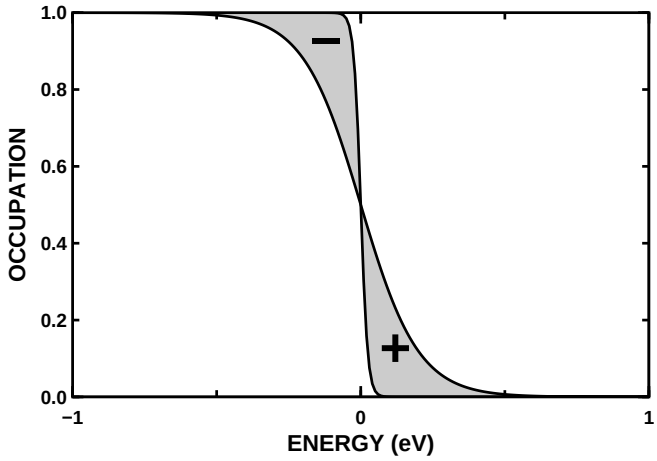

Figure 2.18: The occupation functions of broadenings $T_{\mathrm{el},1}$ = 0.1 eV and $T_{\mathrm{el},1}$ = 0.01 eV used in the reactivity function of Wilke; the positive and negative regions correspond mainly to occupied and unoccupied states, respectively

to the metallic case where there is no gap separating the occupied and unoccupied states and the density of states around the Fermi energy, *i.e.* where the states easily deform and change their occupation under different chemical environments, is large. An alternative scheme for this purpose was developed by Wilke, Cohen and Scheffler (1996): it explores the character of the states around the Fermi energy by changing the broadening of the occupation numbers in a scheme shown in the Figure 2.18 and defining the reactivity function as

$$\mathcal{W}^{\mathrm{N}} = \frac{1}{k_B^2 T_{\mathrm{el}}} \left[\frac{\partial n\left(\mathbf{r}, T_{\mathrm{el}}\right)}{\partial T_{\mathrm{el}}} \right]_{V_{\mathrm{ext}}(\mathbf{r}),\mathrm{N}} \approx \frac{n\left(\mathbf{r}, T_{\mathrm{el},1}\right) - n\left(\mathbf{r}, T_{\mathrm{el},2}\right)}{k_B^2 T_{\mathrm{el},1}\left[T_{\mathrm{el},1} - T_{\mathrm{el},2}\right]} \ , \tag{2.78}$$

where the super-script N denotes that the number of particles is conserved and T_{el} is the temperature used for the broadening of the occupation numbers in the Fermi function. Please note that we use two different finite temperatures whereas Wilke *et al* used $T_{\mathrm{el},2} = 0$. Both densities are calculated self-consistently.

The function yields a spatially resolved function, and the regions where it is positive the states are mostly unoccupied, becoming easily occupied and vise versa. It should be kept borne in mind, however, that the reactivity function is only an approximative estimate for the reactivity, and in chemisorbed systems the actual binding is likely to happen in an energy range not in the vicinity of the Fermi level.

2.5.8 Density differences / induced density

The density differences describe the charge transfer in the system upon a change in the atomic configuration. The change here comprises extraction or inclusion of atoms or molecules: the positions of the corresponding atoms in different calculations have to be the same, *i.e.* they must not be relaxed except in one case and the coordinates to the other calculations are taken from the relaxed one. Generally the system we are interested in is an adsorbate on a surface, and although we refer to the density difference as arising from the adsorption, the geometry is taken from the final state, *i.e.* the adsorbed system. Thus the density difference in this characteristic case would be calculated as

$$\Delta n = n^{\mathrm{A/S}}\left(\mathrm{A/S}\right) - n^{\mathrm{A/S}}\left(\mathrm{S}\right) - n^{\mathrm{A/S}}\left(\mathrm{A}\right) \ , \tag{2.79}$$

where

- $n^{\mathrm{A/S}}\left(\mathrm{A/S}\right)$ is the system with the adsorbate A on the substrate S, and the atoms have been relaxed
- $n^{\mathrm{A/S}}\left(\mathrm{S}\right)$ is the system with only the substrate S, but the coordinates of the substrate atoms have been taken from the calculation with the adsorbate; thus the super-script A/S
- $n^{\mathrm{A/S}}\left(\mathrm{A}\right)$ is the system with only the adsorbate A, but the coordinates of the adsorbate atoms have been taken from the calculation with the adsorbate on the surface; thus the super-script A/S

Usually the atoms match in the sense that from the adsorbed system is subtracted both the substrate and the adsorbate. However, in the case of an alkali metal we also want to see the so-called induced charge because the density of the outer-most, *s* electron differs notably from the atomic density. The induced density is defined similarly to the normal density difference above as

$$\Delta n = n^{\mathrm{A/S}}\left(\mathrm{A/S}\right) - n^{\mathrm{A/S}}\left(\mathrm{S}\right) - n^{\mathrm{A/S}}\left(\mathrm{A}_{\mathrm{semi-core}}\right) \ , \tag{2.80}$$

where, however, $n^{\mathrm{A/S}}\left(\mathrm{A}_{\mathrm{semi-core}}\right)$ contains only the semi-core states of the atomic adsorbate, if present; in our case of cesium the semi-core states are the 5*s* and 5*p* orbitals.

One further consideration is whether for the adsorbate the density is calculated self-consistently in the slab geometry – without the substrate – or as a super-position of the density of the atomic constituents. For laterally large unit cells the difference is negligible, and also in the reasonably small cells this choice the qualitative picture remains the same irrespective of the choice.

2.5.9 Interaction density / energy

The interaction density bears a close relationship to the density difference just explained but it is used to monitor the density changes upon co-adsorption on the substrate. It is defined as

$$\Delta n^i = n^{(\mathrm{A}_1+\mathrm{A}_2)/\mathrm{S}}\left((\mathrm{A}_1+\mathrm{A}_2)/\mathrm{S}\right) - n^{(\mathrm{A}_1+\mathrm{A}_2)/\mathrm{S}}\left(\mathrm{A}_1\right) - n^{(\mathrm{A}_1+\mathrm{A}_2)/\mathrm{S}}\left(\mathrm{A}_2\right) + n^{(\mathrm{A}_1+\mathrm{A}_2)/\mathrm{S}}\left(\mathrm{S}\right). \tag{2.81}$$

Here A_1 and A_2 refer to the two different co-adsorbates. The interaction density arises from the mutual interaction between the co-adsorbates and would vanish for distant or non-interacting co-adsorbates.

A related quantity is the interaction energy

$$-E\left[(\mathrm{A}+\mathrm{B})/\mathrm{S}\right] + E\left[\mathrm{A}/\mathrm{S}\right] + E\left[\mathrm{B}/\mathrm{S}\right] - E\left[\mathrm{S}\right] \ , \tag{2.82}$$

which is defined as the interaction density as a sum and difference of four energies, which in the case of energy can however be calculated all from relaxed systems and even the adsorption sites and coverages can be different and are generally chosen to be the minimum-energy structures. We have chosen the interaction energy to be positive in case of an attractive

2.5.10 Electro-static potential / electric field

The electro-static interaction is an important contribution in the chemical processes, especially when there is a large difference in the electro-negativity of the materials. One good example is the adsorption of an alkali metal to the surface, a system we have studied in the present work. The electro-static potential outside the core regions consists of the electron-electron repulsion and electron-ion attraction; in the calculations employing pseudo potentials the electro-static potential also includes the local and non-local contribution from the pseudo potentials inside the core regions, but since we are interested only in the regions outside the surface this is irrelevant.

Another interesting, related quantity is the electric field arising from the electro-static potential; this is simply the negative of the gradient of the electro-static potential:

$$\mathbf{E}\left(\mathbf{r}\right) = -\nabla V_{\mathrm{e-s}}\left(\mathbf{r}\right) \ . \tag{2.83}$$

This is a three-dimensional, *i. e.* vector quantity and thus difficult to visualise; we show either the magnitude of the field or the components gradient calculated in the cylindrical coordinates since our interest is on the field close to an alkali atom at the surface and this is largely a radial field.

2.5.11 Pseudo scanning tunnelling microscope image

The scanning tunnelling microscope is a powerful tool for studying the surfaces, structures and even reactions on them. However the atomic-scale features in the figures delivered from it are not as straight-forward to interpret as originally was supposed since the tunnelling current does not always simply correlate with the atomic geometry or better, the height of the atoms. A simple example is the oxygen atom on ruthenium, which is imagined as a depression although it resides above the top-most substrate layer. This apparent confusion derives from two effects: First of all, the tunnelling occurs only in the vicinity of the Fermi level and secondly, the tunnelling matrix elements contain many-body contributions and involve also the electronic – and this way, the geometrical – structure of the tip as well as the surface (Lang, 1989).

An easy model for obtaining qualitatively and often also quantitatively useful, but sometimes even qualitatively wrong, theoretical picture which then can be used to compare with the measured image comes from Tersoff and Hamann (1985). In this model the tunnelling current is proportional to the density of states of the surface only for a tip with an *s* like electronic state dominating the tunnelling; Chen (1990; 1994) has derived the corresponding expression for tips with different kinds of electronic structure. Since in our calculations the **k** sampling is finite we include the occupied Kohn-Sham states from a region around the Fermi energy in the density of states and thus the pseudo image. We simulate the operation of the microscope in the constant current mode, *i. e.* we show the interpolated height distribution above the surface where the energy-restricted density of states remains constant. We use a value of the constant density of states which either reproduces an experimentally determined corrugation of an adsorption system, or a value which leads to a realistic distance of 6-7 Å above the surface.

Chapter 3

Results

Contents

3.1 Bulk properties of ruthenium . . . 35
3.2 Clean Ru(0001) surface . . . 36
3.3 Adsorption on Ru(0001) . . . 40
3.3.1 Adsorption of cesium . . . 41
3.3.2 Adsorption of carbon monoxide on Ru(0001) . . . 60
3.3.3 Adsorption of carbon monoxide on other trigonal surfaces . . . 71
3.3.4 Adsorption of oxygen . . . 73
3.4 Co-adsorption on Ru(0001) . . . 75
3.4.1 Co-adsorption of cesium and oxygen . . . 75
3.4.2 Co-adsorption of cesium and carbon monoxide . . . 78
3.4.3 Co-adsorption of oxygen and carbon monoxide . . . 89
3.5 Discussion . . . 91
3.5.1 Bulk ruthenium and clean (0001) surface . . . 91
3.5.2 Adsorption of single species . . . 91
3.5.3 Co-adsorption . . . 92

3.1 Bulk properties of ruthenium

Ruthenium is a platinium-group transition metal with a partly filled 5*s* and 4*d* shells in the free atom, usually designated as [Kr]$4d^7 5s^1$. The next state, 4*p*, is energetically already over 40 eV deeper in energy than the valence states and is thus very inert against taking actively part in chemical bonding in different chemical environments.[1] Under normal temperature and pressure conditions ruthenium crystallises in the hexagonal close-packed structure – *hcp* – shown in the Figure 3.1.

The electronic properties of bulk ruthenium can be described with the total density of states in the Figure 3.2, the electron orbitals projected on the atomic orbitals or the projected density of states in the Figure 3.3 and the band structure in the Figure 3.4. The bulk electronic structure can thus be simplified with the model presented in the Figure 3.6, consisting of an *s* band which starts at deep energies and a rectangular *d* band which is cut off at the Fermi energy. The next clear feature after the *d* band in the total density of states does not begin until 12 eV above the Fermi energy. From the character table

D_{3h} ($\bar{6}2$)

			E	σ_h	$2C_3$	$2S_3$	$3C_2'$	$3\sigma_v$
$x^2+y^2,\ z^2$		A_1'	1	1	1	1	1	1
	R_z	A_2'	1	1	1	1	−1	−1
		A_1''	1	−1	1	−1	1	−1
	z	A_2''	1	−1	1	−1	−1	1
$(x^2-y^2,\ xy)$	(x,y)	E'	2	1	−1	−1	0	0
$(xz,\ yz)$	$(R_x,\ R_y)$	E''	2	−1	−1	1	0	0

of the D_{3h} symmetry group of the hexagonal close-packed crystal we see that the *p* orbitals p_x and p_y, and the *d* orbitals $d_{x^2-y^2}$ and d_{xy} are degenerate with each other, as are d_{xz} and d_{yz}. Therefore there are only three independent *d* orbitals, whereas *e.g.* in the bulk of a face centred crystal all the *d* orbitals are degenerate due to the higher symmetry than in the hexagonal close-packed crystal.

[1] However its absolute energetic position can change somewhat but this is not due to chemical hybridisation of orbitals but a core-level shift

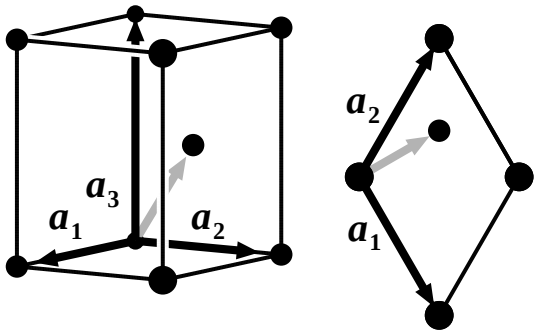

Figure 3.1: The hexagonal close packed structure. The basis vectors are $\mathbf{a}_1 = \left[1/2, -\sqrt{3}/2, 0\right]$, $\mathbf{a}_2 = \left[1/2, \sqrt{3}/2, 0\right]$ and $\mathbf{a}_3 = [0, 0, c/a]$ in the units of the lattice constant a; c/a is the other lattice parameter. The grey arrow shows the basis vector $\left[1/2, 1/(2\sqrt{3}), (c/a)/2\right]$

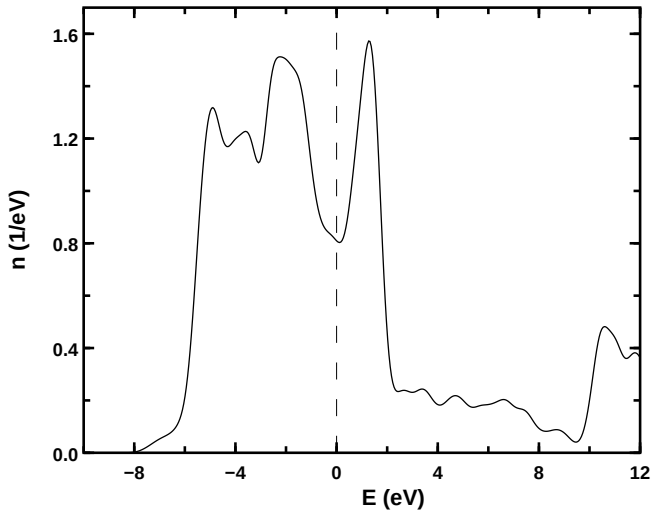

Figure 3.2: The density of states of bulk ruthenium calculated within the generalised gradient approximation of Perdew, Burke and Ernzerhof (1996). The Kohn-Sham eigenvalues were broadened with a Gaussian of decay parameter of 0.3 eV

3.2 Clean Ru(0001) surface

The clean Ru(0001) consists of the close-packed hexagonal layers with a A-B-A-B stacking as seen in the Figure 3.7. The layer distance is simply $c/2$, and the atoms within the layers are located at the nearest-neighbour distance a.

The geometry of the clean surface was calculated several times with different number of atomic layers, number of layers allowed to relax and the exchange-correlation functional; the results are shown in the Figure 3.8. Except for the calculation with a plane wave cut-off of 68 Ry and 9 **k** points the converged values are $-3.0 \ldots -3.3$ % within the generalised gradient approximation and -3.6 % within the local density approximation; we do not know the origin of the discrepancy. The clearly smaller relaxation obtained with only three **k** points is due to the badly converged sampling of the Brillouin zone. The deviation in the values by 0.3 % is not significant as this corresponds to about 5 mÅ and is thus much smaller than *e.g.* the discreteness of the mesh in the real space.

Experimentally the clean Ru(0001) is a benchmark before starting measurements with adsorbates, therefore during the years the relaxation of the surface has been repeatedly measured – please see Menzel (1997). The outer-most layer distance 2.09±0.015 Å at temperatures between 120 and 300 K corresponds to a contraction of $\Delta_{12} = -2.3 \pm 0.7$ % and between 20 and 50 K to $\Delta_{12} = -2.8$ %, and thus the theoretical values are not too far from the experiments. An attempt (Feibelman *et al*, 1994) to explain the systematic overestimation of the absolute value of the magnitude of the outer-most layer expansion by hydrogen contamination was promptly rejected (Menzel, 1994). The contraction of the outer-most layer relaxation is a general trend among the transition metals (Methfessel, Hennig & Scheffler, 1992) and is due to the removed nearest-neighbour atoms of the first layer, causing the outer-most layer to relax towards the second layer in order to strengthen the bonding between the atoms at the first and second layer.

The surface band structure at Ru(0001) is shown in the Figure 3.9; gaps in the projected bulk band structure appear at all energies from five electron volts below to well above the Fermi energy, and the most notable ones below the Fermi energy are at $\bar{\Gamma}$ around -4 eV and at -2 eV at $\bar{K}$, and at the Fermi energy at the line between $\bar{\Gamma}$ and $\bar{K}$. The surface states found in these gaps are shown in the Figure 3.10. In the gap above the Fermi energy there appear some states at energies expected for the image states; however, by inspection of the density profile of these states along the surface normal in the Figure 3.11 it is obvious that even if they would be related to the real image states the vacuum region is too small for the states to decay; furthermore, the generalised gradient approximation should not lead to the formation of image states because its asymptotic form does not approach the $\propto \frac{1}{z}$ which creates the image potential. Thereby the states in the band gaps, *e.g.* between 4 and 10 eV above the Fermi energy at the $\bar{\Gamma}$, are an artifact of the slab geometry, leading to an effective potential well for these states; the lower potential in the vacuum than inside the slab for these electrons is due to the orthonormalisation of these states against the states in the slab, making the slab region effectively more repulsive to these states. Furthermore at the Fermi energy there should be a continuum of states but these are forced into the series of states with increasing number of nodes and thus energy due to the localisation to the region between the slabs.

We also calculated the iso-electronic reactivity function of Wilke *et al* for the surface – please see Section 2.5.7; the result is shown in the Figure 3.12. The first qualitative observation is that the magnitude

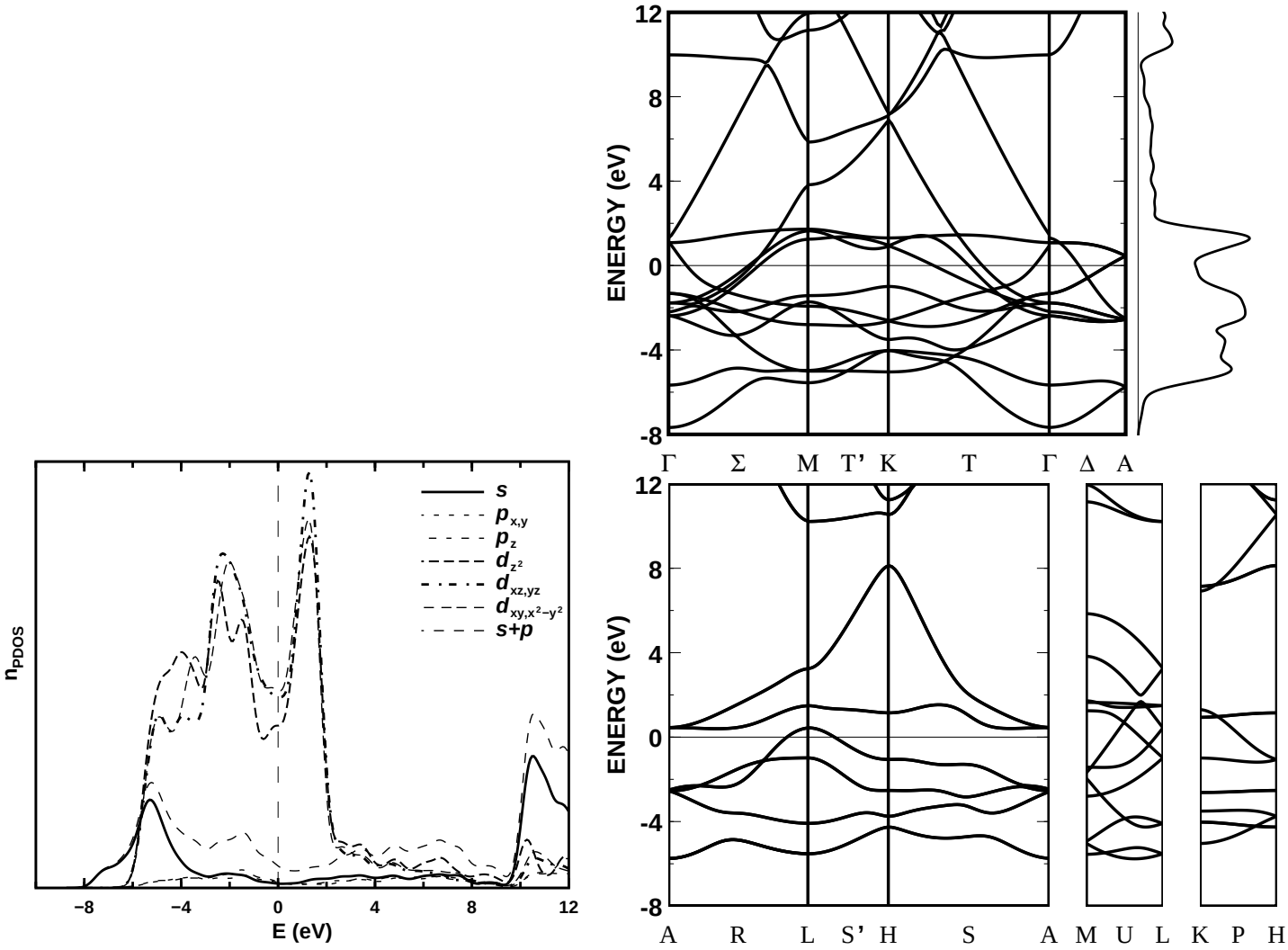

Figure 3.3: The projected density of states of bulk ruthenium calculated within the generalised gradient approximation of Perdew, Burke and Ernzerhof (1996). The Kohn-Sham eigenvalues were broadened with a Gaussian of decay parameter of 0.3 eV

Figure 3.4: The band structure of bulk ruthenium calculated from the Kohn-Sham eigenvalues within the generalised gradient approximation of Perdew, Burke and Ernzerhof (1996). The Brillouin zone of the crystal and the labelling of the **k** points and high-symmetry lines are shown in the Figure 3.5

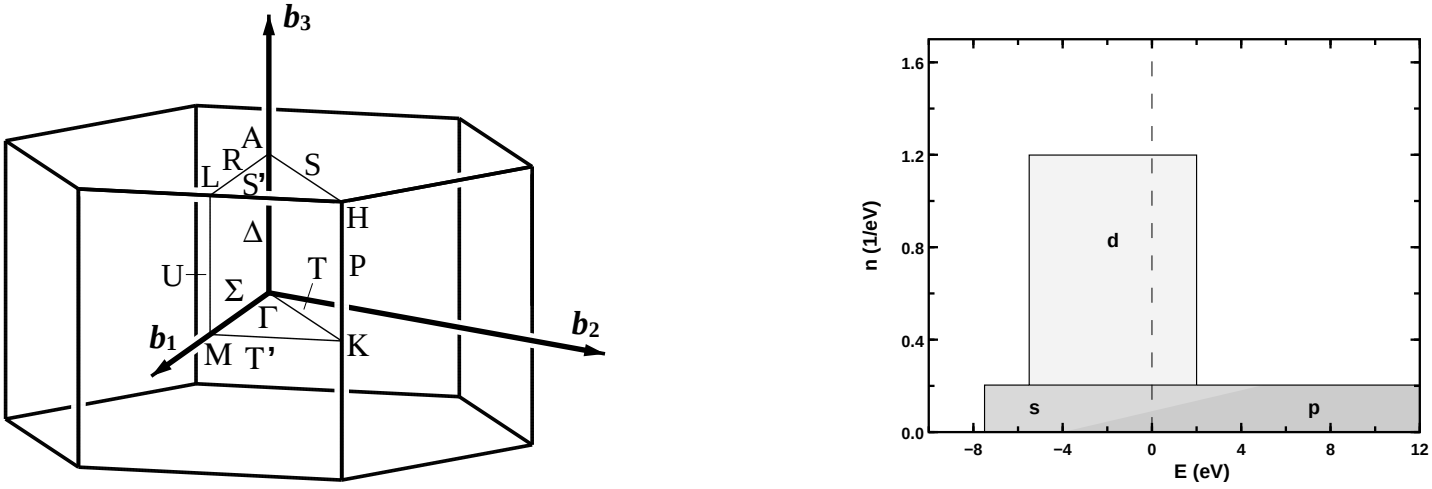

Figure 3.5: The Brillouin zone and the labelling of the **k** points and high-symmetry lines of the hexagonal close-packed structure

Figure 3.6: A model for the density of states of bulk ruthenium

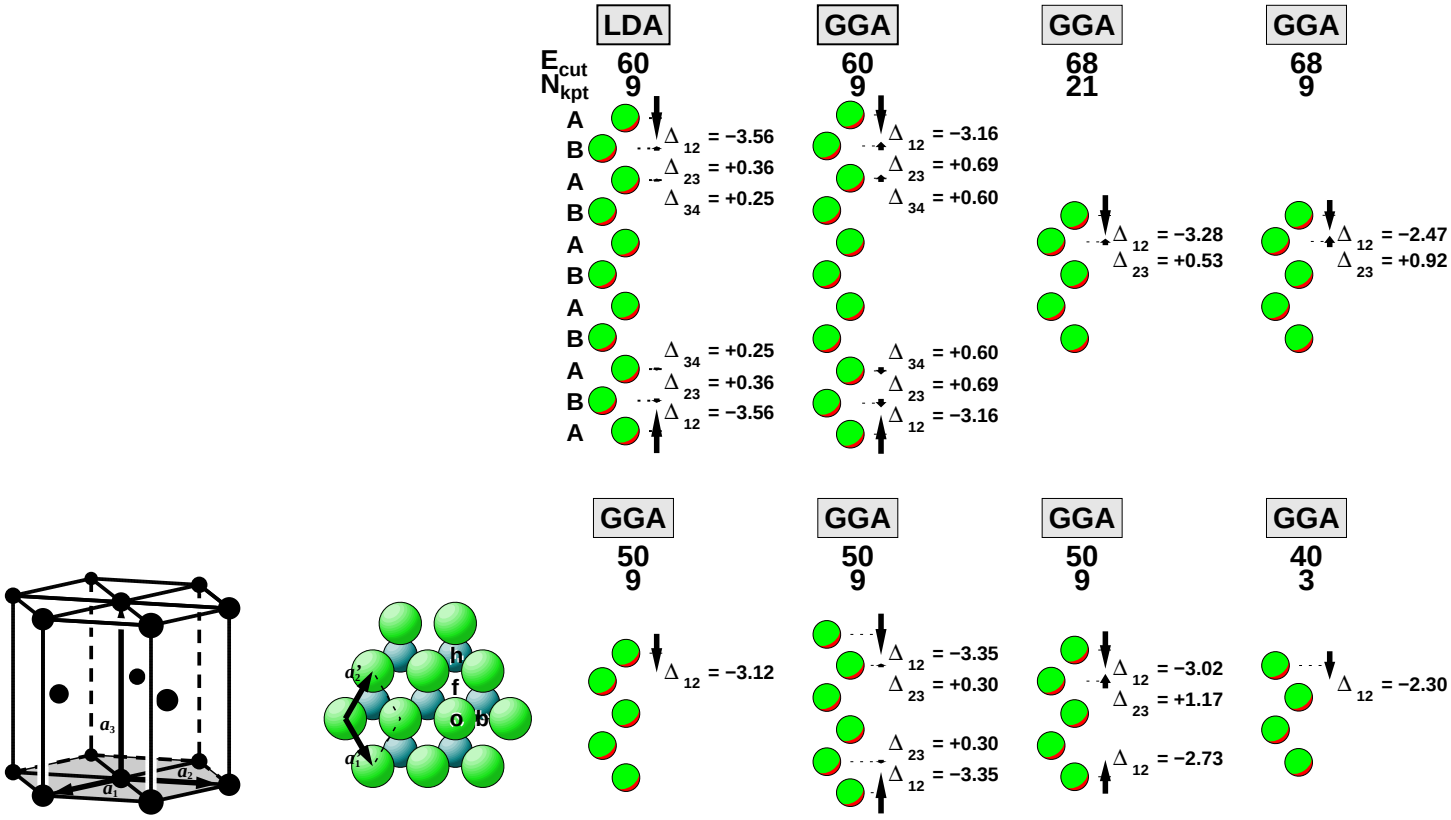

Figure 3.7: The cut of the (0001) surface from the hcp crystal; the stacking is A-B-A-B, and the high-coordinated adsorption sites have been designated with *o*, *h*, *f* and *b* for on-top, hcp, fcc and bridge sites, respectively

Figure 3.8: The relaxation of the clean (0001) surface obtained with different calculational parameters and exchange-correlation functionals; the values are in per cent of the corresponding distance in the ideal bulk structure

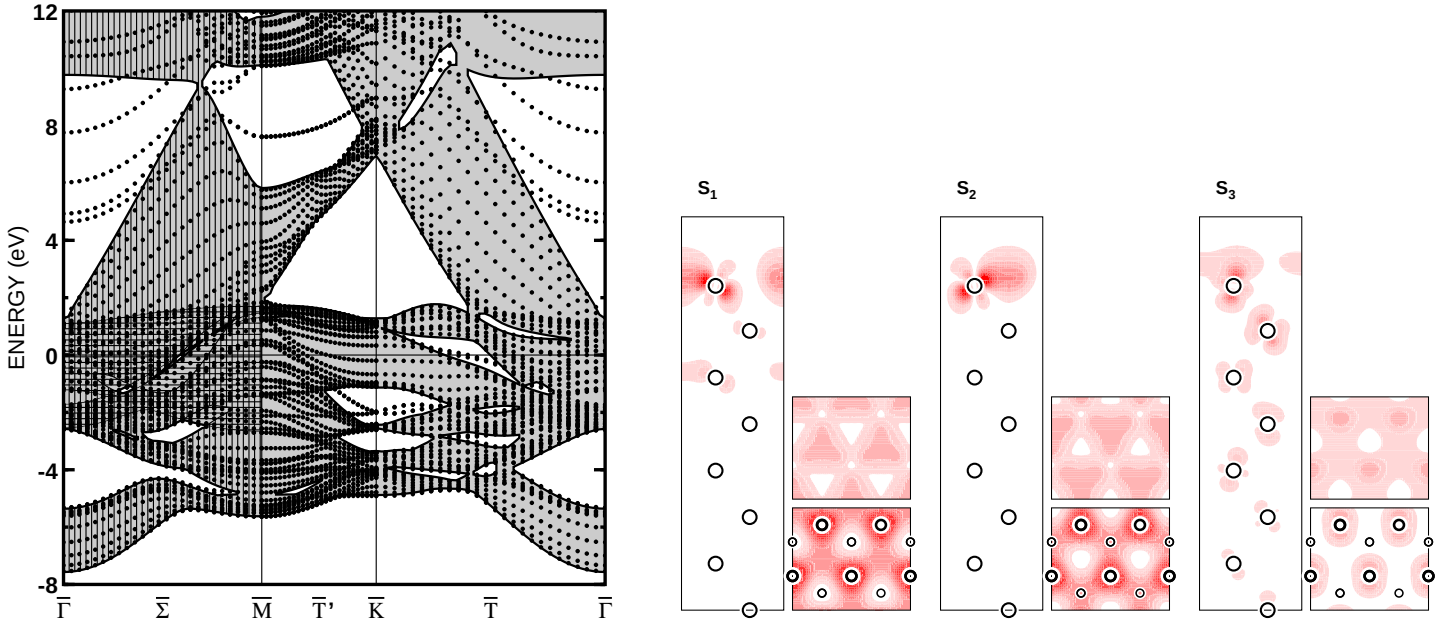

Figure 3.9: The band structure of the clean (0001) surface of ruthenium; the projected band structure of the bulk is shown with the gray areas, and the vertically and horisontally hatched regions between the points $\bar{\Gamma}$ and $\bar{M}$ correspond to states with even and odd symmetry with respect to the mirror plane

Figure 3.10: The surface states – obtained from the Kohn-Sham orbitals – at the clean (0001) surface of ruthenium at **k** points $\bar{K}$ – S_1 and S_2 – and $\bar{T} \approx 2/3\,(\bar{\Gamma} \to \bar{K})$ – S_3. The cuts along the surface are taken at the surface plane and 1 Å above it, and the cut in the plane through half of the slab is vertical at the centre of the lateral cuts

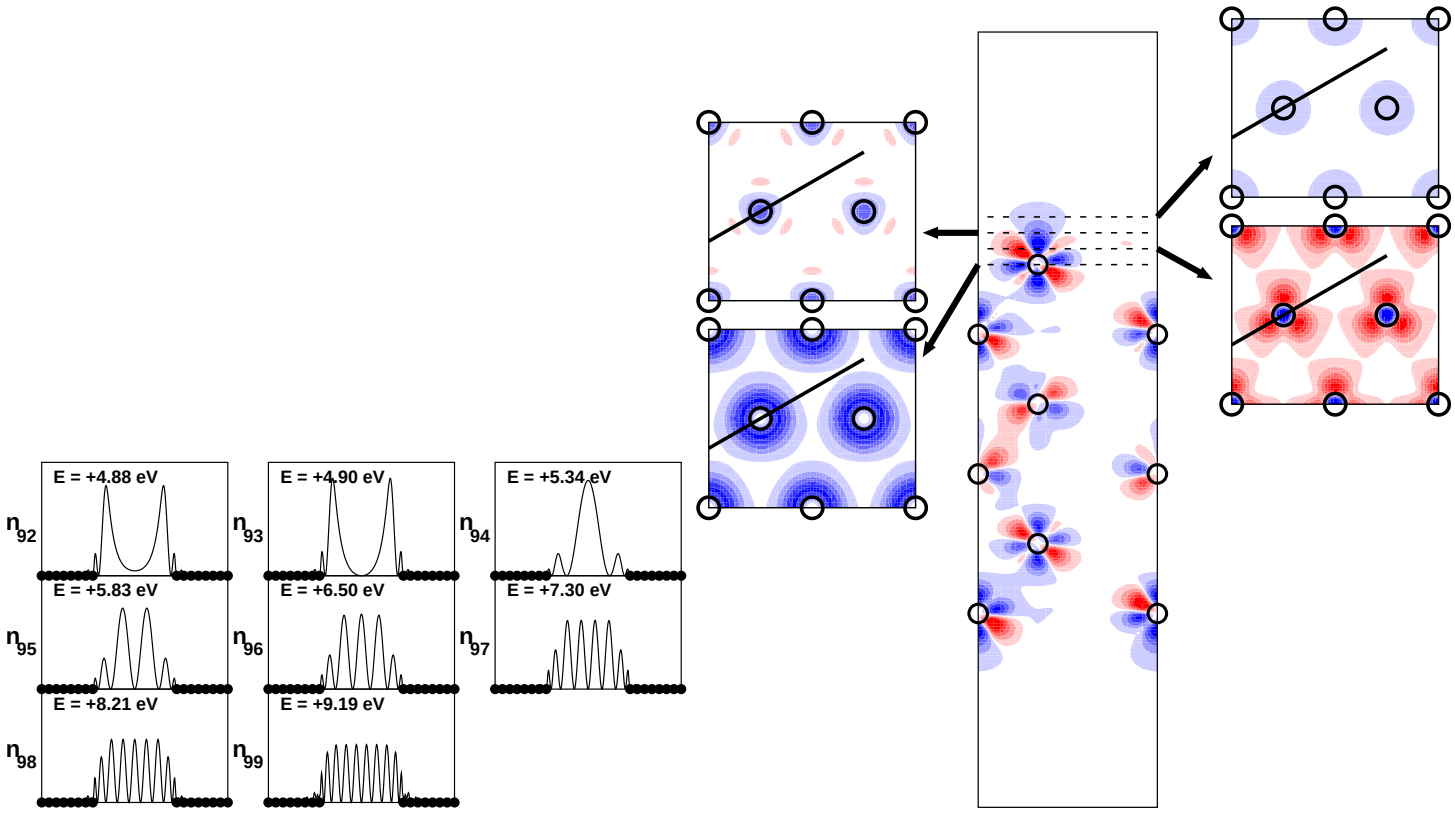

Figure 3.11: The density profiles of Kohn-Sham states at Ru(0001) at the $\bar{\Gamma}$ point in the Brillouin zone; the states are located in the vacuum region – the atomic positions are denoted with filled spheres and are caused by the image potential and repulsion from the states in the slab. The Kohn-Sham eigenvalues are given relative to the Fermi energy and the vacuum level of the potential is at the work function of the surface *i. e.* 5.0 eV

Figure 3.12: The reactivity function of Wilke, Cohen and Scheffler for the clean (0001) surface of ruthenium. The positive – red – regions correlate with unoccupied and the negative – blue – regions with occupied orbitals, the former becoming easily occupied and the latter easily emptied. The black line in the small cuts along the surface show the position of the vertical cut

of $\mathcal{W}_N$ is largest at the d orbitals around the surface atoms: the d_{z^2} and d_{xy,x^2-y^2} orbitals are occupied but easily emptied – blue regions – and the $d_{xz,yz}$ are unoccupied but easily occupied – red regions. A second, more de-localised, effect is the distribution of the reactivity function above the three-fold hollow and on-top adsorption places. This is somewhat complicated because the reactivity function changes its sign when approaching the surface. However at the typical bonding height of $2p$ elements on Ru(0001) – about 1.2 Å – the initially unoccupied $d_{xz,yz}$ orbitals point out towards the hcp site and interestingly much less towards the fcc site; at the on-top site a large number of d_{z^2} provide easily emptied orbitals. Thus a typical situation occurring when adsorbing an electronegative element could be that the $d_{xz,yz}$ orbitals become occupied, leading to a better screening and bonding with the adsorbate while the d_{z^2} orbitals are emptied. An adsorbate more electropositive than this surface would most easily donate some charge density to the surface to the $d_{xz,yz}$ orbitals. However, it is very important to notice that the reactivity function simulates only tiny changes around the Fermi energy whereas chemisorption leads to chemical bonds often several electron volts away from the Fermi energy.

It is instructive to compare the reactivity function with the projected density of density, given in the Figure 3.13: the main change in the projected density of density at the surface relative to bulk is the narrowing of the d band due to the reduced coordination of the surface atoms. Around the Fermi energy the d_{z^2} narrows most, bringing the peak in the projected band structure to intersect the Fermi energy; the reactivity function suggests that these orbitals are then easily pushed up in the energy and thus emptied. The other d orbitals have rather a constant magnitude near the Fermi energy and thus the effects in the reactivity functions are due to some redistribution of these orbitals. It is also easy to understand the small amplitude of the reactivity function in the bulk layers by inspection of the amount of d orbitals in the vicinity of the Fermi energy in the Figure 3.13: all the different bands have almost a constant amplitude, thus leading to small changes when changes occur.

Please notice that the degeneracy of the d orbitals prevails from the bulk because the crystal is cut parallel to the high-symmetry axis of the hexagonal close-packed surface; the mirror planes parallel and rotations with the axis along the surface are removed, though. The symmetry group is C_{3v} whose character table is as follows:

$$C_{3v}\ (3m)$$

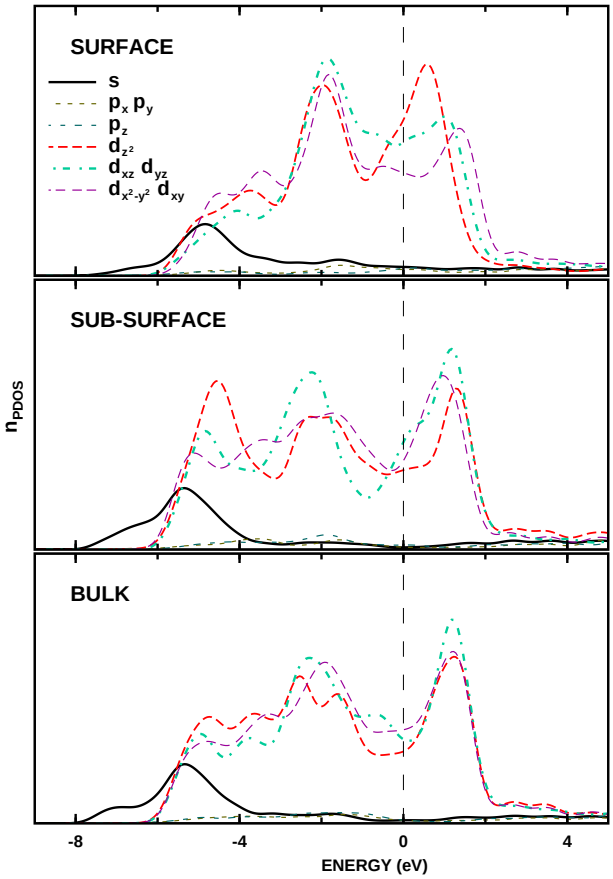

Figure 3.13: The projected density of states of the (0001) surface of ruthenium

Table 3.1: The centre and the width – calculated from the standard deviation – of the d band from the projected density of states

layer	d_{z^2}	$d_{xz,yz}$	$d_{x^2-y^2,xy}$	d_{total}
Surface	−1.3 / 4.0	−1.0 / 4.0	−1.1 / 4.4	−1.1 / 4.2
Sub-surface	−1.6 / 5.1	−1.4 / 4.7	−1.5 / 4.7	−1.5 / 4.8
Middle (bulk)	−1.5 / 4.9	−1.3 / 4.6	−1.3 / 4.6	−1.3 / 4.7

			E	$2C_3$	$3\sigma_v$
$x^2+y^2,\ z^2$	z	A_1	1	1	1
	R_z	A_2	1	1	−1
$(x^2-y^2,\ xy)$ $(xz,\ yz)$	(x,y) $(R_x,\ R_y)$	E	2	−1	0

Thus the same degeneracies – p_x and p_y, $d_{x^2-y^2}$ and d_{xy}, d_{xz} and d_{yz} – prevail; this is expected since all the orbital pairs are identical by a rotation along the three-fold axis, which remains intact at the surface, this rotational identity remains despite the lowering of the overall symmetry. On all the other surfaces this will no longer hold and thus degeneracies will be lost.

3.3 Adsorption on Ru(0001)

The adsorption of atoms and molecules on surfaces has a decisive role in the sequence of catalytic reactions since almost all of them have been confirmed to proceed via the Langmuir-Hinshelwood mechanism, where the reactants adsorb to the surface prior to the reaction, as opposed to the Eley-Rideal mechanism, where at least one of the reactants does not attach to the surface before reacting but rather stays in contact only with

Table 3.2: The integral of the projected density of states multiplied with the occupation numbers

layer	s	$p_{x,y}$	p_z	d_{z^2}	$d_{xz,yz}$	$d_{x^2-y^2,xy}$
Surface	0.26	0.06	0.04	1.08	1.10	1.08
Sub-surface	0.26	0.07	0.08	1.12	1.05	1.11
Middle (bulk)	0.26	0.07	0.08	1.08	1.09	1.10

layer	s	p	d
Surface	0.26	0.16	5.44
Sub-surface	0.26	0.22	5.44
Middle (bulk)	0.26	0.21	5.44

the other adsorbates during the reaction. Of the different ways of adsorption we shall concentrate only on the chemisorption; in this case the adsorbates form chemical bonds with the substrate and are thus strongly bound. Then the site for adsorption is a one with a high symmetry like those shown above for the hcp(0001) surface. The depth of the adsorption well, or the adsorption energy, depends on the adsorption site and thus the lateral coordinates of the adsorbate map – if the vertical coordinate is optimised at each lateral position and we simply forget the small influence of the substrate atoms – a two dimensional potential energy surface whose changes yield the corrugation *i. e.* the dependence of the energy on the lateral position. In a case of large corrugation there usually remain only one or few minima for adsorption, or if the potential energy surface is rather flat the diffusion can occur at lower temperatures and thus the adsorbate can temporarily change the adsorption site.

When the atoms or molecules are adsorbed on the surface they do not only interact with the substrate but – at the latest when the coverage approaches a full mono-layer *i. e.* the atom density is the same as of the substrate – mutually. This can occur directly either due to a direct over-lap of the electronic states of the adsorbates, electro-statically through the space above the surface between the adsorbates or indirectly by a change of the substrate and subsequently at the other adsorbate *i. e.* via substrate. The identification of the governing mechanism is in general difficult since *e. g.* the adsorption initially changes the geometry and thus the electronic structure of the surface although the adsorbate-adsorbate interaction would have a direct mechanism. If the adsorbate-adsorbate interaction is repulsive the adsorbates try to avoid each other, and if the repulsion is larger than the corrugation of the potential energy surface some of the adsorbates may enter an adsorption site different from the one preferred in the case of a single adsorbate, the adsorbates can form small domains inside which the adsorption site is the original one but at the boundaries of the domains the regular pattern is not continuous, the adsorbates can cause a lowering of the symmetry or the adsorbate layer arranges itself into an incommensurate, yet highly symmetric over-layer but with a different adsorbate-adsorbate distance and thus registry than that of the substrate; an example of the latter, a compressed and rotated structure for the carbon monoxide adsorbed at the Ru(0001), will be shown below. Similar structures can form if the adsorbate-adsorbate interaction is attractive and stronger than the corrugation, at low coverages clustering of the adsorbates takes place if the adsorbates only can diffuse along the surface or are deposited to the surface within the range of their attractive interaction. However we shall below concentrate on ordered, commensurate over-layers but changing the coverage we can observe trends in the adsorbate-adsorbate interaction. The adsorbates which we have chosen to be presented here are characteristic ad-species in catalytic reactions and constitute a precursor to the studies on the co-adsorption in the following Section.

We have investigated the adsorption of the most effective alkali metals cesium. The large size of a cesium atom or ion and the long range of the electro-static interaction between the adsorbates make a full mono-layer already energetically inferior with respect to the formation of a second adsorbate layer *i. e.* a bi-layer system. We wanted to perform calculations of the single adsorbate layer over a wide range of adsorbate-adsorbate distance, or coverages, and we shall make a short summary of the other systems of adsorption of an alkali metal we have studied. The carbon monoxide is an important molecule in several catalytic reactions and is the most studied molecular adsorbate in the literature of the surface science. Furthermore we shortly studied the adsorption of the atomic oxygen, an inhibitor to many reactions but also a reactant in some reactions.

3.3.1 Adsorption of cesium

The famous question concerning the adsorption of alkali atoms on a surface is whether the binding mechanism is ionic or covalent. We do not want to elaborate on this issue since according to our opinion it depends on the definition of ionic or covalent bonding and is thus not uniquely defined. However, according to the current understanding the picture which emerges from the vast number of studies devoted to the adsorption of alkalis is that the alkali denotes partially its outer-most, weakly bound *ns* electron to the hybrids formed with the substrate electrons causing the nucleus to be partially positively charged and a simultaneous reduction in the work function. The adsorption of alkali metal atoms on surfaces is an issue in itself but we shall limit ourselves mainly to the basic properties necessary to discuss the co-adsorption later.

The model traditionally used to describe the adsorption of alkali metals originates from the work of Langmuir and Gurney in the 1920's and 1940's – for a review please see *e. g.* Diehl and McGrath (1997). There the alkali has partially donated its loosely bound valence electron as discussed above, leaving the ion partially positive. This model has been widely used in the literature in the past but was challenged by the early density functional calculations of Wimmer *et al* (1983) who concluded that instead of ionisation the alkali polarises by forming hybrids of its loosely bound electron with the surface electrons. The Langmuir-Gurney model states that the density of electronic states of the alkali atom approaching the surface is like shown in the Figure 3.14: when far from the surface the valence electron of the alkali atom resides fully around the alkali atom. When approaching the surface the electronic level broadens and is only partially occupied.

The electron is distributed to the hybrids with the surface electrons and the positive extra charge forms an image charge at the surface like schematically shown in the Figure 3.15 for a free-electron like surface. The interaction energy is

$$E_{\text{image}} \propto -\mu^2/l^3 \ , \tag{3.1}$$

where l is the vertical distance between the charge and its image charge and μ is the dipole moment which can be approximated as two point charges with charge δ and distance l, thus $\mu = l\delta$. Please note that both l and δ would depend on the coverage.

The alkali atoms reveals a positive charge above the surface. Thus when the coverage increases the adsorbate-adsorbate interaction increases and is repulsive; the alkalis repel therefore each other on the sur-

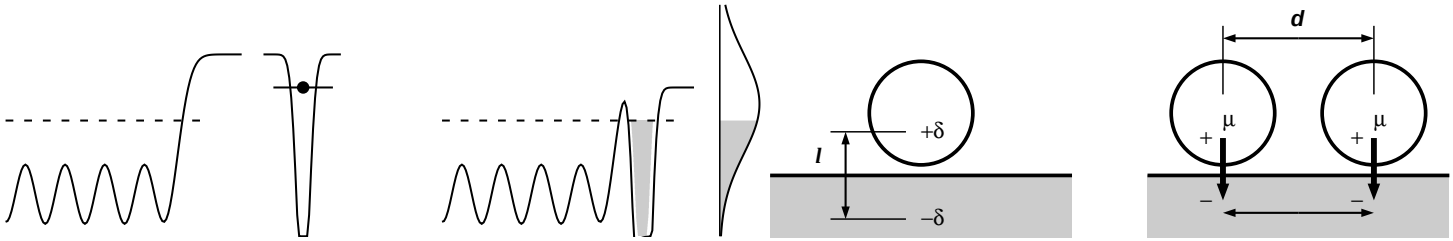

Figure 3.14: A model for the adsorption of an alkali metal due to the Langmuir-Gurney model. On the left the alkali atom is far apart from the surface and its outer-most *s* orbital is occupied with one electron. Upon the adsorption the alkali its *s* level broadens due to hybridisation with the metal bands; the corresponding density of states on the alkali ion is shown at the right, and only the part below the Fermi level – dashed line – is occupied

Figure 3.15: A schematic illustration of the electro-static interactions of electro-positive atoms on a metal surface, described here as a continuous electron gas. The attractive interaction between the charge on the ion and its image charge is on the left and the repulsive dipole-dipole interaction on the right

faces of transition metals. The dipole-dipole interaction is

$$E_{\text{dipole}} \propto +\mu^2/d^3 \ , \tag{3.2}$$

where d is the lateral distance between the dipoles as shown in the Figure 3.15; the adsorbate-adsorbate interaction is thus lateral whereas the image interaction is vertical. From the Equations 3.1 and 3.2 it is obvious that in the high coverages the alkali-alkali repulsion overcomes the attraction of the charge with its image charge. Furthermore the direct Hartree repulsion between the adsorbates increases at smaller distances because the partially screened positive charges start to interact.

When the coverage increases up to about 1/4 the work function begins to increase, approaching the value of the clean alkali metal. In the model of Langmuir and Gurney this is due to metallisation, *i.e.* formation of electronic bands close to the Fermi energy by the over-lapping states due to the adsorbates and thus giving rise to conductivity, in the alkali over-layer because the partially ionised alkali metal atoms start to interact also with each other and in order to reduce the electro-static dipole-dipole repulsion the alkali atoms reduce their ionicity, thereby decreasing the surface dipole and thus the change in the work function. Evidence for the metallisation came from the meta-stable de-excitation spectroscopy – *MDS* – (Woratschek *et al*, 1985) measurements (Fichtner-Endruschat *et al*, 1998), where the enhanced conversion of excited helium atoms from the triplet to singlet states was interpreted as a metallic layer; the earlier results (Böttcher *et al*, 1994; Woratschek *et al*, 1985) from lithium and sodium on Ru(0001) and cesium on Cu(110) have shown the meta-stable de-excitation spectroscopy to be well suited for detecting the state of metallisation. Jacobi *et al* (1994) suggested that the degree of localisation of the valence electrons could be used as an indicator of the metallisation. The vibrational frequency and intensity of the vertical ν(Cs-Ru) mode measured by He and Jacobi (1996) is shown in the Figure 3.16: First the frequency increases with coverage, by a magnitude which has not been explained so far, and then decreases. After the coverage 0.23 the vibrational loss is no longer detectable and an electronic excitation, plasmon, occurs. This was interpreted as full screening of the dynamical surface dipole induced by the cesium due to the metallisation of the over-layer.

As an example of the dipole interactions we show the evaluation of the energy components done by Over *et al* (1995a) based on the measurement of the work function by Hrbek (1985). From the work function one obtains the dipole moment by the Helmholtz equation and using a constant distance l=3.0 Å between the cesium ion and its image one obtains the total energy which is first highly attractive and at coverages > 0.2 repulsive relative to adsorbates at infinite separation. Above the coverage ≈ 0.33 the repulsion weakens slightly, due to the reducing dipole moment. However, the higher coverages are not stable due to the adsorbate-adsorbate repulsion because of the increase of the kinetic energy when the outer-most *s* orbitals start to overlap, and thus the Pauli repulsion increases rapidly. The large extent of the 6*s* wave function is evident from the Figure 3.18 which shows the overlap of the atomic orbitals between the closest-neighbour alkali-alkali pair; the 6*s* orbitals have their maxima close to the mid-point between the two atoms, and therefore a large penalty in the kinetic energy, part of which is won back due to the re-hybridisation, has to be paid in order to orthogonalise these orbitals. Part. The Figure 3.19 gives an estimation of the kinetic energy for a hexagonal mono-layer of cesium as a function of the nearest-neighbour distance; the sum grows approximately linearly with coverage. What is still missing from the energy in the Figure 3.19 is the hybridisation between the adsorbate and the substrate, and the electro-static and exchange-correlation adsorbate-adsorbate interactions beyond the dipole-dipole repulsion.

The effective size, describable *e.g.* with the Pauling radius, of the alkali atoms when adsorbed on the Ru(0001) surface shows that the alkali resides rather far from the surface (please see Over *et al*, 1995a) – even the smallest of them, lithium, in the $(\sqrt{3}\times\sqrt{3})$R30° structure has a larger inter-layer distance than ruthenium (Gierer *et al*, 1995). Therefore the distance to the substrate atoms underneath the alkali atom at different adsorption sites does not vary much and also the features of the electron structure smear out. Thus the corrugation of the potential energy surface for the adsorption of an alkali atom is rather small, and especially at large coverages the adsorbate-adsorbate repulsion determines the adsorption site and geometry rather than the adsorbate-substrate interaction. The Figure 3.20 depicts the phase diagram for Cs adsorption on Ru(0001)

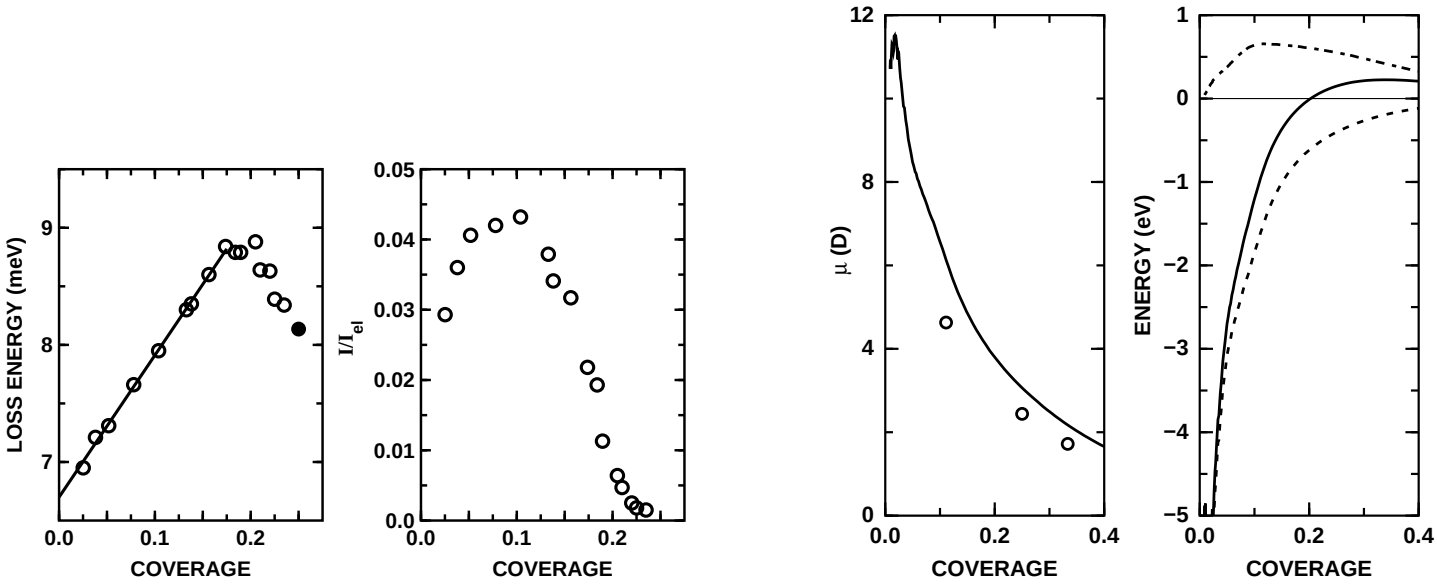

Figure 3.16: The vibrational frequency and intensity of cesium on Ru(0001) measured with the high-resolution electron energy loss spectroscopy by He and Jacobi (1996). The frequency with the filled circle is from our density functional calculations

Figure 3.17: *Left*: The dipole moment of cesium adsorbed on the Ru(0001) surface; *Right*: the estimated resulting image force – dashed line – and dipole-dipole – dot-dashed line – energies, and their sum – solid line. The circles are values from our density-functional calculations. After Over *et al* (1995a)

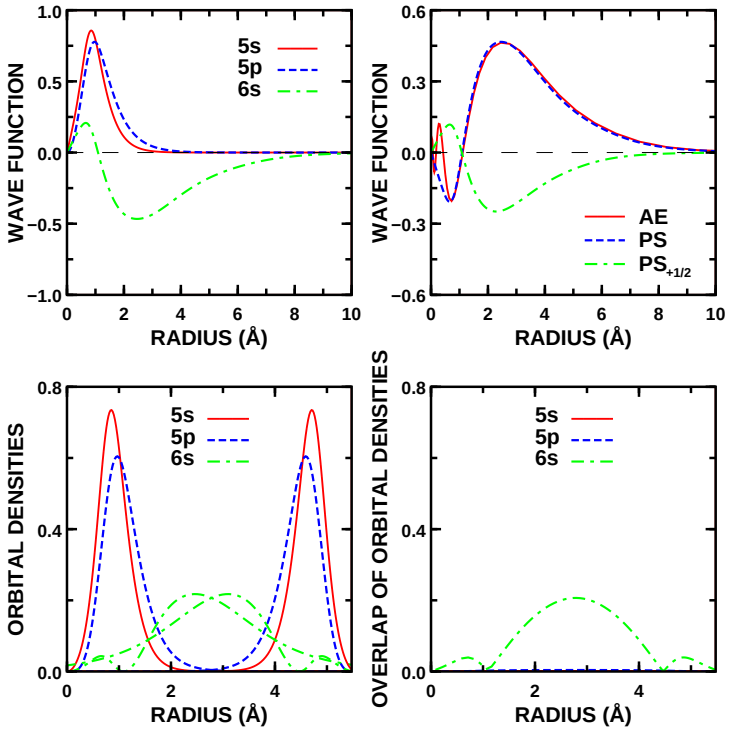

Figure 3.18: The pseudo wave functions of the valence and semi-core orbitals – upper left –, the 6*s* wave function in the neutral and half-ionised atom – upper right –, the orbitals of nearest-neighbour atoms corresponding to the distance in the (2×2) structure on Ru(0001) – lower left – and the overlap of the orbital densities – lower right, defined as $\sqrt{u_{lm}^2(|\mathbf{r}-\mathbf{R}_1|)\cdot u_{lm}^2(|\mathbf{r}-\mathbf{R}_2|)}$. The wave functions are multiplied with the radius so that the integral of the squared wave function over the radius gives one electron. In the ionised case the orbital was scaled with the occupation factor 1/2

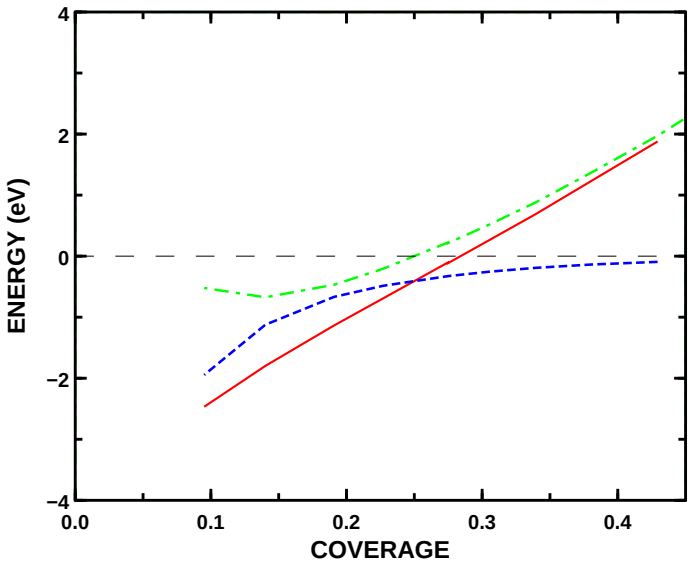

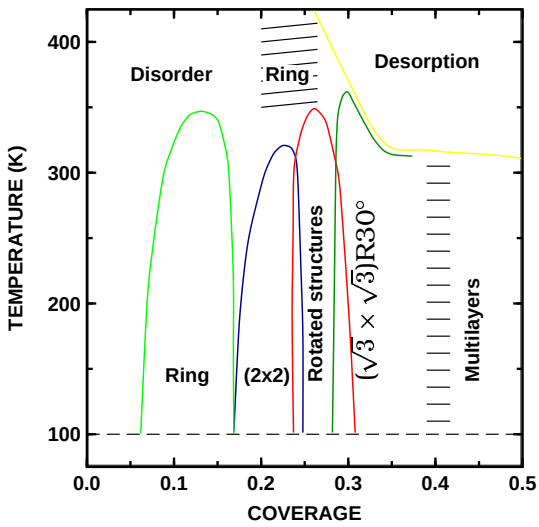

Figure 3.19: The kinetic energy of a free mono-layer of cesium – dot-dashed line –, the dipole-dipole and dipole-image interactions of cesium on Ru (0001) – dashed line – and the sum of them – solid line; the kinetic energy of the free atom has been subtracted, and the absolute position of the vertical axis is arbitrary

Figure 3.20: Phase diagram for the adsorption of cesium on the Ru (0001) surface as determined from the low energy electron diffraction experiments by Over *et al* (1992b)

Table 3.3: The adsorption energy, the change in work function from the clean surface, the dipole moment, the height of cesium above the nearest ruthenium atom and the cesium-ruthenium distance for cesium adsorbed on Ru (0001). All energies are in electron volts and distances in Ångströms; the dipole moments are in Debyes

Structure	Site	E_{ads} (eV)	$\Delta\phi$ (eV)	μ (D)	Z_{Cs} (Å)	d_{Cs-Ru}
$(\sqrt{3}\times\sqrt{3})$R30°	hcp	1.760	-3.24	1.73	3.08	3.50
	fcc	1.754	-3.22	1.72	3.09	3.51
	on-top	1.674	-3.23	1.72	3.14	3.14
(2×2)	hcp	1.945	-3.48	2.47	3.11	3.52
	fcc	1.945	-3.45	2.45	3.11	3.52
	on-top	1.936	-3.44	2.44	3.16	3.16
(3×3)	hcp	2.275	-2.90	4.63	3.19	3.58
	on-top	2.242	-2.93	4.68	3.22	3.22

determined from low energy electron diffraction experiments by Over *et al* (1992b); in addition to the two ordered structures – $(\sqrt{3}\times\sqrt{3})$R30° and (2×2) – there appear rotated structures where the adsorption sites are no longer only the high-symmetry sites. The ring structures indicate a liquid-like structure with a constant mean spacing between the adsorbates and no azimuthal ordering with respect to the substrate.

The weak corrugation of the potential energy surface for the alkali adsorption makes the prediction of the adsorption site difficult, and on the Ru (0001) the adsorption site changes between the $(\sqrt{3}\times\sqrt{3})$R30° and (2×2) over-layers for alkali atoms sodium, potassium, rubidium and cesium (Over *et al*, 1995a). For lithium only Doering and Semancik (1986) have reported a (2×2) pattern but it has not been reproduced up to date. In all the $(\sqrt{3}\times\sqrt{3})$R30° structures the alkali resides on the three-fold hollow hcp site whereas except for the on-top site of cesium the lighter alkali atoms sit on the other three-fold hollow site – fcc – in the observed (2×2) structures.

We have performed density functional calculations for cesium in the $(\sqrt{3}\times\sqrt{3})$R30°, (2×2) and (3×3) structures. The main results are summarised in the Table 3.3 and the geometries in the Figure 3.21. Higher coverages with pseudo-morphic ordering are not probable since the next ordered structure with a single adsorption site would contain nearest-neighbour distances of 2.70 Å, while the smallest of the Pauling radii, ionic radius, of cesium is 1.69 Å and thus even the ionic radii would overlap. Thereby no nearest-neighbour pair of cesium is likely to occur and furthermore, as discussed above, at these coverages the cesium atoms are more metallic than ionic and the covalent and metallic radii of cesium are much larger, 2.35 Å and 2.67 Å respectively.

The adsorption energy demonstrates clearly the repulsion between the adsorbates – cf the Figure 3.22, being still large beyond the third-nearest neighbour distance in the (2×2) structure; the magnitude is in good agreement with the heat of adsorption estimated from the simulations of thermal desorption experiments by Payne *et al* (1996). Here it is important to compare the values derived from the experiments with the theoretical desorption energies obtained assuming a "sequential abstraction" as explained in the Section 2.5.2. The calculated values are above the values of Payne *et al* at all the three coverages but this can be a systematic

Table 3.4: A comparison between the results obtained with two different pseudo potentials for the cesium. The first pseudo potential is used in all the other calculations, and the second one has only smaller core radii at the *s* and *p* channels

Structure	Site	E_{ads}	$\Delta\phi$ (eV)	μ (D)	Z_{Cs} (Å)	d_{Cs-Ru}
1st pseudo potential	hcp	1.945	-3.48	2.47	3.11	3.52
	on-top	1.936	-3.44	2.44	3.16	3.16
2nd pseudo potential	hcp	1.756	-3.46	2.49	3.14	3.54
	on-top	1.756	-3.50	2.46	3.18	3.18

overestimation, namely if the alkalis still interact in the (3×3) structure the first point, at the coverage 1/9, should be lower and this would decrease also the value at the coverage 1/4. The cohesion energy, marked with the arrow at the right hand side in the Figure 3.22, of bulk cesium from the density functional calculations is slightly smaller than in the results of Payne *et al.* Since the experimental desorption temperature between the first and subsequent cesium layers differs only slightly the adsorption energy at full- and multi-layer coverages must be similar at different coverages of cesium beyond $\Theta_{Cs} \approx 0.25$. Our results of the lower adsorption energy in the (3×3) than in the (2×2) structure does not necessarily imply the formation of an ordered (3×3) structure at coverage of 1/9 even at very low temperatures since the energy difference between the adsorption sites or in different over-layer spacings is close to the thermal energy k_BT. Please note further that the change in the work function is linear only up to a distance corresponding to about (5×5) structure – $\theta = 0.04$ – suggesting an interaction between the adsorbates, possibly via the substrate or electro-statically, up to these distances.

The very small difference in the adsorption energy between the different adsorption sites agrees well with the experimental findings of disordering already at low temperature (Over *et al*, 1992b), low frequency for the lateral motion and the large amplitude of displacement (Over *et al*, 1995d) in the low-energy energy diffraction measurement employing the method of split positions. The small differences set very high demands for the accuracy of the calculations, and the adsorption site in the (2×2) structure is erroneous in our results – the on-top site preferred in the experiments is higher in energy than the three-fold hollow sites. The difference from $(\sqrt{3} \times \sqrt{3})R30°$ to (2×2) is, however, correct since the adsorption energy of cesium on the on-top site becomes relatively more attractive than the three-fold hollow sites. Therefore – and considering the magnitude of the energy differences – we do not regard the error as significant. A possible source of error besides the numerical approach and usage of pseudo potentials in our calculations is the negligence of the zero-point and thermal vibrations; to estimate their effect the potential energy surface or at least the lateral and vertical vibrational frequencies should be calculated.

In order to identify the possible sources of error in predicting adsorption site we repeated the calculation of the cesium on the hcp and on-top sites in the (2×2) structure using a different pseudo potential which had smaller core radii for the 5*s* and 5*p* projectors and included the non-linear core-valence exchange correlation scheme explained in the Section 2.3.4. The results are collected in the Table 3.4, and they show very close agreement otherwise but the adsorption energies of the hcp and on-top sites are not practically identical, suggesting the difficulty in the prediction of the adsorption sites might be caused by small but in this case sensitive details of the calculation. A further test *e.g.* on the effect of the **k** sampling should be still performed to exclude an error due to it alone. Also the neglect of spin-orbit coupling and relavistic effects among the valence electrons might be responsible for the small but non-vanishing error.

The long adsorption distance is evident from the geometries shown in the Figure 3.21 and the Table 3.3. Our distances agree well in the magnitude with the results from the low energy electron diffraction. Again the exclusion of the zero-point and thermal vibrations can cause an error; their inclusion – especially the vertical one – would prefer a larger distance from the surface since the potential energy rises more steeply towards the surface, and this effect is largest at the on-top site where there is a ruthenium atom beneath the alkali atom. In order to gain insight on the magnitude of this effect we calculated the one-dimensional potential energy surface for the vertical motion of cesium – *i.e.* the surface is kept fixed and neglecting lateral degrees of freedom of cesium are neglected – in the (2×2) cell with the cesium atom at the on-top adsorption site. The potential energy is shown in the Figure 3.23 together with the ten lowest-energy wave packets obtained from the one-dimensional Schrödinger equation for a particle with a mass equal to that of the cesium atom. The frequency obtained from the potential energy surface is included in the Figure 3.16 and is 8.135 meV if evaluated classically, *i.e.* directly from the curvature and 8.168 meV if taken as twice the energy of the lowest-energy solution of the quantum mechanical Schrödinger equation, in very good agreement with the experiments. The large amplitude of the wave packets already prompts to a large amplitude for the vertical movement, but they are almost symmetric and thus the centre of mass of the wave packet, calculated at an kinetic energy $\frac{1}{2}k_BT$ corresponding to a temperature of 100 K where the experiments are usually carried out, shows only an increase in the vertical distance of 5 mÅ.

The atomic distances and heights between the cesium and nearest-neighbour ruthenium atoms show interesting trends: The height of Cs above the ruthenium surface is almost identical at a given coverage between different adsorption sites; thus the Cs-Ru distance is much smaller at the on-top sites, in variance with the expectation from the model of Langmuir and Gurney that the alkali atom would prefer a high-coordinated site in order to bond to as many atoms as possible since in the (2×2) geometry the alkali adsorbs at the on-top site leading to a much smaller and single bond than it would achieve at the three-fold hollow sites. Furthermore the Cs-Ru layer height and distance on a given site decreases with increasing coverage, although the metallic radius of cesium is larger than the ionic radius and thus the metallisation occurring beyond coverage $\approx$1/4

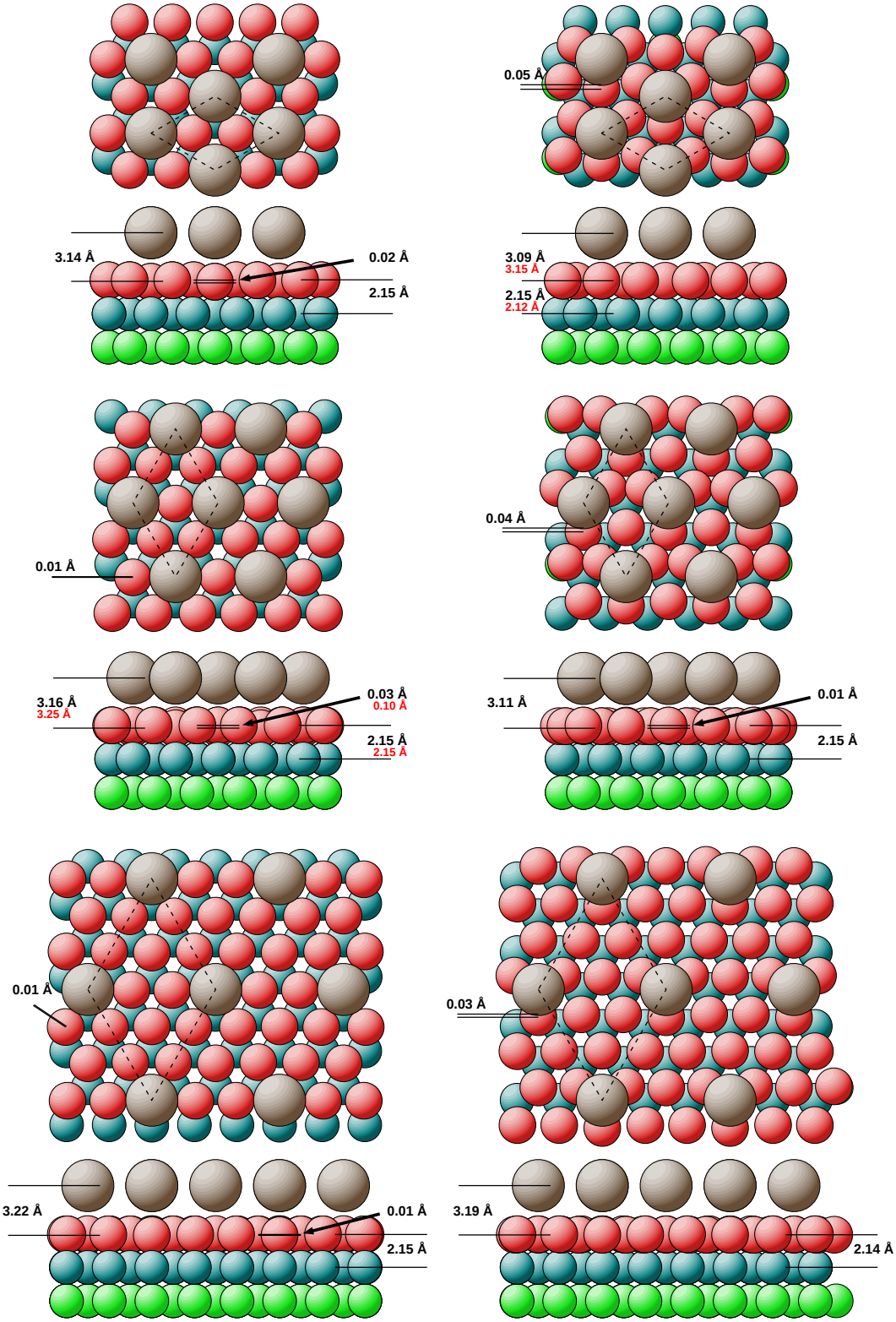

Figure 3.21: The adsorption geometry of cesium on Ru(0001) from our density functional calculations and experiments in the $(\sqrt{3} \times \sqrt{3})$R30°, (2×2) and (3×3) structures; the structures with the cesium atoms adsorbed at the on-top site are on the left and at the hcp site are on the right side. The experimental results from Over *et al* (1992b) are shown with the smaller font

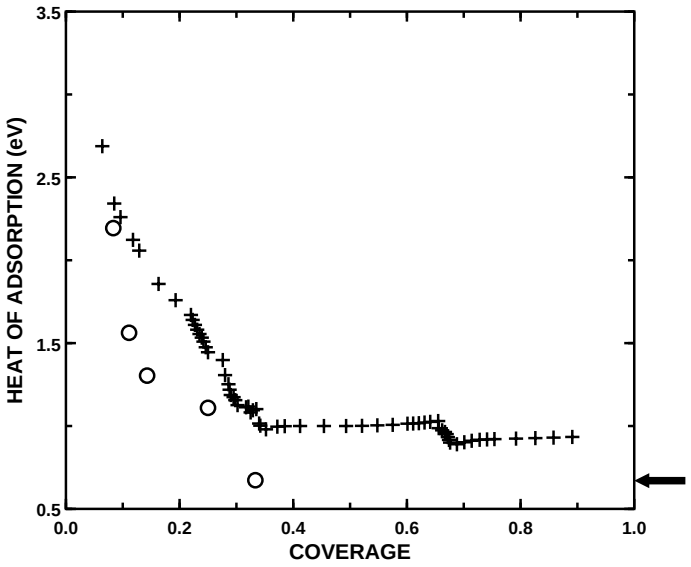

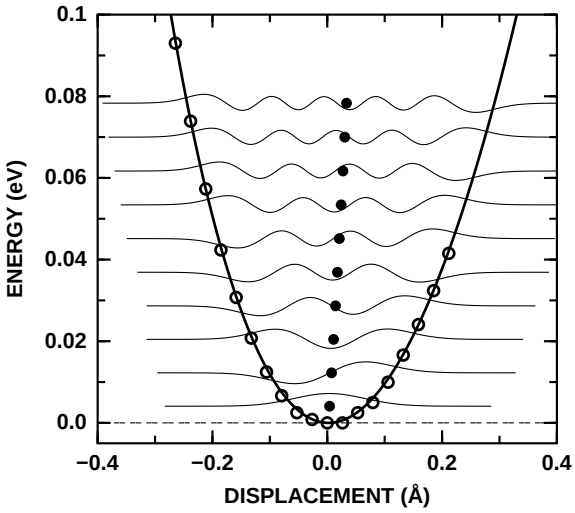

Figure 3.22: The heat of adsorption estimated by Payne *et al* (1996) – crosses – from the simulated thermal desorption curves and the adsorption energy from our density functional calculations – circles; the calculated cohesion energy of bulk cesium is shown with the arrow on the right of the plot

Figure 3.23: The potential energy surface – circles, calculated points by empty spheres and a polynomial fit by the thick line – for the vertical movement of cesium on Ru(0001) from our density functional calculations in the (2×2) structures. The ten lowest-energy solutions of the Schrödinger equation and their centres of mass in this potential are also shown

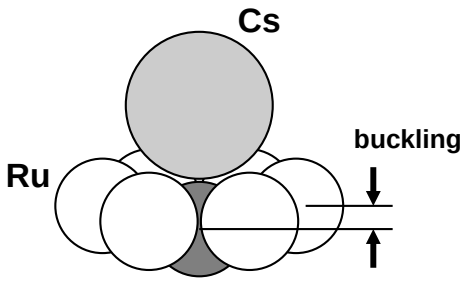

Figure 3.24: The schematic adsorption geometry of cesium at the on-top site forming a semi-seven-fold coordination

would require an increase upon increasing coverage. The same trend of apparently decreasing size of the alkali atom with increasing coverage was seen in the experiments of Schuster, Eng and Robinson (1995) using X-ray diffraction for cesium on the Ag(110), from the low energy electron diffraction studies of Kaukasoina *et al* (1997) for potassium, rubidium and cesium on the Ag(111), and by Wedler *et al* (1993) employing diffuse low electron energy diffraction for potassium on the Ni(100) surface.

Over *et al* (1995a) connected the site preference upon adsorption to the buckling of the outer-most substrate layer and this way to the bulk modulus of the substrate: in the (2×2) structure – and lower coverages – the cesium atom at the on-top site can form a semi-seven-fold adsorption site depicted in the Figure 3.24 by shifting the atom beneath the cesium towards the bulk – *i.e.* buckling – thereby better screening the dipoles from the other cesium atoms; the smaller the bulk modulus of the substrate, the easier it is to achieve the buckling. This effect is no longer efficient in the $(\sqrt{3} \times \sqrt{3})$R30° structure since the cesium atoms are already too close to each other and the screening by ruthenium atoms would no longer be sufficient, and therefore cesium now adsorbs on the high-coordinated hcp site. The lighter alkalis have a smaller dipole at the surface and are also smaller, and they do not need to adsorb at the on-top site in order to screen their dipoles but are placed at the fcc site in the $(\sqrt{3} \times \sqrt{3})$R30° structure. However, in our calculations the change in work function for potassium at the hcp site in the $(\sqrt{3} \times \sqrt{3})$R30° structure is smaller by 0.13 eV than for cesium, thus the dipole moment is only about 4 % smaller for potassium than for cesium. This does not support a large difference between the two different alkalis, again demonstrating the delicate balance between the adsorption at different sites.

Next we come to discuss the work function upon the adsorption; the Figure 3.25 shows the change in work function as a function of the coverage; the experimental data are from Hrbek (1985). Although our calculations reproduce the qualitative trend with the minimum correctly the magnitude is severely underestimated, most likely due to the applied generalised gradient approximation for the exchange-correlation functional since we have seen considerable errors in work functions for the clean aluminium and ruthenium surfaces, and on all adsorbate systems studied in the present work where a comparison to experiments is possible. It is interesting to note that although the work function of the clean ruthenium surface is too low, the change in the work

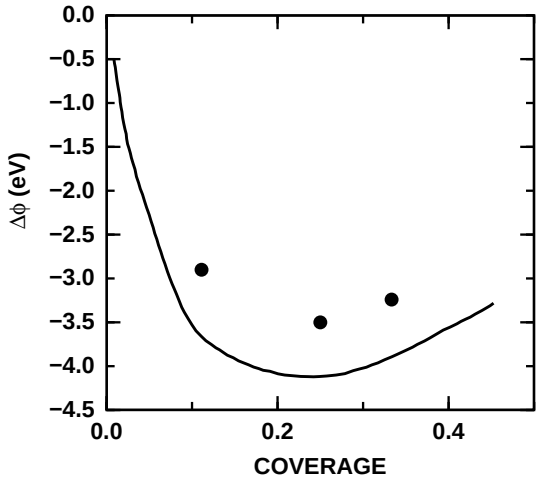

Figure 3.25: The change in the work function upon adsorption of Cs on Ru(0001); the solid line is from experiments by Hrbek (1985) and circles from our density functional calculations. At each coverage the adsorption site with largest adsorption energy was used in our results – please see the text

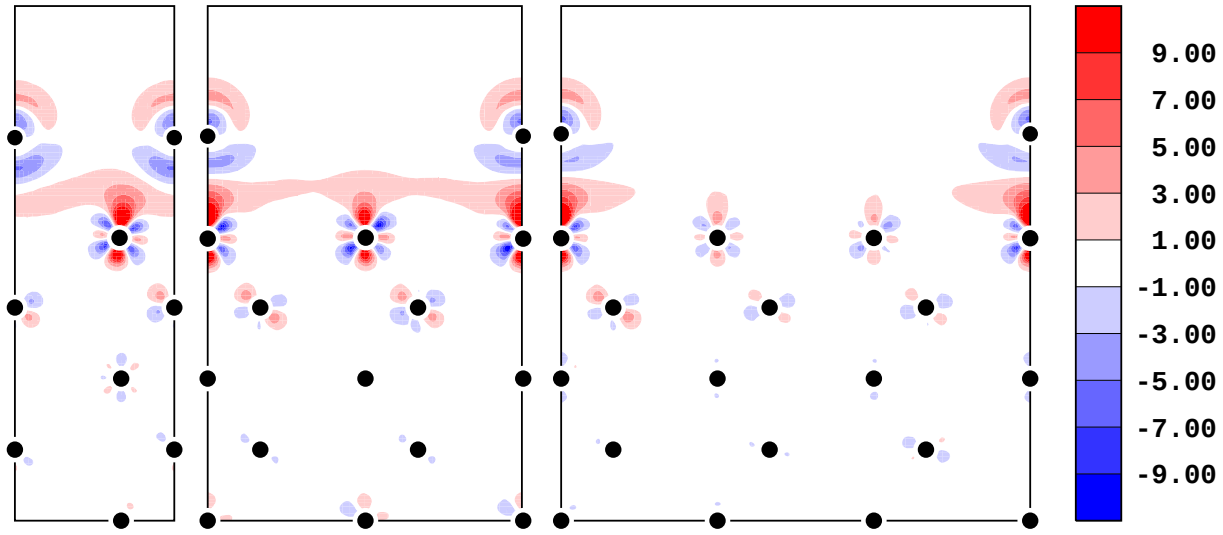

Figure 3.26: The change in the electron density upon the adsorption of Cs on Ru(0001) from our density functional calculations

function for an electropositive species like cesium is too small whereas for an electronegative species *e.g.* oxygen it is too large. Thus the work function of the surface with the adsorbate is overestimated or the too low a work function of the clean surface is responsible for the error.

The Figure 3.26 shows the change in the density upon adsorbing cesium to the surface both at the hcp and on-top site in the $(\sqrt{3} \times \sqrt{3})$R30°, (2×2) and (3×3) structures; the density of pure cesium layers needed in the differences was obtained from the superposition of a layer of cesium atoms in the corresponding cell. Common features in all of the structures are easily distinguishable, among them the most prominent is the increase of electron density in the d_{z^2} orbitals of the outer-most layer ruthenium atoms, and the decrease of the d_{xz} and d_{yz} orbitals of the same atoms. Furthermore the changes around the cesium atom are in all the cases similar, being smaller than expected from the large decrease in the work function and somewhat in a wrong direction expected if the decrease would be assigned only to the ionisation of the cesium atoms because there is for example a region of increased density above the cesium atom; this increases the dipole moment and subsequently the work function. However, the decrease in the work function is not entirely due to an "ionisation" or "charge transfer" – or rather, hybridisation of the states of the alkali and the surface – of the alkali but the work function of the surfaces of pure alkalis are about 2 eV, *i.e.* about three electron volts lower than that of Ru(0001), and the value of the work function of multi-layers of alkali on Ru(0001) should finally approach this value although in the multilayers the cesium atoms are not ionised. We acknowledge Alberto Morgante for reminding about this consideration.

The decomposition of the charge density difference to the contribution from the 5*s*, 5*p* and valence orbitals, shown in the Figure 3.27, indicates that also the semi-core states 5*s* and 5*p* polarise strongly upon the adsorption, although their participation to the bonding is expected to be small. A close inspection, shown in the Figure 3.28, clearly reveals a bonding-like hybrid of d_{z^2} character at the nearest-neighbour ruthenium atom with the 5*p* orbital of the cesium atom. Even if not a bonding at least some kind of an effect of the nearest-neighbour ruthenium atom on the cesium 5*p* level is expected based on the orbital overlap of the two free

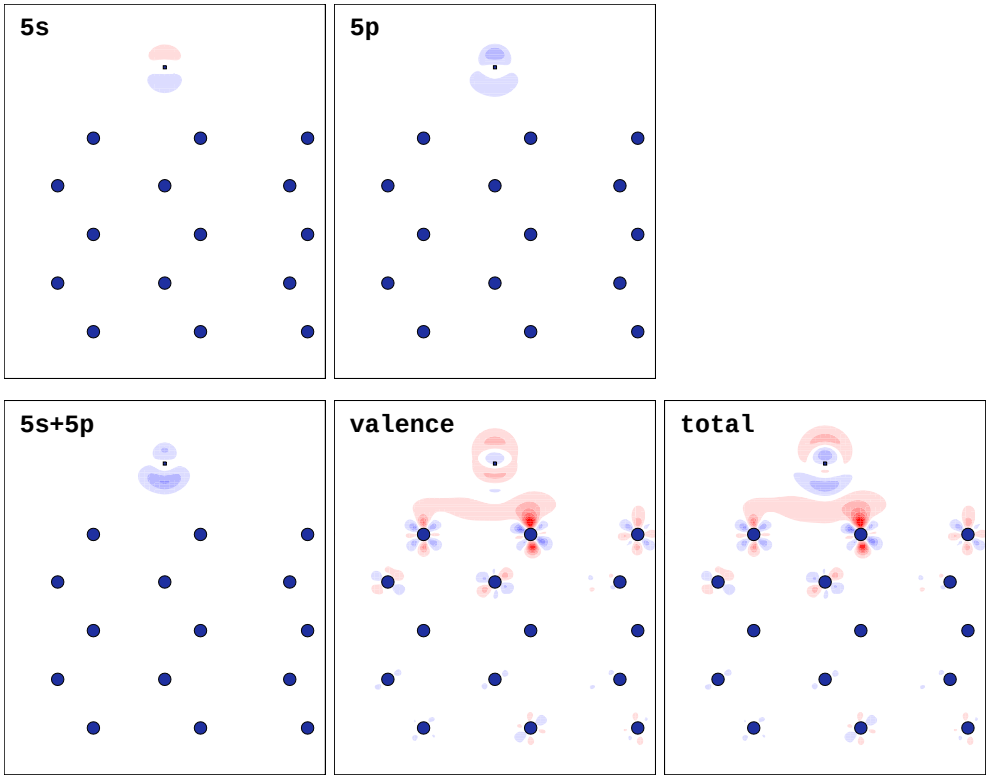

Figure 3.27: The change in the electronic density of the Cs_{5s} – upper left panel –, Cs_{5p} – upper middle –, sum of Cs_{5s} and Cs_{5p} – lower left –, valence energy region – lower middle – and the total density – lower right – upon the adsorption of Cs on Ru(0001) in the (3×3) structure from our density functional calculations

atoms in the Figure 3.29, resulting in a Pauli repulsion with mainly the Ru_{5s} and Ru_{4d} orbitals due to the ortho-normalisation of the single-particle states.

Please notice that the large changes of an increase above the atom and a reduction below was seen to happen also with the second pseudo potential with smaller core radii for the 5*s* and 5*p* orbitals, proving that these effects are not an artifact of the pseudo potential treatment of the region close to the nuclei because in this pseudo potential were smaller than the region around the atom where the major part of the change occurs.

An indication of the charge density distribution upon adsorption can be obtained from the asymptotic behaviour of the charge density outside the surface, into the vacuum, because this is different for different surface atoms and different chemical states of the same atom because the potential depends on the electronic structure of the adsorbate and this determines the tail of the charge density into the vacuum.[2] The asymptotic densities are collected into the Figure 3.30: The (3×3) curve clearly deviates from the curves at the higher coverages, or from the curve for the free mono-layer; only the curve with the ionised cesium atom can follow the density at the low-coverage structure; however the amount of ionisation is unrealistically large.

A further measure of the asymptotic electronic structure is provided by the pseudo scanning tunnelling microscope images in the Figure 3.31, calculated using the Tersoff-Hamann model introduced in the Section 2.5.11. At the clean surface the corrugation is negligible, and a large corrugation and a distance much larger than at a clean surface is immediately obvious. This is of course as expected since the loosely bound 6*s* electron decays slowly into the vacuum, causing the density to be increased by a small but sufficient amount. Except for the largest tunnelling current *i.e.* largest electron density in the left-most panels in the Figure 3.31 the corrugation extracted from the plot for the total density or the density in the vicinity of the Fermi level only are very similar; this is because the major effect of the adsorption of cesium on the surface happens in the neighbourhood of a couple of electron volts around the Fermi energy as we shall discuss below. Qualitatively the effect is so large that changing the electron density and thus the tunnelling current by four orders of magnitude does not lead to qualitative changes beyond the apparently smaller size of the bump around cesium; only at the largest tunnelling currents would the tip approach the surface to the same distance as at the clean surface. Since the coverage was only 1/9 in these images this is a clear indication of the large effective size of the adsorbed cesium and in higher coverages the corrugation would decrease – also due to the increased metalicity – and the tip would remain still further from the surface even at the minima.

An useful concept to investigate the distribution of the charge density upon the adsorption of an alkali metal is the induced density, which was discussed in the Section 2.5.8 and used *e.g.* by Neugebauer and Scheffler (1992). Please notice that if the 6*s* orbital of the free atom would also be subtracted this would be equal to the ordinary density differences. Therefore qualitatively the induced density describes where the 6*s* is located in

[2]Please note that the generalised gradient approximation yields an incorrect decay of the potential into the vacuum; we hope that the qualitative behaviour is correctly reproduced, which is likely since the geometry, work function *etc* are well described within our current approach

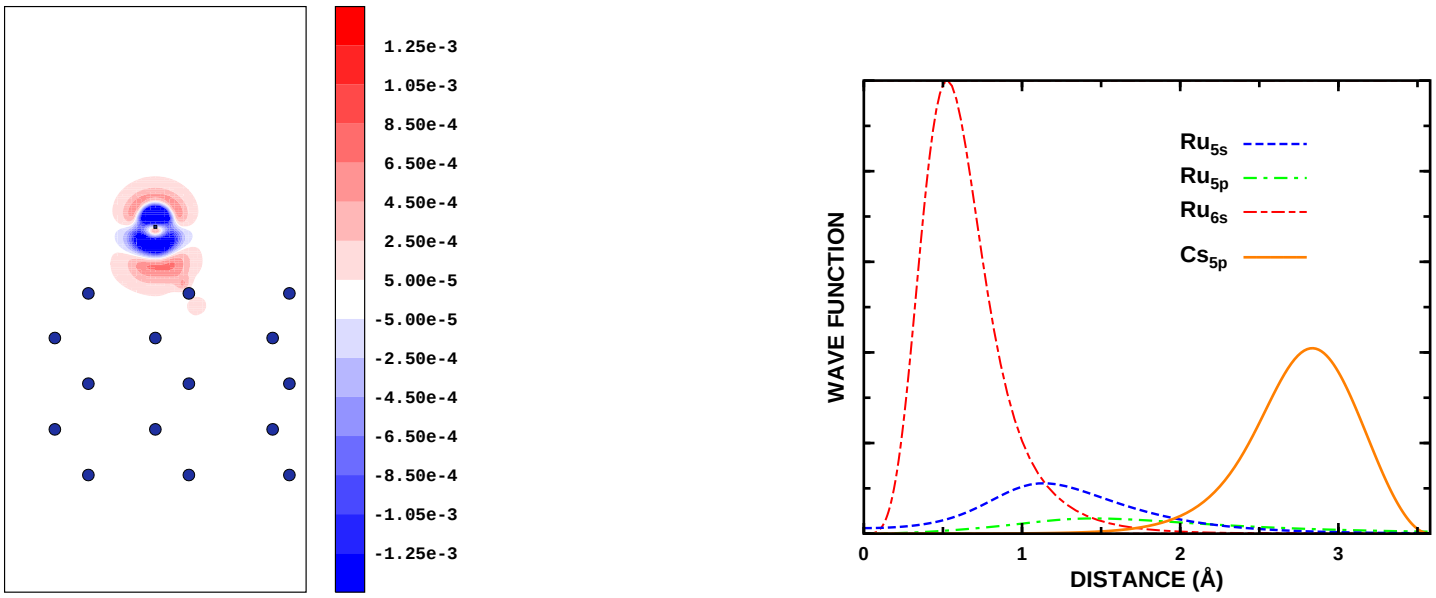

Figure 3.28: The change in the electronic density of the Cs_{5p} energy region upon the adsorption of Cs on Ru (0001) in the (3×3) structure; this is the same figure as the middle panel in the upper row of the Figure 3.27 but on a finer scale

Figure 3.29: An illustration of the orbital densities from free-atom wave functions of ruthenium and their overlap with the semi-core state $5p$ of a cesium atom; the distance between the ruthenium and cesium atoms is taken as a typical bond length of cesium on the Ru (0001) surface

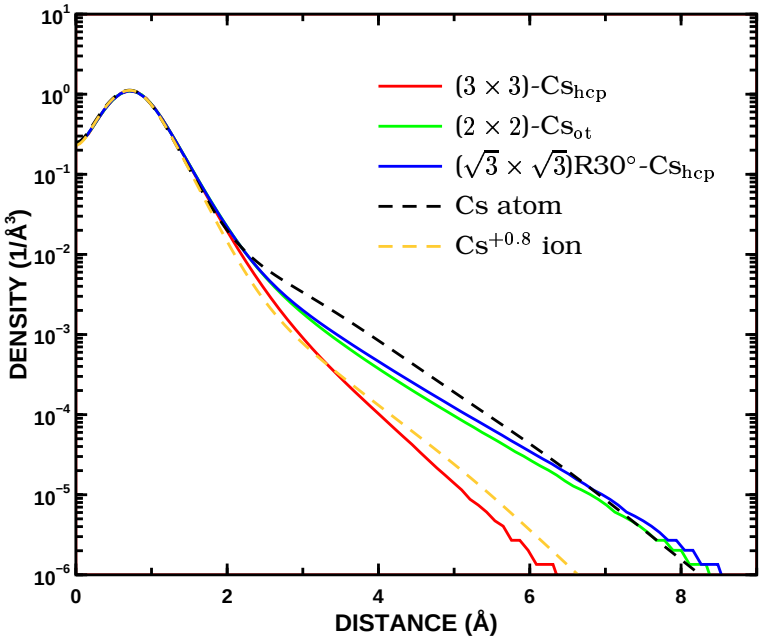

Figure 3.30: The asymptotic density above the cesium atom in different structures on the Ru (0001) surface as obtained in our calculations. The black and orange dashed lines are the asymptotic densities of a neutral cesium atom and a cesium ion with the net charge of +0.8 of the absolute of the charge of an electron, respectively; the blue, green and red lines are the densities in the $(\sqrt{3} \times \sqrt{3})$R30°, (2×2) and (3×3) structures

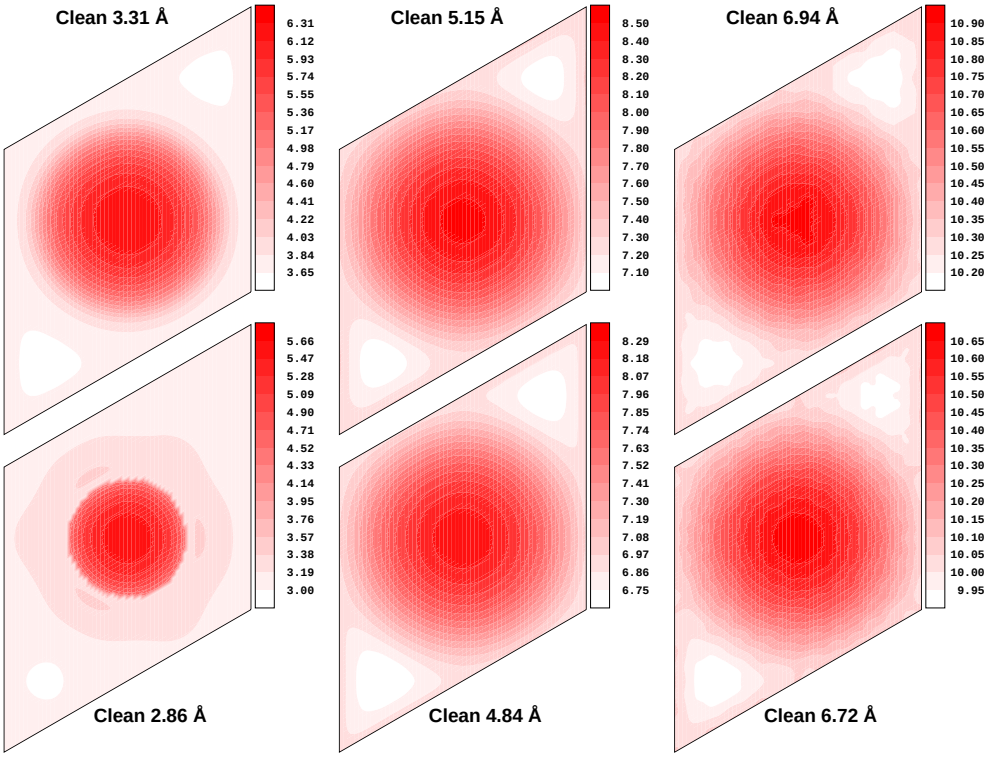

Figure 3.31: The pseudo scanning tunnelling microscope images produced via the Tersoff-Hamann model for cesium at the hcp site on the Ru(0001) surface in a (3×3) geometry using our calculated Kohn-Sham orbitals. In the upper panel the total density and in the lower the density arising from the Kohn-Sham states $\pm 1/2$ eV around the Fermi energy was used, and shown is the distance – in Ångströms – from the upper-most ruthenium layer in the constant density mode with the values 10^{-4}, 10^{-6} and 10^{-8} e^-/Bohr^3 from the left-most to the right-most panel; the corresponding average distances at the clean surface are indicated

the adsorbed system and how the electron density has changed during the interaction. The induced density in the Ru(0001)-(3×3)-Cs_{hcp} structure is compared face to face against the super-imposed charge densities from free cesium atoms in the Figure 3.32. The shapes are reminiscent, with the spherical shape above the atoms and a region of density in between the subsequent cesium atoms, but especially the radial density is largely contracted; also in the region between the cesium atoms the density above the line connecting the alkali atoms undergoes a slight reduction. Therefore qualitatively the alkali decreases in size and donates part of its long-range tail of the 6*s* orbital most likely to the hybrids with the surface; but most importantly, the long range of the 6*s* orbital would cause a large Pauli repulsion with the surface atoms and thus the character of the orbital must be changed and a partial ionisation alone would not suffice to eliminate the repulsion, only a complete ionisation of the cesium can prevent the repulsion. These observations lead to a qualitative picture like in the Figure 3.33 where the density of the 6*s* orbital is reduced, mostly by a shift from below the atom and from the long range towards the nucleus. It is important to realise that also in the higher coverages the 6*s* orbital has to face the repulsion with the surface electron, independent whether the atom would or would not be ionised, as the distance from the surface atoms hardly varies with the coverage. The induced charge density in the Figure 3.34 for the Ru(0001)-(2×2)-Cs_{ot} structure indicates how the apparent size of the cesium atom has now increased relative to the lower-coverage structure and between the cesium atoms the density remains higher throughout the surface unit cell, with the smallest contour staying almost at constant height. This is naturally exactly what was expected to happen in the pseudo scanning tunnelling microscope images: the corrugation would be small and the tip would reside at remarkable heights from the ruthenium atoms at the surface.

The electro-static potential is shown in the Figure 3.35 for the clean Ru(0001) surface and with the adsorbed cesium in an (3×3) over-layer, with their difference in the panel on the right; this is the electro-static potential created by the induced density of the cesium atom since the electro-static potential is a linear operator. The difference shows how fast the changes in the electronic structure due to the alkali metal are screened towards the bulk of the slab, and this also validates that the thickness of our slab is sufficient to treat the adsorption of the alkali metal. The difference has been normalised to zero in the vacuum of the side of the clean surface of the slab, and thus the difference gives us the change in the work function, and now it can be studied varying in space whereas the usual definition of the work function is an integral over the region parallel to the surface. The lateral variation has been studied experimentally with the method of the photo-emission of adsorbed xenon – *PAX* – (Wandelt, 1987), where the xenon atoms experience a different electro-static potential depending on the adsorption site and thus their polarisation and subsequently the electron binding energy depends on the local environment around the xenon atoms. Wandelt and co-workers have applied this method to several cases of alkalis adsorbed on metal surface, and the results (Markert & Wandelt, 1985) for potassium adsorbed on

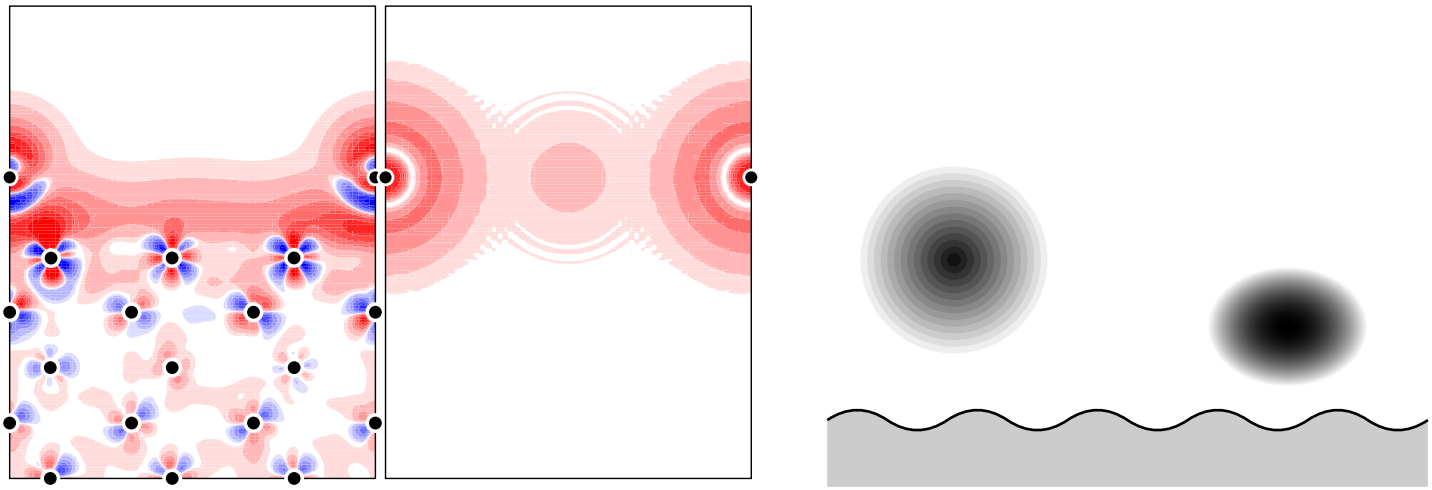

Figure 3.32: The charge density induced by the adsorption of cesium in the Ru (0001)-(3 × 3)-Cs_{hcp} structure – left – and the superposition of the charge densities from free cesium atoms in the same cell – right

Figure 3.33: The schematic change in the 6s orbital upon adsorption; the atomic state at left is before and at right – deformed and split among many hybrids with the states of the substrate – after the adsorption: The hybrids formed upon adsorption are more localised especially vertically since the weak potential into the vacuum and strong Pauli repulsion with the states of the substrate oppress the states from both sides

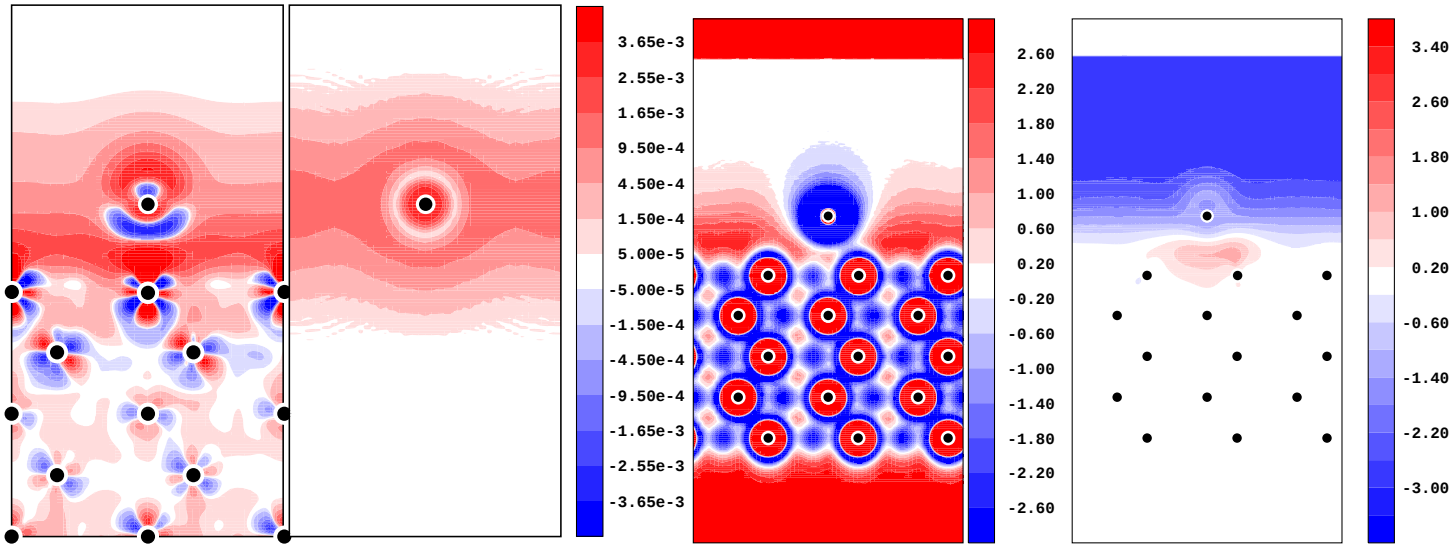

Figure 3.34: The charge density induced by the adsorption of cesium in the Ru (0001)-(2 × 2)-Cs_{ot} structure – left – and the superposition of the charge densities from the 6s orbitals from free cesium atoms in the same cell – right

Figure 3.35: The electro-static potential of the system Ru (0001)-(3 × 3)-Cs_{hcp} – left – and the change in electro-static potential relative to the clean surface – right

Table 3.5: The local work function at different sites for potassium from experiments (Markert & Wandelt, 1985) and cesium from density functional calculations on th Ru(0001) surface; the process of determining the value from the calculation is described in the text. ϕ(Xe/Ru), ϕ(Xe/A/Ru) and ϕ(Xe/A) are the work function at the patches of the clean surface, at the surface next to the alkali and above the alkali atom, respectively. All entries are in electron volts

	θ(A)	ϕ(Xe/Ru)	ϕ(Xe/A/Ru)	ϕ(Xe/A)
	0	5.52	—	—
	K: 1/60	5.44	4.89	4.17
Experiments	K: 1/30	5.17	4.54	3.77
	K: 1/15	5.02	4.19	3.27
	K: 1/10	—	3.86	2.97
Calculations	Cs: 1/9	—	2.67	1.89

the Ru(0001) surface are reproduced in the Table 3.5. Unfortunately we have not studied the adsorption of potassium on this surface at low coverages, and the lowest coverage we have studied with cesium is only the largest coverage of potassium in the investigations of Markert and Wandelt, and the cesium is furthermore larger than the potassium. Despite these differences we found it interesting to make a comparison to these experiments, and to approximate the value of the "local work function", as termed by Wandelt and co-workers, we determined the adsorption height by taking the density at a clean Ru(0001) surface corresponding to the adsorption height in the Ru-($\sqrt{3} \times \sqrt{3}$)R30°-Xe_{ot} structure; the height from our calculations (Ari P Seitsonen, unpublished results) – 4.09 Å with the generalised gradient approximation – is much larger than the experimental value of 3.54 Å by Narloch and Menzel (1997); our value with the local density approximation is in turn too small, 2.84 Å. However, we continue to use the value from the generalised gradient approximation since a slight error in the density will not lead to qualitative changes in the final results of our studies. This gives us the density 1.02×10^{-4} Å^{-3} in which the xenon atom likes to reside, and with this density we obtain the map of the local work function in the Figure 3.36, and from this data we extract the approximate work function in the Table 3.5. We acknowledge the drastic approximations made in our estimation, but the qualitative agreement with the experimental results gives some creditability to the procedure. We find about the same value of the work function for cesium as was obtained in experiments for potassium, being in agreement with the too small a change in the calculation as shown in the Figure 3.25. We took the value for the xenon adsorbing at the surface under the influence of alkali – Xe/A/Ru – from the site furthest away from the alkali in the unit cell; for the adsorption at the clean surface – Ru – our coverage 1/9 is still too large and unit cells (4×4) and beyond should be used.

It is instructive to compare the change in the electro-static potential at the Ru(0001) surface to the corresponding change at a jellium surface, as shown in the Figure 3.37 together with the change in the electron density in both cases; a (2×2) cell was used. The qualitative change is obvious, although the potentials somewhat differ.

The electro-static potential, or rather the changes in it, give rise to electric fields which then influence the electrons of the co-adsorbates; the electric field is the negative gradient of the electro-static potential,

$$E = -\nabla V_{\mathrm{els}} \; . \tag{3.3}$$

The field is a vector quantity and has thus three components; in order to represent the results in a clear way we show either the three components separately or show only the magnitude of the field, and since we are interested in the changes in the electric field caused by the cesium we use cylindrical coordinate system for the gradient where the vertical axis goes through the centre of the cesium atom, along the surface normal; thus we have the radial, azimuthal and vertical components of the field like in the Figure 3.38 for cesium in the (2×2)-Cs_{ot} structure. In this case the vertical component is clearly dominating the lateral field, and thus the magnitude of the field is approximately the magnitude of the vertical field, being about 1.7 eV/Å; this is in a good agreement with the simple kind of prediction by Mortensen *et al* (1997): from the change in the potential of -3.5 eV in the work function over a distance of about $\approx$2 Å the estimated field would be -1.7 eV/Å. These are strong fields on the molecular scale. In the Figure 3.39 the vertical component of the electric field at the surface shows a clear reduction as a function of coverage, being only 0.9 eV/Å in the lowest coverage furthest away from the cesium.

We now come to study the electronic structure of the cesium over-layer and its bonding to the substrate in more detail using the calculated change in the total density of states in the Figure 3.40 and the projected density of states at the site of the cesium atom at different adsorption sites in the Figure 3.41 and as a function of coverage in the Figure 3.42. The change in the total density of states shows little difference between the two different adsorption sites studied in the low coverage, and overall rather a small dependence on the coverage; there are two dips, at 5.5 eV below and 0.5 eV above the Fermi energy, and an increase between these two energies and above the dip at 0.5 eV. In the projected density of states at the cesium atom the magnitude of the *s* component grows from 4 eV below the Fermi energy, having a peak and a dip at half of an electron volt below and above the Fermi energy, corresponding qualitatively the change in the total density of states; however, the dip at low energy and the depth of the peak at just above the Fermi energy remain unexplained, although we expect the former to be an artifact of changes at the other, clean surface of the slab. The difference between the hcp and on-top sites is small, but at 2 eV below the Fermi energy there appears a peak which is present only in configurations with the cesium at the hcp site; in the geometries with the cesium on the on-top site there

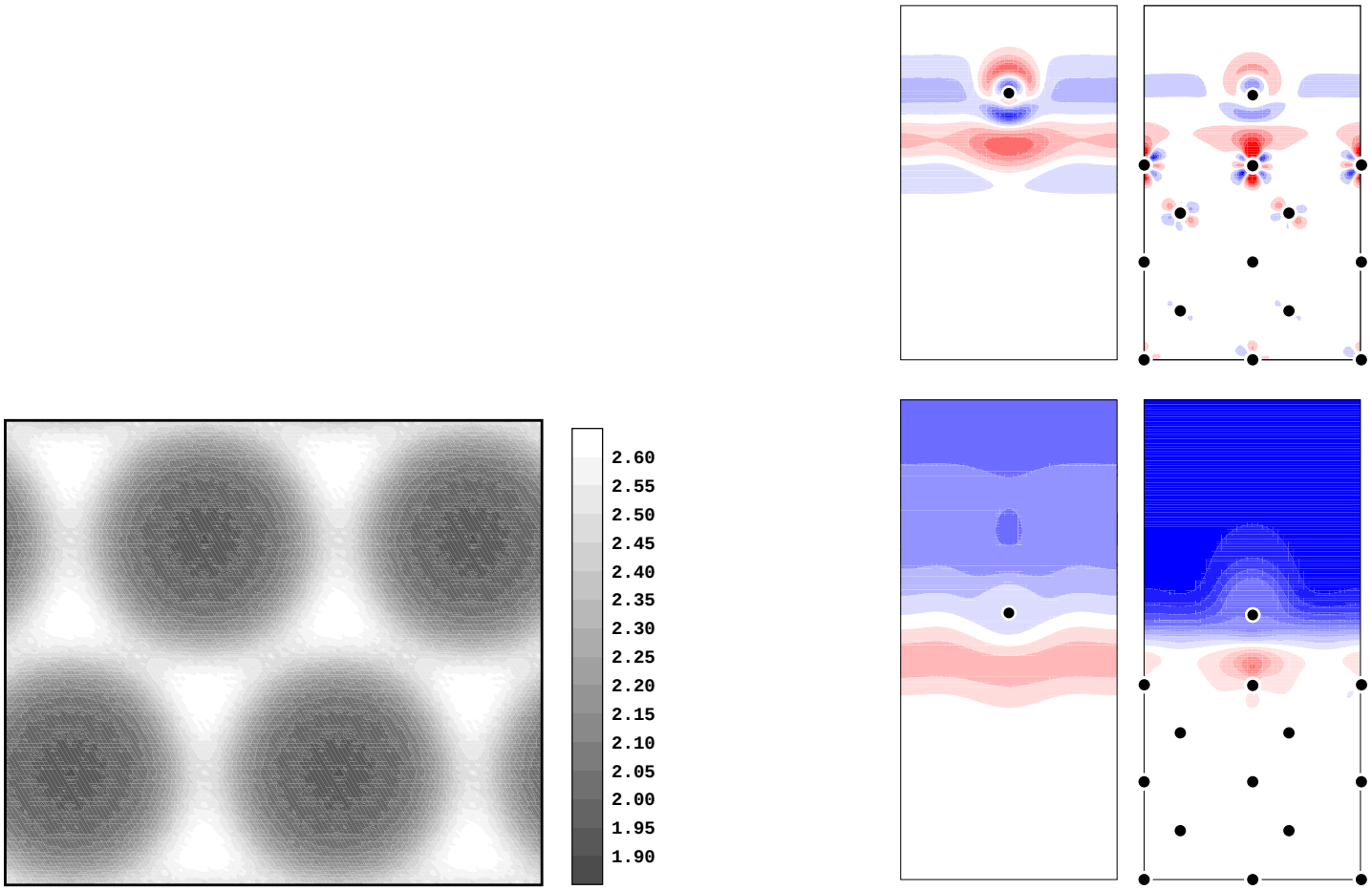

Figure 3.36: The local work function in the structure Ru (0001)-(3×3)-Cs_{hcp}; the values are in electron volts. Please refer to the text for details about the evaluation of the local work function. The cesium atoms reside below the minima of the work function

Figure 3.37: The change in the electron density – upper panels – and electro-static potential – lower panels – upon the adsorption of cesium on a jellium surface – left – and on the Ru (0001) surface – right – in the (2×2)-Cs_{ot} structure. The density parameter of the jellium slab was $r_s = 3$ Bohr

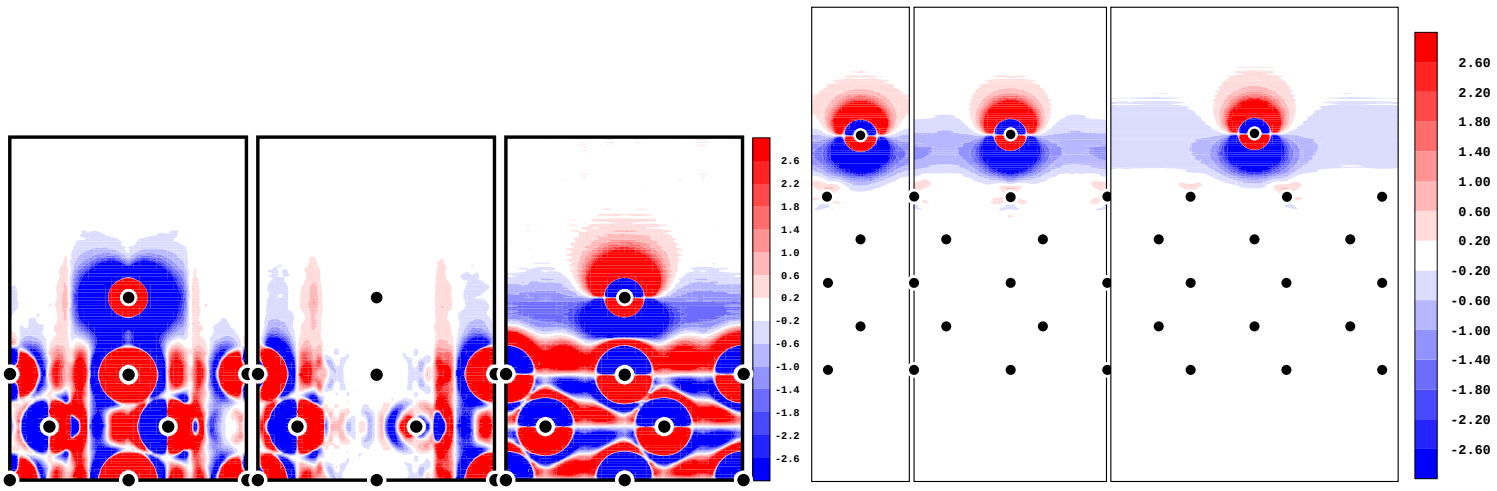

Figure 3.38: The radial, azimuthal and vertical components of the electric field – from left to right, in electron volts per Ångström – arising from the electro-static potential in the Ru (0001)-(2×2)-Cs_{ot} structure

Figure 3.39: The change in the vertical component of the electric field induced upon the adsorption of cesium in the $(\sqrt{3} \times \sqrt{3})$R30°-$Cs_{hcp}$, (2×2)-Cs_{ot} and (3×3)-$_{hcp}$ structures, from left to right. All the fields are in electron volts per Ångström

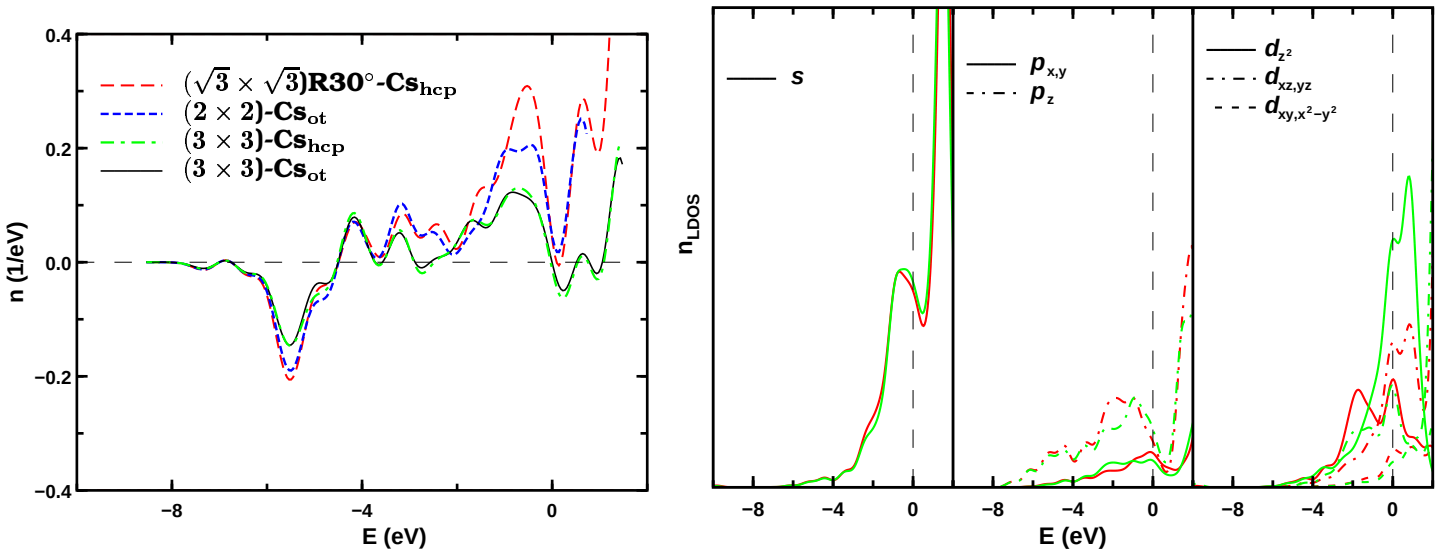

Figure 3.40: The change in the total density of states – calculated from the Kohn-Sham eigenvalues – due to the adsorption of cesium on the Ru(0001) surface

Figure 3.41: The local density of states projected to the cesium atom in the Ru(0001)-(3 × 3)-Cs_{hcp} – red – and Ru(0001)-(3 × 3)-Cs_{ot} structures – green

Table 3.6: The integral of the density of states projected on the cesium atom at different coverages and adsorption sites

System	s	$p_{x,y}$	p_z	d_{z^2}	$d_{xz,yz}$	$d_{x^2-y^2,xy}$
Ru-($\sqrt{3}\times\sqrt{3}$)R30°-Cs_{hcp}	0.30	1.79	1.78	0.03	0.02	0.01
Ru-(2 × 2)-Cs_{ot}	0.28	1.79	1.78	0.03	0.02	0.01
Ru-(3 × 3)-Cs_{hcp}	0.26	1.79	1.79	0.03	0.02	0.00
Ru-(3 × 3)-Cs_{ot}	0.26	1.79	1.78	0.03	0.02	0.00

is a corresponding, though weaker, increase in the $d_{xz,yz}$ orbitals. Also the peak in the d_{z^2} is in lower energies at the on-top than at the hcp site; otherwise the magnitude of the s component clearly scales with the cesium coverage whereas the p components do not.

In the Table 3.6 we have collected the density of states projected at the site of the cesium, multiplied with the Fermi occupation function as in our self-consistent calculation and then integrated over the energy. Thus the values resemble the number of electrons with the corresponding angular quantum numbers but the magnitude should not be taken too seriously, rather the changes in the magnitude, due to the considerations mentioned in the Section 2.5.4. For cesium we used the 5p wave function for all the p-like electrons and the 6s wave function for both the semi-core and valence s-like orbitals although the latter is largely changed due to the influence of the surface; please see the Figure 3.33. Beyond this the change in the p and d orbitals is small at different coverages and adsorption sites but the magnitude of the s component increases, most likely since due to the metallisation of the valence electrons, which leads to a recovery of the more atomic-like 6s orbital. It is also interesting to notice that the 5d orbitals at the cesium site are indeed somewhat filled at the surface like we found to occur also in a free mono-layer of cesium, whereas they are empty in the free atom. However they lie only about -1.7 eV above the 6s orbital in the free atom and can thus become easily occupied in a suitable environment.

The ruthenium atoms in the surface layer showed characteristic features upon the adsorption of cesium: firstly there is a region of increased charge above the first layer between the surface atoms, and secondly the d orbitals of the surface atoms polarise strongly. Whereas the former is due to weakly bound and long-tail electronic states, the latter is localised around the ruthenium atoms and thus it can be clearly seen in the projected density of states; this is shown in the Figure 3.43 as the change from a clean surface for the different coverages, together with this change multiplied by the Fermi occupation statistics and integrated over the energy in the Table 3.7. The most prominent effect is the filling of the d_{z^2} orbitals just above the Fermi energy by moving them downwards in the energy, thus causing an increase in the integral over the projected density of states. Especially in the lower coverages the other d orbitals have a double peak structure with a decrease between them. The s and d orbitals have a component along the z axis have a small dip at -5.5 eV below the Fermi energy where the dip was found also in the change of the total density of states.

An interesting feature in the change of the projected density of states is how similar especially the d_{z^2} orbitals are in spite of the different coverage and even adsorption site of the cesium. Therefore we extracted the change in the density of states projected on the different ruthenium surface atoms for the same system – Ru(0001)-(3 × 3)-Cs_{on-top} as there the distance from the cesium to the nearest neighbour ruthenium atom is one of the shortest and the distance to the next-next nearest neighbour is the largest in the systems studied here

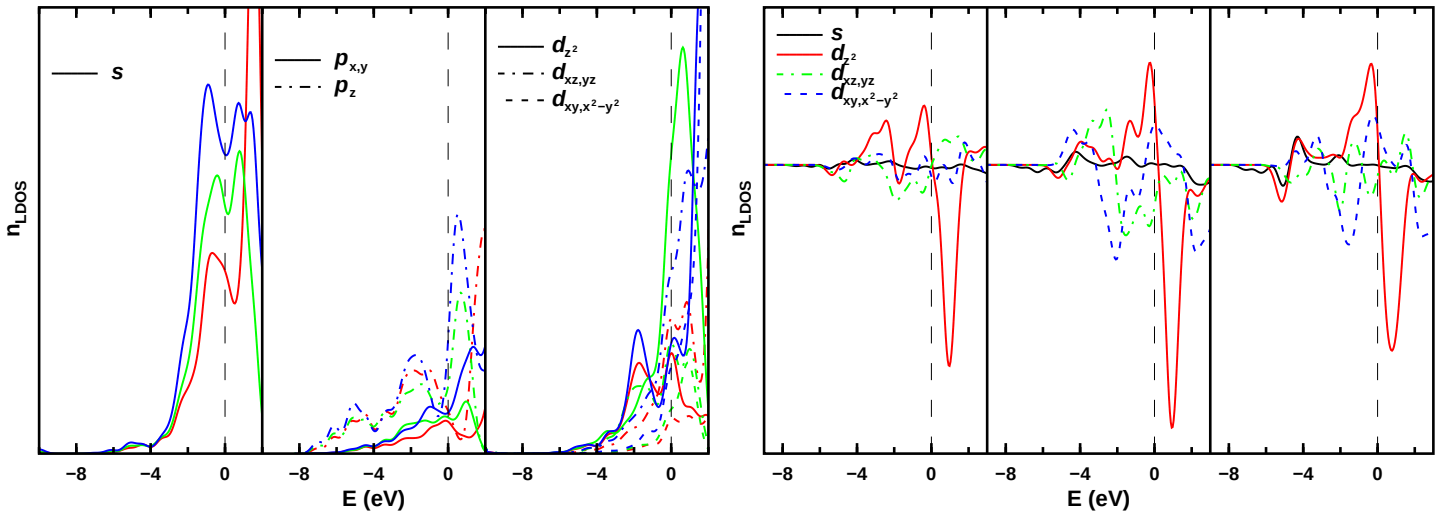

Figure 3.42: The local density of states projected to the cesium atom in the Ru (0001)-($\sqrt{3} \times \sqrt{3}$)R30°-Cs_{hcp} – blue –, Ru (0001)-(2 × 2)-Cs_{ot} – green – and Ru (0001)-(3 × 3)-Cs_{hcp} – red – structures

Figure 3.43: The change upon the adsorption of cesium onto Ru (0001) in the density of states projected on the orbitals of the nearest-neighbour ruthenium atom of the cesium as a function of the coverage; the structures are Ru (0001)-($\sqrt{3} \times \sqrt{3}$)R30°-Cs_{hcp} – left –, Ru (0001)-(2 × 2)-Cs_{on-top} – middle – and Ru (0001)-(3 × 3)-Cs_{hcp} – right. The *p* orbitals have been neglected due to their small magnitude because they were projected on the radial wave function of the semi-core 5*p* state

Table 3.7: The change in the integral of the density of states projected on the ruthenium atoms at the surface layer; nn, nnn and nnnn correspond to the nearest, next-nearest and next-next-nearest ruthenium surface atom from the cesium. The last column shows the distance of the cesium and the ruthenium atoms

System	Atom	*s*	$p_{x,y}$	p_z	d_{z^2}	$d_{xz,yz}$	$d_{x^2-y^2,xy}$	*d* (Å)
Ru-($\sqrt{3} \times \sqrt{3}$)R30°-Cs_{hcp}	Ru(nn):	+0.001	+0.002	+0.005	+0.074	−0.048	+0.001	3.50
Ru-(2 × 2)-Cs_{ot}	Ru(nn):	+0.008	+0.003	+0.005	+0.103	−0.041	−0.047	3.16
	Ru(nnn):	+0.002	+0.000	+0.003	+0.093	−0.049	−0.045	4.19
Ru-(3 × 3)-Cs_{hcp}	Ru(nn):	+0.005	−0.001	+0.004	+0.104	−0.032	−0.028	3.58
	Ru(nnn):	+0.003	−0.001	+0.002	+0.074	−0.023	−0.026	4.53
	Ru(nnnn):	+0.004	−0.000	+0.002	+0.064	−0.018	−0.026	5.31
Ru-(3 × 3)-Cs_{ot}	Ru(nn):	+0.007	+0.000	+0.005	+0.128	−0.040	−0.028	3.22
	Ru(nnn):	+0.003	−0.001	+0.003	+0.086	−0.031	−0.025	4.25
	Ru(nnnn):	+0.003	−0.002	+0.002	+0.063	−0.014	−0.030	5.79

– and the result is given in the Figure 3.44. The similarity at the different distances is obvious although the largest distance, from the cesium to the third-nearest neighbour, is 2.56 Å or 80 % longer than the shortest one from the cesium to the ruthenium below it, and the angle to this atom is 56° from the direction to the nearest-neighbour ruthenium atom beneath the cesium. To test the idea of scaling with the distance we multiplied the change in the projected density of states with the distance from the cesium atom, with the result in the Figure 3.45 for the d_{z^2} orbital and in the Table 3.8 for all the different angular functions integrated over the energy. The scaling is very close to linear in the distance especially in the d_{z^2} orbital and reasonable in the other *d* orbitals.

As the cesium is adsorbed on the surface the coordination of the ruthenium atoms on the surface increases and thus the centre and width of the *d* band are expected to approach the values in the bulk, thus the position of the centre should become deeper in energy and the width increase. This is just what is seen to happen in the Table 3.9, although the changes do not yet recover the bulk values; changes of −0.2 eV and +0.5 eV in the position of the centre and width of the *d* band, respectively, would be necessary to achieve this.

We finally studied the change in the 5*p* eigenvalues of cesium as a function of coverage in order to estimate to what extent they participate to bond formation directly and indirectly via the change of the potential upon adsorption. We show in the Figure 3.46 the binding energies from the 5*p* Kohn-Sham eigenvalues and ultra-violet photoemission spectra by Hrbek (1985). The theoretical Cs_{5s} and Cs_{5p} eigenvalues are given in the Table 3.10, where the values are given at the **k** points used in the self-consistent calculations. The deviation in the points arises from eigenvalues at different **k** points and shows the dispersion of the bands and thus illustrates the amount of interaction, whereas the change in the average position is due to the adsorbate-substrate interaction.

One immediate discrepancy in the experimental and theoretical values arises, beyond a shift in the magnitude: The Kohn-Sham eigenvalues shift downwards in energy with increasing coverage whereas the experimental binding energies decrease, after the initial increase at low coverages. This could be due to several effects, like the final-state relaxation effects which would lower the binding energies, the inadequency of the

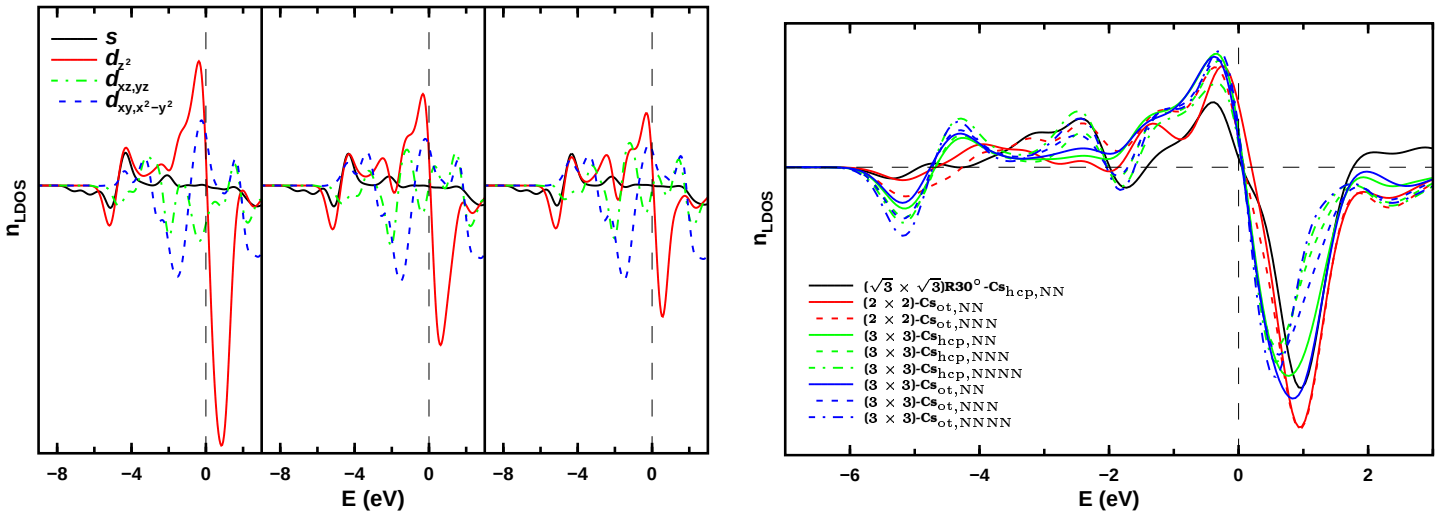

Figure 3.44: The change upon the adsorption of cesium into the Ru(0001)-(3 × 3)-Cs_{on-top} structure in the density of states projected on the orbitals of the nearest-neighbour – left –, next-nearest neighbour – middle – and next-next-nearest neighbour – right – ruthenium atom of the cesium. The projection onto the *p* orbitals has been neglected

Figure 3.45: The change in the density of states projected on the d_{z^2} orbital of the surface ruthenium atoms at the different coverages and adsorption sites upon the adsorption of cesium onto the Ru(0001) surface

Table 3.8: The change in the integral over the density of states on the surface ruthenium atoms upon the adsorption of cesium scaled with the distance from the cesium atom

System	Atom	*s*	$p_{x,y}$	p_z	d_{z^2}	$d_{xz,yz}$	$d_{x^2-y^2,xy}$
Ru-$(\sqrt{3} \times \sqrt{3})$R30°-$Cs_{hcp}$	Ru(nn):	+0.00	+0.01	+0.02	+0.26	−0.17	+0.00
Ru-(2 × 2)-Cs_{ot}	Ru(nn):	+0.03	+0.01	+0.02	+0.33	−0.13	−0.15
	Ru(nnn):	+0.01	+0.00	+0.01	+0.39	−0.21	−0.19
Ru-(3 × 3)-Cs_{hcp}	Ru(nn):	+0.02	−0.00	+0.01	+0.37	−0.11	−0.10
	Ru(nnn):	+0.01	−0.01	+0.01	+0.33	−0.10	−0.12
	Ru(nnnn):	+0.02	−0.00	+0.01	+0.34	−0.10	−0.14
Ru-(3 × 3)-Cs_{ot}	Ru(nn):	+0.02	+0.00	+0.02	+0.41	−0.13	−0.09
	Ru(nnn):	+0.01	−0.00	+0.01	+0.37	−0.13	−0.11
	Ru(nnnn):	+0.02	−0.01	+0.01	+0.36	−0.08	−0.17

Table 3.9: The change in the centre and width of the *d* band upon the adsorption of cesium and when applying an electric field with a magnitude of 0.4 eV/Å on the slab

Structure	Site	Coverage	Atom	E_d (eV)	W_d (eV)
$(\sqrt{3} \times \sqrt{3})$R30°	hcp	1/3	NN	−0.04	0.15
(2 × 2)	on-top	1/4	NN	−0.14	+0.13
			NNN	−0.05	+0.08
(3 × 3)	hcp	1/9	NN	−0.06	+0.07
			NNN	−0.04	+0.08
(3 × 3)	on-top	1/9	NN	−0.08	+0.10
			NNN	−0.05	+0.09
E_{field}				−0.01	+0.01

Table 3.10: The Kohn-Sham eigenvalues – in electron volts – corresponding to the 5*s* and 5*p* orbitals of cesium at different coverages absorbed on the Ru(0001) surface. The ranges corresponds to the dispersion of the eigenvalues at the **k** points at different regions of the Brillouin zone

Structure	Site	Coverage	Cs_{5s}	Cs_{5p}
$(\sqrt{3}\times\sqrt{3})$R30°	hcp	1/3	23.1	9.8–10.1
	on-top		23.2	9.9–10.2
(2×2)	hcp	1/4	23.0	9.9–10.0
	on-top		23.1	9.9–10.0
(3×3)	hcp	1/9	23.0	9.8–9.8
	on-top		23.0	9.8–9.9

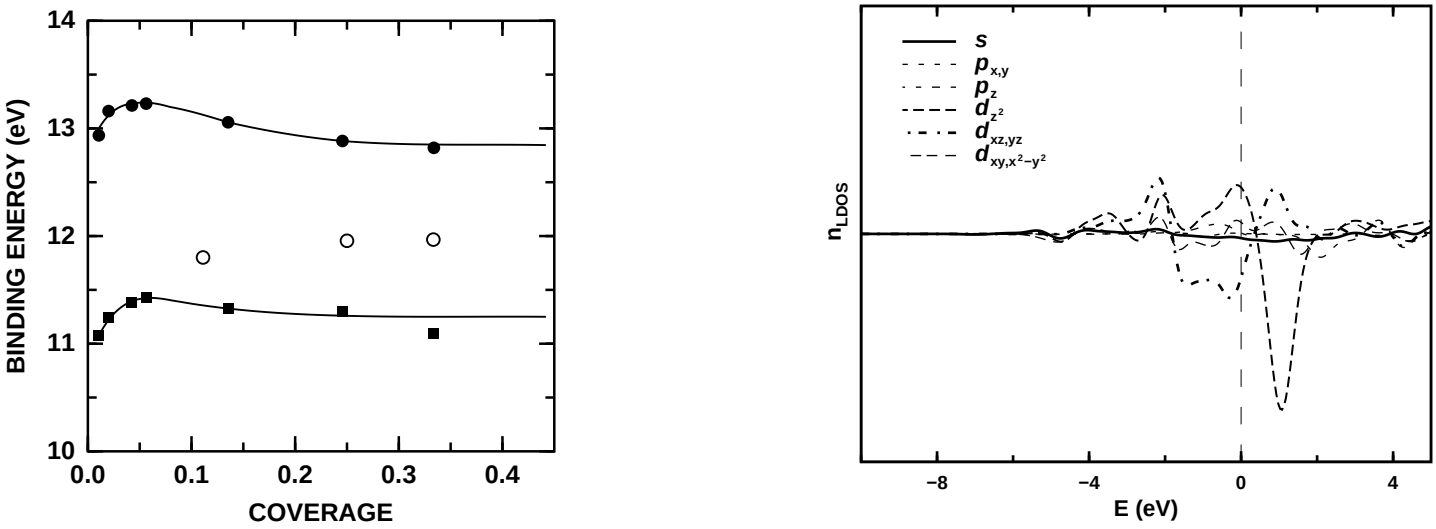

Figure 3.46: The binding energies of the 5*p* orbitals from ultra-violet photoemission spectra and the Kohn-Sham eigenvalues of cesium on Ru(0001) at different coverages; the filled symbols are from experiments by Hrbek (1985), split due to spin-orbit coupling, and the open symbols from the calculations, the latter being shifted two electron volts to larger binding energies to improve comparability

Figure 3.47: The difference in the density of states projected on the ruthenium atoms on the opposite surfaces of the Ru(0001) slab upon the application of a vertical electric field of 0.4 eV/Å

Kohn-Sham eigenvalues to predict real excitation energies or the use of the generalised gradient approximation in our calculations instead of the exact exchange-correlation functional.

Modelling of alkali adsorption via an electric field As we saw above the adsorption of the alkali metal induces an electro-static potential above the surface, with a magnitude in the excess of one electron volt in the (2×2) arrangement of the adsorbates. We thus calculated the response of the clean Ru(0001) surface and a jellium with $r_s = 3$ Bohr to an electric field. The projected density of states in the Figure 3.47, the change in the lateral – the Figure 3.48 and vertical – the Figures 3.49 and 3.50 – density and potential all resemble the changes seen above upon the adsorption of cesium onto the surface. Therefore it is beguiling to assign the effects of the alkali metal to the electric field arising from it, without any chemical binding being necessary. Yet it might be important to achieve the polarisation of the alkali atom which then gives rise to the electric field.

We further compare the change in the electron density and electro-static potential of a jellium slab with r_s=3 Bohr in the Figure 3.51. It is not very useful to compare this to the result for the Ru(0001) in the Figure 3.50 since in the latter the polarisation of the *d* orbitals mostly hides the change in the *s* and *p* electrons; it is more useful to compare the values with the regions above the fcc or hcp adsorption sites in the Figure 3.48. There the maximal change is about 3×10^{-4} e$^-$/Å^3, whereas it is only about 3×10^{-5} e$^-$/Å^3 on the jellium surface although the electric field has the same magnitude in both cases. Therefore we conclude that the electric field is much faster screened off on the jellium surface.

Other cases of alkali adsorption We shortly studied other cases of alkali adsorbed on the close-packed surfaces of transition metals. The main results are shown in the Table 3.11, and for some of the systems we show the density difference in the Figure 3.52. The calculations for Na/Rh(111) were performed with two substrate layers only because we only wanted to obtain a qualitative picture of the adsorption quickly. The density difference for K/Pt(111) looks very similar to the case of Cs/Ru(0001), but sodium on either platinium or rhodium – not shown – appears as qualitatively different; this is mainly due to the semi-core states of cesium and potassium, which are included as active states in these pseudo potentials, whereas in sodium the semi-core states were incorporated to the core and can thus not polarise at the surface. This choice of

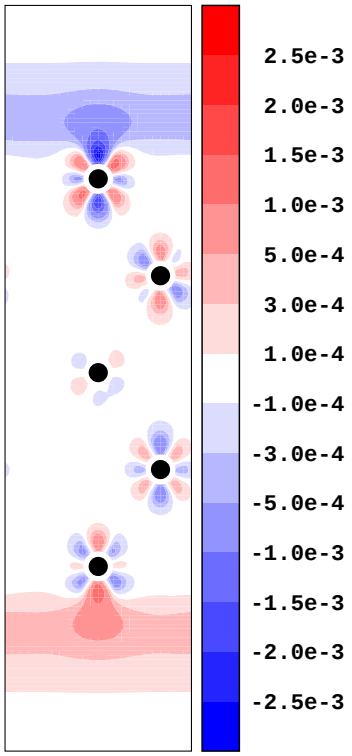

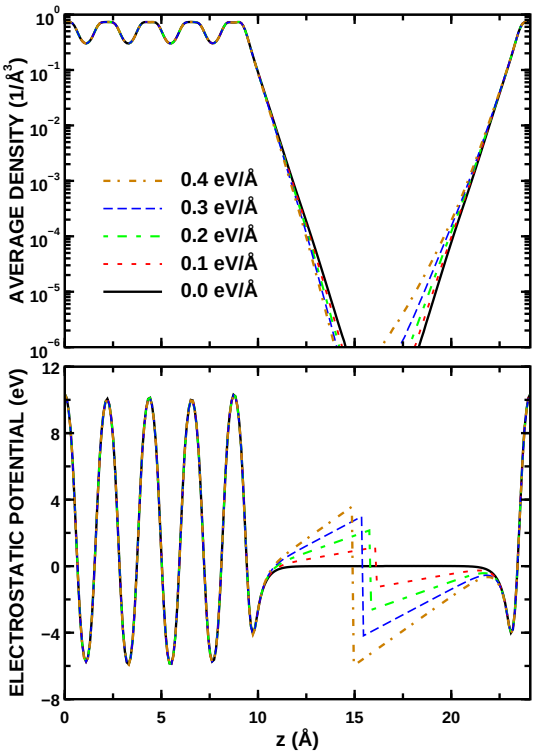

Figure 3.48: The change in the electron density of a Ru(0001) slab upon the application of a vertical electric field of 0.4 eV/Å

Figure 3.49: The vertical density and electro-static potential averaged parallel to the surface in a Ru(0001) slab upon the application of a vertical electric field of 0 eV/Å – solid, black line –, 0.1 – red –, 0.2 – green –, 0.3 – blue – and 0.4 eV/Å – dot-dashed, orange line

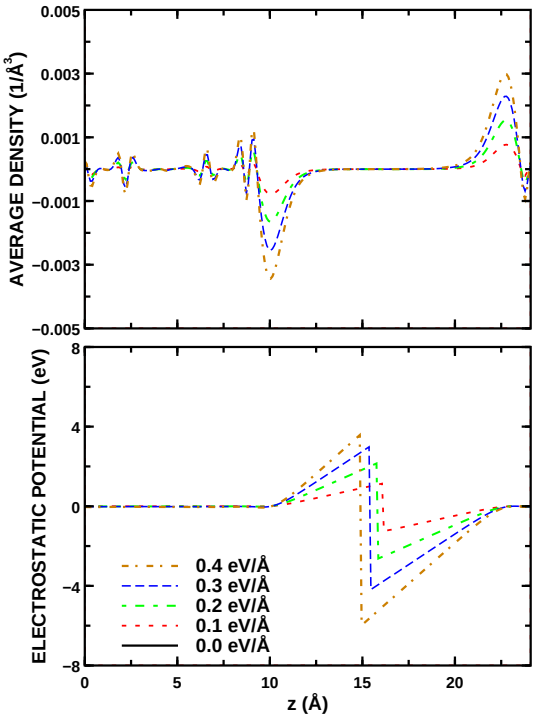

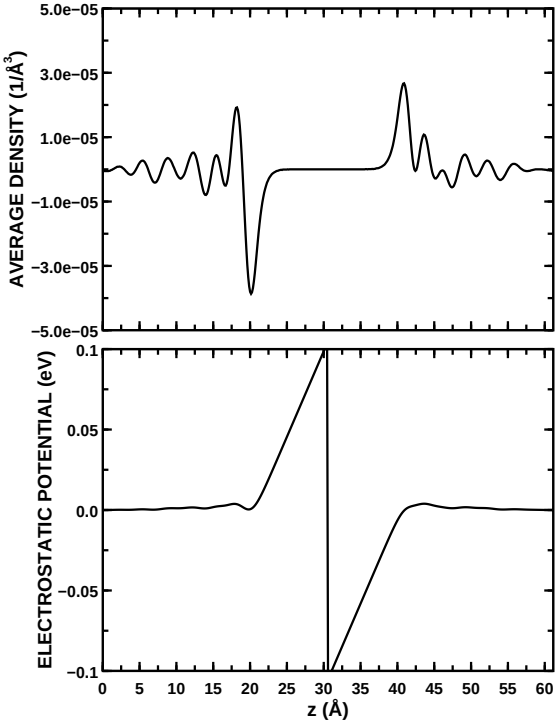

Figure 3.50: The change in the vertical density and electro-static potential averaged parallel to the surface in a Ru(0001) slab upon the application of a vertical electric field of 0.1 – red –, 0.2 – green –, 0.3 – blue – and 0.4 eV/Å – orange line

Figure 3.51: The change in the vertical density and electro-static potential averaged parallel to the surface in a jellium slab with the density corresponding to r_s=3 Bohr upon the application of a vertical electric field of 0.4 eV/Å

Table 3.11: Different adsorption structures of alkalis onto transition metal surfaces studied in the present work. The experimental results have been emphasised and are from Kiskinova, Pirug and Bonzel (1983) – $\Delta\phi$ – except for Na/Pt(111) from Bonzel, Pirug and Ritke (1991) – and Moré (1998) for Na/Pt(111) and K/Pt(111), van Hove (1994) for Na/Rh(111) and Gierer *et al* (1992) for K/Ru(0001). $\Delta\phi$ is the change in the work function from the clean in surface in electron volts, ΔE the energy difference for adsorption at the hcp site minus at the fcc site in milli electron volts, $z_{\mathrm{A-S}}$ the layer height of the adsorbate above its nearest-neighbour substrate atoms, $d_{\mathrm{A-S}}$ the corresponding distance, d_{12}, d_{23} and d_{bulk} are the average distances between first and second, second and third, and two layers in the bulk, correspondingly, b is the buckling in the first substrate layer and a the lateral relaxation in the first substrate layer. Positive values of b in the (2×2) cells denote that the unique atom is higher than the three symmetrically equivalent atoms of the top-most layer of the substrate

Unit cell	Site	$\Delta\phi$	ΔE	$z_{\mathrm{A-S}}$	$d_{\mathrm{A-S}}$	d_{12}	d_{23}	d_{bulk}	b	a
Na/Pt(111)										
$(\sqrt{3} \times \sqrt{3})$R30°	**hcp**	**−4.0**		**2.36**	**2.77**	**2.34**	**2.27**	**2.26**	**0**	
	hcp	−3.99	12	2.30	2.84	2.37	2.32	2.32	—	0.03
	fcc	−3.98		2.31	2.85	2.37	2.32	2.32	—	0.02
(2×2)	**hcp**	**−4.0**		**2.29**		**2.24-2.27**	**2.33**	**2.26**	**+0.09...+0.13**	
	hcp	−3.95	10	2.32	2.85	2.36	2.31	2.32	+0.08	0.02
	fcc	−3.96		2.31	2.85	2.36	2.31	2.32	+0.07	0.02
K/Pt(111)										
$(\sqrt{3} \times \sqrt{3})$R30°	**hcp**	**−4.1**		**2.71**	**3.15**	**2.29**	**2.25**	**2.26**	**0**	
	hcp	−3.62	11	2.69	3.16	2.36	2.31	2.32	—	0.02
	fcc	−3.52		2.70	3.17	2.36	2.31	2.32	—	0.02
(2×2)	**hcp**	**−4.4**		**2.70**	**3.12**	**2.28**	**2.26**	**2.26**	**0.07**	
	hcp	−4.07		2.68	3.15	2.36	2.31	2.32	0.03	0.02
Na/Rh(111)										
$(\sqrt{3} \times \sqrt{3})$R30°	**hcp**			**2.36**		**2.18**	**2.19**	**2.19**	**0**	**0.02**
	hcp	−3.39	20	2.38	2.89	2.19		2.25	—	0.05
	fcc	−3.38		2.40	2.90	2.20		2.25	—	0.04
K/Ru(0001)										
$(\sqrt{3} \times \sqrt{3})$R30°	**hcp**	**−3.8**		**2.94**	**3.33**	**2.10**	**2.14**	**2.14**	**0**	
	hcp	−3.12		2.93	3.36	2.15		2.19	—	0.04
Cs/Ru(0001)										
$(\sqrt{3} \times \sqrt{3})$R30°	**hcp**	**−3.9**		**3.16**	**3.52**	**2.09**	**2.14**	**2.14**	**0**	
	hcp	−3.26	6	3.10	3.51	2.15		2.19	—	0.03
	fcc	−3.24		3.09	3.51	2.15		2.19	—	0.05
(2×2)	**ot**	**−4.1**								
	hcp	−3.50	−0	3.11	3.52	2.15		2.19	+0.01	0.04
	fcc	−3.47		3.11	3.52	2.15		2.32	+0.02	0.05
(3×3)		**−3.7**								
	hcp	−2.90		3.19	3.58	2.14		2.32	+0.00	0.03

semi-core and valence is justified with the energetically deeper position of $2s$ and $2p$ states in sodium than of the corresponding states in potassium or cesium. Thus we believe this to be a real effect, and be due to the different chemical character of the sodium.

3.3.2 Adsorption of carbon monoxide on Ru(0001)

The adsorption of carbon monoxide on surfaces of transition metals has been studied by many experimental methods and semi-empirical and electronic structure methods – please see *e.g.* Over (1998) and references therein. On some of the transition metals – those on the left hand side of the periodic table – CO adsorbs dissociatively whereas on the surfaces of transition metals at the middle of the periodic table CO adsorbs molecularly. The adsorption on ruthenium and rhodium for example is molecular, with the molecular axis parallel to the surface normal (Dowben, 1997). Earlier, before the appearance of even qualitative studies using the low energy electron diffraction, the adsorption site was concluded mainly from the internal vibration C–O, a vibration at 1950 – 2100 cm^{-1} assigned to a one-fold on-top position, 1800 – 1950 cm^{-1} to two-fold bridge site and 1700 – 1800 cm^{-1} to three- or four-fold hollow site; this follows the trend of a weakened internal bond at higher coordination site. This procedure of concluding the adsorption site based solely on the vibrational frequency has been criticised lately by Bradshaw and co-workers; please see *e.g.* the references cited by Davis *et al* (1997). The electronic effect upon adsorption is traditionally discussed in terms of the Blyholder model which is introduced in the Section 2.5.6. We will here also discuss the similarities between the adsorption of N_2 and CO; the molecules are iso-electronic but CO naturally carries a molecular dipole moment whereas N_2 not and the electronic states have higher symmetries in the latter molecule.

On Ru(0001) the adsorption was found to occur with the molecular axis parallel to the surface normal and with the carbon towards the surface in the electron stimulated desorption ion angle distributions – *ESDIAD* – by Madey (1979); the ultraviolet photoemission (Fuggle, Steinkilberg & Menzel, 1975) and electron energy loss spectroscopic (Thomas & Weinberg, 1978) results had already suggested this. The vibrational frequency for the internal C-O stretch mode was found from the high-resolution electron energy loss (Thomas & Weinberg, 1979; He, Dietrich & Jacobi, 1996) and infra-red adsorption spectra – *IRAS* – (Pfnür *et al*, 1980; Jakob, 1996) to be about 2000 cm^{-1}, thus close to the border-line between the on-top and bridge adsorption. However

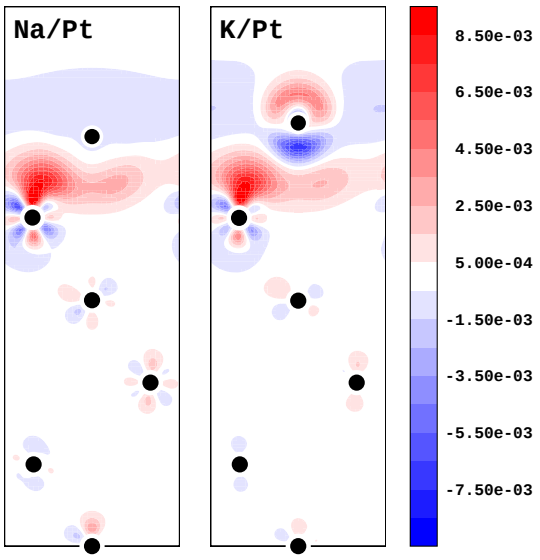

Figure 3.52: The change in the electron density upon the adsorption of the alkali atom sodium – left – and potassium – right – onto the Pt(111) surface in the $(\sqrt{3} \times \sqrt{3})$R30°-$A_{hcp}$ structure, A = Na, K

the on-top site was concluded first based on the vibrational frequency and the first structural determination with the low energy electron diffraction by Michalk *et al* (1983). In the low energy electron diffraction a clearly ordered pattern was observed at the coverage 1/3, showing the $(\sqrt{3} \times \sqrt{3})$R30° order. The maximum coverage found using various methods is 0.68, thus close to 2/3. Already at low coverages the $(\sqrt{3} \times \sqrt{3})$R30° pattern is detected, pointing to island formation with patches of the $(\sqrt{3} \times \sqrt{3})$R30° structure; this indicates an attractive second-nearest neighbour interaction, and since higher-concentration islands are not observed at any coverage, the nearest-neighbour interaction is either negligible or repulsive. The geometry of the high-coverage structure has not been qualitatively obtained but $(2\sqrt{3} \times 2\sqrt{3})$R30° and $(5\sqrt{3} \times 5\sqrt{3})$R30° structures are observed along coverages exceeding 1/3 by Thomas and Weinberg (1979), Williams and Weinberg (1979) and Braun *et al* (1997). The established interpretation is that compressed structures are formed when the coverage exceeds the 1/3; a suggestion by Thomas and Weinberg (1979) for the structure $(2\sqrt{3} \times 2\sqrt{3})$R30° is shown in the Figure 3.53. The compressed structures demands some of the CO molecules to adsorb also on sites other than the on-top site; this is possible if the adsorbate-adsorbate interaction dominates over the adsorbate-substrate interaction. Frequencies different from the ones found at the on-top site are expected but the change in the ν(C-O) is small between coverages 1/3 and the maximum coverage – please see below. The $(2\sqrt{3} \times 2\sqrt{3})$R30° structure is not observed in the low energy energy diffraction at room temperature (Pfnür *et al*, 1980); thus the corrugation of the adsorbate-substrate potential energy surface is very weak.

The Figure 3.54 shows the different eigenmodes of a two-dimensional molecule adsorbed along the surface normal. From these the frustrated translational and hindered rotational modes are parallel to the surface and thus do not create a dynamic dipole moment perpendicular to the surface; thereby the scattering amplitude of electrons *e.g.* in the high resolution energy energy loss spectroscopy is very small and the intensity negligible in the measurements. These modes can however be accessed *e.g.* with helium atom scattering (Braun *et al*, 1997) or methods accessing the diffraction of electrons (Over *et al*, 1993; 1995d; Gierer *et al*, 1996). The main observable in the vibrational measurements is usually only the internal ν(C-O) mode, and its variation at different coverages. If CO is adsorbed at low temperature 80 K the resulting over-layer is not fully ordered as concluded from the different frequencies than when dosing CO at higher a temperature; upon annealing the system dosed at a low temperature becomes equivalent to the structure adsorbed at higher temperature. Beyond the shift in the infra-red adsorption spectra shown in the Figure 3.55 Pfnür *et al* observed also a splitting of frequencies into two peaks; this appears also at coverages below 1/3 and is thus most likely due to molecules at island boundaries and their internals, or due to isolated molecules and molecules attached to islands.

Studies employing the scanning tunnelling microscope, at low temperatures due to the weak interaction and diffusion barrier, of the adsorption at low and high coverages might reveal the existence of island formation and the pattern of compressed structures, respectively, and are thus called for.

Geometry and energetics

We have performed density functional calculations for the CO adsorbed on Ru(0001) at different coverages from the (2×2) up to the mono-layer structure. The geometry of the principal structure $(\sqrt{3} \times \sqrt{3})$R30°-CO along with the model from the low energy electron diffraction measurements is shown in the Figure 3.56 and listed in the Table 3.12. The overall agreement is good, although the size of the vertical rumpling in the first layer is larger in the density functional calculations. The binding energy of CO in this structure is 1.83 eV; a desorption energy of 1.81 eV was obtained in the experiments of Pfnür, Feulner and Menzel (1983), showing an excellent

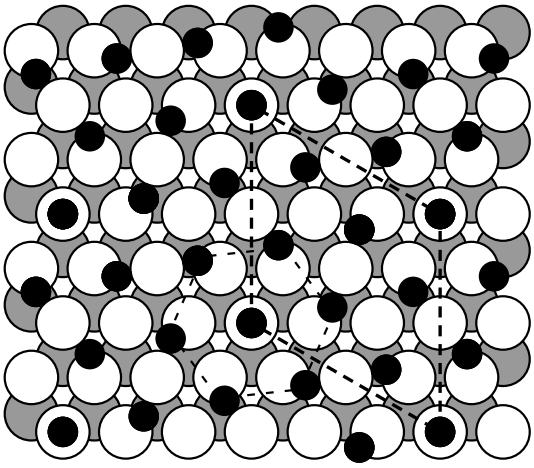

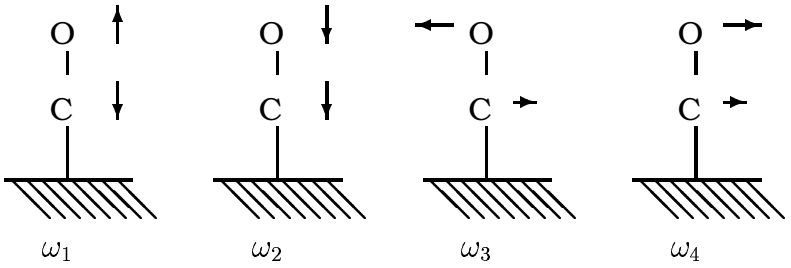

Figure 3.53: A suggested model for the $(2\sqrt{3} \times 2\sqrt{3})$R30° by Thomas and Weinberg (1979); the coverage is 7/12. Please notice the quasi-hexagonal, incommensurate arrangement of the molecules shown around one molecule

Figure 3.54: The vibrational modes of a dimer adsorbed in the up-right geometry on a surface

Table 3.12: The geometry and electronic properties of CO adsorbed on the Ru(0001) in the $(\sqrt{3} \times \sqrt{3})$R30° structure as yield by our density-functional calculations and experiments by Michalk *et al* (1983) and Over, Moritz & Ertl (1993) – geometry –, and Pfnür, Feulner and Menzel (1983) – binding energy and change in the work function. The distance $z_{Ru_1-Ru_2}$ was calculated from the averaged layer positions

	DFT	Experiments
d_{C-O} (Å)	1.158	1.10±0.05
d_{Ru-C} (Å)	1.928	1.93±0.04
b (Å)	0.167	0.07±0.03
$z_{Ru_1-Ru_2}$ (Å)	2.102	2.08±0.04
$z_{Ru,bulk}$ (Å)	2.190	2.138
E_{bind} (eV)	1.83	1.81
$\Delta\phi$ (eV)	+0.79	+0.44

agreement between the calculations and the experimental work; the energy difference between the on-top and the three-fold hollow hcp site was only about 60 meV, lower than what would be expected from the experiments where occupation of no other sites than the on-top sites has been observed even at high temperatures. Yet the low barrier for diffusion, 0.4 eV on the terrace at $\theta_{CO} = 0.27$, fits to the result of a low corrugation of the potential energy surface for the adsorption of the CO. The change in the work function is largely over-estimated in our results, being almost two times too large. In the following we shall mostly analyse the adsorption of the CO in the (2×2) super-cell as we needed these results for the studies of the co-adsorption more than in the $(\sqrt{3} \times \sqrt{3})$R30° cell.

An interesting quantity is how the geometry and electronic properties are modified with a changing coverage; the Figure 3.57 collects these for CO/Ru(0001), and the Figure 3.55 contains the calculated frequency of the internal C-O stretching mode for CO/Ru(0001) and a hexagonal, free-standing mono-layer of CO. With the increasing coverage the C-O bond length decreases and the Ru-C distance increases, but the changes are very small; the change in the C-O bond length is much larger on the ruthenium surface than in the pure CO mono-layer. The change in the work function is qualitatively similar to the one in the experiments by Pfnür and Menzel (1983) but this time over-estimated by about 0.15 eV; the under-linear increase above the coverage 1/3 is reproduced in our calculations.

CO-CO interaction

In order to investigate the adsorbate-adsorbate interaction we performed the density functional calculations at different coverages; we did not go beyond the coverage 1/4 due to computational limitations. However, beyond the third- nearest neighbour interaction the CO-CO interaction is most likely small. We studied the structures (1×1)-1CO, (2×2)-3CO, $(\sqrt{3} \times \sqrt{3})$R30°-2CO, (2×1)-1CO, $(\sqrt{3} \times \sqrt{3})$R30°-1CO and (2×2)-1CO corresponding to the coverages 1, 3/4, 2/3, 1/2, 1/3 and 1/4. The interaction energies of the type of interactions shown in the Figure 3.58 were extracted like explained in the section in the Section 2.5.2; the molecule in the (2×2) structure was regarded as being isolated. The parameters thus obtained are given in the Table 3.13 with the same quantities fitted to desorption experiments by Payne, Zhang and Kreuzer (1992); it is seen that these two sets are rather similar to some extent but major differences occur. This does not surprise us considering that the numbers by Payne, Zhang and Kreuzer are derived semi-empirically and the neglect of the interactions beyond the third-nearest neighbour distance in the density functional study.

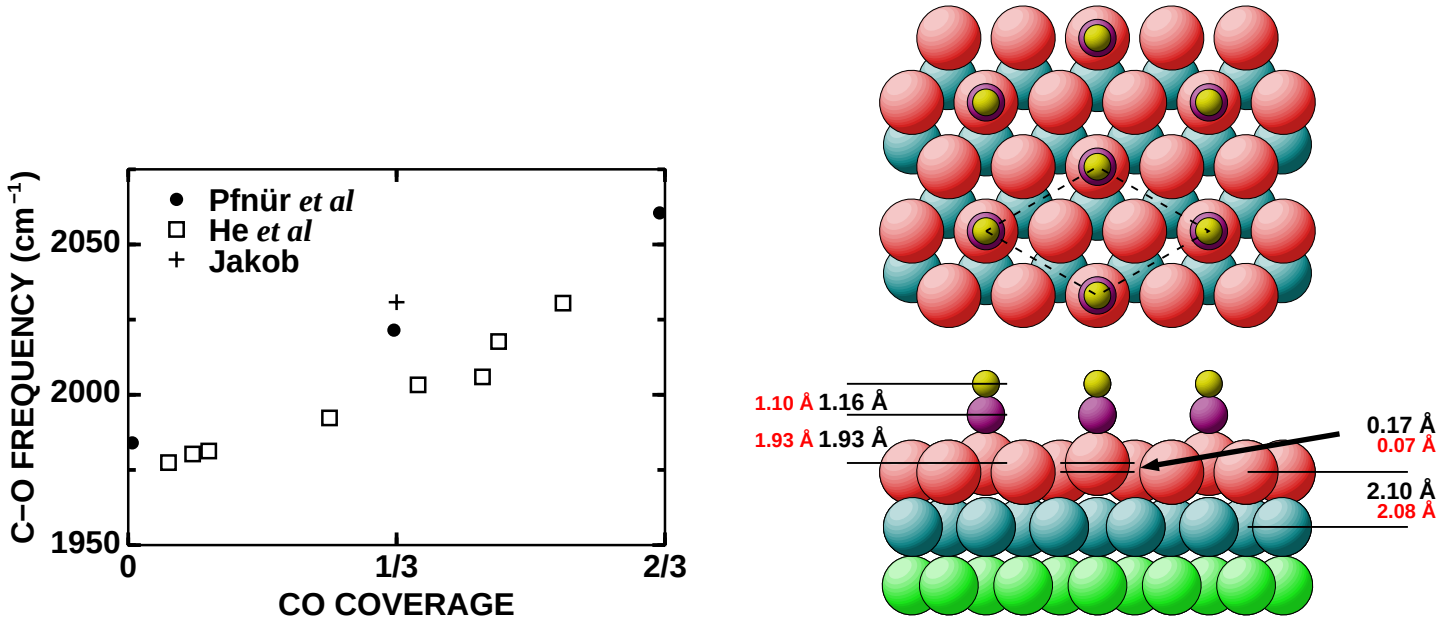

Figure 3.55: The vibrational frequency of CO from the infra-red adsorption spectroscopy by Pfnür *et al* (1980) and Jakob (1997) and the high-energy electron energy loss spectra of He, Dietrich and Jacobi (1996)

Figure 3.56: The geometry of CO in the $(\sqrt{3} \times \sqrt{3})$R30° structure from the density-functional calculations. The experimental values of Michalk *et al* (1983) and Over, Moritz and Ertl (1993) are indicated with the smaller font

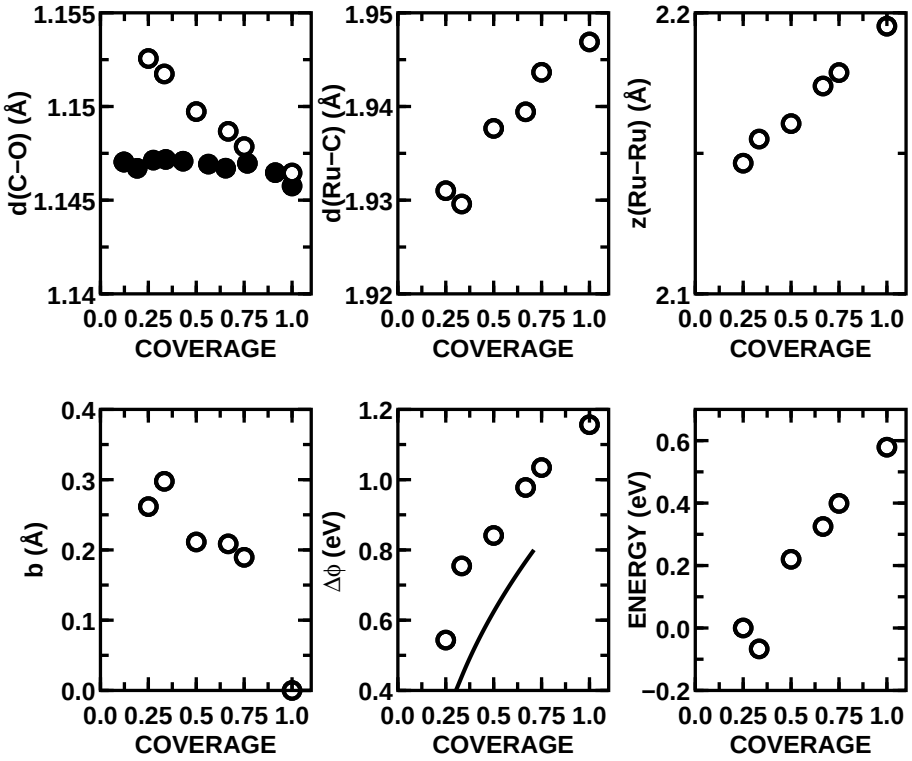

Figure 3.57: The geometry, binding energy and change of work function induced by the adsorption of the CO from the density-functional calculations; the binding energies are taken with respect to a molecule in the (2×2) structure, and b is the buckling in the first layer of the substrate. In the panel of the C-O distance the bond length of the CO in a hexagonal, free-standing mono-layer is included with filled circles, and in the panel of the change of the work function the experimental data from Pfnür and Menzel (1983) with a solid line

Table 3.13: The two- and three-particle interaction parameters extracted from our density functional calculations; the fit to the experimental data is from Payne, Zhang and Kreuzer (1992). All values are in electron volts

	E_0	V_2	V_2'	V_t	V_t'
DFT	−1.76	0.157	−0.022	−0.098	+0.085
Fit	−1.59	0.124	+0.087	0.087	

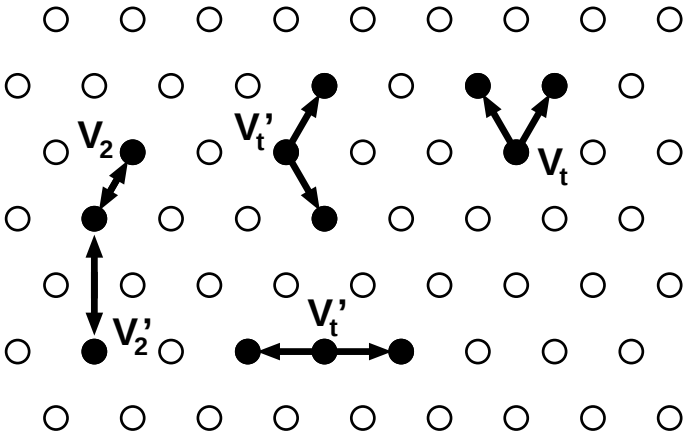

Figure 3.58: The definition of the parameters for the extraction of two- and three-particle interactions; all the CO molecules are placed at the on-top sites. V_t' and V_t" of the Figure 2.14 are set to equal as we do not have enough structures to differentiate them

Table 3.14: The dispersion of the 3σ and 4σ levels of CO at different coverages adsorbed on the Ru(0001) surface and a free-standing, hexagonal mono-layer of CO, marked with the sub-script ML; the dispersions are calculated from the Kohn-Sham eigenvalues at the **k** points of the self-consistent calculations and provide an equivalent sampling of the surface Brillouin zone

Coverage	3σ	4σ	$3\sigma_{\mathrm{ML}}$	$4\sigma_{\mathrm{ML}}$
1/4	0.00	0.01	0.00	0.00
1/3	0.00	0.04	0.00	0.01
1/2	0.30	0.79	0.04	0.11
2/3	0.42	1.11	0.09	0.21
3/4	0.44	1.19	0.19	0.29
1/1	0.64	1.71	0.59	1.00

We shortly estimated the qualitative range of the CO-CO interaction from the dispersion of the 3σ and 4σ orbitals of CO, given in the Table 3.14: The major change occurs at the coverage 1/2 when the first nearest-neighbour sites become filled the dispersion increases rapidly, and a large jump occurs only upon at the distance of a (1×1) structure in the eigenvalues of a free-standing, hexagonal mono-layer of CO with the same density of molecules. This shows that the nearest-neighbour distance of 2.70 Å is a border-line for a strong inter-molecular interaction of the 3σ and 4σ orbitals.

Electronic structure

Next we shall analyse the electronic structure and binding of CO onto the ruthenium surface. We begin by showing the change in the total density of states in the Figure 3.60; the reference structure of CO is also calculated in the same super cell and thus contains a small but negligible contribution from CO-CO interaction. The density of states projected on the atomic orbitals of the carbon in the Figure 3.59 provide a better insight to the character of the states contributing to the density of states at different energies. The position of the levels 3σ, 4σ, 1π and 5σ of CO are clearly identifiable: The σ orbitals only have *s* and p_z components whereas the π orbitals consist only of $p_{x,y}$ character. It is remarkable that the σ orbital at -6.2 eV lies below the π orbital; thus a theory based strictly on the frontier orbitals, in a molecular case the highest occupied molecular orbital – *HOMO* – and the lowest un-occupied molecular orbital – *LUMO* –, would face difficulties because the energetic ordering of the highest occupied orbitals has changed upon the adsorption.

The change in electronic density when the CO adsorbs on the Ru(0001) surface is illustrated in the Figure 3.62. The adsorption to the on-top and hcp sites leads into a similar change, and qualitatively the change agrees well with the Blyholder model: An increase is observed at the sides of the CO and a decrease along the axis of the molecule, just where the $2\pi^*$ and 5σ states are located, respectively. In the Figure 3.61 we also show some of the Kohn-Sham states which have a considerable magnitude at the CO molecule. The emerging picture resembles closely to that found by Hu *et al* (1995) for CO adsorption on Pd(110): the orbitals of the CO hybridise with the substrate states suggesting a chemical bond mechanism rather than a clear charge transfer from or to the highest occupied and unoccupied states as assumed in the Blyholder model. To clarify the hybridisation mechanism over the one suggested by the Blyholder model we show the projected densities of states in the Figures 3.64 and 3.65; in the former projected onto the σ and in the latter π Kohn-Sham orbitals of a CO molecule in the corresponding super-cell as the calculations of the adsorbed structure. The peaks are now clearly resolved according into the σ and π orbitals, and whereas the 1π and $2\pi^*$ mix only marginally, especially on the on-top site, the peak assigned to the 4σ contains some character of 5σ and vice versa. At the hcp site the difference is larger, 33 %, as also indicated in the Table 3.15 where the numbers were obtained by integrating the projected densities of states up to the Fermi energy. This effect is not in agreement with the Blyholder model, which states that the 4σ remains inert upon adsorption, but in qualitative agreement with the

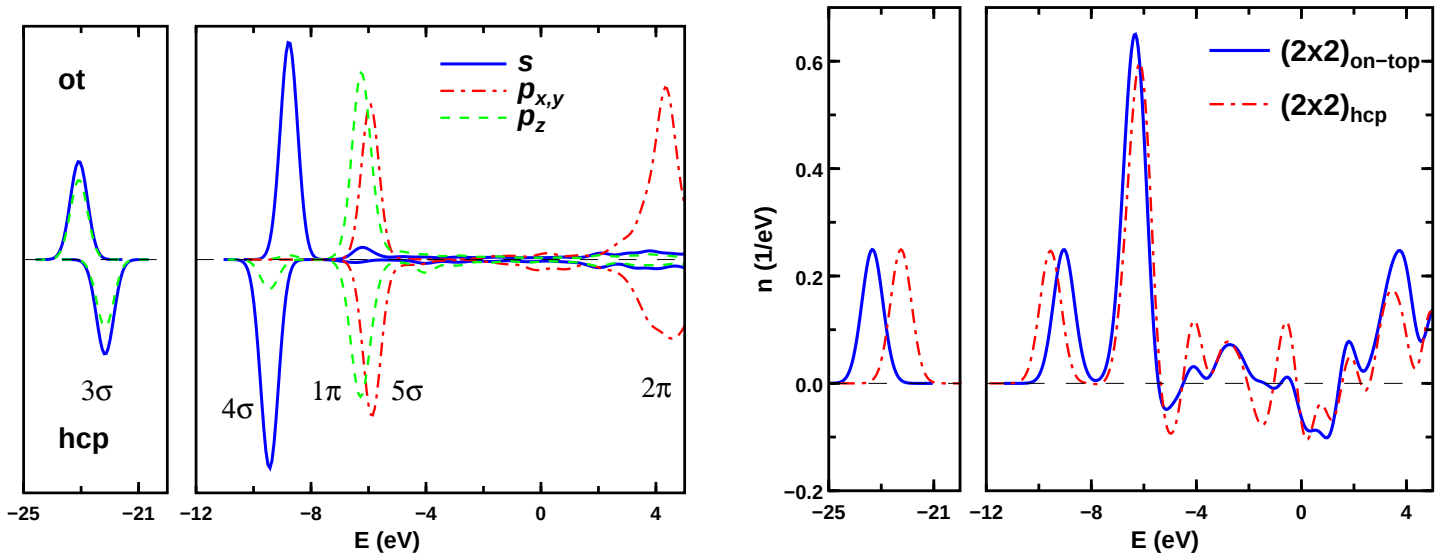

Figure 3.59: The density of states in the (2×2)-CO structure projected onto the *s* and *p* orbitals of the carbon atom; the corresponding plot for oxygen is very similar

Figure 3.60: The change in density of states upon CO adsorption into the (2×2) structure on the on-top and hcp site

Table 3.15: The occupation factors of different levels deduced from the projection of the Kohn-Sham states of the adsorption system on the molecular orbitals, and the mixing of 4σ and 5σ defined as the amount of molecular 5σ character of the 4σ in the adsorption system and vise versa. The results of Mortensen *et al* (1997) are included for Ru(0001)-$(\sqrt{3} \times \sqrt{3})$R30°-$CO_{ot}$ and Ru(0001)-$(\sqrt{3} \times \sqrt{3})$R30°-$N_{2,ot}$

Structure	Orbital						$4\sigma/5\sigma$ mixing (%)
	3σ	4σ	5σ	6σ	1π	$2\pi^*$	
Ru(0001)-$(\sqrt{3} \times \sqrt{3})$R30°-$N_{2,ot}$	1.000	0.992	0.974	0.226	0.998	0.159	16
Mortensen *et al*		0.990	0.970		0.997	0.175	
Ru(0001)-(2×2)-CO_{ot}	1.000	0.998	0.922	0.134	0.998	0.291	17
Mortensen *et al*		0.997	0.916		0.996	0.298	
Ru(0001)-(2×2)-CO_{hcp}	1.000	1.000	0.926	0.155	0.990	0.397	33

measurements of Nilsson *et al* (1997) who found a similar mixing of the 4σ and 5σ in the experiments. In the Section 3.4.2 we shall further discuss the consequence of the adsorption on the different sites to the amount of the mixing.

Adsorption of N_2 versus CO

The adsorption of N_2 is often placed on a level with the adsorption of the iso-electronic CO, but sometimes a different mechanism is proposed; for a discussion of the issue please see de Paola *et al* (1987). Whereas the adsorption sites of the molecules are identical and the quantitative geometry very similar (Bludau *et al*, 1994) in the $(\sqrt{3} \times \sqrt{3})$R30° structure, notable differences are *e.g.* the following:

- The work function increases upon the adsorption of CO but decreases when N_2 is adsorbed
- The internal stretching frequency C-O increases as a function of the coverage while the N_2 stretching frequency remains constant
- The pre-adsorption of potassium prevents the co-adsorption of N_2, already at coverages of $\theta_K = 0.08$, whereas the adsorption of CO occurs up to high alkali coverages, and the alkali-CO interaction is attractive

The established explanation for these effects is along the lines of the Blyholder model, so that the 5σ orbital acts as a electron donator like in the carbon monoxide but the $2\pi^*$ orbital becomes much less occupied in N_2 than in CO. This model explain *e.g.* the lowering of the work function because the nitrogen dimer would lose part of its electrons and thus creates a dipole lowering the work function, and the repulsion with a co-adsorbed alkali atom is due to an electro-static repulsion. Mortensen *et al* (1997) addressed the difference between the adsorption of N_2 and CO on Ru(0001) based on calculations employing the density functional theory. In their results they indeed found a smaller occupation of the $2\pi^*$ in the case of N_2.

We also studied the N_2 onto the Ru(0001) surface, but only in the $(\sqrt{3} \times \sqrt{3})$R30°-$N_{2,ot}$ structure. The resulting geometry in the Figure 3.66 agrees well with the results of Mortensen *et al* (1997), but the buckling of the first substrate layer in both calculations is not found in the measurements by Bludau *et al* (1994). In

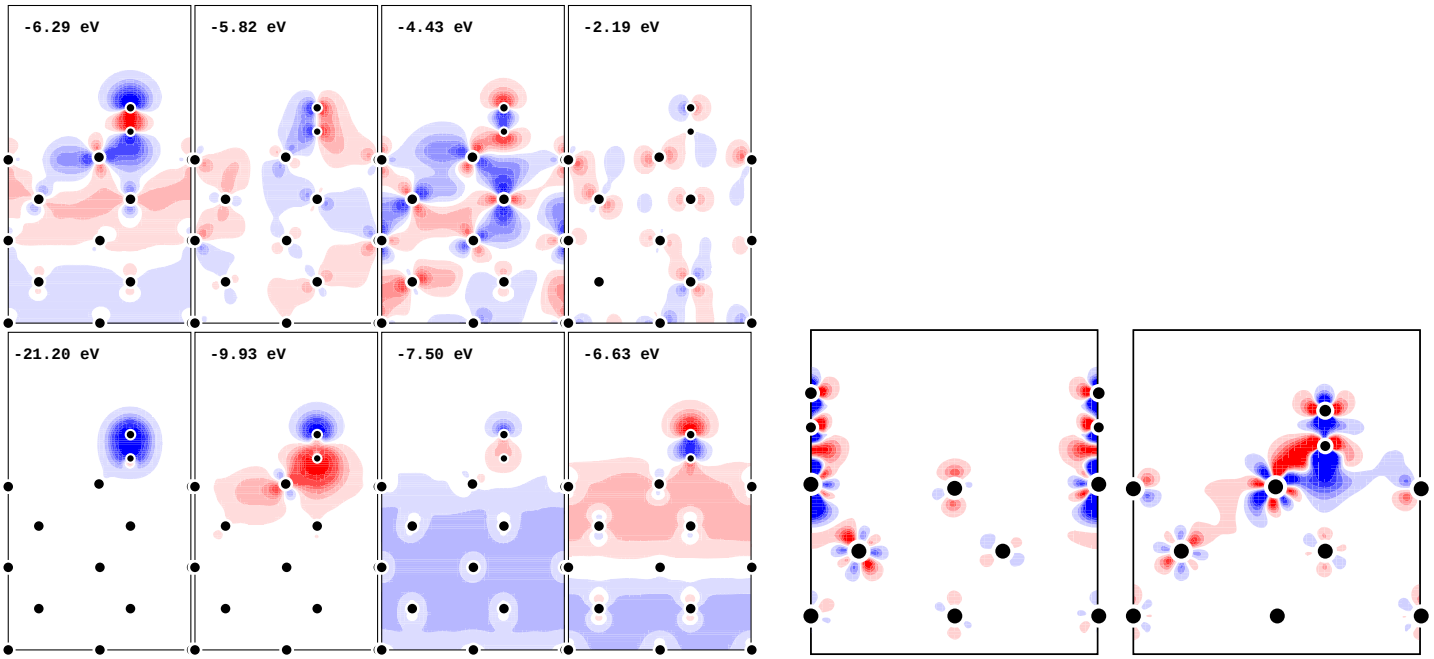

Figure 3.61: Some Kohn-Sham states at the Γ point of the Brillouin zone which have a considerable magnitude at the CO molecule in the (2×2)-CO_{hcp} structure

Figure 3.62: The change in the electron density upon CO adsorption into the (2×2) structure at the on-top – left – and hcp site – right

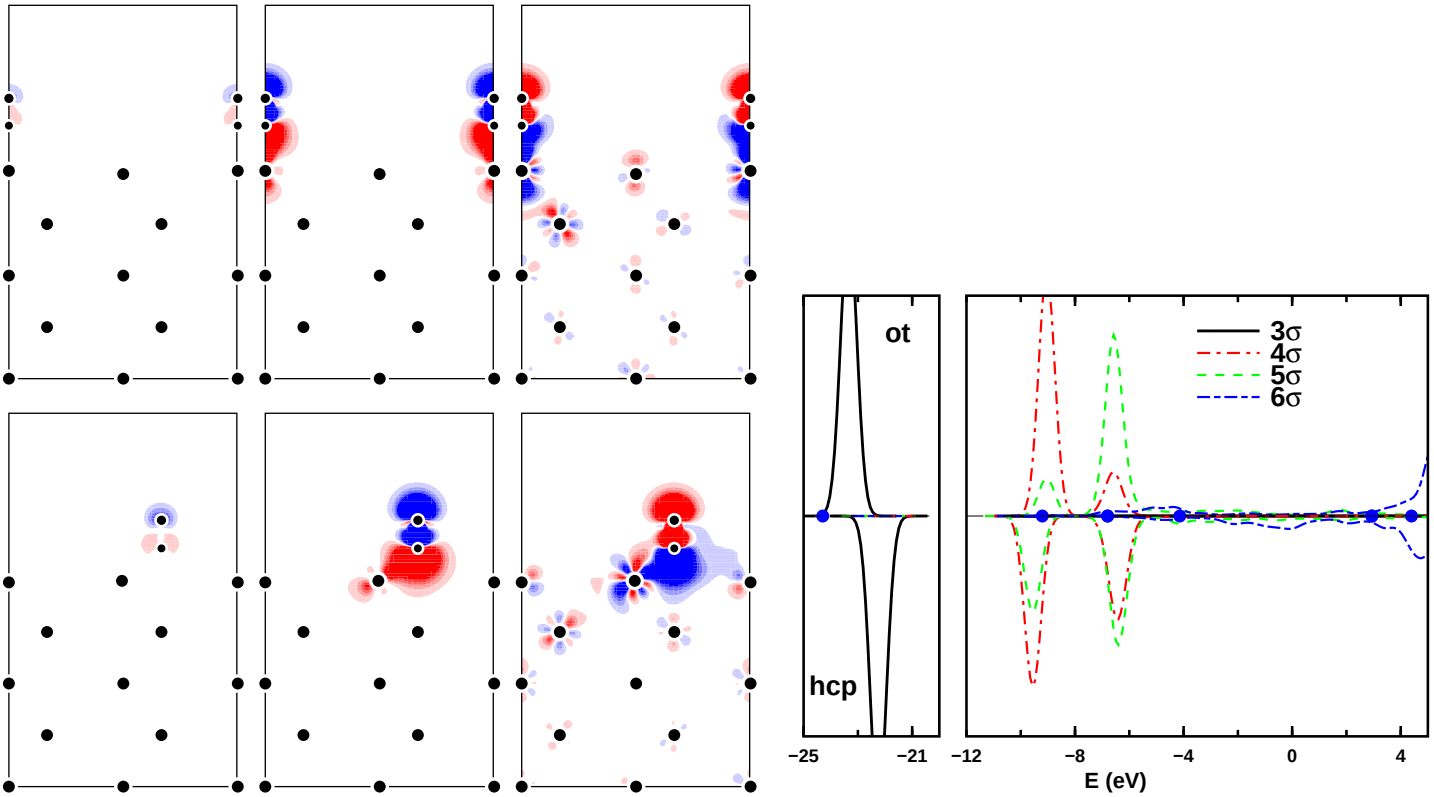

Figure 3.63: The change in electron density of the 3σ – left – and 4σ – middle – states and the rest of the valence electron density – right – upon CO adsorption into the (2×2)-CO structure at the on-top – top panels – and hcp sites – bottom panels

Figure 3.64: The density of states in the (2×2)-CO structure projected onto the molecular σ orbitals of the carbon monoxide. The dots indicate the Kohn-Sham eigenvalues of an isolated molecule; however the absolute location of them on the energy scale is arbitrary

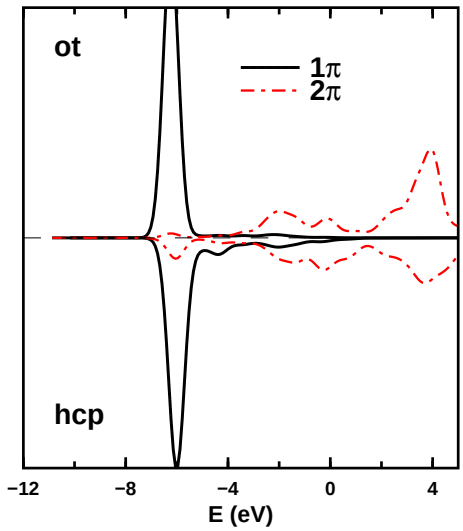

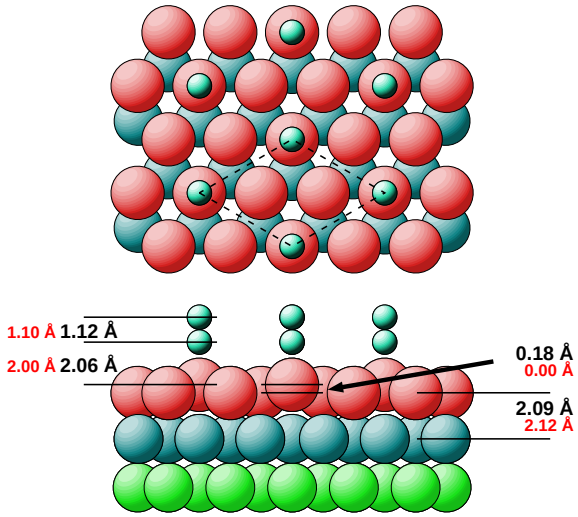

Figure 3.65: The density of states in the (2×2)-CO structure projected onto the molecular π orbitals of the carbon monoxide

Figure 3.66: The geometry of N_2 in the $(\sqrt{3} \times \sqrt{3})$R30° structure from the density-functional calculations. The experimental values of Bludau *et al* (1994) are indicated with the smaller font

the calculations the buckling is about as large as in the case of the CO, and there the experiments gave a buckling – yet only half of the computed one – so a slight buckling due to the experimental analysis for the geometry of the N_2 on Ru(0001) cannot be excluded. The work function increases by +0.21 eV from the clean surface, thus in disagreements with the experiments (de Paola *et al*, 1987) which yielded a decrease of the work function by −0.52 eV. We obtained a value of 0.55 eV for the binding energy of the molecule to the surface in the $(\sqrt{3} \times \sqrt{3})$R30°-$N_{2,ot}$ structure, close to the value obtained by Mortensen *et al* (1997), being much lower than the binding energy 1.83 eV of the CO agreeing well with the experimental trend. Mortensen *et al* explain this difference with the smaller overlap of the $2\pi^*$ state with the substrate states and thus a smaller energy gain from hybridisation; please compare the Figures 2.16 and 3.67, and note especially how both the 5σ and $2\pi^*$ have a larger weight on the carbon end in the CO than at the nitrogen ends of the N_2. The origin for the larger work function for the CO is apparent in the Figure 3.68, which shows the change upon the adsorption in the density averaged parallel to the surface: The density increases just above the outer-most substrate atom in the case of the nitrogen dimer, whereas the increase in the charge is close to the carbon atom for the carbon monoxide; this shift to further above from the surface increases the surface dipole and consequently the work function. It is interesting that the difference in the adsorption energy of the N_2 between different adsorption sites is much larger than of the CO; the three-fold hollow sites are by 0.66 eV less favourable than the on-top site and thus only meta-stable against desorption. The largest difference in the electronic bonding mechanism between CO and N_2 is the deeper energy of the 4σ- and 1π-derived peaks, and the smaller occupation of the $2\pi^*$ orbital for the adsorbed N_2. The latter was also confirmed by the integral over the projected density of states in the Table 3.15.

We shortly studied the properties of the nitrogen dimer when the charge state and the relative population of the 5σ and $2\pi^*$ states was changed. Although the $2\pi^*$ state is anti-bonding a small filling increases the binding energy as seen from the Figure 3.69. The vibrational frequency decreases and the bond length increases monotonously when electrons are fractionally added to the molecule. The transfer of electrons from the 5σ to the $2\pi^*$ or the application of an electric field along the molecular axis affects the molecular properties similarly. These results also make implications to the effect of an added alkali metal to the adsorption and dissociation properties of the N_2 molecule; this was recently studied by Mortensen *et al* (1997; 1998; Mortensen, 1998).

The densities of states projected on the molecular σ and π states for the CO and N_2 adsorbed on the Ru(0001) are shown in the Figures 3.70 and 3.71, respectively. The σ orbitals of the two molecules are very similarly structured except for the lower location of the 4σ orbital of the N_2. The main peaks of the 1π and $2\pi^*$ orbitals in the nitrogen dimer are lower in energy but the $2\pi^*$ less occupied as was shown in the Table 3.15.

An interesting comparison to the experiments can be done between the Figure 3.72 and the results and conclusions by Nilsson *et al* (1997). The former shows the density of states projected onto the atomic orbitals of the nitrogen atoms in the structure Ru(0001)-$(\sqrt{3} \times \sqrt{3})$R30°-$N_{2,ot}$, and in the latter the spatial distribution of the molecular orbitals were derived from the X-ray emission spectra. The arising picture from the calculations and these experiments along with the Blyholder model is shown in the Figure 3.73: The agreement between the calculational and experimental model is reasonable, considering that the experiments are for the Ni(100) surface and our calculations for the Ru(0001). However the agreement between the calculations and the experiments is superb, after the slight inaccuracy in the notation of the 4σ orbitals by Nilsson *et al* has been taken into account.

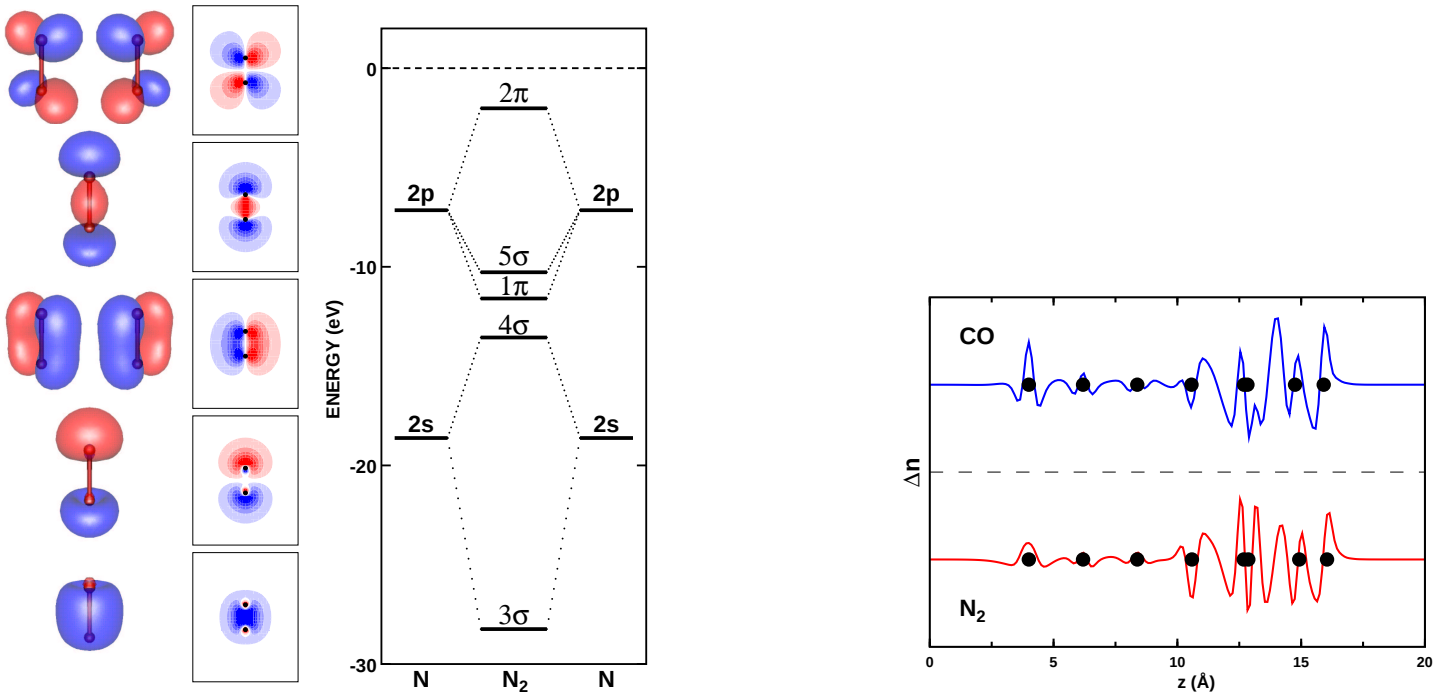

Figure 3.67: The significant Kohn-Sham single particle states of the nitrogen dimer; right are the energy levels of the orbitals from our density functional calculation. Please refer to the corresponding states of the carbon monoxide in the Figure 2.16

Figure 3.68: The change in electron density averaged parallel to the surface upon the adsorption of CO and N_2 to the Ru (0001) surface; the filled circles denote the atomic positions, and the dimers are the two right-most circles

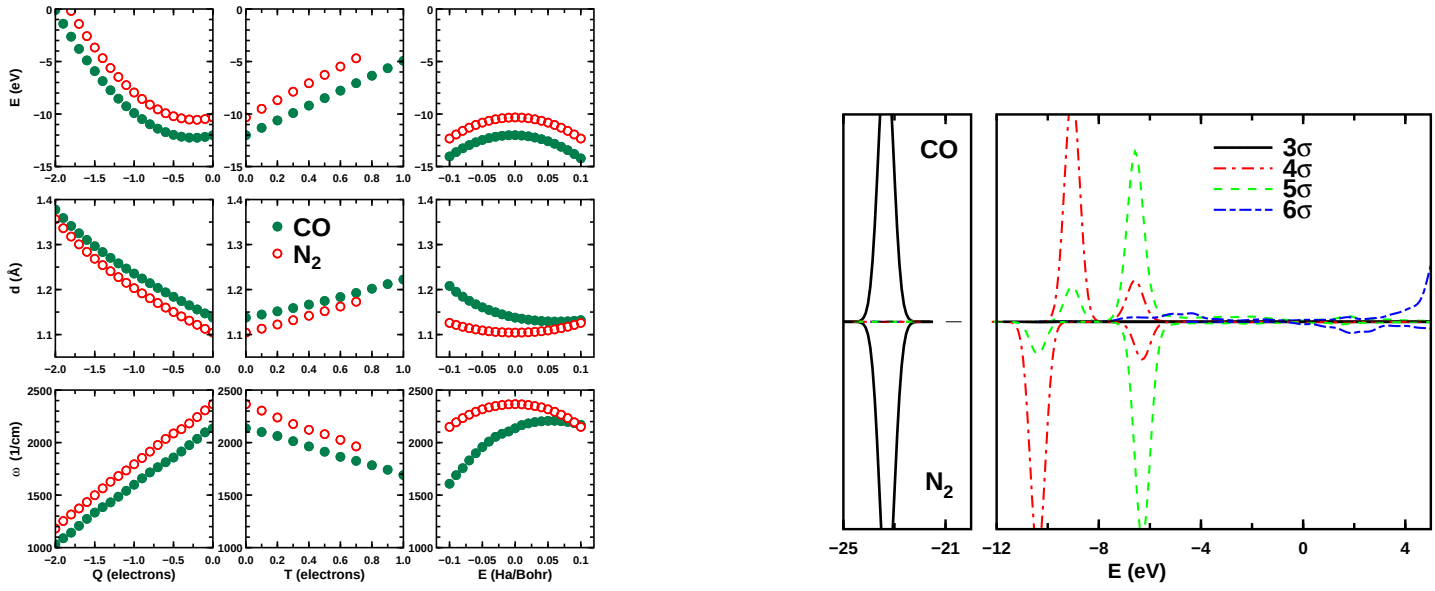

Figure 3.69: The binding energy – top panel, in electron volts –, bond length – middle panel, in Ångstroms – and vibrational frequency – bottom panel, in inverse centi-meters – of a carbon monoxide and nitrogen dimer as a function of the charge of the molecule Q – left –, the amount of the electron transfer $5\sigma \rightarrow 2\pi^*$ T – middle – and the magnitude of an electron field E along the molecular axis – right; the results were calculated with an all-electron cluster program. The green, filled circles denote results for the carbon monoxide and the red, hollow circles for the nitrogen dimer

Figure 3.70: The density of states weighted with the projection of the molecular CO and N_2 σ orbitals to the Kohn-Sham states of the adsorption systems Ru (0001)-(2×2)-CO_{ot} and Ru (0001)-$(\sqrt{3} \times \sqrt{3})$R30°-$N_{2,ot}$

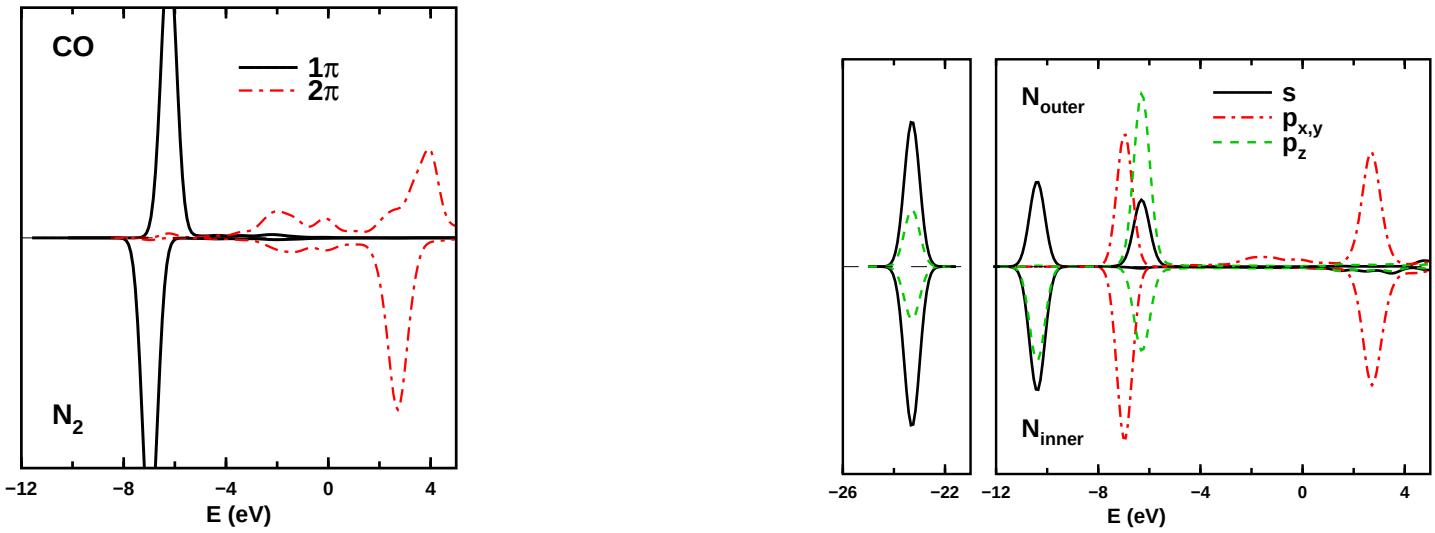

Figure 3.71: The density of states weighted with the projection of the molecular CO and N_2 π orbitals to the Kohn-Sham states of the adsorption systems Ru(0001)-(2×2)-CO_{ot} and Ru(0001)-$(\sqrt{3} \times \sqrt{3})$R30°-$N_{2,ot}$

Figure 3.72: The density of states projected onto the atomic orbitals of the inner – *i.e.* closer to the surface – an outer nitrogen atoms in the structure Ru(0001)-$(\sqrt{3} \times \sqrt{3})$R30°-$N_{2,ot}$

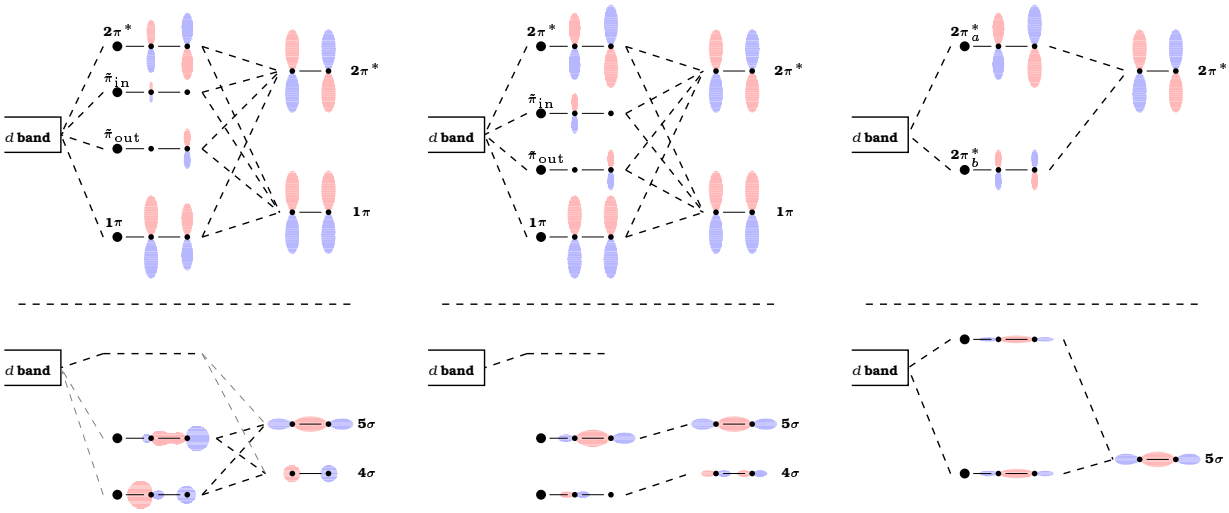

Figure 3.73: The schematic illustration of the molecular orbitals of the nitrogen dimer with the *d* bands of the substrate from our calculation – left –, the experiments of Nilsson *et al* (1997) – middle – and the Blyholder model – right; please notice that there is some inaccuracy in the notation of the 4σ orbitals by Nilsson *et al*

Vibrations of the CO

The CO molecule, since adsorbed parallel to the surface normal and bound to a single atom, and the heavier oxygen is the outer-more atom, the molecule can easily vibrate in the frustrated translational mode shown in the Figure 3.54. The recent measurement by Over *et al* (1995d; Gierer *et al*, 1996), using the concept of split positions (Over *et al*, 1993), were the first to investigate an anisotropic dynamical effect using low-energy electron diffraction. They obtained the r_P factor as a function of the displacement of the oxygen and carbon atoms – or, equivalently the tilt of the molecule – and were thus able to conclude the preferred displacement from the surface normal. The Figure 3.74 shows r_P as a function of the displacement of carbon and oxygen. From the minimum the tilt angle can be derived, and this is shown in the Figure 3.75 together with the results of Landskron *et al* (1996). The agreement in the two different experimental determinations – although both derived using the method of low energy electron diffraction – casts reliability on the result. A value for the frequency of the frustrated translational mode was further achieved by Over *et al*, being 5.5 ± 1.0 meV; it agrees well with the more established method to measure frequencies, the helium atom scattering, which provided a value (Braun *et al*, 1997) of 5.75 meV. Thus also the different methods yield frequencies very close to each other.

We studied the dynamic, temperature induced tilt with static calculations in the $(\sqrt{3} \times \sqrt{3})$R30° structure by determining the part of the potential energy surface which is necessary to investigate the dynamic movement of CO. These calculations were performed earlier than the other calculations in this works, with a different computer code and somewhat different calculational parameters due to computational restrictions. The `fhi94md`

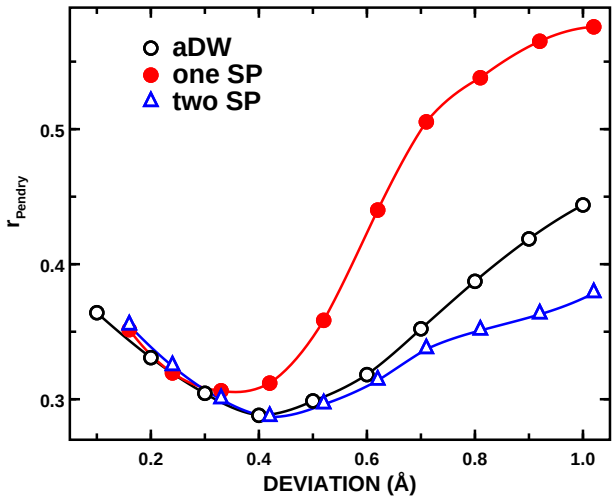

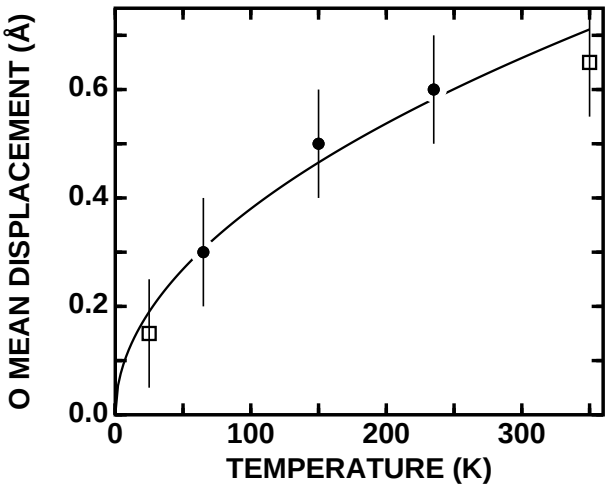

Figure 3.74: The r_P reliability factor for the temperature induced dynamic displacement of the oxygen atom defined as the root mean square deviation from the equilibrium position in the $(\sqrt{3} \times \sqrt{3})$R30°-CO structure at 150 K; from the low energy electron diffraction measurements of Gierer *et al* (1996). The different curves correspond to analysis with an an-isotropic Debye-Weller factor – aDW – and with one – one SP – and two – two SP – split-positions along the direction of the displacement

Figure 3.75: The dynamic displacement of the oxygen atom in the $(\sqrt{3} \times \sqrt{3})$R30°-CO structure from the low energy electron diffraction measurements of Gierer *et al* (1996) – filled circles – and Landskron *et al* (1996) – open squares

computer code – please see Stumpf and Scheffler (1994) or Kley (1997) – was used to perform the calculations, the plane wave cut-off was 40 Ry and a **k** point set with only one **k** point in the irreducible wedge of the surface Brillouin zone in the highly symmetric case – in one twelfth of the full Brillouin zone.

First we studied the corrugation of the potential energy surface by moving the oxygen atom laterally away from the equilibrium site towards the different high-coordinated sites; due to the high symmetry the three directions – shown in the Figure 3.76 – this scans the whole azimuthal angle of 360° accurately enough. The carbon atom is kept fixed to save computational time; however, it would naturally be more affected by a lateral displacement due to its location closer to the surface. The change in energy as a function of the displacement of oxygen is given in the Figure 3.76. The corrugation seen by the oxygen atom is negligible and thus we conclude that the CO molecule can tilt with an equal probability into each direction; this is also supported by the electron stimulated desorption ion angular distribution measurements by Madey (1979). Thus in the subsequent calculations we considered only the tilt towards the hcp and fcc sites because in this case a mirror plane symmetry is conserved and less **k** points needed than for an arbitrary direction of the tilt.

We examined the energetics of the tilt both disallowing and allowing the relaxation of the carbon atom. The relaxation was performed by letting the carbon atom to move for each displacement of the oxygen atom until the forces on the carbon atom and the vertical coordinate of the oxygen atom were zero. The energy versus displacement is shown in the Figure 3.77; near the minimum the curve resembles closely a harmonic potential and thus we shall in the following model the potential energy with the harmonic form

$$V(\Delta R) = \frac{1}{2} c \left(\Delta R\right)^2 \quad . \tag{3.4}$$

The harmonic form has also the advantage that the displacements in the two directions x and y can be decoupled which is not the case in an anharmonic potential. ΔR is the lateral displacement of the oxygen atom, and the potential is assumed to be independent of the azimuthal angle due to small corrugation discussed above. Please note that we consider a static lateral displacement of the oxygen atom where all the other degrees of freedom are allowed to relax; to find the correct one the eigenmodes of the dynamical matrix should be calculated, but when the displacement is small the error is negligible. We shall consider only the case where the displacement of the carbon atom is allowed and thereby the mass of the vibrating particle is the mass of CO molecule. A fit to the calculated values gives a coefficient $c = 181$ meV/Å^2.

Since the molecule has two degrees of freedom it has a thermal energy of $k_B T$, or $\frac{1}{2} k_B T$ per direction. The classical and quantum mechanical mean probabilities of displacement of a particle in a harmonic potential are

$$\overline{\Delta R_{\rm cl}} = \sqrt{\frac{E_{\rm kin}}{\mu \omega^2}} \tag{3.5}$$

and

$$\overline{\Delta R_{\rm qm}} = \sqrt{\sum_{n=0}^{\infty} f_n \left(n + \frac{1}{2}\right) \frac{1}{\mu \omega}} \ , \tag{3.6}$$

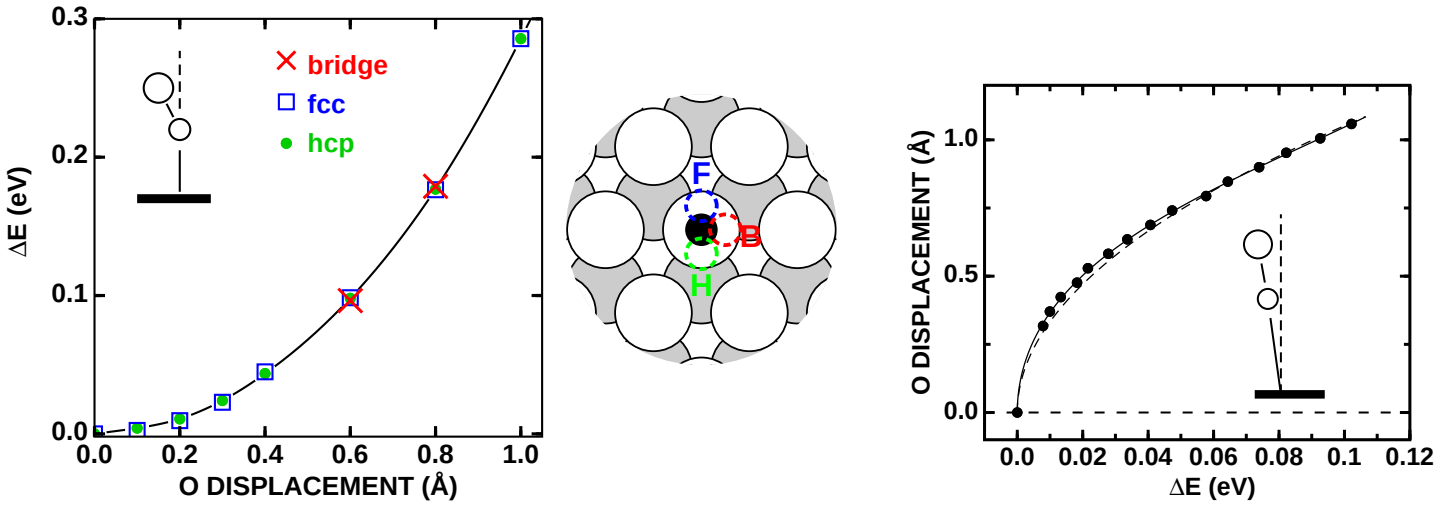

Figure 3.76: The change in energy upon a displacement towards different lateral directions of the oxygen atom from the equilibrium position in the $(\sqrt{3}\times\sqrt{3})$R30°-CO structure

Figure 3.77: The lateral displacement of the oxygen atom from the equilibrium position in the $(\sqrt{3}\times\sqrt{3})$R30°-CO structure as a function of the change in the energy required; the carbon atom and the vertical coordinate of the oxygen are allowed to relax. The dashed and solid line correspond to a harmonic and anharmonic fit to the calculated points

respectively; μ is the mass of the oscillator and ω the frequency, and f_n the occupation of the mode n which depend on the kinetic energy and obey boson statistics. These classical and quantum mechanical results are shown in the Figure 3.78 together with the experimental ones.

We further studied the effect of anharmonicity by fitting an anharmonic function to our potential energy shown in the Figure 3.77. Due to the isotropy only the even powers of the displacement occur in the fit and we use the function

$$V(\Delta R) = \frac{1}{2!}c_2\,(\Delta R)^2 + \frac{1}{4!}c_4\,(\Delta R)^4 + \frac{1}{6!}c_6\,(\Delta R)^6 \quad . \tag{3.7}$$

The fitted coefficient are $c_2 = 0.137$ eV/Å^2, $c_4 = 1.149$ eV/Å^4 and $c_6 = -17.912$ eV/Å^6. We then solved the quantum mechanical probability function using a numerical program to solve the eigenstates of a particle in this potential. Please notice that there is an inherent error in our analysis because the two-dimensional potential energy surface is no longer exactly separable into two one-dimensional components; we expect the error to be small. The resulting displacement is shown in the Figure 3.78, and the results of the harmonic oscillator and experiments are shown for comparison; The agreement is seen to improve along the inclusion of the anharmonicity.

The frequency corresponding to the anharmonic fit is obtained either from the coefficient c_2 and is 4.31 meV or from the excitation energy from the lowest to the first excited state, yielding 4.65 meV. This is in a reasonable agreement with the experimental values 5.75 meV from the helium atom scattering by Braun *et al* (1997) and 5.5 meV from the low energy electron diffraction by Over *et al* (1995d; Gierer *et al*, 1996). The good agreement in both the vibrational frequency of the frustrated translational mode and the thermally induced tilt is not surprising since it is just this vibration which mostly causes the tilt. Over *et al* also suggest a very small displacemental amplitude in the direction perpendicular to the surface and thus a large anisotropy in the vibrations; this is easily understandable from the large difference in the frequencies of CO parallel ≈6 meV and perpendicular ≈50 meV to the surface, illustrating a much larger force constant for varying the Ru–C distance than the polar angle. For a system where CO adsorbs on a hollow site the anisotropy is probably much smaller, already due to the reduced Ru–CO frequency and furthermore due to a higher lateral corrugation.

3.3.3 Adsorption of carbon monoxide on other trigonal surfaces

We shortly discuss the adsorption of carbon monoxide also on other trigonal fcc(111) and hcp(0001) surfaces. The Table 3.16 shows a collection of the experimentally determined adsorption site of CO in the $(\sqrt{3}\times\sqrt{3})$R30°-CO structure on various group VIII and noble metal surfaces; please note that in addition to the $(\sqrt{3}\times\sqrt{3})$R30°-CO structure CO forms also other ordered, more complicated structures like the c(2 × 4)-2CO on Pd(111) and Pt(111), (2 × 2)-3CO on Rh(111) *etc.* On these surfaces CO adsorbs on-top except on Ni(111) and Pd(111); it is remarkable that on platinium, which has the same number of valence electrons as nickel and palladium, the CO adsorbs however at the on-top site. On the other hand the surface stress has a larger influence on Pt(111), and reconstructions on this clean surface are known. Also a definite structural analysis for the Pt(111)-$(\sqrt{3}\times\sqrt{3})$R30°-CO structure does not exist up to date and it is possible that this arrangement cannot exist as a long-order structure.

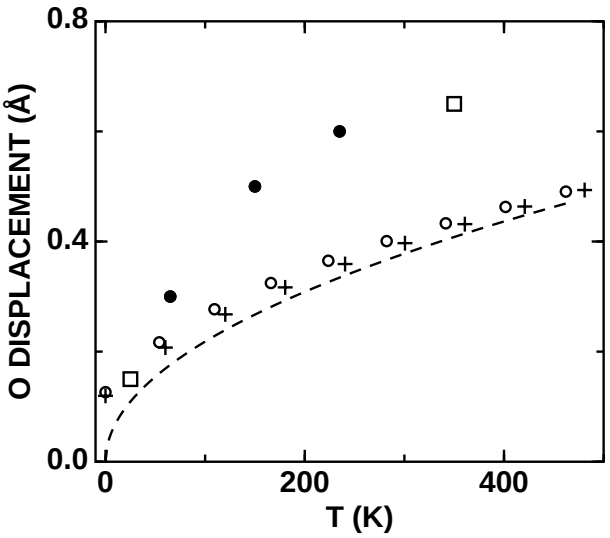

Figure 3.78: The lateral displacement of the oxygen atom from the equilibrium position in the $(\sqrt{3}\times\sqrt{3})$R30°-CO structure as a function of the temperature; the crosses are from a quantum mechanical calculation with a harmonic potential, the empty circles are from a quantum mechanical calculation with an anharmonic potential, the dashed line from a classical calculation with an harmonic potential and the filled circles and empty boxes are the experimental results

Table 3.16: The experimental adsorption site of CO on fcc(111) and hcp(0001) trigonal surfaces of group VIII and noble metals. The adsorption structure is always $(\sqrt{3}\times\sqrt{3})$R30°-CO. The data are extracted from Wei, Skelton and Kevan (1997) except Co(0001) which is measured by Lahtinen, Vaari & Kauraala (1998)

	Co ot	Ni fcc	Cu ot
Ru ot	Rh ot	Pd fcc	
	Ir ot	Pt ot	

We performed density functional calculations for CO adsorption on the surfaces listed in the Table 3.17. The adsorption site is correctly reproduced at Ru(0001), Rh(111), Pd(111) and Ir(111) but on Pt(111) the calculations predict adsorption on the fcc site although from measurements it has been assigned to the on-top site. The differences in adsorption energy at different adsorption site in the Table 3.18 reveal the preference for the fcc site to be small but of the order of the energy differences on the other surfaces where the adsorption site was correctly predicted. Of the several possible sources for this discrepancy we believe the most likely are:

- The applied generalised gradient approximation for the exchange-correlation functional; this is always possible, although less probable since all the other cases are correctly reproduced. A recent calculation (Frank Wagner, personal communication) employing the local density approximation yields also the fcc site
- The pseudo potential approximation; this is unlikely since at least the carbon and oxygen pseudo potentials have shown good transferability so far. A recent all-electron calculation (Frank Wagner, personal communication) again agrees with our calculation
- The non-relativistic treatment of the valence electrons; however, relativity is actually included in the relativistically created pseudo potentials since the core electrons used to generate the pseudo atom have been calculated relativistically and thus the valence electrons, though calculated using the non-relativistic Kohn-Sham equation, sense the relativistic core *etc.* Recently Pacchioni *et al* (1997) calculated the adsorption of CO on several group VIII metals and found the relativity, already when included at the scalar relativistic level, to reproduce the correct adsorption site but a non-relativistic calculation gave the same discrepancy as in our results

The adsorption energies along the rows of the periodic table decrease the more the *d* shell is filled. This is probably due to the more compact structure of the almost filled *d* bands, thus making extra bonding or hybridisation less likely.

Hammer, Morikawa and Nørskov (1996) also made a study of the CO adsorption on metal surfaces. However, they did not relax the system and placed the CO molecule always on the on-top site. They obtained a very good agreement between the fully self-consistent adsorption energies and values predicted from a tight-binding type of model as shown in the Figure 3.79; the quality of correspondence of the model and self-consistent calculation casts confidence to the applicability of the model. The point of intersection – ≈0.45 eV – gives the interaction energy of CO with the *s* and *p* electrons, in good agreement with the values for Al(111), whereas the change

Table 3.17: The adsorption site of CO determined by our density functional calculations on fcc(111) and hcp(0001) trigonal surfaces of group VIII and noble metals. The adsorption structure is always $(\sqrt{3} \times \sqrt{3})$R30°-CO

			Cu fcc
Ru ot	Rh ot	Pd fcc	
	Ir ot	Pt fcc	

Table 3.18: The adsorption energy of CO determined by density functional calculations on fcc(111) and hcp(0001) trigonal surfaces of group VIII and noble metals. The adsorption structure is $(\sqrt{3} \times \sqrt{3})$R30°-CO in all the cases. Negative values are the binding energies at the preferred adsorption site and the positive values differences to this value; all values are in electron volts. The emphasised values are experimental values listed by Hammer, Morikawa and Nørskov (1996) except Rh(111) which is from Wei, Skelton and Kevan (1997)

	on-top	fcc
Ru(0001)	−1.83	+0.22
	−1.66	
Rh(111)	−1.75	+0.04
	−1.79	
Pd(111)	+0.50	−1.87
		−1.47
Ir(111)	−1.99	+0.53
Pt(111)	+0.13	−1.62
	−1.50	

between different elements arises from the interaction of CO $2\pi^*$ and 5σ states with the transition metal d bands; Hammer, Morikawa and Nørskov conclude their results to be in good agreement with the prediction of the Blyholder (1964) model and the studies of Bagus and Pacchioni (1992). Hammer, Morikawa and Nørskov also discuss the correlation between the core level shifts of the transition metals and the CO chemisorption energy observed by Rodriguez and Goodman (1992) and later studied theoretically by Weinert and Watson (1995) and Hennig, Ganduglia-Pirovano and Scheffler (1997).

We finally show the changes of work function in the Table 3.19; the differences between different adsorption sites are large and although the magnitude of the changes is most likely overestimated the determination of the adsorption site based on the change in work function should still be possible. That the work function is higher at the three-fold site in all cases studied here is in line with the observation that the emptying of the 5σ orbital – located mostly at and below the carbon atom – and filling of the $2\pi^*$ – having more weight at both atoms – would shift the centre of average charge further away from the substrate, leading to an increase in the work function. Along the rows of the periodic table the change in work function decreases with the binding energy, and the change is less positive – even negative at Pt(111) – at the $5d$ metals than at the $4d$'s.

3.3.4 Adsorption of oxygen

Since the adsorption of oxygen is not central for the present work we shall here only list the main properties relative to the similar adsorption system of nitrogen on Ru(0001), which was recently studied by Schwegmann *et al* (1997). The major differences between N/Ru(0001) and O/Ru(0001) are:

- Oxygen does not form a $(\sqrt{3}\times\sqrt{3})$R30° but a (2×1) structure; at a coverage of 1/3 rather islands of domains of (2×2) and (2×1) structures would form as is obvious from the Figure 3.80 which shows the adsorption energy at different coverages: The point at the coverage $\theta = 1/3$ lies considerably above the line joining the points at the coverages 1/2 and 1/4. Yet at the coverage 2/3 in the structure $(\sqrt{3} \times \sqrt{3})$R30°-2O our calculations yield a binding energy close to the line connecting the energy at coverages 1/2 and 3/4, and thus could be almost a stable one; however, such a structure has not been observed experimentally, and is peculiar considering the low binding energy of the similar structure $(\sqrt{3} \times \sqrt{3})$R30°

Table 3.19: The change in work function determined by our density functional calculations upon the adsorption of CO on fcc(111) and hcp(0001) trigonal surfaces of group VIII and noble metals. The adsorption structure is always $(\sqrt{3} \times \sqrt{3})$R30°-CO. All values are in electron volts

	on-top	fcc
Cu(111)	−0.04	+0.71
Ru(0001)	+0.81	+1.22
Rh(111)	+0.55	+1.34
Pd(111)	+0.05	+1.13
Ir(111)	+0.17	+1.07
Pt(111)	−0.39	+0.93

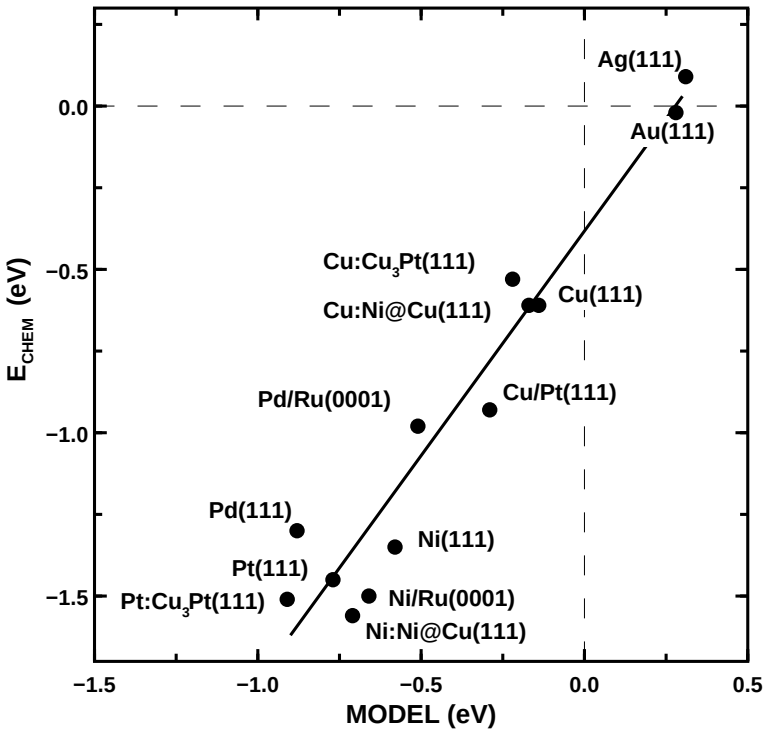

Figure 3.79: The adsorption energy of CO from the Newns-Anderson model versus the self-consistent density functional calculation in a model geometry in the $(\sqrt{3} \times \sqrt{3})$R30°-CO structure; from Hammer, Morikawa and Nørskov (1996)

Table 3.20: The two- and three-particle interaction parameters for oxygen on Ru(0001) extracted from density functional calculations by us and Stampfl *et al* (1999), and from a statistical analysis (Renisch *et al*, 1999) of atomic jumps observed with the scanning tunneling microscopy; the parameters have been defined like in the Figure 3.58 except that here (3×3) structure was regarded as isolated and V_2" is the pair-wise interaction energy between adsorbates at the third-nearest neighbour sites; all values are in electron volts

	E_0	V_2	V_2'	V_2"	V_t	V_t'
DFT	−2.821	0.371	0.080	−0.017	0.063	−0.103
Stampfl	−2.503	0.265	0.044	−0.025	0.058	−0.085
STM			0.028	−0.042		

- The (2×2) is a more attractive structure than (3×3) also in our calculations and (2×2) islands of oxygen are formed in coverages less than 1/4 (Wintterlin *et al*, 1997; Nagl *et al*, 1998); the results from these scanning tunnelling microscope studies are also shown in the Figure 3.80, and regarding the possible amounts of error both in the analysis of the measurements and our calculations the agreement is very good, the remaining errors are 70 meV

- Coverages up to a full (1×1) mono-layer are stable against desorption at low temperatures as concluded from the Figure 3.80; this had been experimentally verified by low energy energy diffraction measurements in the group of Herbert Over as was suggested by density functional calculations (Stampfl *et al*, 1996). The difference between oxygen and nitrogen is not in the adsorption as the adsorption energies relative to atoms in gas phase are very similar but the large difference in the binding energy of the dimers – 9.76 eV for N_2 and 5.12 eV for O_2 – makes the desorption as N_2 preferable at much lower a temperature than in the case of oxygen

The adsorbed oxygen atom on Ru(0001) shows the same, although smaller, trend of shortening adsorption bond distance as recently found by Schwegmann *et al* (1998) on the Ru$(10\bar{1}0)$ surface: whereas oxygen-ruthenium distance shortens by 0.05 Å from the Ru$(10\bar{1}0)$-c(2×4)-2O to Ru$(10\bar{1}0)$-(2×1)-*p2mg*-2O on the Ru(0001) surface this distance in the (1×1) structure is shorter by 0.03 Å than in the (2×2) structure. However, the densities in these structures on the two different surfaces are smaller by about a factor of two which makes the comparison somewhat more complicated.

We did a similar analysis to extract the parameters for the two and three particle potentials as was done for carbon monoxide on Ru(0001) in the Section 3.3.2; the results are collected into the Table 3.20. Although the agreement between the analysis between the parameters from the analysis of scanning tunnelling microscope images and the density functional calculations is not very good it is important to realise that the experimental values correspond to binding or attachment energies at island boundaries rather than the binding energies in ordered layers like we have used them here.

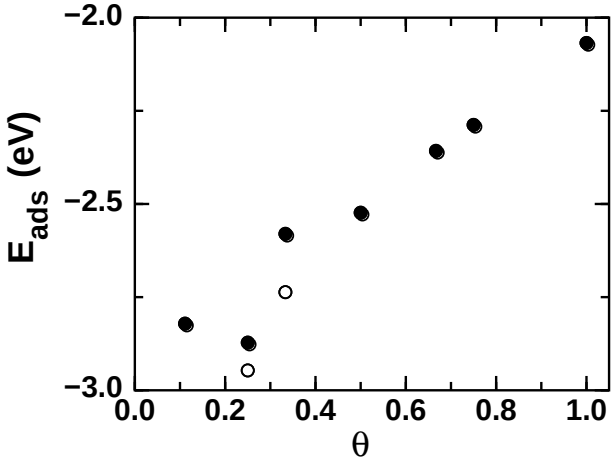

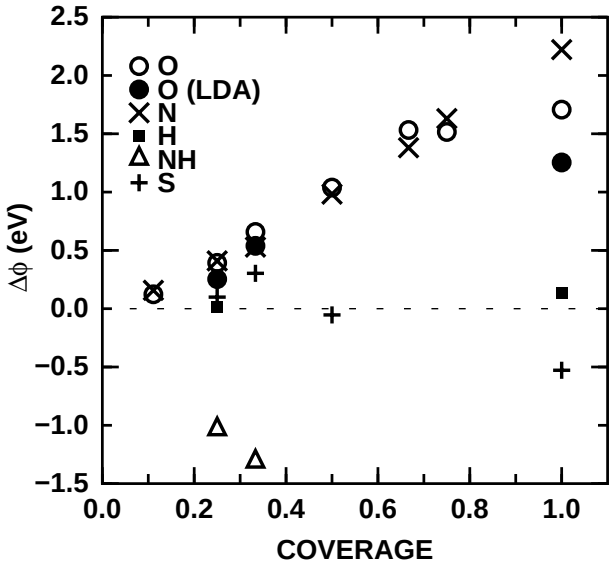

Figure 3.80: The adsorption energy of oxygen on Ru(0001) from our density functional calculations – filled circles – and derived from the statistical distribution of atom in the scanning tunnelling microscope measurements by Wintterlin *et al* (1997) and Renisch *et al* (1999) – open circles – in different ordered structures. The energies are calculated with respect to O_2 molecule in the gas phase, and the experimental values are normalised to be equal to the calculations in the (3×3) structure

Figure 3.81: The change in work function upon adsorption on Ru(0001) for several electro-negative species; oxygen has been calculated both with the local density and generalised gradient approximations, all the other calculations (Ari P Seitsonen, unpublished results) were done employing the generalised gradient approximation

We made still a qualitative study about the change work function upon the adsorption of electro-negative atoms and the NH molecule on the Ru(0001) surface. The result in the Figure 3.81 shows interesting differences between the adsorbates: for example whereas the change for oxygen and the iso-electronic sulphur is positive and about of the same magnitude but as nearest-neighbour sites start to be occupied the work function for sulphur starts to decrease; although the high coverages of sulphur have not been produced experimentally to the best of our knowledge they might be possible since the atomic and covalent radii of sulphur are smaller than half of the nearest-neighbour distance on Ru(0001); we have obtained a binding energy in the excess of 1.5 eV in the (1×1)-S structure. The change in the work function of oxygen within the local density approximation is smaller than in the generalised gradient approximation and thus closer to the experimental values. The change in the case of oxygen is very similar to the one induced by nitrogen, except that at high coverage the change for oxygen levels off but continues for nitrogen.

3.4 Co-adsorption on Ru(0001)

As mentioned in the Introduction the co-adsorption is extremely important since in the Langmuir-Hinshelwood mechanism of the catalytic reaction the reactants, in addition to the possible promoters and inhibitors, adsorb to the surface prior to the reaction. A recent review which covers the structural and electronical aspects of co-adsorption has been published by Herbert Over (1998). Here we shall present our calculated results for three different co-adsorption system where two of the adsorbates of the previous Section, cesium, carbon monoxide and oxygen, are combined at the Ru(0001) surface at a time. This gives us an opportunity to monitor the changes on the adsorbates when they are exposed to a chemically different species on the surface; also the important reactants and test molecule carbon monoxide is combined with the electro-positive cesium and the electro-negative oxygen, which is also the other reactants in the oxidation process of the CO.

3.4.1 Co-adsorption of cesium and oxygen

The co-adsorption of alkali and oxygen atoms has been widely studied (Surnev, 1989). One interesting occurrence of the system is in the ammonia catalysts as discussed *e.g.* by Ertl (1991). On Ru(0001) the co-adsorbed cesium and oxygen has been the subject of studies employing the low energy electron diffraction (Over *et al*, 1992a; Bludau *et al*, 1995; Trost, Wintterlin & Ertl, 1995), scanning tunnelling microscope (Trost, 1995; Trost, Wintterlin & Ertl, 1995) and high-resolution electron energy loss spectroscopy (Jacobi *et al*, 1995). With cesium as very electro-positive and oxygen electro-negative atom the interaction between them is attractive but the repulsion between like atoms makes the O-Cs-Ru(0001) phase diagram versatile as found by Bludau *et al* (1995); the most abundant phases are arranged into the $(\sqrt{7} \times \sqrt{7})$R19.1°, $(3 \times 2\sqrt{3})$ and $(\sqrt{3} \times \sqrt{3})$R30° unit cells. It is was not until recently that an ordered structure (2×2) with both the cesium and oxygen coverage 1/4 was found (Over, personal communication); however this phase might be only meta-stable against re-ordering into

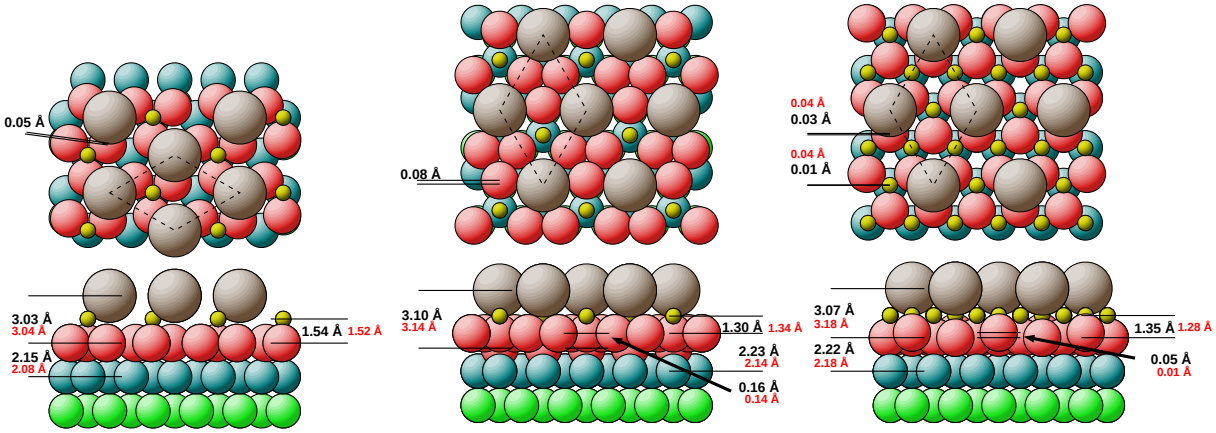

Figure 3.82: The geometries of the Ru (0001)-($\sqrt{3}\times\sqrt{3}$)R30°-(1Cs+1O), Ru (0001)-(2 × 2)-(1Cs+1O) and Ru (0001)-(2 × 2)-(1Cs+3O) structures and the separated adsorption structures as obtained from our density functional calculation and the low energy electron diffraction measurements of Over *et al* (1992a) and Kim *et al* (1998); the experimental values are shown with a smaller font

Table 3.21: The adsorption energy, change in work function, layer distances and distance of cesium, cesium and oxygen, and oxygen adsorbed on Ru (0001) in the ($\sqrt{3}\times\sqrt{3}$)R30°-(1Cs+1O) structure from our density functional calculations. E_{ads,O_2} is the adsorption energy relative to the oxygen dimer, E_{ads} the mixing energy from the separated ($\sqrt{3}\times\sqrt{3}$)R30°-Cs and ($\sqrt{3}\times\sqrt{3}$)R30°-O phases

	Cs/Ru	O/Cs/Ru	O/Ru
E_{ads,O_2} (eV)	—	3.19	2.81
E_{mix} (eV)	—	0.37	—
$\Delta\phi$ (eV)	−3.24	−3.36	+0.66
d_{Cs-Ru} (Å)	3.50	3.45	—
d_{O-Ru} (Å)	—	2.19	2.07
d_{12} (Å)	2.15	2.15	2.16
z_{Cs-Ru} (Å)	3.09	3.03	—
z_{O-Ru} (Å)	—	1.54	1.29
Δx (Å)	+0.05	+0.05	+0.02

the ($\sqrt{39}\times\sqrt{39}$)R16.1° structure. This is peculiar since both atoms alone form this phase. The cesium-to-oxygen ratio 1:2 corresponds to the existing bulk oxide CsO_2, and structural models close to the (010) face was proposed in the (3 × 2$\sqrt{3}$)rect and ($\sqrt{7}\times\sqrt{7}$)R19.1° unit cells.

Trost, Wintterlin and Ertl (1995) studied the phase ordering of the cesium-oxygen "liquid"; in particular they observed the evolution and interplay between the ($\sqrt{7}\times\sqrt{7}$)R19.1° structure and the dis-ordered phase. Jacobi *et al* (1995) studied the re-appearance of the Cs-Ru vibrational mode upon adsorption of different gases; it was found that also oxygen, dissociating readily to atomic species, makes the Cs-Ru mode visible at the cesium coverages larger than 0.22 where the loss became undetectable due to the metallisation of the cesium layer. The co-adsorbed oxygen probably causes a localisation of the electronic states arising from cesium and thus a de-metallisation and subsequently the re-appearance of the energy loss in the spectra.

We performed density functional calculations for the structures Ru (0001)-($\sqrt{3}\times\sqrt{3}$)R30°-(1Cs+1O), Ru (0001)-(2 × 2)-(1Cs+1O) and Ru (0001)-(2 × 2)-(1Cs+3O) only due to the larger unit cells and less well known atomic structure in the other configurations. The atoms were placed at the hcp sites in the ($\sqrt{3}\times\sqrt{3}$)R30°-(1Cs+1O) and (2 × 2)-(1Cs+3O) structures and the oxygen at the hcp and cesium on-top sites in the (2 × 2)-(1Cs+1O) arrangement, as found in the low energy energy diffraction studies by Over *et al* (1992a; Kim *et al*, 1998). Please note that while cesium adsorbs exactly on the hcp site in the coverage 1/3 the corresponding oxygen-only phase would be unstable towards island formation to domains of (2 × 2) and (2 × 1) structures as was discussed in Section 3.3.4. The resulting geometry is shown in the Figure 3.82 with the results from the low energy electron diffraction measurements by Over *et al* (1992a) and listed in the Table 3.21 together with the separated phases.

The most remarkable effect in the co-adsorption geometry is the short Cs-Ru and longer O-Ru distance compared to the separated phases; this is a consequence of the change in the height of the atoms since the lateral relaxation – and the first interlayer distance d_{12} – are hardly affected. The same trend was found in the low energy energy diffraction measurements of Over *et al* (1992a), although the reduction in the height z_{Cs-Ru} is larger in the experiments, −0.11 Å; however, in the structure ($\sqrt{3}\times\sqrt{3}$)R30°-Cs the distance was too small in the calculations, maybe due to the neglect of zero-point and thermal vibrations which are probably diminished in the more tightly packed co-adsorbed phase. Except for the layer distance d_{12} the experimental and theoretical geometries agree extremely well.

From the energies we see that the mixing of the cesium and oxygen layers stabilises both atoms compared to the separated phases by 0.37 eV. However, the ($\sqrt{3}\times\sqrt{3}$)R30°-O would not be stable without cesium and we

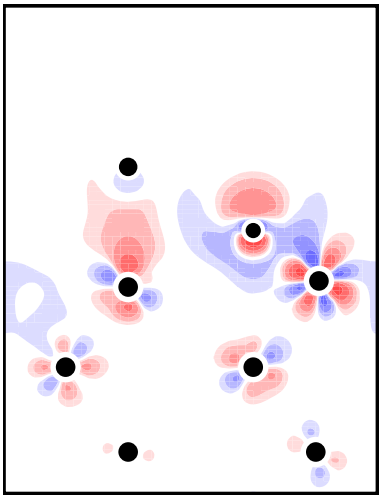

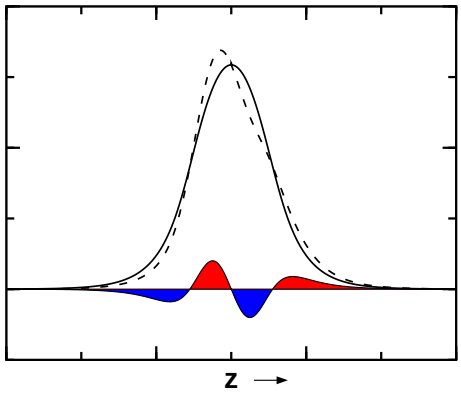

Figure 3.83: The change in the electron density due to the co-adsorption of cesium and oxygen to form the (2×2)-(1Cs+1O) structure

Figure 3.84: A schematic illustration of the change in the electron density on the vertical line passing through the centre of the oxygen atom due to the co-adsorption of cesium and oxygen to form the (2×2)-(1Cs+1O) structure

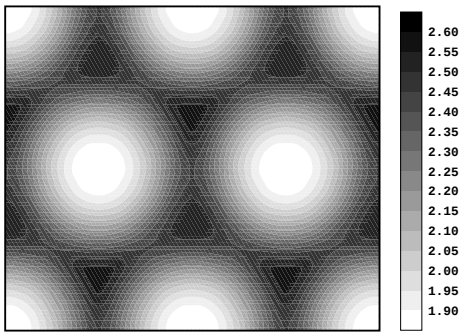

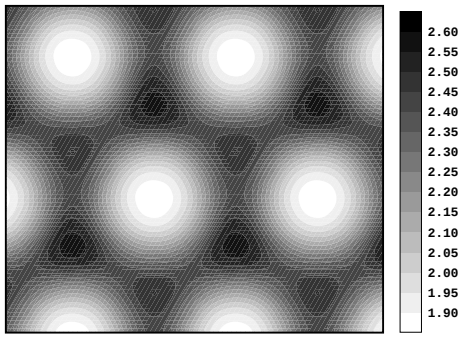

Figure 3.85: A pseudo scanning tunnelling microscope image from the Tersoff-Hamann model in the (2×2)-(1Cs+1O) structure

Figure 3.86: A pseudo scanning tunnelling microscope image from the Tersoff-Hamann model in the $(\sqrt{3} \times \sqrt{3})$R30°-(1Cs+1O) structure

estimate from the (2×2)-O and (2×1)-O structures in the Figure 3.80 that the oxygen phase $(\sqrt{3} \times \sqrt{3})$R30°-O would have to be bound by 2.91 eV in order to be the preferred structure at the oxygen coverage 1/3, *i.e.* in order to prevent formation of domains. Therefore the real mixing energy of the combined cesium-oxygen phase is actually 0.28 eV, compared to the separated phases; thus the formation of the mixed phase is still rather favourable but this does not imply that islands of $(\sqrt{3} \times \sqrt{3})$R30°-(1Cs+1O) would be formed, even at concentration ratio 1:1, since the other structures with coverages different from 1/3 can be more stable. We have no access to the full phase diagram from our density functional calculations until many more unit cells and structures have been studied.

The work function in the mixed phase is lowered even from the pure cesium structure. This could be expected based on the geometry where the oxygen layer is below the cesium atoms and the cesium is closer to the first ruthenium layer in the mixed phase. All this agrees (Over *et al*, 1992a) with the model of the cesium denoting charge to the oxygen, fitting well to the electro-positivity of cesium and electro-negativity of oxygen; however it also could be explained from interaction between the cesium and oxygen, leading to a reduction in the layer distance between them. To obtain insight to this question we show the density difference in the structure (2×2)-(1Cs+1O) in the Figure 3.83. The change around the cesium atom is very small, whereas around the oxygen and ruthenium atoms there appears a polarisation, which for the oxygen can be qualitatively represent like the change in the Figure 3.84. Please notice that the largest change in the magnitude appears in the core region.

We further compare our results to the experimental images produced by the scanning tunnelling microscope; the measurements are from Trost (1995; Trost, Wintterlin & Ertl, 1995). In the Figures 3.85 and 3.86 we show the height maps of the constant density *i.e.* of a constant current within the Tersoff-Hamann model. The value of the density was chosen so that it reproduced the maximal corrugation from the experiments along a cut through the adsorbates. The Figure 3.87 can be compared to the measured images in the work of Trost (1995); the agreement is very good in both cases.

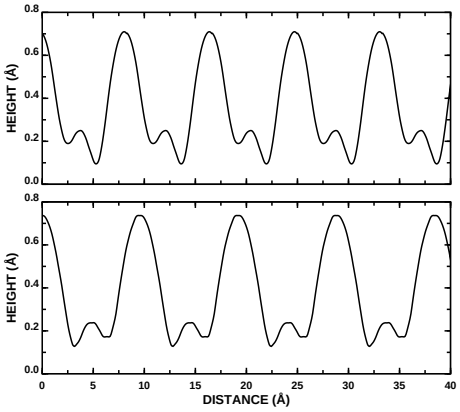

Figure 3.87: A cut through the pseudo scanning tunnelling microscope image from the Tersoff-Hamann model in the $(\sqrt{3} \times \sqrt{3})$R30°-(1Cs+1O) – upper panel – and (2×2)-(1Cs+1O) – lower panel – structures

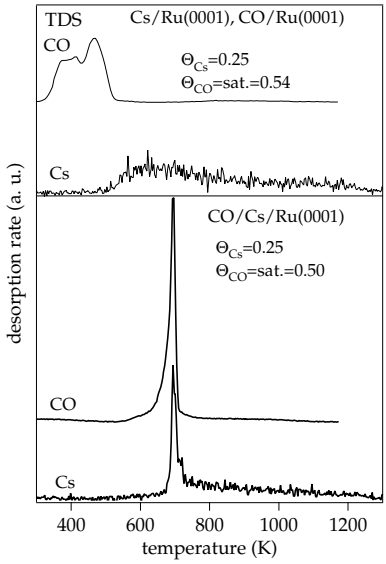

Figure 3.88: The thermal desorption spectra for cesium, carbon monoxide and the co-adsorbed phase on Ru(0001); from Over *et al* (1995b)

3.4.2 Co-adsorption of cesium and carbon monoxide

Also the co-adsorbed alkali metal and carbon monoxide mutually stabilise each other as was found in the thermal desorption spectroscopy for example in the case of K and CO on Ni(110) (Brodén, Gafner & Bonzel, 1979), Na, K and Cs with CO on Ni(100) (Kiskinova, 1981), and K and CO on Ru(0001) (Madey & Benndorf, 1985); an example of the thermal desorption spectra (Over *et al*, 1995b) is shown in the Figure 3.88 for Cs and CO on Ru(0001): whereas the desorption of Cs alone begins already at 450 K and the one of CO at 350 K, in the co-adsorbed layer the desorption does not begin until 650 K, and then the desorption occurs simultaneously.

The stabilisation of the co-adsorbates is due to an attractive interaction between the electro-positive alkali and the electro-negative carbon monoxide. The attraction has been concluded from the thermal desorption and vibrational spectra, since at low alkali coverages there appears two distinct states: In addition to the almost unchanged component and second one, with a higher desorption temperature and lower internal C-O stretching frequency. At low coverages of carbon monoxide only the second state, affected by the co-adsorbed alkali, is occupied, showing that it is the preferred adsorption state and thus a clustering of the co-adsorbates must take place; this implies that the adsorption is attractive. If the coverage of the alkali is large enough, all the carbon monoxide molecules must adsorb to sites at the vicinity of the alkali and are affected by it: only CO molecules in one state are thus observed. Due to the two different CO species, once the neighbourhood of the alkali has been filled, a short-range interaction between the alkali and CO was concluded, since the adsorption of further molecules is no longer significantly perturbed by the presence of the alkali on the surface.

The reduction of the C-O stretching frequency on all the systems studied so far points to a common mechanism in the co-adsorption systems. The usual interpretation is that the bond length of CO increases, yielding a lower frequency. In the few qualitative structural determinations up to date this has indeed been confirmed in the case of K and CO on Ni(111) (Davis *et al*, 1995; 1997), Cs and CO on Ru(0001) (Over *et al*, 1995b; 1995c), K and CO on Ru(0001) (Over *et al*, 1999), Na and CO on Pt(111) (Sette *et al*, 1985), and K and CO on Pt(111) (Moré, 1998). Simultaneously the size of the alkali metal atom is expected to decrease – *i.e.* the atom to move closer to the surface – since in the intuitive model the alkali acts as an electron donor, increasing the

degree of ionisation when the CO is co-adsorbed because more of the charge from the *ns* state of the alkali would be transfered via the substrate to the partially empty, acceptor orbital $2\pi^*$ along the lines of the Blyholder model; the filling of this state, because anti-bonding and thus weakening for the internal C-O bond, also partially explains the lowering of the C-O vibrational frequency upon the co-adsorption of the alkali. The size of the alkali metal, characterised by its hard-ball radius, is however found to increase when CO is adsorbed, in contradiction with the simple charge-transfer model; in cases where the adsorption site of the alkali does not change this effect has so far been found in the systems Co(0001)-(2 × 2)-(K+2CO) (Lahtinen *et al*, 1998), Co(10$\bar{1}$0)-c(2 × 2)-(K+CO) (Kaukasoina *et al*, 1995), Ni(111)-(2 × 2)-(K+2CO) (Davis *et al*, 1995; 1997), Ru(0001)-(2 × 2)-(Cs+*n*CO), *n*=1,2 (Over *et al*, 1995b; 1995c) and Pt(111)-($\sqrt{3}$ × $\sqrt{3}$)-(K+CO) (Moré, 1998). In the case of Co(10$\bar{1}$0)-c(2 × 2)-(K+CO) the increase in the size of the potassium is extraordinarily large, 0.4 Å. The origin of the change of the size is still not understood.

Whereas the carbon monoxide alone adsorbs either on the three-fold hollow fcc – Ni(111) and Pd(111) – or on-top sites – Co(0001), Cu(111), Ru(0001), Rh(111) and Ir(111) on the trigonal surfaces, in the co-adsorbed phases with an alkali only three-fold adsorption sites have been found. Likewise although the alkali often adsorbs on a hollow site in the phase of a single adsorbate, in the co-adsorbate structure the alkali is exclusively found on the on-top site, with Pt(111) violating the rule. These effects point out to a general interaction mechanism in the mutual attraction between the ad-particles.

We studied the co-adsorption of cesium and carbon monoxide in the configurations with coverages equal to those which were solved experimentally using the low energy electron diffraction by Over *et al* (1995b; 1995c), namely Ru(0001)-(2 × 2)-(1Cs_{ot}+1CO_{hcp}) and Ru(0001)-(2 × 2)-(1Cs_{ot}+2$CO_{hcp,fcc}$); furthermore we calculated the structure Ru(0001)-(2 × 2)-(1Cs_{hcp}+1CO_{ot}), which is not experimentally observed but is instructive for studying why this structure is less stable than the Ru(0001)-(2 × 2)-(1Cs_{ot}+1CO_{hcp}). In addition to extract qualitative understanding of the nature of the effect of the alkali on the carbon monoxide we also studied the adsorption of CO alone but with an applied electric field, in the structures Ru(0001)-(2×2)-($CO^{\mathbf{E}}_{ot}$) Ru(0001)-(2×2)-($CO^{\mathbf{E}}_{hcp}$); the superscript **E** denotes the electric field. Similar density functional calculations on the poisoning and promotion upon co-adsorption were done by Mortensen *et al* (1998); however, their results cover a broader range and are more qualitative.

The geometries of our final geometries are compared in the Figure 3.89 and the Table 3.22 to the experimental observations, where possible. The C-O, Ru-C and co-adsorbate-to-nearest neighbour Ru bond lengths are also shown in the Table 3.23, where they are shown contrasted to the different chemical environment. Like in the experiments, the C-O bond length clearly increases relative to the isolated C-O phase from 1.15 Å to 1.26 Å by 0.11 Å, although in the experiments the change is only about 0.02 Å; however the error bars in the experimental analysis are large. The change in the bond length seems to consist of two origins:

- The change of adsorption site of the CO-only phase from on-top to hcp site accounts to 0.04 Å
- The co-adsorption of Cs when the molecule is on the hcp site causes the rest of the change, 0.07 Ä; this change can be understood as arising from the electric field created by the alkali. The magnitude of the electric field used in our calculation in the (2 × 2)-($CO^{\mathbf{E}}_{ot}$) system was only 0.6 eV/Å since at larger fields the slab becomes ionised; this value is, however, only one third or one quarter of the value felt by the CO in the case of co-adsorption with the alkali – please see the Section 3.3.1, and therefore we multiplied the change obtained, 0.02 Å, by a factor of three, where we have assumed that the change is almost linear with the applied field. The resulting change is 0.06 Å, very close to the change with the actual co-adsorption with the alkali metal

This observation that about 30-50 % of the change in the bond length is due to the site change and the rest from the field generated by the alkali is difficult to verify from the experimental observations due to the large error bars, which are often almost of the size of this effect. The changes of 0.05 Å for K+2CO/Ni(111), 0.07 Å for K+CO/Ru(0001) and 0.13 Å for K+CO/Pt(111) are similar in magnitude to our results, noting that there are two molecules per one alkali in the first structure, where CO adsorbs already on a three-fold hollow site in the isolated phase.

We made a further study on the effect of the electric field on the properties of an isolated CO molecule. This study we performed with a cluster program since we wanted too see the effect on the 1*s* states of carbon and oxygen. The results in the Table 3.24 suggest that in the electric field and charge state – please see below – which we have estimated to occur at the surface, namely Z=−1.5 electrons and 2.6 eV/Å, the change in the vibrational frequency, −143.6 meV from the free CO molecule agrees well with the experimental change of −141 meV, but the increase in the bond length 0.26 Å is much too large compared to the experimental value. However, the experimental results suffer from the large error bars and the shortening of the bond found recently (Over *et al*, 1995b; 1995c) is clearly not realistic. In our results we have not taken into account the screening and hybridisation of the molecular levels by the substrate and thus the eigenvalues in different charge states cannot be compared directly. The experiments of Strisland *et al* (1998) yield a reduction in the C and O 1*s* binding energies upon the co-adsorption of K to the CO/Rh(111) system, which is very similar to system in our study. Our values show a small increase, but we do not include any subtle many-body or final state effects present in the experiments, so a full comparison is not possible.

The Ru-C bond length can be seen to increase slightly with the electro-negativity of the co-adsorbate at the hcp site, but the change is much larger at the on-top site, achieving −0.10 Å. The Ru-C distance anti-correlates thus mostly with the C-O distance, whereas in the only experimental case to which we can compare, Ni(111), both C-O and Ru-C distances increase when the potassium is co-adsorbed (Schindler *et al*, 1993; Davis *et al*,

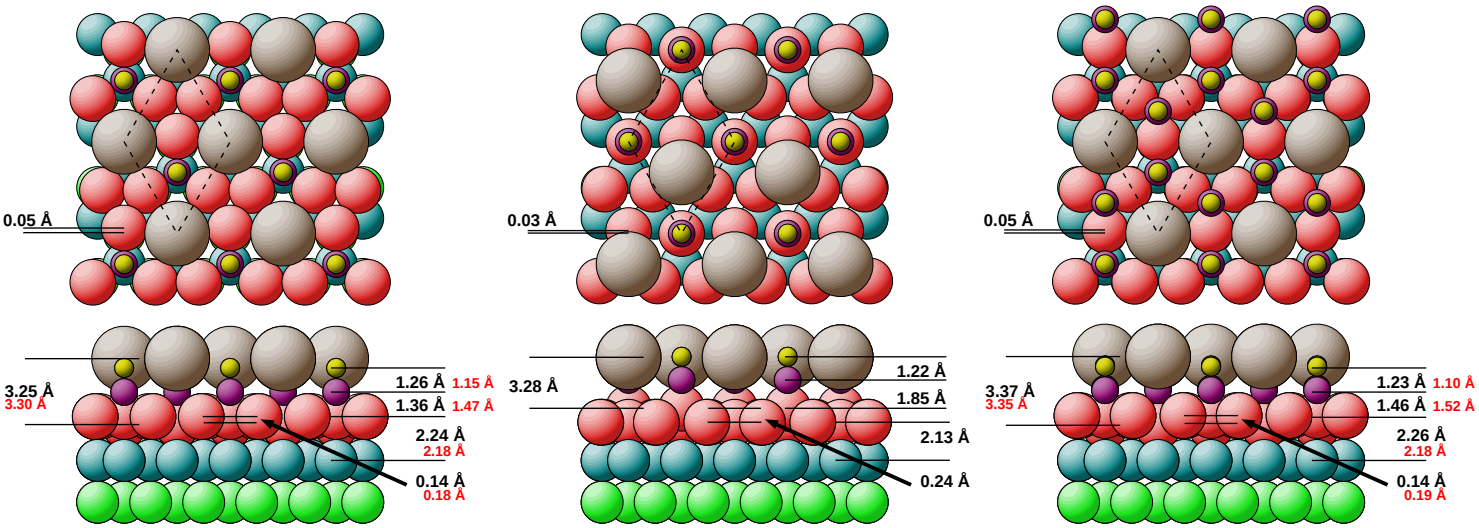

Figure 3.89: The geometries obtained from our calculations for the Cs+CO co-adsorption on Ru(0001); the experimental results by Over *et al* (1995b; 1995c) are denoted with a smaller font

Table 3.22: The adsorption energy, change in work function, layer distances and distance of the cesium in the $(2\times2)°$-Cs_{ot}, cesium and carbon monoxide adsorbed on the Ru(0001) in the $(2\times2)°$-($1Cs_{ot}$+$1CO_{hcp}$) and $(2\times2)°$-($1Cs_{ot}$+$2CO_{hcp,fcc}$) structures, and the carbon monoxide adsorbed in the $(2\times2)°$-CO_{ot} from our density functional calculations. $E_{ads,Cs}$ and $E_{ads,CO}$ are the adsorption energies relative to a free cesium atom and carbon monoxide dimer, E_{mix} the mixing energy from the separated phases – Cs+CO and CO in the case of 1Cs+2CO – and $\Delta\phi$ the change in the work function from the clean surface; z_{12} is the average height between the first and second substrate layer, z_{C-Ru} and z_{Cs-Ru} the layer height from the nearest-neighbour atoms and d_{C-Ru} and d_{C-O} the corresponding distances

	Cs/Ru	CO/Cs/Ru	2CO/Cs/Ru	CO/Ru
$E_{ads,CO}$ (eV)	—	2.68	2.06	1.83
$E_{ads,Cs}$ (eV)	1.94	2.79	—	—
E_{mix} (eV)	—	0.85	0.26	—
$\Delta\phi$ (eV)	−3.44	−3.32	−2.74	+0.81
d_{C-Ru} (Å)	—	2.14	2.17, 2.17	1.93
d_{C-O} (Å)	—	1.26	1.23, 1.23	1.16
z_{Cs-Ru} (Å)	3.16	3.25	3.37	—
z_{C-Ru} (Å)	—	1.36	1.42, 1.49	1.93
z_{12} (Å)	2.15	2.20	2.21	2.16
b (Å)	0.03	0.14	0.18	0.17
Δx (Å)	+0.01	+0.05	+0.03	+0.01

Table 3.23: The distances and peaks in the density of states projected to the atomic orbitals in systems containing carbon monoxide in the (2×2)-(A+CO), A = co-adsorbate, structures from our density functional calculations; the second column from right is the peak due to the 2*s* level of oxygen or 5*s* level of cesium depending on which one is present on the surface in the structure

	d_{C-O} (Å)	d_{C-Ru} (Å)	d_{A-Ru} (Å)	$\bar{\varepsilon}_{CO,3\sigma}$	$\bar{\varepsilon}_{CO,4\sigma}$	$\bar{\varepsilon}_{CO,1\pi}$	$\bar{\varepsilon}_{CO,5\sigma}$	$\bar{\varepsilon}_{O,2s}$ / $\bar{\varepsilon}_{Cs,5s}$	$\bar{\varepsilon}_{Cs,5p}$
CO^{E}_{hcp}/Ru	1.21	2.16	—	−22.1	−9.7	−6.0	−6.6	—	—
Cs_{ot}/Ru	—	—	3.16	—	—	—	—	−23.1	−10.0
CO_{hcp}/Cs_{ot}/Ru	1.26	2.14	3.25	−21.8	−10.1	−6.0	−6.8	−22.5	−9.4
$2CO_{hcp,fcc}$/Cs_{ot}/Ru	1.23	2.17	3.37	−22.0	−9.9	−6.0	−6.9	−22.4	−8.9
CO_{hcp}	1.19	2.16	—	−22.3	−9.6	−6.0	−6.4	—	—
CO^{E}_{ot}	1.18	1.90	—	−23.3	−9.0	−6.4	−6.8	—	—
Cs_{hcp}/Ru	—	—	3.52	—	—	—	—	−23.0	−9.9
CO_{ot}/Cs_{hcp}/Ru	1.22	1.85	3.67	−23.5	−10.2	−6.8	−7.2	−23.5	−9.7
CO_{ot}	1.16	1.92	—	−23.3	−9.0	−6.2	−6.6	—	—
CO_{ot}/O_{hcp}/Ru	1.15	1.95	2.07	−23.4	−9.0	−6.3	−6.6	−19.0	—
CO_{ot}/$2O_{hcp,fcc}$/Ru	1.15	1.97	2.11	−23.4	−8.9	−6.3	−6.5	−18.5	—
O_{hcp}/Ru	—	—	2.07	—	—	—	—	−19.0	—

Table 3.24: The properties of a CO molecule in an applied electric field and in different charge states; calculated using an all-electron cluster code. The results for the neutral molecule in no field are shown as absolute, the other entries are changes relative to this configuration

Charge	$\|\mathbf{E}\|$ (eV/Å)	d_{C-O} (Å)	$\varepsilon_{1\sigma}$ (eV)	$\varepsilon_{2\sigma}$ (eV)	$\varepsilon_{3\sigma}$ (eV)	$\varepsilon_{4\sigma}$ (eV)	$\varepsilon_{1\pi}$ (eV)	$\varepsilon_{5\sigma}$ (eV)	$\varepsilon_{2\pi}$ (eV)	D (Debye)	ω (meV)
0.0	0.0	1.14	−515.2	−272.9	−29.2	−14.2	−11.8	−9.1	−2.1	+0.12	266.2
0.0	2.6	0.02	−0.1	−0.1	0.2	−0.6	0.0	1.1	0.4	1.7	−21.4
−0.8	0.0	0.08	8.2	8.1	9.1	7.6	8.3	7.5	6.7	1.0	−54.5
−0.8	2.6	0.13	8.1	8.5	9.7	7.2	8.6	8.6	7.3	1.4	−85.2
−1.5	0.0	0.17	14.6	14.2	16.6	13.8	15.1	13.5	12.1	2.0	−102.4
−1.5	2.6	0.26	14.4	14.9	17.6	13.7	15.5	14.5	12.6	1.4	−143.6

1995); at the corresponding coverage, $1Cs_{ot}$+$2CO_{fcc,hcp}$, a slight increase is seen also on the Ru(0001). Thus a general rule of the change in the Ru-C bond length might be difficult to achieve, also due to the small magnitude of the effect.

That the experimentally deduced interaction between the alkali metal and carbon monoxide is attractive is confirmed if the mixing energy

$$E_{\mathrm{mix}} = -E\,(\mathrm{Cs} + \mathrm{CO/Ru}) + E\,(\mathrm{CO/Ru}) + E\,(\mathrm{Cs/Ru}) - E\,(\mathrm{Ru}) \tag{3.8}$$

is positive. In the configuration Ru(0001)-(2 × 2)-(Cs_{ot}+CO_{hcp}) this energy is very large, −0.85 eV, and thus explains the clustering of alkali and carbon monoxide at low coverages and the large mutual stabilisation. We can make an estimate on how much the desorption temperature should change if the pre-factor would not change; we recognise that this might be a drastic approximation and can justify it only *a posteriori*. If we however make the assumption, the change in the desorption energy is only due to the change in the activation energy for desorption, and since

$$e^{-E_a/(k_B T)} = e^{-E'_a/(k_B T')} = \text{constant}\ , \tag{3.9}$$

where E'_a is the activation energy in the presence of the co-adsorbate; then $T' = T \times E'_a/E_a$. As estimates for the activation energies of the isolated phases we use the binding energy, thus $E_a[(2\times2)-\mathrm{Cs}] = 1.94$ eV, $E'_a[(2\times2)-\mathrm{Cs}] = E_a[(2\times2)-\mathrm{Cs}] + E_{\mathrm{mixing}} = 1.94 + 0.85 = 2.79$ eV, $E_a[(\sqrt{3}\times\sqrt{3})\mathrm{R30^\circ}-\mathrm{CO}] = 1.83$ eV and $E'_a[(\sqrt{3}\times\sqrt{3})\mathrm{R30^\circ}-\mathrm{CO}] = E_a[(\sqrt{3}\times\sqrt{3})\mathrm{R30^\circ}-\mathrm{CO}] + E_{\mathrm{mixing}} = 1.83 + 0.85 = 2.68$ eV. If we use as the corresponding temperatures where significant amount of desorption occurs $T[(2\times2)-\mathrm{Cs}] \approx 500$ K and $T[(\sqrt{3}\times\sqrt{3})\mathrm{R30^\circ}-\mathrm{CO}] = 440$ K, we obtain

$$T'[(2\times2)-\mathrm{Cs}] \approx 720\ \mathrm{K} \tag{3.10}$$

$$T'[(\sqrt{3}\times\sqrt{3})\mathrm{R30^\circ}-\mathrm{CO}] = 640\ \mathrm{K}\ . \tag{3.11}$$

Since the latter one is lower it would be limiting the desorption; it is in surprisingly good value of the temperature 660 K where the desorption indeed occurs in the experiments of Over *et al* (1995b), giving further reliability to our calculated values for the adsorption and mixing energies.

Next we come to study in detail the electronic structure of the co-adsorption phase, and start with the density differences in the Figure 3.90; we show both the changes induced by adsorption of either adsorbate and the interaction density. Upon the adsorption of cesium to the surface pre-covered with CO the changes around the site of the alkali itself and at the substrate are very similar to the change by adsorption of cesium to the plane surface in the Figure 3.26; the form of the change at the CO site will be discussed soon below. When the carbon monoxide is adsorbed the change is again almost identical as when adsorbing on the clean surface around the molecule, but small around the cesium and rather opposite to the change when cesium was adsorbed. These changes are carried over into the interaction density in the right-most panel in the Figure 3.90: The changes at the near vicinity of the cesium are small and opposite to the changes when cesium adsorbs on the surface alone, and the change at carbon monoxide consists of a polarisation where the charge from carbon flows to oxygen; furthermore the ruthenium atoms of the top-most layer polarise, in the same direction as when cesium adsorbs on the clean surface. Thus the carbon monoxide induces a further polarisation of the surface, although the CO could also be expected to de-screen partially the polarisation of the surface atoms caused by the alkali.

The inner polarisation due to the co-adsorbed alkali is the most significant change in the electron density and seems to contradict the simple picture, based on the Blyholder model, that the co-adsorption of cesium should increase the occupation of the $2\pi^*$ orbital of CO. As will be shown below the occupation indeed does increase, but the change is rather small, only 15 % from the occupation of the value of CO adsorbed alone on the hcp site. Compared to the CO on the on-top site the change is, however, almost 70 %. This is the weak point of the interaction density: the constituent adsorbates are forced to the sites in the co-adsorbate structure instead of the equilibrium sites of the separated phases. We continue to analyse the interaction density since it gives valuable information on the characteristics of the interaction between the alkali and CO.

In order to pin-point the origins of the details in the density changes we study in which energy regions the changes occur. Therefore in the Figure 3.91 we plot the interaction density arising from different energy regions. What surprises most in the figure is that there is hardly no net gain visible in the energy region $E_F - 4\,\mathrm{eV} < E < E_F$, where the bonding hybrids of $2\pi^*$ orbitals should be located. Rather the increase in the

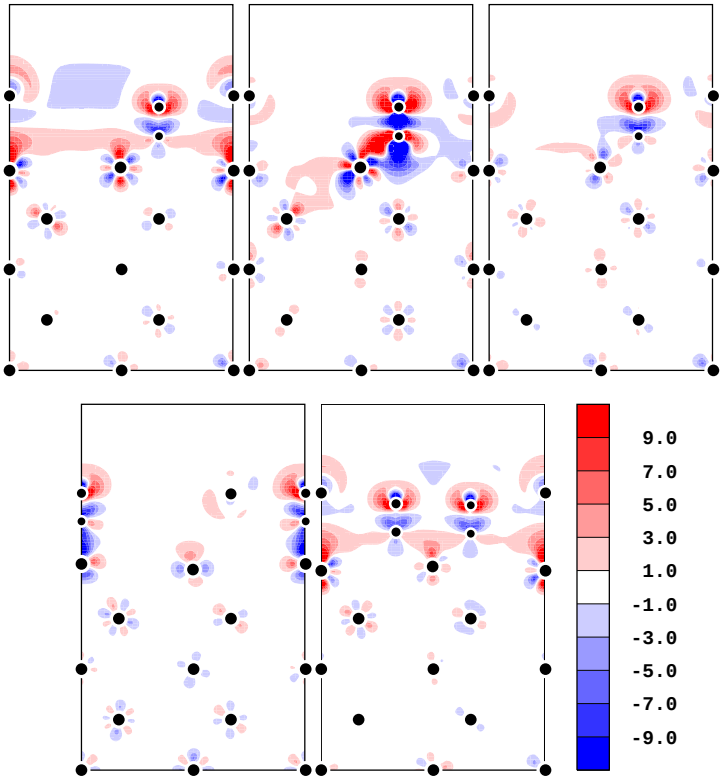

Figure 3.90: The change in the electron density obtained from our calculations upon the Cs+CO co-adsorption on Ru(0001). The upper panels from left to right: the change due to adsorption of cesium, due to carbon monoxide, and the interaction density in the Ru(0001)-(2×2)-(Cs_{ot}+CO_{hcp}) structure; the lower panels: the interaction density in the Ru(0001)-(2×2)-(Cs_{hcp}+CO_{ot} structure – left – and the change in the electron density due to the adsorption of cesium in the Ru(0001)-(2×2)-($1Cs_{ot}$+$2CO_{hcp,fcc}$) structure – right

density comes from the energy region $E_F - 20 < E < E_F - 5$ eV where the other molecular orbitals of CO are located. However the choice of the energy ranges modifies the plot somewhat, and a unique interpretation might be more involved than what is presented here.

It is instructive to compare the change in the electron density of the carbon monoxide due to the co-adsorption with an alkali metal to the change induced by an electric field only. This is shown in the Figure 3.92, and qualitatively the change is almost identical at the carbon monoxide; the nearest-neighbour ruthenium atom has a polarisation of different sign though. Unfortunately we cannot apply a field whose magnitude would be comparable in magnitude to the one arising from the alkali metal. However, already this figure is convincing enough to allow the assignment of the major electronic effect of the cesium – beyond the induced site change – to be due to the induced electric field.

The change in the electron density along the surface normal gives insight into the formation and change of surface dipoles. The Figure 3.93 shows the change in the density both averaged perpendicular to the normal of the surface and two lines intersecting the adsorption sites of cesium and one of the three other, equivalent ruthenium atoms. The average change reduces further above the cesium atom from the value of cesium-covered surface only; this might be related to why the work function initially decreases when CO is adsorbed on the surface covered with alkali as found by Weimer, Umbach and Menzel (1985) for K+CO/Ru(0001). However, the internal polarisation of CO tends to increase the surface dipole since the charge is moved from carbon towards the oxygen. The density along the line through the centre of cesium shows the same interesting fact as the density differences in the Figure 3.90 that the density increases somewhat above the cesium atom; furthermore the density is almost independent of the co-adsorbates. Along the other line, passing through the three equivalent ruthenium atoms of the surface layer, the density just above and below shows an increase due to the filled d_{z^2} orbitals, but further away from the surface there is a depletion of charge density from the long-range 6s orbital of cesium.

The work function in the co-adsorbate phase 1Cs+1CO has increased by 0.1 eV compared to the Cs-only surface, and already by 0.7 eV in the phase 1Cs+2CO. These values are rather small compared to the increase caused by CO alone on the surface, 0.6 eV in the (2×2)-1CO cell, although the density is more polarised away from the surface when co-adsorbing with cesium and thus straight-forwardly thinking the work function should increase stronger.

It is difficult to learn about the electronic structure around the cesium atom by studying the radial electron density in the Figure 3.94 since it is very similar in all the cases studied here; it's not until the density of ruthenium or co-adsorbate atoms starts to contribute that differences occur. Therefore we rather study the asymptotic density above the cesium like was done in the case of adsorption of cesium alone in the Section 3.3.1. The results of the calculations in the Figure 3.95 illustrate basically two different kind of asymptotic densities: those in (3×3)-Cs_{hcp}, (2×2)-(Cs_{ot}+CO_{hcp}) and (2×2)-($1Cs_{ot}$+$2CO_{hcp,fcc}$), and on the other hand in (2×2)-Cs_{ot} and

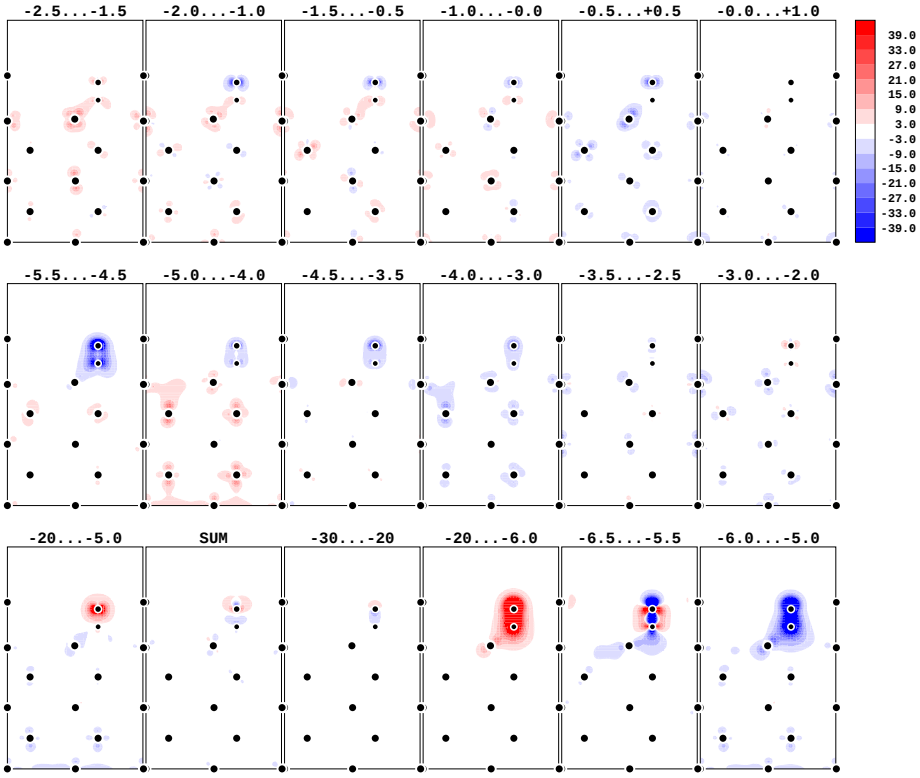

Figure 3.91: The interaction density in different energy regions obtained from our calculations for the Cs+CO/Ru co-adsorbed system; the energy regions are given in electron volts with respect to the Fermi energy. Please note that the region $E_F - 20$ eV... $E_F - 5.5$ eV has been summed in the left bottom corner as the states at the carbon monoxide switch the energy regions and thus make the comparison otherwise difficult

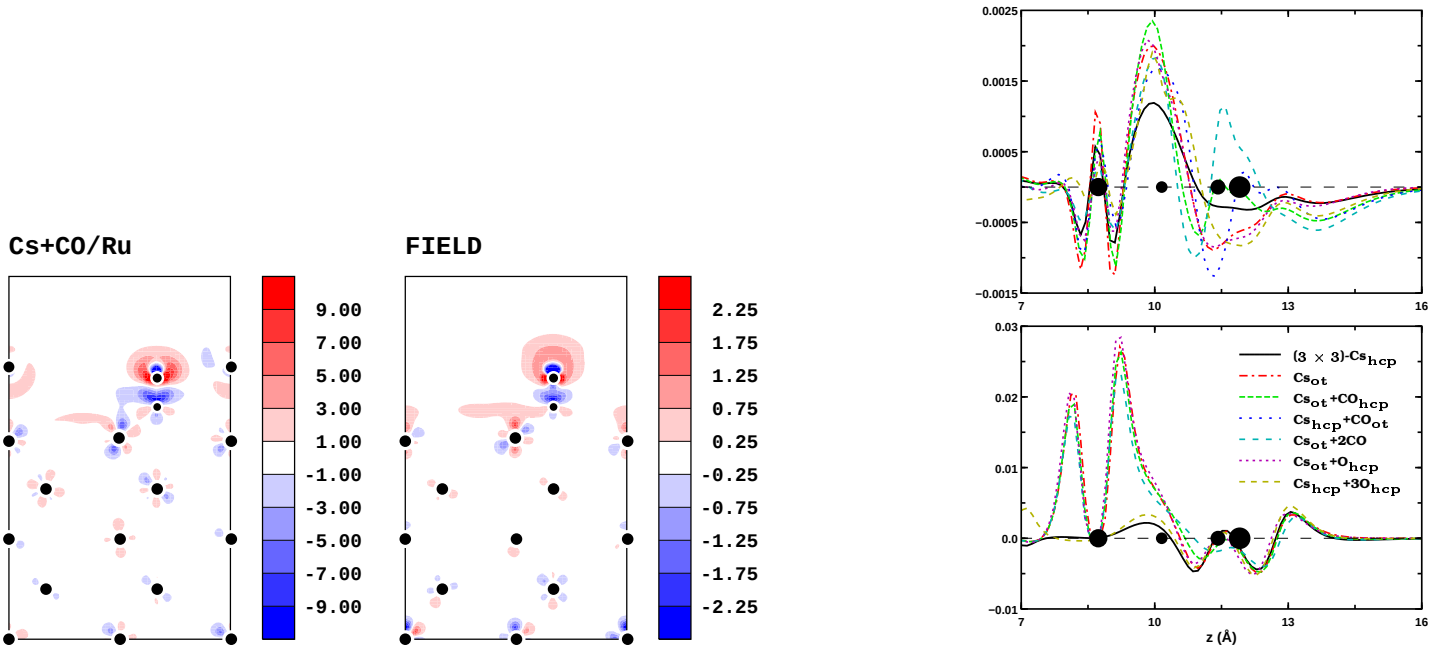

Figure 3.92: The change in the electron density obtained from our calculations for the Cs+CO/Ru co-adsorbed system; left is the interaction density and right the change in electron density due to an electric field of 0.6 eV/Å applied to CO adsorbed on the Ru(0001)

Figure 3.93: The change in the electron density averaged parallel to the surface – top panel – upon the adsorption of cesium onto the clean Ru(0001) and the surface covered with one and two carbon monoxide molecules or one and three oxygen atoms from our density functional calculations; also the changes along the surface line passing through the centre of the cesium – bottom panel – are shown. The atomic positions from the structure (2×2)-(Cs_{ot}-CO_{hcp}) are shown with filled circles of growing radii in the order carbon, oxygen, ruthenium and cesium. The positions are very similar also in the other structures; the oxygen atoms adsorb at a height close to that of carbon atom in the carbon monoxide. The unit cell is (2×2) except in the (3×3)-Cs_{hcp} structure indicated

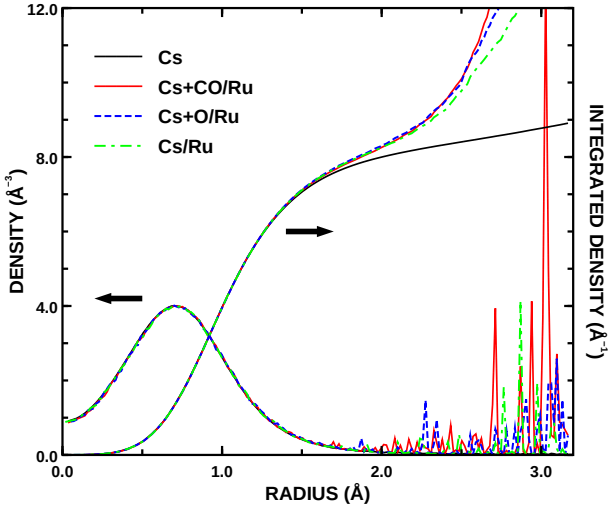

Figure 3.94: The density around the cesium atom in different structures: Free atom, Ru (0001)-(2 × 2)-(Cs_{ot}-CO_{hcp}), Ru (0001)-(2 × 2)-(Cs_{ot}-O_{hcp}) and Ru (0001)-(2 × 2)-Cs_{ot} and the integrated density; the scatter at large distances is due to the entrance of the density from the other atoms and is different in different directions. The numerical scale on both vertical axis is the same

(2 × 2)-(Cs_{ot}+O_{hcp}). That the CO seems to decrease the density from the Cs_{6s} orbital more than the oxygen atoms, even when the oxygen coverage is 3/4, is consistent with the results of meta-stable de-excitation spectroscopy measurements by Over *et al* (Fichtner-Endruschat *et al*, 1998; Herbert Over, personal communication, 1998). This difference between oxygen and carbon monoxide can also be seen in the change in the electron density around the Fermi energy in the Figure 3.96: Whereas the oxygen causes an increase above most of the surface the carbon monoxide causes a decrease. Thus from the calculated density changes the signal in the meta-stable de-excitation spectra from the cesium should be enhanced if oxygen is co-adsorbed and reduced if carbon monoxide is dosed onto the surface, exactly like seen in the experiments.

The densities of states projected onto the atomic states of the carbon atom of the carbon monoxide, onto the molecular orbitals of the carbon monoxide and onto the atomic 5*p* and 6*s* states of the cesium atom are shown in the Figures 3.97, 3.98 and 3.99, respectively, and the integrated densities of states are in the Tables 3.25 and 3.26. The energy-resolved curves can more conveniently be used to study the position of peaks and the integrated values the amount of different orbital characters.

The most notable qualitative feature in the states localised at the carbon monoxide – mainly the 3σ and the energy difference between the 5σ and 1π – is that they are almost insensitive to co-adsorbates and thus the only significant factor determining the position of these peaks is the adsorption site of the carbon monoxide; however the structure (2 × 2)-(Cs_{hcp}+CO_{ot}) forms an exception. The position of the 4σ level is not affected by the co-adsorbed oxygen, but the cesium causes a shift to energy close to that found at the hcp site, where the cesium does not change it. This contradicts the conclusion derived from the experimental results by Strisland *et al* (1998) who stated that the position of the peaks would be determined by the adsorption site only; however they could not be aware of the peak positions in the structure Cs_{hcp}+CO_{ot} since it is only metastable. For the other peaks their reasoning works. At the hcp site the Kohn-Sham eigenvalue of the 3σ state is at lower and that of 4σ at deeper binding energies, and the eigenvalue of the 5σ orbital becomes lower than of the 1π state, whereas at the on-top site the latter two peaks overlap almost exactly. Also the occupation of the $2\pi^*$ orbital is systematically larger when the CO is adsorbed at the hcp site, as well as the $4\sigma/5\sigma$ mixing. The "charge" at the CO molecule, obtained by summing up the integrals of the projections onto the molecular orbitals, shows a larger value at the hcp site, and as expected at the on-top site the charge decreases – along with an increase of the $4\sigma/5\sigma$ mixing – when the electro-negativity of the co-adsorbate increases. This is mainly due to the increased occupation of the $2\pi^*$ level; such a trend is in accord with the Blyholder model, although the change of the 5σ orbital is minimal. We warn, however, that the "charge" and orbital overlap should be regarded with some caution as the overlap in the adsorbed structure can also include some of the states of the substrate because the orthogonality between the substrate and molecular states does not hold when the hybrids have been formed.

The density of states projected at the atomic orbitals of the cesium atom reveals that the position of the semi-core 5*s* and 5*p* states shifts first upon its adsorption and further when co-adsorbates are added; the carbon monoxide increases the Kohn-Sham eigenvalues more than oxygen, and the more co-adsorbates the larger the increase. As was also seen in the Section 3.3.1 these eigenvalues are almost independent of the adsorption site, which is easily understandable due to the large distance of the cesium from the surface and the subsequent small corrugation and shallow site registry. The amount of 6*s* component of the states slightly reduces upon co-adsorption, and simultaneously the *d* states become increasingly occupied, especially the d_{z^2}. In the phases with the cesium co-adsorbed with carbon monoxide the 5*s* slightly hybridises with the energetically close-lying 3σ forming a bonding and an anti-bonding hybrids; however the amount of hybridisation is small as expected at such deep binding energies.

The structure with the two carbon monoxide molecules in the unit cell, Ru (0001)-(2 × 2)-(1Cs_{ot}+2$CO_{hcp,fcc}$),

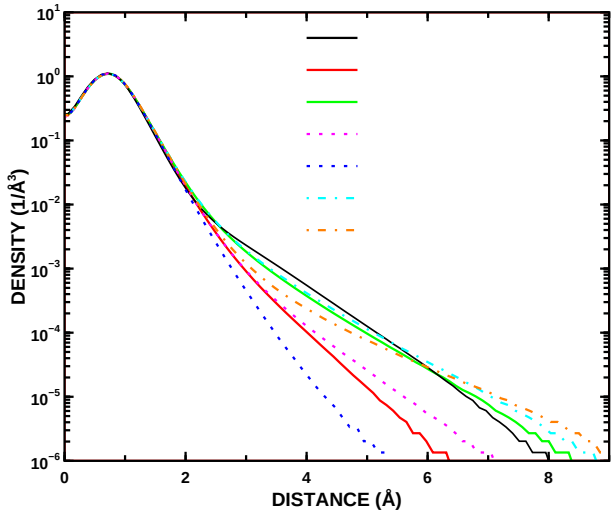

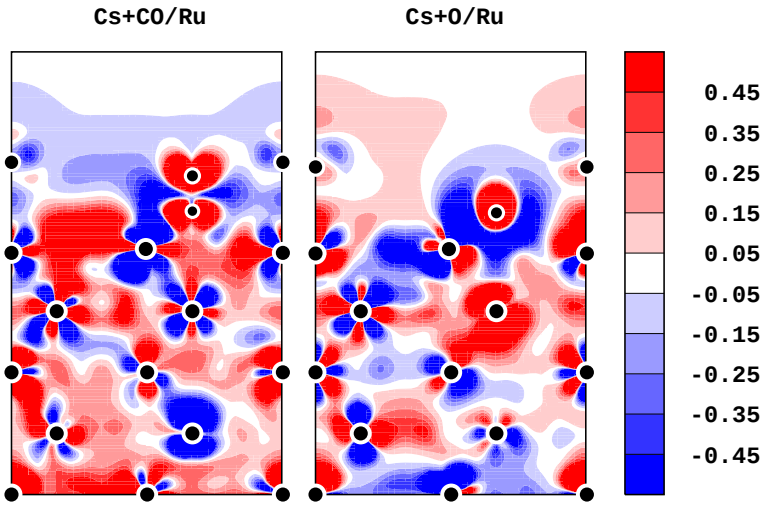

Figure 3.95: The asymptotic density above the cesium atom in different structures on the Ru(0001) surface as obtained from our calculations. The black line is the asymptotic density of a neutral cesium atom; the red, green, violet, blue, lila and orange lines are the densities in the (3 × 3)-Cs_{hcp}, (2 × 2)-Cs_{ot}, (2 × 2)-(Cs_{ot}+CO_{hcp}), (2 × 2)-(1Cs_{ot}+2$CO_{hcp,fcc}$), (2 × 2)-(Cs_{ot}+O_{hcp}) and (2 × 2)-(1Cs_{hcp}+3O_{hcp}) structures, respectively. Please notice that the structures with co-adsorbed CO are shown with short-dashed and the structures with co-adsorbed O with dot-dashed lines

Figure 3.96: The induced density ±1/2 eV around the Fermi energy due to the adsorption of carbon monoxide into the Ru(0001)-(2 × 2)-(Cs_{ot}-CO_{hcp}) – left – and oxygen into the Ru(0001)-(2 × 2)-(Cs_{ot}-O_{hcp}) – right – structure

Table 3.25: The integrals of the densities of states projected on the atomic orbitals. Ru_1 refers to the unique and Ru_2 to the three equivalent ruthenium atoms in the surface layer

Structure	Atom	s	$p_{x,y}$	p_z	d_{z^2}	$d_{xz,yz}$	$d_{x^2-y^2,xy}$
Ru(0001)-(2 × 2)-CO_{ot}	Ru_1	0.25	0.06	0.11	0.88	1.20	1.07
	Ru_2	0.24	0.06	0.04	1.06	1.20	1.07
	C	0.29	0.15	0.27			
	O	0.79	0.57	0.62			
Ru(0001)-(2 × 2)-CO_{hcp}	Ru_1	0.24	0.06	0.04	1.04	1.13	1.07
	Ru_2	0.24	0.07	0.05	1.09	1.10	1.07
	C	0.28	0.16	0.24			
	O	0.79	0.57	0.60			
Ru(0001)-(2 × 2)-(CO_{ot}+O_{hcp})	Ru_1	0.24	0.06	0.11	0.85	1.20	1.09
	Ru_2	0.24	0.07	0.05	1.10	1.08	1.07
	C	0.30	0.14	0.27			
	O	0.79	0.57	0.62			
	O	0.79	0.56	0.56			
Ru(0001)-(2 × 2)-(CO_{ot}+2$O_{hcp,fcc}$)	Ru_1	0.24	0.06	0.10	0.81	1.22	1.10
	Ru_2	0.23	0.07	0.07	1.10	1.05	1.08
	C	0.30	0.14	0.28			
	O	0.79	0.56	0.63			
	O	0.80	0.55	0.58			
	O	0.80	0.55	0.56			
Ru(0001)-(2 × 2)-Cs_{ot}	Ru_1	0.25	0.06	0.04	1.10	1.11	1.06
	Ru_2	0.24	0.06	0.04	1.09	1.10	1.06
	Cs	0.20	1.84	1.83	0.04	0.03	0.01
Ru(0001)-(2 × 2)-(Cs_{hcp}+CO_{ot})	Ru_1	0.25	0.07	0.11	0.93	1.14	1.10
	Ru_2	0.24	0.06	0.04	1.11	1.10	1.06
	Cs	0.16	1.85	1.84	0.04	0.02	0.01
	C	0.29	0.15	0.25			
	O	0.78	0.59	0.58			
Ru(0001)-(2 × 2)-(Cs_{ot}+CO_{hcp})	Ru_1	0.25	0.06	0.04	1.10	1.11	1.06
	Ru_2	0.24	0.07	0.05	1.12	1.08	1.07
	Cs	0.16	1.85	1.83	0.04	0.02	0.01
	C	0.27	0.17	0.22			
	O	0.78	0.60	0.56			
Ru(0001)-(2 × 2)-(Cs_{ot}+2$CO_{hcp,fcc}$)	Ru_1	0.25	0.07	0.04	1.11	1.11	1.06
	Ru_2	0.23	0.07	0.07	1.19	1.07	1.06
	Cs	0.15	1.86	1.84	0.03	0.01	0.01
	C_h	0.27	0.16	0.23			
	C_f	0.28	0.16	0.23			
	O_h	0.78	0.59	0.57			
	O_f	0.78	0.59	0.58			
Ru(0001)-(2 × 2)-(Cs_{ot}+O_{hcp})	Ru_1	0.25	0.07	0.04	1.11	1.10	1.08
	Ru_2	0.23	0.07	0.05	1.12	1.06	1.03
	Cs	0.18	1.85	1.83	0.05	0.03	0.01
	O	0.79	0.56	0.57			
Ru(0001)-(2 × 2)-(1Cs_{hcp}+3O_{hcp})	Ru_2	0.22	0.07	0.07	1.15	1.02	1.10
	Ru_1	0.22	0.08	0.09	1.22	0.94	1.12
	Cs	0.16	1.85	1.84	0.05	0.02	0.01
	O	0.79	0.56	0.56			

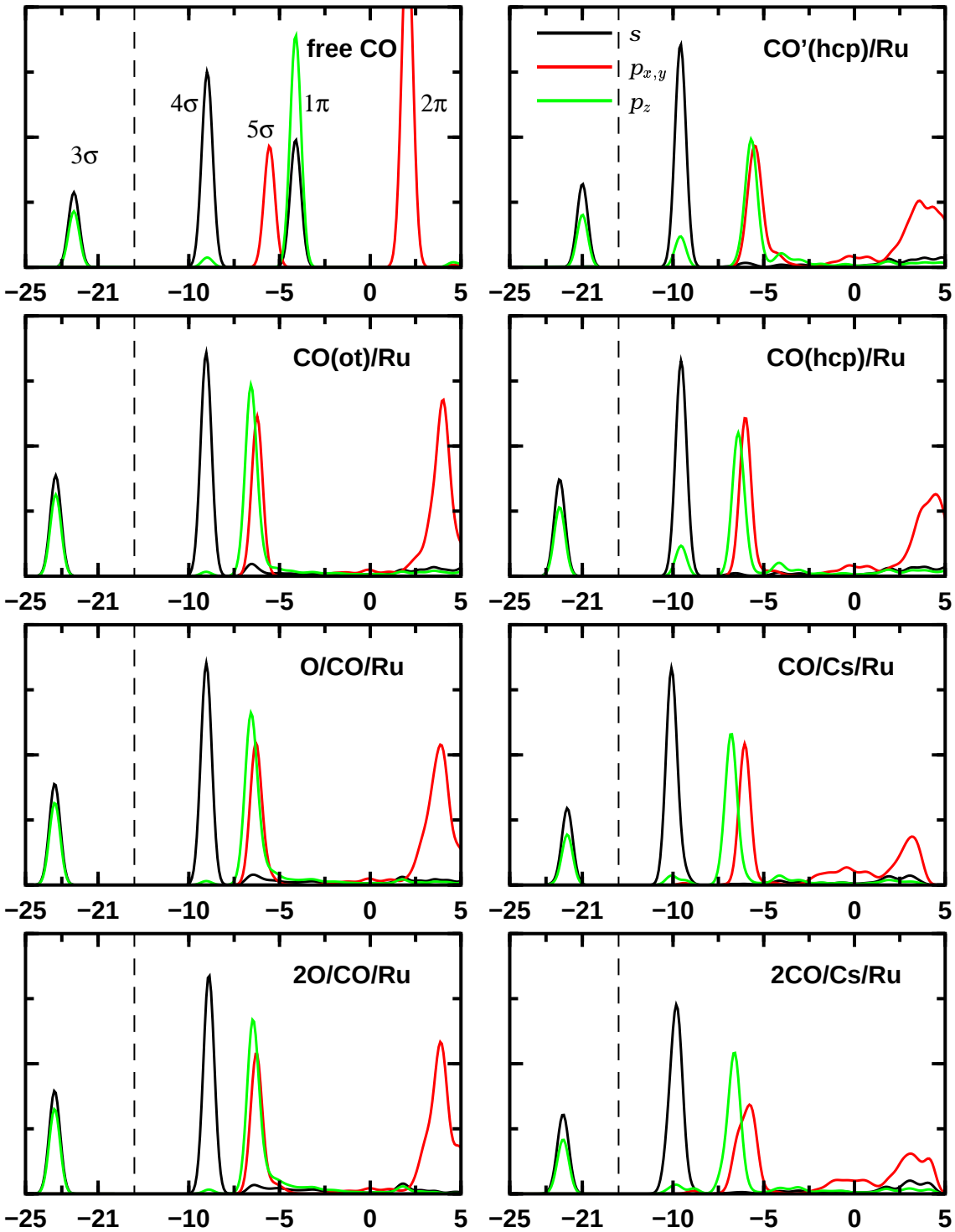

Figure 3.97: The density of states projected on the atomic orbitals of the carbon atom in different systems containing the carbon monoxide. "CO′(hcp)/Ru" refers to a CO molecule at hcp site with the geometry of the structure Ru-(2×2)-(Cs_{ot}+CO_{hcp}). The normalisation of the zero of energy is arbitrary in the case of the free molecule. The colours are s – black –, $p_{x,y}$ – red – and p_z – green

Table 3.26: The occupation factors of different molecular levels of CO deduced from the projection of the Kohn-Sham states of the adsorption system on the molecular orbitals, and the mixing of 4σ and 5σ defined as the amount of molecular 5σ character of the 4σ in the adsorption system and vise versa

Structure	Orbital 3σ	4σ	5σ	6σ	1π	$2\pi^*$	$4\sigma/5\sigma$ mixing (%)	Charge at CO (e^-)
Ru (0001)-(2 × 2)-(Cs_{hcp}+CO_{ot})	0.998	0.988	0.883	0.062	0.969	0.350	5	−1.14
Ru (0001)-(2 × 2)-CO_{ot}	0.999	0.995	0.898	0.099	0.984	0.241	12	−0.88
Ru (0001)-(2 × 2)-(CO_{ot}+O_{hcp})	0.999	0.996	0.901	0.059	0.984	0.225	13	−0.75
Ru (0001)-(2 × 2)-(Cs_{ot}+CO_{hcp})	0.998	0.985	0.897	0.090	0.961	0.423	18	−1.48
Ru (0001)-(2 × 2)-CO_{hcp}	0.999	0.995	0.905	0.091	0.977	0.349	34	−1.28

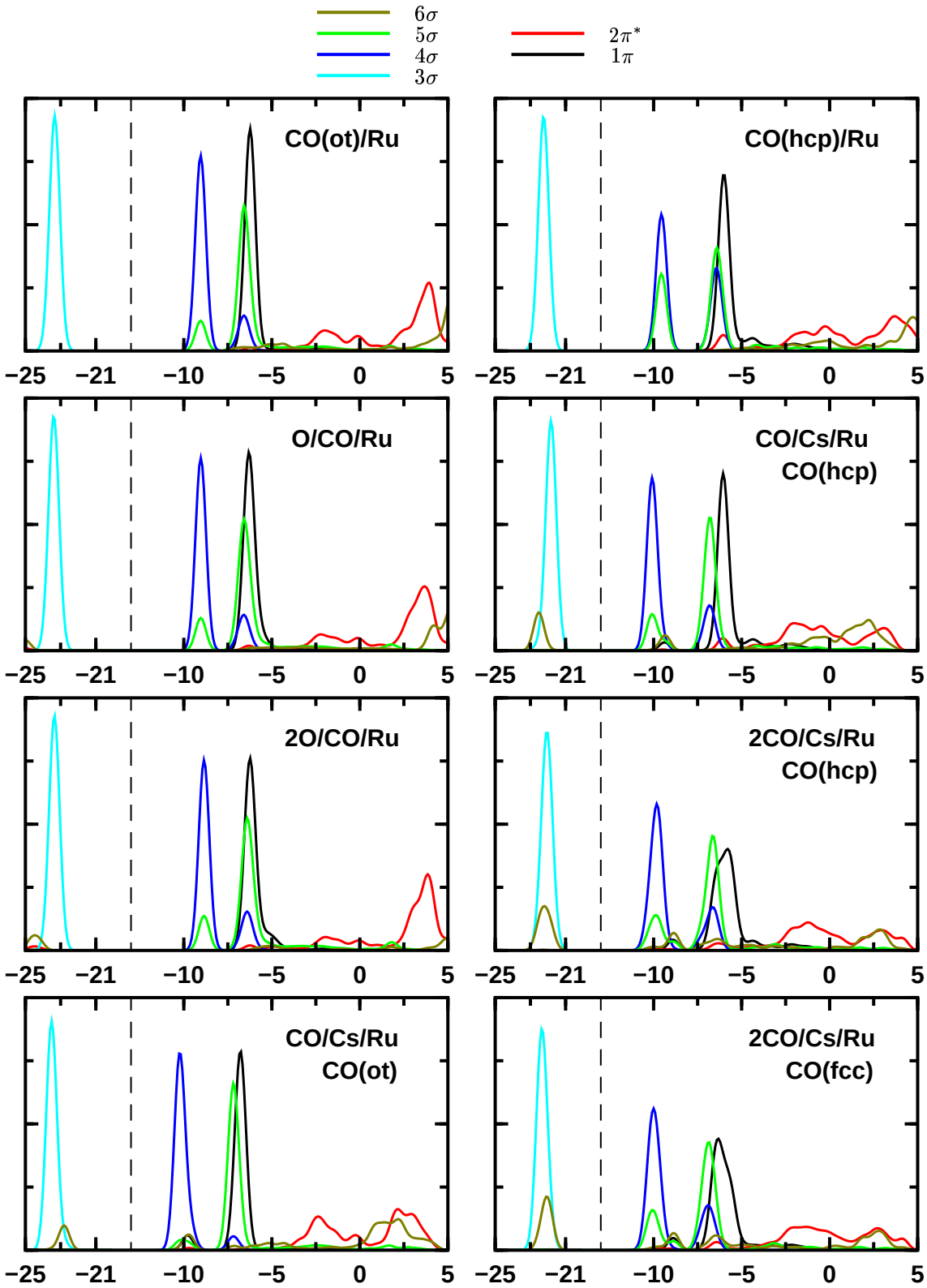

Figure 3.98: The density of states projected on the molecular orbitals of the carbon monoxide in different systems containing the molecule. The lines are lila – 3σ –, blue – 4σ –, green – 5σ –, brown – 6σ –, black – 1π – and red – 2π. The contributions of the π orbitals are symmetrised and halved

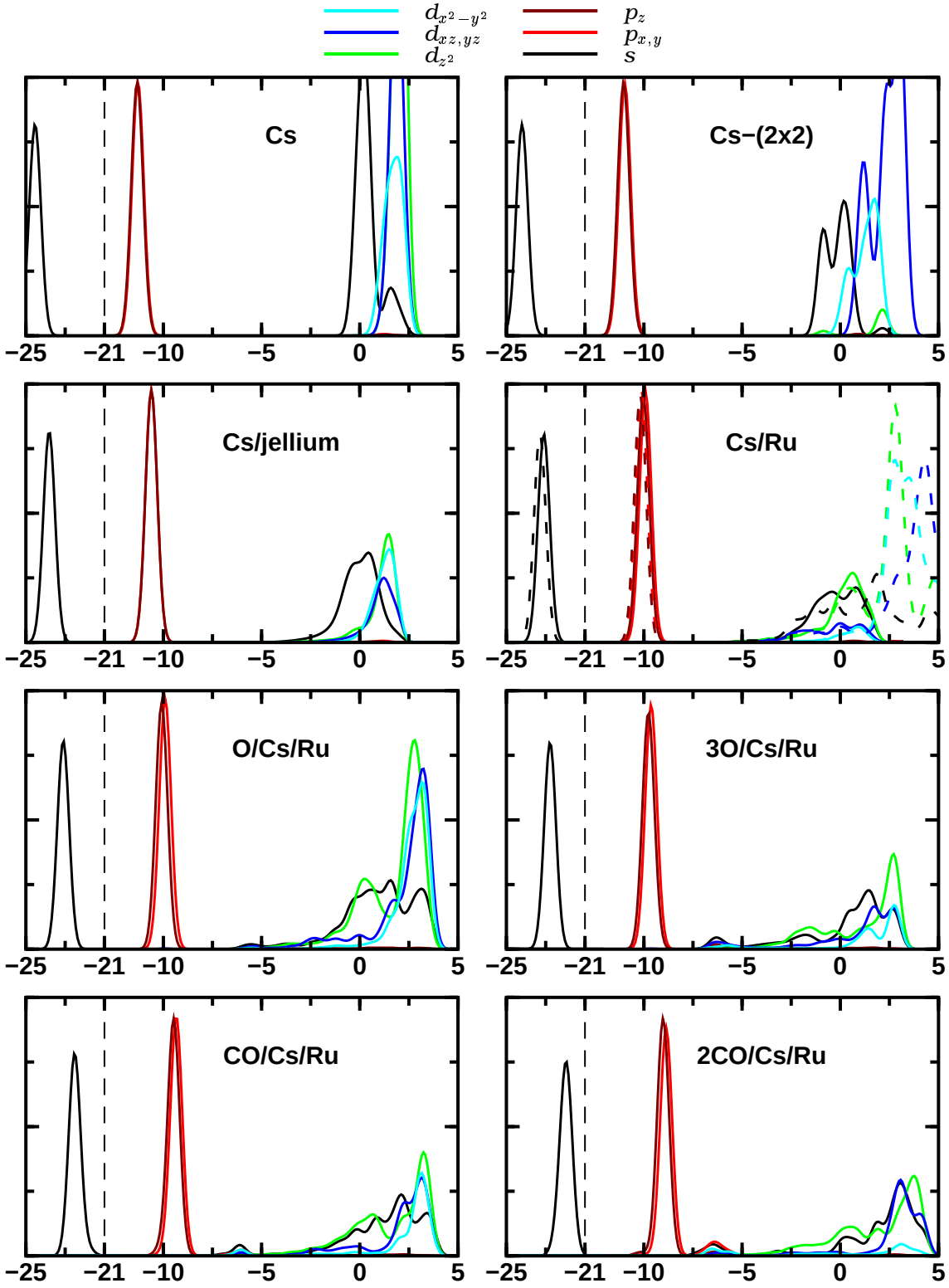

Figure 3.99: The density of states projected on the atomic orbitals of the cesium atom in different systems containing the cesium. The system "Cs" is a free atom in the (3 × 3) cell, "Cs-(2 × 2)" in the (2 × 2) cell. The system in "Cs/Ru" with the dashed lines is the cesium on ruthenium at the on-top site but in the geometry of the structure Ru-(2×2)-(Cs_{ot}+CO_{hcp}) but without the carbon monoxide; the system with solid line has been relaxed. The lines are black – s –, dark red – $p_{x,y}$ –, light red – p_z –, green – d_{z^2} –, blue – $d_{xz,yz}$ – and lila – $d_{x^2-y^2}$

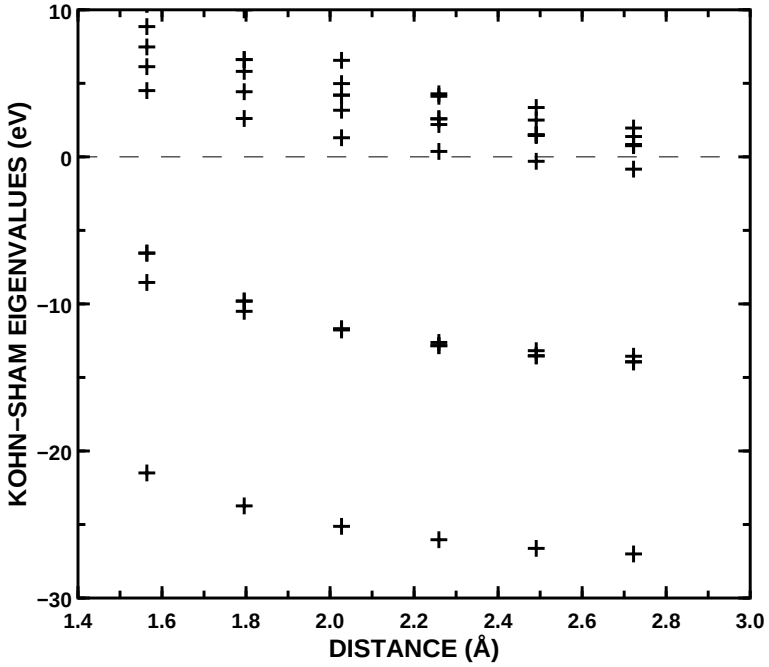

Figure 3.100: The Kohn-Sham eigen-values of a cesium atom in a hexagonal parallelepiped equivalent to the (2×2) cell used in the slab calculations. The free space between the atoms was reduced by applying a highly repulsive potential with the hexagonal shape. The zero of energy is set to the electro-static potential far away from the atom

behaves very similarly to the case of one molecule, yet the binding energy of the second molecule is naturally lower than of the first one but still more bound than in the adsorbed phase of the carbon monoxide alone; this demonstrates one cesium can easily bind two CO molecules as seen in the experiments. The work function raises further from the value of the alkali-covered surface, and the bond lengths d_{C-O} and d_{C-Ru} increase towards the value of the separated phase as the effect from the cesium has to divided up to the two molecules.

We shortly studied also the the bonding of the inverted molecule, *i. e.* with the oxygen towards to the surface, both with and without the co-adsorbed cesium. However, the molecule desorbed without even a local minimum from both the on-top and hcp sites from the Ru(0001)-(2×2)-OC geometry and the co-adsorbed Ru(0001)-(2×2)-(Cs_{ot}+OC_{hcp}) structure. Thus the possibility for a state with the rotated molecule as an intermediate in the oxidation reaction $^1/_2\,O_2$+CO→CO_2

3.4.3 Co-adsorption of oxygen and carbon monoxide

The co-adsorption of oxygen and carbon monoxide has not only interest because of the oxidation reaction but also since the real catalysts always contain oxygen. The oxidation rate has been shown to be enhanced by the sub-surface oxygen, first using catalysts in high pressures – please see *e. g.* the references in Peden (1992) or Rodriguez and Goodman (1991) – and later using quantitative single-crystal measurements in the ultra-high vacuum (Böttcher *et al*, 1997). We performed calculations only in the Ru(0001)-(2×2)-(CO_{ot}+O_{hcp}) co-adsorption structure shown in the Figure 3.101, and the Ru(0001)-(2×2)-($1CO_{ot}$+$2O_{hcp}$) – measured by Narloch, Held and Menzel (1994); the Ru(0001)-(2×2)-(2CO+1O) (Schiffer, Jakob & Menzel, 1997) has been realised in experiments but not calculated here. The relatively small repulsion between the adsorbed oxygen and carbon monoxide is possible since the change in the electro-static potential at the site of the carbon monoxide caused by the pre-adsorbed oxygen is weak. The interaction or mixing energy of the two is very small, 0.18 eV from our calculations, which can be understood since both oxygen and carbon monoxide are electro-negative adsorbates as can be deduced from the change in the work function of the separated (2×2) phases $\Delta\phi_{O/Ru} = +0.36$ eV and $\Delta\phi_{CO/Ru} = +0.61$ eV. The change in the co-adsorption phase 1CO+1O is +0.83 eV and in the 1CO+2O +1.37 eV, slightly smaller than the sum of the changes from the separated phases, which is probably since the ruthenium atoms cannot provide the charge and polarisation for both, and the electro-static repulsion might force the adsorbates to reduce their polarisation somewhat.

The occupation of the molecular levels in the co-adsorption phase, calculated as the projection of the co-adsorption states onto the orbitals of the free CO molecular, in the Table 3.27 support the very weak interaction between the co-adsorbates since the change from the case of only CO/Ru is very small, only a fraction of the total occupations. Furthermore the large energy separation of the 3σ level of the CO and the $2s$ state of the oxygen, together with a strong localisation of them, makes a hybridisation between the two very unlikely. This is confirmed in the Figure 3.102, which shows the orbital densities from the 3σ, O_{2p} and mixed $4\sigma/5\sigma$ states: indeed no mixing between the states from the co-adsorbates is seen. This is different for the co-adsorbed Cs and CO as we have seen above.

In their structural analysis of the Ru(0001)-(2×2)-(CO_{ot}+O_{hcp}) phase Narloch, Held and Menzel (1995) found

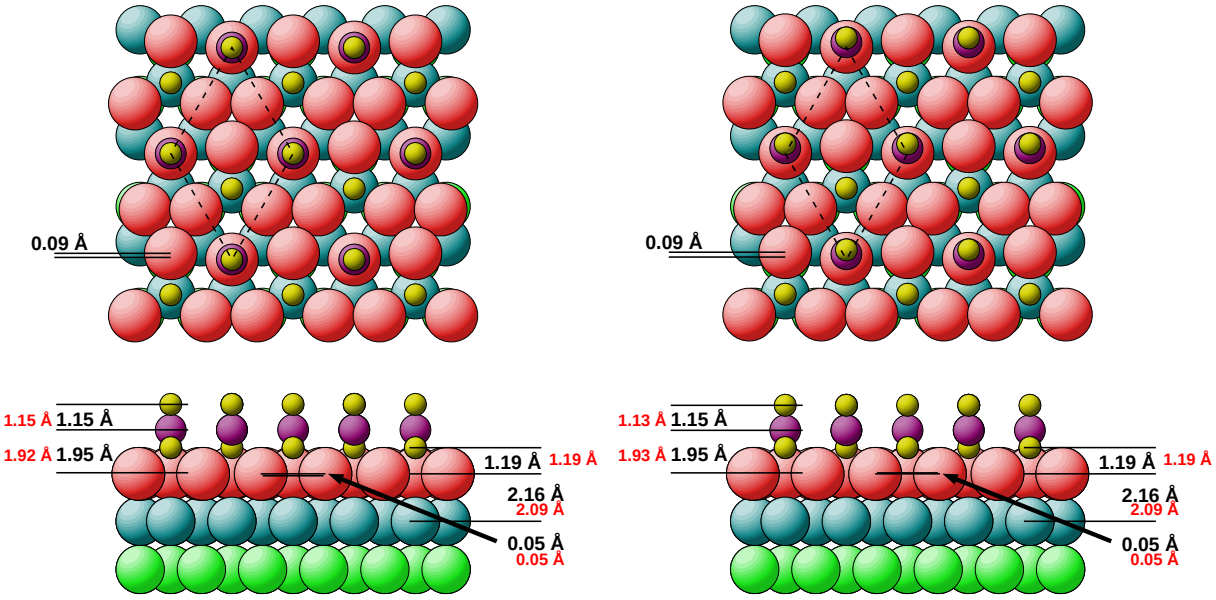

Figure 3.101: The geometry of the Ru (0001)-(2 × 2)-(CO_{ot}+O_{hcp}) from the density functional calculations; the experimental geometry is from Narloch, Held and Menzel (1995). The left panel gives the geometry without the static tilt *i. e.* with the full C_{3v} symmetry group and the right when the tilt is allowed

Table 3.27: The occupation factors of different levels deduced from the projection of the Kohn-Sham states of the adsorption system on the molecular orbitals, and the mixing of 4σ and 5σ defined as the amount of molecular 5σ character of the 4σ in the adsorption system and vise versa

Structure	Orbital						$4\sigma/5\sigma$ mixing (%)
	3σ	4σ	5σ	6σ	1π	$2\pi^*$	
Ru (0001)-(2 × 2)-CO_{ot}	1.000	0.998	0.922	0.134	0.998	0.291	17
Ru (0001)-(2 × 2)-(CO_{ot}+O_{hcp})	1.000	0.999	0.923	0.150	0.998	0.279	14

a static tilt of the CO molecule from the surface normal; this tilt breaks the three-fold symmetry, and only a mirror-plane is preserved. We tried to reproduce their result, a tilt of 12.6°, and we started from somewhat a larger tilt angle in order to diagnose whether the tilt would reduce to the experimental one. However, the final geometry, where the forces on the atoms were zeroed, in the Figure 3.103 shows a smaller tilt, 7.9°, but the main problem is the energetics: most likely due to the discretisation errors, discussed in the Section A.3, the energy at the up-right geometry is some 20 meV lower than in the tilted one, yet the atoms of the CO molecule did not relax to this geometry when let to move freely. Thus either there is a meta-stable minimum at the tilt angle 7.9° in our calculations or it is due to the discretisation errors. In any case the potential energy surface for a tilt is rather flat; more studies would be necessary to clear this issue.

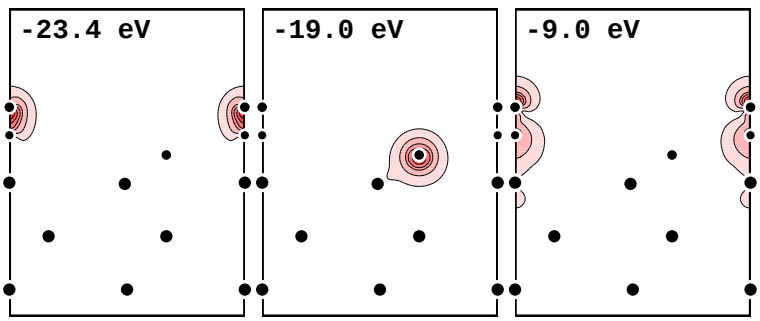

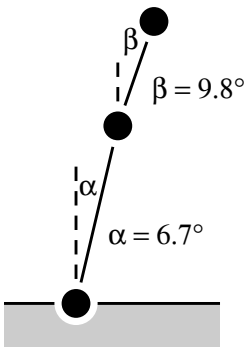

Figure 3.102: The orbital density of the deepest Kohn-Sham states in the structure Ru (0001)-(2 × 2)-(CO_{ot}+O_{hcp})

Figure 3.103: The final tilted geometry of the structure Ru (0001)-(2×2)-(CO_{ot}+O_{hcp}) when the lateral coordinates were allowed to relax

3.5 Discussion

Here we shall collect and analyse the main results achieved in the previous Sections and view them from a wider perspective. Especially the trends upon changes in the coverage and co-adsorption will be paid special attention for and whenever possible the accuracy of the calculations is measured against the experiments. References to literature and our unpublished work will be made whenever appropriate.

3.5.1 Bulk ruthenium and clean (0001) surface

Ruthenium with its location in the platinium group metals in the Periodic Table has the Fermi level cutting through the 4*d* band and thus an open *d* shell which easily hybridises with more electro-positive or -negative species. The (0001) surface, with the highest atomic density of the hexagonal close packed lattice, is very similar to the (111) surface of the face centred crystal and the difference does not affect the electronic structure appreciably (Ari P Seitsonen, unpublished results). At the surface layer the density of states gets narrower especially for the *d* states due to the reduced coordination and thus a smaller dispersion; the centre of the band has to raise slightly energetically in order to maintain the charge neutrality, and the most significant different difference in the electronic states to the bulk layers is the last peak of the d_{z^2} states which has lowered itself partially to the Fermi level already. It is these states which are emptied upon the adsorption of *e.g.* nitrogen to the surface (Schwegmann *et al*, 1997). The outer-most layer of the clean surface is found to relax slightly inwards, in agreement with the experiments and the earlier calculations, as response to the reduced coordination of the atoms at the surface layer.

3.5.2 Adsorption of single species

The present studies bring a large amount of previously unexplored details of the adsorption of alkali metals into daylight, although we haven't yet even fully understood all of them. Our main concern in these calculations was the use of pseudo potentials to describe the cesium atom since the outer-most 6*s* state might change considerably during the adsorption also in the core region and would thus invalidate the frozen-core approximation. However include the semi-core states 5*s* and 5*p* into the active valence states of the pseudo potential we have achieved, with the exception of the slightly erroneous binding energies, a level of accuracy in comparison to the experiments which has been qualitatively found in the results for the generalised gradient approximation, namely the geometries are generally in agreement with the experiments beyond the over-estimation of the lattice constant, and the magnitude of the change in the work function is underestimated but the qualitative trend is accurately reproduced. Thus we are confident that our results are quantitatively correct within the limits of the generalised gradient approximation and we can access also new information about the applicability of the generalised gradient approximation for the configurations at hand and catalytic systems in general.

The geometries of cesium on the Ru(0001) agree reasonably with the experimental values from the low energy energy diffractive measurements (Over *et al*, 1992b): The cesium-ruthenium layer heights are too small and the buckling is too large; yet the change when going from the $(\sqrt{3} \times \sqrt{3})$R30° to the (2×2) cell is more accurately tracked. It would also be interesting to see the whole effect of a finite temperature on the geometries of our structures since the potential energy surface for the lateral and vibrational movement of the cesium is very shallow. The adsorbed cesium pushes the atoms laterally away from it at the hcp site and vertically on the on-top site – vice versa the changes are negligible – and the magnitude of these changes decreases towards the lower coverages which at first sounds counter-intuitive as at low coverages the adsorbates are further away and thus there would be more atoms of the substrate in between to adjust for the local changes in the geometry around the adsorbates. However the larger changes at the high coverages might be due to a need to electronically screen the remaining dipole-dipole repulsion between the cesium atoms (Over *et al*, 1995a). The distance between the first and second ruthenium layer remains practically constant throughout the range of coverages studied here, but remarkably the height of the cesium from the outer-most substrate layer increases towards the lower coverages when rather a smaller distance would be expected since according to the the dipole moment, and thus also the "ionicity", of the cesium increases and the ionic radius of a cesium atoms is smaller than the covalent one. For the time being this trend remains mysterious and awaits for a confirmation from the experiments; yet an equivalent behaviour was found from the low energy electron diffraction measurements for several alkali metals on the Ag(111) surface (Kaukasoina *et al*, 1997), potassium on the Ni(100) (Wedler *et al*, 1993) and a similar effect was suggested (Schuster, Eng and Robinson, 1995) for Cs on the Ag(110) surface. The difficulty in reaching these occurrences is due to the low coverages and temperatures, in order to avoid the easy diffusion of the alkali metal atoms, required and then the surface becomes quickly polluted by the residual gases. We further note here that an increase in the distance of the cesium from the surface atoms could explain the unexpected down-ward shift in the Cs-Ru frequency when going to lower coverages (He & Jacobi, 1996).

The main effect caused by the cesium on the electronic structure of the ruthenium substrate is the polarisation and filling of the d_{z^2} orbitals *i.e.* exactly those which were largely abundant just above the Fermi energy at the clean surface. Exactly the same result can be achieved by instead of adsorbing the cesium an electric field is applied parallel to the normal of the surface. In the (2×2)-Cs structure we find the magnitude of the vertical component of the electric field at the other high-symmetry sites to be about 1.7 eV/Å and still 1 eV/Å at the site furthest away from the cesium at the coverage of 1/9. The change in the electronic charge density around the cesium is dominated by the counter-polarisation of the 5*s* and 5*p* states against the change in the 6*s* orbitals, and it remains to be seen from all-electron calculations to which extent this effect would be an error due to the use of pseudo potentials. Furthermore the change in the density on the jellium is similar as on the Ru(0001)

surface; the adsorption energy is 0.91 eV, half of the adsorption energy on the Ru(0001) surface which can be regarded to be large. The fcc(111) surfaces of rhodium and platinium seem to behave qualitatively in the same manner as the Ru(0001) upon the adsorption of alkalis to them.

In the case of the carbon monoxide we studied coverages from 1/4 to 1 mono-layer, and the adsorption site was always the on-top position although it is known experimentally that at the coverages above 1/3 up to the maximum coverage achieved $\simeq 2/3$ the molecules adsorb also at different sites, most likely in compressed over-layers, and the only ordered structures found up to date are the $(\sqrt{3} \times \sqrt{3})$R30°, $(2\sqrt{3} \times 2\sqrt{3})$R30° and $(5\sqrt{3} \times 5\sqrt{3})$R30°; however our results act as a model for the adsorbate-adsorbate interactions. We see the internal carbon-oxygen bond length decreasing towards the values of the free molecule and simultaneously the distance from the nearest-neighbour ruthenium increasing; the change in the work function is similar, although somewhat larger, than in the experiments. The binding energy is attractive at the coverage of 1/3, in agreement with the experiments, where island formation to the $(\sqrt{3} \times \sqrt{3})$R30° is found at lower coverages.

Electronically we find the adsorption mechanism to support the Blyholder model, where the main changes upon a bonding to the surface is via the states 5σ and $2\pi^*$ as seen from the Figure 3.62. Yet quantitatively the mechanism is closer to the one proposed by Nilsson *et al* (1997) the 4σ and 1π taking part to the bonding as well; this effect was already seen in the calculations of Aizawa and Tsuneyuki (1998) but not discussed any further. However we find one more state in addition to the mixed 4σ and 5σ states; please see the Kohn-Sham state at -7.50 eV in the Figure 3.61. Its magnitude in the densities of states remain small though, or is inherent in the eigenvalues caused by the 5σ state. The 4σ forms a strong covalent bond with a *d* state of the substrate. At the Fermi energy the adsorption of the carbon monoxide causes a reduction in the density of states similar to the atomic nitrogen (Schwegmann *et al*, 1997) and opposite to the case of the electro-positive cesium as seen above.

The adsorption at different sites has a definitive consequence on the energetic location of the molecular states of the carbon monoxide agreeing with the conclusions derived by Strisland *et al* (1998) for K+CO/Rh(111); the very small energy difference between the on-top and hcp sites might be a short-coming of the generalised gradient approximation since in the cases of the Pt(111) and Cu(111) the three-fold hollow site is incorrectly to be the stable adsorption site and also at the Rh(111) the corrugation of the potential energy surface is obtained as very small. On at the Pd(111) and Ir(111) the energy difference came out as appreciable; at the former the co-adsorption experiments (Conrad, Ertl & Küppers, 1978; Oed *et al*, 1988) with oxygen can indeed be interpreted as proving a larger corrugation with a preference for the fcc site as discussed by Over (1998).

We have found the N_2 to behave much more similarly to the carbon monoxide than what was deduced by de Paola *et al* (1987); the same qualitative difference is present also upon the co-adsorption with cesium (Ari P Seitsonen, unpublished results). We have no explanation for the discrepancy at the time being; yet the electronic states behave beautifully like seen in the experiments by Nilsson *et al* (1997) for N_2/Cu(100).

The adsorption of the atomic oxygen onto the Ru(0001) proceeds similarly to the nitrogen (Schwegmann *et al*, 1997) with the exceptions mentioned earlier. However the sulphur, despite the iso-electronic valence with the oxygen, yields a decrease in the work function at high coverages relative to the clean surface (Ari P Seitsonen, unpublished results). The local density approximation gives similar but slightly lower changes in the work function as the generalised gradient approximation in the case of the oxygen; a very similar difference is found also for oxygen on Ru$(10\bar{1}0)$ (Schwegmann *et al*, 1998; Ari P Seitsonen, unpublished results). We notice that in both cases the changes obtained from the local density approximation are very close to the experimental values and since also the values of the clean surfaces are accurate we conclude that in these cases the local density approximation can be used in quantitative comparisons with the experiments and has thus also predictive power. On the contrary the values from the generalised gradient approximation produces too low a work function for the clean surface, by 0.4 eV, and too large changes in the case of cesium, carbon monoxide and oxygen on the Ru(0001) based on the present work, and the over-estimations vary being respectively about 0.6, 0.3 and 0.2 eV; therefore although the changes correct the under-estimation of the value at the clean surface the amount of the correction might not be reliable and thus even the absolute values of work function from the generalised gradient approximation must be used with care.

3.5.3 Co-adsorption

Experimentally (Over, 1998) the co-adsorbed cesium and oxygen has been found to possess a rich phase diagram, with structures which can be described already as surface oxides rather than as co-adsorbate phases with the identity of the individual adsorbates. Unfortunately we are still limited to smaller unit cells, but even then there are experiments to compare our results with.

In the structure $(\sqrt{3} \times \sqrt{3})$R30°-(1Cs+1O) the symmetry necessarily decreases, in this case from C_{3v} of the phase $(\sqrt{3} \times \sqrt{3})$R30°-Cs to C_3 *i.e.* the mirror plane symmetries are absent. This gives the three ruthenium atoms of the first substrate layer the freedom to rotate by 1.1° around the three-fold rotational axis and the ruthenium atoms move laterally closer to the oxygen atom the the cesium or the third, empty hcp site. This causes the surprisingly large adsorption height of the oxygen of 1.54 Å compared to the height 1.19 Å in the (2×2) or 1.28 Å in the $(\sqrt{3} \times \sqrt{3})$R30° phases of the oxygen alone; this might have an electro-static origin if a small layer height between the cesium and oxygen would be preferred, which however is un-probably since it is not seen in the other phases studied here.

In the phase (2×2)-(1Cs+1O) then the oxygen pushes its nearest-neighbour ruthenium atoms away with a lateral magnitude of 0.08 Å and thus the oxygen atoms can get deeper towards the surface, to be compared with 0.09 Å of the isolated phase (2×2)-O; in the pure structure (2×2)-Cs_{ot} the change is in the same direction

as in the co-adsorptive case but is only 0.01 Å. Now that a vertical buckling is possible the ruthenium atom below the cesium is pushed inwards decreasing the cesium-oxygen distance which remains though larger by 0.15 Å than in the $(\sqrt{3} \times \sqrt{3})$R30° phase. The three oxygen atoms in the structure (2×2)-(1Cs+3O) force the cesium again to the hcp site, and both the lateral shift and the buckling decrease as the coverage of the layer thus increases. However whereas the agreement to the experiments is good – within the typical accuracy of the generalised gradient approximation – in the previous two phases here the vertical distances match rather poorly, an effect which awaits for an explanation.

Overall the interaction between the cesium and oxygen is of an attractive type as expected from a combination of an electro-positive and -negative species: The hard-sphere radius of the cesium atom is smaller throughout the systems here than in the isolated Cs/Ru phase in agreement with the simple picture of a charge transfer from the cesium to the oxygen and thus a decrease in the effective size of the cesium towards its ionic radius.

The co-adsorption of cesium and carbon monoxide forms an important model for the interaction between the carbon monoxide, or a simple reactant, with the alkali promoter. As in the co-adsorbate system of cesium and oxygen also here the adsorbate pair consists of the electro-positive alkali atom and a particle which can act as an electron acceptor, in this case the carbon monoxide can fill the initially unoccupied $2\pi^*$ orbital, which was already seen to occur at the single-adsorbate phase, according to the Blyholder model. Thus our results can reveal whether, and if yes to what extent, this trend is enhanced upon the co-adsorption of the cesium.

Unfortunately we are currently incapable of studying the co-adsorption as a function of the coverages of both the adsorbates, and thus our chances to learn about the range of the mutual interaction are limited. Yet the carbon monoxide can occupy the otherwise un-preferable fcc site in the structure (2×2)-(1Cs_{ot}+2$CO_{hcp,fcc}$) to increase the CO coverage to 1/2. Based on the occurrence of two separate C-O vibrational frequencies in the high resolution electron energy loss spectra He, Xu and Jacobi (1996) suggested that the phase (2×2)-(1Cs+2CO) begins to form already before the (2×2)-(1Cs+1CO) phase has been completed; however we obtain the separation of the two islands (2×2)-(1Cs+2CO) and (2×2)-Cs to be energetically by 0.62 eV compared to the homogeneous layer (2×2)-(1Cs+1CO): The repulsion among the cesium atoms in the pure (2×2)-Cs structure over-weights the modest energy win of clustering the higher-coverage co-adsorption structure from the CO/Ru-only phase. A possible explanation for the different behaviour from the experiments and our calculations could be that at the inter-mediate coverage the CO molecules are rather immobile and molecules sticking to the (2×2)-(1Cs+2CO) islands cannot diffuse to the cells with only (2×2)-Cs. Otherwise the attraction between the cesium and carbon monoxide is strongly attractive as expected, with a mutually stabilising effect of nearly 1 eV relative to the isolated phases.

Since both the carbon monoxide and the cesium atom prefer the on-top site in the single-adsorbate phases with the (2×2) registry – although the energetics of the cesium is somewhat erroneous and the corrugation of the potential energy surface for the adsorption of the carbon monoxide under-estimated – in the (2×2) co-adsorbate cell either the symmetry has to be lowered to C_{1h} or at least either one of the adsorbates has to occupy an adsorption site different from its isolated phase, and the latter scenario has been found to take place in the experiments. Although the move of the cesium to a three-fold hollow site would be energetically easier than of the carbon monoxide the structure (2×2)-(1Cs_{ot}+1CO_{hcp}) is much more, by 0.44 eV, more stable than (2×2)-(1Cs_{hcp}+1CO_{ot}); possible explanations would be a preferred electro-static interaction – the oxygen atom of the carbon monoxide is positioned lower in the former structure and thus the increase in the density around the oxygen is located further away from the density increase above the cesium atom – or an easier filling of the $2\pi^*$ orbital of the carbon monoxide as found by Müller (1989) from the cluster calculations for the system K+CO/Pt(111). In both Cs+CO/Ru structures the interaction density is consistent with an enhanced Blyholder mechanism due to a increase in the density at the sides of the CO molecule, where the $2\pi^*$ orbital resides, and a decrease on the molecular axis between and above the atoms nicely correlating with the density of the 5σ orbital; however the main effect in the stable (2×2)-(1Cs_{ot}+1CO_{hcp}) structure is the internal polarisation of the CO molecule. This change can be accurately reproduced with an electric field perpendicular to the surface as was also the case for the clean surface. The density around the cesium is little changed upon the adsorption of the carbon monoxide.

The change in the density around the cesium by the asymptotic density above the atom; this shows a clear qualitative difference between the structures with co-adsorbed carbon monoxide or oxygen: In the case of the former the asymptotic density is largely depressed and in the latter closer to the phase of (2×2)-Cs only; the decrease in the case of the co-adsorbed CO occurs simultaneously with an increase of the height of the cesium layer from the out-most layer of the substrate. The same trend in the induced density arising from the Kohn-Sham states near the Fermi energy a small but definite effect is seen: Whereas the co-adsorption with oxygen increases the density above and close to the surface the carbon monoxide reduces it. The same conclusion was derived from the meta-stable de-excitation spectra of impinging helium and neon atoms by Fichtner-Endruschat *et al* (1998). Thus this gives promise for the applicability of the calculated densities to the interpretation of the experimental spectra.

An effect which has been found already in most of the measurements on the quantitative geometry of the co-adsorption of an alkali atom and the carbon monoxide is the bond lengthening of the internal carbon-oxygen distance in the CO molecule. We have observed the same effect and we can also observe the gradual raise and origin of the effect: The total change from the isolated (2×2)-CO_{ot} to the co-adsorbed (2×2)-(Cs_{ot}+CO_{hcp}) phase amount to 0.10 Å, from which 0.03 Å occurs already upon the change of the adsorption site $CO_{ot} \Rightarrow CO_{hcp}$ and further 0.02 Å is achieved by the applied electric field in the absence of the cesium; however we were limited to a magnitude of about one third of the electric field above the hcp site which is created by the cesium, and if we assume a linear dependence of the C-O bond length on the strength of the electric field we obtain a total change

of 0.03 Å+3×0.02 Å = 0.09 Å, close to the real value in the co-adsorption structure of 0.10 Å. The increased carbon-oxygen bond distance due to the site change, probably combined with the electric field arising from the alkali atom, accounts for the reduced C-O vibrational frequency seen in the vibrational spectroscopies upon the co-adsorption. The increase in the bond length upon the adsorption of the carbon monoxide and further when the alkali atom is added to the vicinity of the molecule could simply be explained by the increasing filling of the molecular $2\pi^*$ state which is anti-bonding with respect to the internal C-O bond and this way the carbon atom can be bind more strongly to the surface; the increased binding energy of the CO in the presence of the alkali can also be of an electro-static origin. Another scheme to explain the bond lengthening is that first the carbon atom forms the bond to the surface and subsequently the internal C-O bond has to be weakened. Our increase values for "charge" from the projection of the electronic states of the adsorbed system onto the orbitals of the CO molecule support the former scenario. The properties of a free, charged CO molecule behave qualitatively similarly to the adsorbed molecule upon the change caused by a co-adsorbed alkali atom.

According to our results the adsorption site is the most important factor in determining the energy of the peak position of the molecular states of the carbon monoxide, with the single exception in the structure Ru(0001)-(2×2)-($1Cs_{hcp}$+$1CO_{ot}$) which however is not the stable configuration of this co-adsorption system. In the other cases for example the 3σ peak varies between -22.3 and -21.8 eV at the hcp and only between -23.4 and -23.3 eV at the on-top site; similarly for the 4σ peak the energies are hcp: $-10.1 \ldots -9.6$ eV, on-top: $-9.0 \ldots -8.9$ eV. Especially small is the influence of one or even two co-adsorbed oxygen atoms: no peak moves more than 0.1 eV, pointing towards rather a weak interaction. All in all the set of energies of the molecular states are – with the one case violating the rule – a characteristic feature of a deterministic adsorption site and less of the chemical environment of the carbon monoxide. The same conclusion was recently suggested by Strisland *et al* (1998) from photoemission experiments, and the core level spectroscopy often relies on such assignments.

The opposite effect of the co-adsorptive electro-positive cesium and electro-negative oxygen on the carbon monoxide is apparent from several factors: The bond length increases when cesium is co-adsorbed but even decreases in the case of oxygen; as mentioned above the energetic positions of the CO are hardly changed with co-adsorbed oxygen but more with cesium; the cesium decreases, oxygen increases the bond length from the carbon to the nearest-neighbour atoms at the substrate.

A clear indicator of the site determination induced by either the co-adsorbed cesium or oxygen is obtained from the comparison of the two co-adsorption systems K+CO/Ru(0001) and O+CO/Ni(111): Whereas in the former the potassium causes the carbon monoxide to move from the on-top site to the hcp site in the latter the oxygen forces the CO in the opposite direction from the other three-fold hollow fcc site to on-top; so far there has been no counter-example of a change of the adsorption site in the "forbidden" direction (Over, 1998). Thus again the reasoning of the electro-positivity and -negativity of co-adsorbates supports the qualitative out-come of the Blyholder model.

Finally we still remark that large changes in the vertical corrugation – up to 0.24 Å – and lateral shifts – 0.09 Å – have been obtained in the studies of the present work; these are large effects on the chemical length scale and thus imply rather an active interplay of the surface during the adsorption and thus the catalytic processes.

Chapter 4

Conclusions

Now what have we learnt from all this? We have presented the principles of a numerical method, within the density functional theory, which is nowadays in a wide use in the scientific community and with similar approaches is making its way to industrial research and development, and we believe it to establish such an important position as the quantum chemistry and eventually the small-scale semi-empirical simulations have currently there. The beauty of the density functional methods lies on the needlessness of fitting to experimental output in the calculation. Excellent examples of recent density functional calculations on industrially important catalytic reactions include the study of the rate-limiting step in the synthesis of ammonia, the dissociation of nitrogen dimer, and the effect of the alkali promoter on the the dissociation by Bjørk Hammer, Jens Nørskov and co-workers (Mortensen *et al*, 1997; Mortensen, Hammer & Nørskov, 1998); the oxidation of carbon monoxide on Pt(111), which is an important reaction in purification of the exhaust gases from the burning of fossil fuels (Alavi *et al*, 1998); the Ziegler-Natta polymerisation by Michele Parrinello and co-workers (Boero, Parrinello & Terakura, 1998).

We first gave a short overview of the method which was then applied for the calculations in the present work. This was meant to give an unexperienced reader some background to the methods used, and to clarify how the results were analysed. It also emphasises the Author's interest to the numerical approach itself, and hopefully helps newcomers to the field with thorough discussions on seldomly published issues of calculational details.

The first application of the method was to bulk ruthenium and the clean Ru(0001) surface. This provides the basis of comparison for the effects due to adsorbed species. An agreement with experiments typical for the exchange-correlation energy functional used, the generalised gradient approximation, was observed in our results, thus giving us the confidence on the approximations and calculational parameters chosen. The single adsorbate phase of cesium on the Ru(0001) was found to behave similarly to the adsorption at aluminium surfaces, and the dominating response of the surface to the adsorbate was the electric field due to the polarisation of the cesium atom upon adsorption. The field strength at typical adsorption sites for co-adsorbates exceeded 1 eV/Å, which is very strong on the chemical scale. Other alkali metals on surfaces of different transition metals were found to behave qualitatively similarly, yet the polarisation of the semi-core – p – states was remarkable in the heavier alkali metals.

In the case of carbon monoxide we concentrated on the validity of the Blyholder model for adsorption at surfaces. We found there to be significant deviations from the original model, where only the highest occupied molecular orbital 5σ and the lowest unoccupied molecular orbital $2\pi^*$ would be involved in the bonding, but the overall picture of the adsorption of carbon monoxide can still be satisfactorily discussed with the Blyholder model. A significant mixing of the 4σ and 5σ orbitals within the molecule was observed. The nitrogen dimer molecule behaves similarly to the isoelectronic carbon monoxide. Further we found that the adsorption of carbon monoxide on the platinium group transition metals and copper is very delicate, and the stable adsorption site is even errorneously yielded in some cases.

The co-adsorption of cesium with the more electro-negative carbon monoxide or oxygen fitted in the general picture of the alkali being more polarised upon the adsorption, and that the interaction between the co-adsorbates is attractive – naturally they would not mix otherwise. Since the carbon monoxide and oxygen are more electro-negative than the substrate, ruthenium, the co-adsorbed alkali increased the effect seen on the adsorption of the single species. However, in the case of carbon monoxide the main effect, besides the changes due to Blyholder model, the molecule also internally polarised strongly due to the vertical electric field arising due to the alkali. The lengthening of the carbon–oxygen bond in the carbon monoxide molecule from the gas phase to the co-adsorbed one was seen to be due to three effects, first the adsorption and strengthening of the bond due to the alkali, second the electric field because of the polarised alkali and third because of the site change from on-top in the isolated phase to the three-fold hollow in the co-adsorbed structure. The latter fits in the framework of Blyholder model, where the molecule at hollow sites could fill the $2\pi^*$ orbital anti-bonding with respect to the internal molecular bond more efficiently, thus weakening and increasing the bond length. The induced density close to the Fermi energy above the cesium atom was found to behave qualitatively differently due to co-adsorption with carbon monoxide or oxygen, in a good agreement with the recent experimental results.

Since both the carbon monoxide and oxygen are usually regarded as electro-negative adsorbates it is somewhat contradictory that they do co-adsorb in a mixed structure. Yet the mixing energy is very small, and the effect of co-adsorption on the internal bond-length in the carbon monoxide molecule is to increase, opposite to the case of co-adsorption with cesium.

The results which we have presented here in length both further demonstrate the good agreement obtained

with current-day electronic structure calculations with the experiments and thus give credit to the usefulness of the approach employed here, and on the other hand they provide explanations or at least hints for effects which are difficult if not even impossible to derive from experiments. Our results provide a consistent description of systems ranging from the clean (0001) surface of ruthenium to the co-adsorbed ad-species. Furthermore the adsorption of single atom or molecule has enlarged our understanding of the coverage dependence of the interactions between the adsorbate and substrate and between the adsorbates themselves. The co-adsorption systems have enabled us to gain an improved knowledge of the mechanism upon bringing the ad-particles together.

We hope that the out-come of the present work will inspire new studies on these model systems. Yet we realise the small audience which shall directly benefit from our results but hope that it acts as an initiator for wide activity on the field of the basic, some day the applied research and even industry and will eventually bring together the chemists, physicists, process analysts and industrial researchers.

Chapter 5

References

- K Aashamar, T M Luke & J D Talman, Atomic Data and Nuclear Data Tables **22**, 443 (1978)
- Hideaki Aizawa & Shinji Tsuneyuki, *First-principles study of CO bonding to Pt(111): validity of the Blyholder model,* Surface Science Letters (399), 364 (1998)
- Ali Alavi, Peijun Hu, Thierry Deutsch, Pier Luigi Silvestrelli & Jürg Hutter, *CO Oxidation on Pt(111): An Ab Initio Density Functional Theory Study,* Physical Review Letters **80**, 3650 (1998)
- T A Arias, *Multi-resolution analysis of electronic structure: semicardinal and wavelet bases,* Reviews of Modern Physics **71**, 267 (1999)
- C O Almbladh & U von Barth, Physical Review B **31**, 3231 (1985)
- J A Alonso & L A Girifalco, Solid State Communications **24**, 135 (1977)
- J A Alonso & L A Girifalco, Physical Review B **17**, 3735 (1978)
- K Altenburg, H Bosch, J Van Ommen & P J Gellings, Journal of Catalysis **66**, 326 (1980)
- J B Anderson, International Reviews in Physical Chemistry, **14** 85 (1995)
- T A Arias, M C Payne & J D Joannopoulos, Physical Review Letters **69**, 1077 (1992)
- T Aruga, H Tochihara & Y Murata, *Structure and transitions of K mono-layers on Cu(001),* Surface Science **158**, 490 (1985); *Two-dimensional condensation of K ad-atoms on Cu(001),* Surface Science Letters **175**, 725 (1986); *Valence-electronic structure of potassium adsorbed on Cu(001) deduced from work-function change and electron-energy-loss spectroscopy,* Physical Review B **34**, 8237 (1986)
- N Ashcroft & Mermin, *Solid State Physics,* Harcount Brace College Publishers, Fort Worth (1976)
- G B Bachelet, D R Hamann & M Schlüter, Physical Review B **26**, 4199 (1982)
- Paul S Bagus & Gianfranco Pacchioni, *The contribution of metal sp electrons to the chemisorption of CO: theoretical studies of CO on Li, Na and Cu,* Surface Science **278**, 427 (1992)
- A D Becke, *Density-functional exchange-energy approximation with correct asymptotic behaviour,* Physical Review A **38**, 3098 (1988)
- A D Becke, *Density functional thermochemistry: III The role of exact exchange,* Journal of Chemical Physics **98**, 5648 (1993)
- A D Becke, *Density functional thermochemistry: IV A new dynamical correlation functional and implications for exact-exchange mixing,* Journal of Chemical Physics **104**, 1040 (1996)
- Lennart Bengtsson, *Dipole correction for surface supercell calculations,* Physical Review B **59**, 12 301 (1999)
- Peter E Blöchl, PhD Thesis, Universität Stuttgart 1989
- Peter E Blöchl, *Projector augmented wave method,* Physical Review B **50**, 17 953 (1994)
- Peter E Blöchl, O Jepsen & O K Andersen, *Improved tetrahedron method for Brillouin zone integrations,* Physical Review B **49**, 16 223 (1994)
- H Bludau, M Gierer, H Over & G Ertl, *A low-energy electron diffraction analysis of the* $(\sqrt{3} \times \sqrt{3})R30°$ *structure of molecular nitrogen adsorbed on Ru(0001),* Chemical Physics Letters **219**, 452 (1994)
- H Bludau, H Over, T Hertel, M Gierer & G Ertl, *Structural aspects of cesium-oxygen phases on Ru(0001),* Surface Science **342**, 134 (1995)
- George Blyholder, *Molecular Orbital View of Chemisorbed Carbon Monoxide,* The Journal of Physical Chemistry **68**, 2772 (1964)
- M Bockstedte, A Kley, J Neugebauer & M Scheffler, *Density functional theory calculations for poly-atomic systems: Electronic structure, static and elastic properties and ab initio molecular dynamics,* Computational Physics Communications **107**, 187 (1997)
- M Boero, M Parrinello & K Terakura, *First principles molecular dynamics study of Ziegler-Natta heterogeneous catalysis,* Journal of the American Chemical Society **120**, 2746 (1998)
- H B Bonzel, G Pirug & C Ritke, *Adsorption of* H_2O *on alkali-metal-covered Pt(111) and Ru(0001): A systematic comparison,* Langmuir **7**, 3006 (1991)
- A Böttcher, A Morgante, R Grobecker, T Greber & G Ertl, *Singlet-to-triplet conversion of meta-stable He atoms at alkali-metal over-layers,* Physical Review B **49**, 10 607 (1994)
- A Böttcher, H Niehus, S Schwegmann, H Over & G Ertl, *CO oxidation reaction over oxygen-rich Ru(0001) surfaces,* Journal of Physical Chemistry B, **101**, 11 185 (1997)

- J Braun, K L Kostov, G Witte & Ch Wöll, *CO over-layers on Ru(0001) studied by helium atom scattering: Structure, dynamics and the influence of Co-adsorbed H and O,* Journal of Chemical Physics **106**, 8262 (1997)
- G Brodén, G Gafner & H P Bonzel, Surface Science **84**, 295 (1979)
- Karl D Brommer, B E Larson, M Needels & J D Joannopoulos, *Implementation of the Car-Parrinello algorithm for ab initio total energy calculations on a massively parallel computer,* Computers in Physics **7**, 350 (1993)
- Kieron Burke, John P Perdew & Mel Levy, *Nonlocal Density Functionals for Exchange and Correlation: Theory and Applications,* in *Modern Density Functional Theory: A Tool for Chemistry,* Editors J M Seminario & P Politzer, Elsevier, Amsterdam 1995
- D M Bylander & Leonard Kleinman, *Good semiconductor band gaps with a modified local-density approximation,* Physical Review B **41** 7868 (1990)
- J Callaway & N H March, *Density functional methods: Theory and applications,* Solid State Physics **38**, 135 (1984)
- R Car & M Parrinello, *Unified Approach for Molecular Dynamics and Density-Functional Theory,* Physical Review Letters **55**, 2471 (1985)
- W J Carr, Jr, *Energy, specific heat and magnetic properties of the low-density electron gas,* Physical Review **122**, 1437 (1961)
- W J Carr & Maradudin, *Ground-state energy of a high-density electron gas,* Physical Review A **133**, 371 (1964)
- D M Ceperley & B J Alder, *Ground State of the Electron Gas by a Stochastic Method,* Physical Review Letters **45**, 566 (1980)
- D Ceperley & B Alder, *Quantum Monte Carlo,* Science **231**, 555 (1986)
- D M Ceperley & L Mitas, *Quantum Monte Carlo Methods in Chemistry,* in *New Methods in Computational Quantum Mechanics: Advances in Chemical Physics,* XCIII, Editors I Prigogine and S A Rice, 1996
- D J Chadi, *Special points for Brillouin-zone integrations,* Physical Review B **16**, 1746 (1977)
- D J Chadi & M L Cohen, *Special Points in the Brillouin Zone,* Physical Review B **8**, 5747 (1973)
- C Julian Chen, *Tunnelling matrix elements in three-dimensional space: The derivative rule and the sum rule,* Physical Review B **42**, 8841 (1990)
- C Julian Chen, *Corrugation reversal in scanning tunnelling microscopy,* Journal of Vacuum Science and Technology B **12**, 2193 (1994)
- L J Clarke, I Štich & M C Payne, *Large-scale ab initio total energy calculations on parallel computers,* Computer Physics Communications **72**, 14 (1992)
- Renato Colle & Oriano Salvetti, *Approximate Calculation of the Correlation Energy for the Closed Shells,* Theoretica Chimica Acta (Berlin) **37**, 329 (1975)
- Renato Colle & Oriano Salvetti, Theoretica Chimica Acta (Berlin) **53**, 55 (1979)
- H Conrad, G Ertl & J Küppers, Surface Science **76**, 323 (1978)
- S L Cunningham, *Special points in the two-dimensional Brillouin zone,* Physical Review B **10**, 4988 (1974)
- R Davis, R Toomes, D P Woodruff, O Schaff, V Fernandez, K-M Schindler, Ph Hofmann, K-U Weiss, R Dippel, V Fritzsche & A M Bradshaw, *Quantitative structural study of the co-adsorption of CO and K on Ni(111) using photoelectron diffraction,* Surface Science **393**, 12 (1997)
- R Davis, D P Woodruff, O Schaff, V Fernandez, K-M Schindler, Ph Hofmann, K-U Weiss, R Dippel, V Fritzsche & A M Bradshaw, *Structure Determination of an Alkali Metal-CO Co-adsorption Phase: Ni(111)-K/CO,* Physical Review Letters **74**, 1621 (1995)
- D R Diehl & R McGrath, *Current progress in understanding alkali metal adsorption on metal surfaces,* Journal of Physics: Condensed Matter **9**, 951 (1997)
- S Dietrich, in *Phase Transitions and Critical Phenomena,* Vol. 12, Editor C Domb & J L Lebowitz, Academic Press, London (1983), page 1
- P A M Dirac, *Note on exchange phenomena in the Thomas atom,* Proceedings of the Cambridge Philosophical Society **26**, 376 (1930)
- D L Doering & S Semancik, Surface Science **175**, L730 (1986)
- P A Dowben, *Determining the Bonding Orientation of Molecular Adsorbates on Metal Surfaces by Angle-Resolved Photoemission,* Zeitschrift für Physikalische Chemie **202**, 227 (1997)
- R M Dreizler & E K U Gross, *Density Functional Theory, An Approach to the Quantum Many-Body Problem,* Springer-Verlag Berlin Heidelberg, 1990
- E Engel, A Facco Bonetti, S Keller, I Andrejkovics & R M Dreizler, *Relativistic optimised potential method: Exact transverse exchange and Møller-Plesset-based correlation potential,* Physical Review A **58**, 964 (1998)
- G E Engel & W E Pickett, *Investigation of density functionals to predict both ground-state properties and band structures,* Physical Review B **54**, 8420 (1996)
- E Engel & S H Vosko, *Fourth-order gradient corrections to the exchange-only energy functional: Importance of* $\nabla^2 n$ *contributions,* Physical Review B **50**, 10 498 (1994)
- Gerhard Ertl, *Elementary Steps in Ammonia Synthesis: The Surface Science Approach,* in *Catalytic Ammonia Synthesis,* Editor J R Jennings, Plenum, New York (1991), page 109
- Gerhard Ertl, H Knözinger & J Weitkamp, *Handbook of Heterogeneous Catalysis,* VCH, Weinheim (1997)
- W R Fehlner & S H Vosko, Canadian Journal of Physics **55**, 2041 (1977)
- P J Feibelman, J E Houston, H L Davis & D G O'Neill, *Relaxation of the clean, Cu- and AH-covered Ru(0001) surface,* Surface Science **302**, 81 (1994)

- S Fichtner-Endruschat, V De Renzi, A Morgante, S Schwegmann, H Bludau, R Schuster, A Böttcher & H Over, *Electronic properties of Cs+CO co-adsorbed on the Ru(0001) surface,* Journal of Chemical Physics **108**, 774 (1998)
- A Filippetti, David Vanderbilt, W Zhong, Yong Cai & G B Bachelet, *Chemical Hardness, Linear Response and Pseudo Potential Transferability,* Physical Review B **52**, 11 793 (1995)
- A Filippetti, A Satta, David Vanderbilt & W Zhong, *Hardness Conservation as a New Transferability Criterion: Application to Fully Nonlocal Pseudo Potentials,* International Journal of Quantum Chemistry **61**, 421 (1997)
- M Fuchs & M Scheffler, *Ab initio pseudo potentials for electronic structure calculations of poly-atomic systems using density-functional theory,* submitted for publication (1998)
- J C Fuggle, M Steinkilberg & D Menzel, *Angular Dependence of UV Photoemission Spectra from Clean Ru(001) and from Adsorbed Oxygen and CO,* Chemical Physics **11**, 307 (1975)
- Peter Fulde, *Electron Correlations in Molecules and Solids,* Springer-Verlag Berlin Heidelberg (1991)
- R Gáspár, *Über dine approximation des Hartree-Fock schen potentials durch eine universelle potential funktion,* Acta Physica Academiae scientiarum Hungaricae **3**, 263 (1954)
- M Gell-Mann & K A Brueckner, Physical Review **106**, 364 (1957)
- M Gierer, H Bludau, H Over & G Ertl, *The bending mode vibration of CO on Ru(0001) studied with low-energy electron-diffraction,* Surface Science **346**, 64 (1996)
- M Gierer, H Over, H Bludau & G Ertl, *Structural properties of ordered alkali metal over-layers: a LEED analysis of the Ru(0001)-($\sqrt{3} \times \sqrt{3}R30°$)-Li phase in comparison with related systems,* Surface Science **337**, 198 (1995)
- M J Gillan, *Calculation of the vacancy formation energy in aluminium,* Journal of Physics: Condensed Matter **1**, 689 (1989)
- Stefan Goedecker, *Linear scaling electronic structure methods,* Reviews of Modern Physics **71**, 1085 (1999)
- Xavier Gonze, Peter Käckell & Matthias Scheffler, *Ghost states for separable, norm-conserving, ab initio pseudo potentials,* Physical Review B **41**, 12 264 (1990)
- Xavier Gonze, Roland Stumpf & Matthias Scheffler, *Analysis of separable potentials,* Physical Review B **44**, 8503 (1991)
- Andreas Görling & Mel Levy, *Exact Kohn-Sham scheme based on perturbation theory,* Physical Review A **50**, 196 (1994)
- E K U Gross & R M Dreizler, *Gradient expansion of the Coulomb exchange energy,* Zeitschrift der Physik A **302**, 103 (1981)
- O Gunnarsson & R O Jones, *Total-energy differences: Sources of error in local-density approximations,* Physical Review B **31** 7588 (1985)
- O Gunnarsson, M Jonson & B I Lundqvist, *Exchange and Correlation in Inhomogeneous Electron Systems,* Solid State Communications **24**, 765 (1977)
- O Gunnarsson, M Jonson & B I Lundqvist, *Descriptions of exchange and correlation effects in inhomogeneous electron systems,* Physics Review B **20**, 3136 (1979)
- F Gygi, *Adaptive Riemannian Metric for Plane-Wave Electronic-Structure Calculations,* Europhysics Letters **19**, 617 (1992)
- D R Hamann, *Generalised norm-conserving pseudo potentials,* Physical Review B **40**, 2980 (1989)
- D R Hamann, M Schlüter & C Chiang, *Norm-Conserving Pseudo Potentials,* Physical Review Letters **43**, 1494 (1979)
- B Hammer, L B Hansen & J K Nørskov, *Improved adsorption energetics within density functional theory using revised PBE functionals,* accepted for publication in the Physical Review B (1999)
- B Hammer, Y Morikawa & J K Nørskov, *CO Chemisorption at Metal Surfaces and Over-layers,* Physical Review Letters **76**, 2141 (1996)
- B Hammer, K W Jacobsen & J K Nørskov, *Role of nonlocal exchange correlation in activated adsorption* Physical Review Letters **70**, 3971 (1993)
- Bjørk Hammer, Matthias Scheffler, Karsten W Jacobsen & Jens K Nørskov, *Multi-dimensional potential energy surface for H_2 dissociation over Cu(111),* Physical Review Letters **73**, 1400 (1994)
- B L Hammond, W A Lester Jr & P J Reynolds, *Monte Carlo Methods in ab initio Quantum Chemistry,* World Scientific, Singapore (1994)
- A Harju, B Barbiellini, S Siljamäki, R M Nieminen & G Ortiz, *Stochastic Gradient Approximation: An Efficient Method to Optimise Many-Body Wave Functions,* Physical Review Letters **79**, 1173 (1997)
- P He, H Dietrich & K Jacobi, *Lateral interaction of CO chemisorbed on Ru(0001),* Surface Science **345**, 241 (1996)
- P He & K Jacobi, *Vibrational analysis of cesium on Ru(0001),* Physical Review B 53, 3658 (1996)
- Peimo He, Yabo Xu & Karl Jacobi, *Vibrational analysis of the (Cs+CO)-(2×2) compound layer on Ru(0001),* Journal of Chemical Physics **104**, 8118 (1996)
- D Hennig, M V Ganduglia-Pirovano & M Scheffler, *Ad-layer core-level shifts of ad-metal mono-layers on transition-metal substrates and their relation to the surface chemical reactivity,* Physical Review B **53**, 10 344 (1996)
- F Herman, J P van Dyke & I B Ortenburger, Physical Review Letters **22**, 807 (1969)
- P Hohenberg & W Kohn, *Inhomogeneous Electron Gas,* Physical Review **136**, B864 (1964)
- M A van Hove, *Another unusual adsorption site for alkali adsorption on a metal, found by automated tensor LEED on a notebook computer: Rh(111)-($\sqrt{3} \times \sqrt{3}$)R30°-Na,* Surface Review and Letters **1**, 9 (1994)
- J Hrbek, *Adsorption of cesium on Ru(0001),* Surface Science **164**, 139 (1985)
- P Hu, D A King, S Crampin, M-H Lee & M C Payne, *Gradient corrections in density functional theory calculations for surfaces: CO on Pd(110),* Chemical Physics Letters **230**, 501 (1995)

- Jürg Hutter, Hans Peter Lüthi & Michele Parrinello, *Electronic structure optimisation in plane-wave-based density functional calculations by direct inversion in the iterative subspace,* Computational Materials Science **2**, 244 (1994)
- Jürg Hutter, Mark E Tuckerman & Michele Parrinello, *Integrating the Car-Parrinello equations. III. Techniques for ultra-soft pseudo potentials,* Journal of Chemical Physics **102**, 1302 (1995)
- K Jacobi, H Shi, H Dietrich & G Ertl, *Adsorbate-induced electronic modification of Cs over-layers on Ru(0001),* Surface Science **331-333**, 69 (1995)
- K Jacobi, H Shi, M Gruyters & G Ertl, *Adsorbate-induced electronic modification of alkali-metal over-layers,* Physical Review B **49**, 5733 (1994)
- P Jakob, *Dynamics of the C-O Stretch Overtone Vibration of CO/Ru(001),* Physical Review Letters **77**, 4229 (1996)
- P Jakob, *Fermi resonance distortion of the Ru-CO stretching mode of CO adsorbed on Ru(001),* Journal of Chemical Physics **108** 5035 (1998)
- O Jepsen & O K Andersen, *The Electronic Structure of hcp Ytterbium,* Solid State Communications **9**, 1763 (1971)
- Benny G Johnson, Peter M W Gill & John A Pople, *The performance of a family of density functional methods,* Journal of Chemical Physics **98**, 5612 (1993)
- Benny G Johnson, Carlos A Gonzales, Peter M W Gill & John A Pople, *A density functional study of the simplest hydrogen abstraction reaction. Effect of self-interaction correction,* Chemical Physics Letters **221**, 100 (1994)
- R O Jones & O Gunnarsson, *The density functional formalism, its applications and prospects,* Reviews of Modern Physics **61**, 689 (1989)
- Yu-Min Juan & Efthimios Kaxiras, *Application of gradient corrections to density-functional theory for atoms and solids,* Physical Review B **48**, 14 944 (1993)
- Tomohiko Kato, *Attractive interaction between alkali-metal ad-atoms on metal surfaces,* Physical Review B **47**, 13 895 (1993)
- P Kaukasoina, M Lindroos, P Hu, D A King & C J Barnes, *Full structure determination of an alkali-metal/CO co-adsorption phase for Co(10$\bar{1}$0)-c(2 × 2)-(K+CO),* Physical Review B **51**, 17 063 (1995)
- P Kaukasoina, M Lindroos, G S Leatherman & R D Diehl, *Adsorption site change for Cs, Rb or K adsorption on Ag(111),* Surface Review and Letters **4**, 1215 (1997)
- G P Kerker, *Non-singular atomic pseudo potentials for solid state applications,* Journal of Physics C: Solid State Physics **13**, L189 (1980)
- Alexander Khein, *Analysis of separable non-local pseudo potentials,* Physical Review B **51**, 16 608 (1995)
- Y D Kim, S Wendt, S Schwegmann, H Over & G Ertl, *Structural analyses of the pure and cesiated Ru(0001)-(2 × 2)-3O phase,* Surface Science **418**, 267 (1998)
- M P Kiskinova, Surface Science **111**, 584 (1981)
- M Kiskinova, G Pirug & H P Bonzel, Surface Science **133**, 312 (1983)
- Leonard Kleinman & D M Bylander, *Efficacious Form for Model Pseudo Potentials,* Physical Review Letters **48**, 1425 (1982)
- Alexander Kley, *Theoretische Untersuchungen zur Adatomdiffusion auf niederindizierten Oberflächen von GaAs,* Doktorarbeit (PhD Thesis), Technische Universität Berlin (1997)
- W Kohn & L J Sham, *Self-Consistent Equations Including Exchange and Correlation Effects,* Physical Review **140**, A1133 (1965)
- Georg Kresse, *Ab initio Molekular Dynamik für flüssige Metalle,* Doktorarbeit (PhD Thesis), Technische Universität Wien, 1993
- G Kresse, J Furthmüller & J Hafner, *Theory of the crystal structures of selenium and tellurium: The effect of generalised gradient corrections to the local density approximation,* Physical Review B **50**, 13 181 (1994)
- G Kresse & J Furthmüller, *Efficiency of ab initio total energy calculations for metals and semi-conductors using a plane-wave basis set,* Computational Materials Science **6**, 15 (1996a)
- G Kresse, J Furthmüller, *Efficient iterative schemes for ab initio total-energy calculations using a plane-wave basis set,* Physical Review B **54**, 11 169 (1996b)
- H J Kreuzer & S H Payne, in *Equilibria and dynamics of gas adsorption on heterogeneous solid surfaces,* Editors W Rudzinski, W A Steele and G Zgrablich, Vol. 104, Elsevier (1997)
- J B Krieger, Yan Li & G J Iafrate, *Construction and application of an accurate local spin-polarised Kohn-Sham potential with integer discontinuity: Exchange-only theory,* Physical Review A **45**, 101 (1992)
- F W Kutzler & G S Painter, Physical Review Letters **59**, 1285 (1987)
- K Laasonen, F Csajka & M Parrinello, Chemical Physics Letters **194**, 172 (1992)
- K Laasonen, A Pasquarello, R Car, C Lee & D Vanderbilt, *Car-Parrinello molecular dynamics with Vanderbilt ultra-soft pseudo potentials,* Physical Review B **47**, 10 142 (1993)
- J Lahtinen *et al*, unpublished results (1998)
- J Lahtinen, J Vaari & K Kauraala, *Adsorption and structure dependent desorption of CO on Co(0001),* Surface Science **418**, 502 (1998)
- J Landskron, W Woritz, B Narloch & D Menzel, Verhandlungen der Deutschen Physikalischen Gesellschaft (VI) **31**, 1901 (1996); J Landskron, W Woritz, B Narloch, G Held & D Menzel, Surface Science, to be submitted
- N D Lang, *Theory of single-atom imaging in the scanning tunnelling microscope,* Comments in Condensed Matter Physics **14**, 253 (1989)
- N D Lang & W Kohn, *Theory of metal surfaces: Charge density and surface energy,* Physical Review B **1**, 4555 (1970)
- N D Lang & W Kohn, *Theory of metal surfaces: Work function,* Physical Review B (1971)

- Chengteh Lee, Weitao Yang & Robert G Parr, *Development of the Colle-Salvetti correlation energy formula into a functional of the electron density,* Physical Review B **37**, 785 (1988)
- G Lehmann & M Taut, *On the Numerical Calculation of the Density of States and Related Properties,* physica status solidi b **54**, 469 (1972)
- M Levy, International Journal of Quantum Chemistry **S23**, 617 (1989)
- M Levy & J P Perdew, *Hellmann-Feynman, virial and scaling requisites for the exact universal density functionals. Shape of the correlation potential and diamagnetic susceptibility for atoms,* Physical Review A **32**, 2010 (1985)
- E H Lieb & S Oxford, International Journal of Quantum Chemistry **19**, 427 (1981)
- S G Louie, S Froyen & M L Cohen, Physical Review B **26**, 1738 (1982)
- S Lundqvist & N H March (Editors), *Theory of the Inhomogeneous Electron Gas,* Plenum Press, New Your and London (1983)
- A H MacDonald, *Comment on special points for Brillouin zone integrations,* Physical Review B **18**, 5897 (1978)
- Theodore E Madey, *The Geometry of CO on Ru(001): Evidence for Bending Vibrations in Adsorbed Molecules,* Surface Science **79**, 575 (1979)
- T E Madey & C Benndorf, Surface Science **164**, 602 (1985)
- G D Mahan, *Many-Particle Physics,* Plenum, New York 1981
- K Markert & K Wandelt, *The short range of the electronic promoter effect of potassium,* Surface Science **159**, 24 (1985)
- Dominik Marx & Michele Parrinello, *Ab initio path-integral molecular dynamics,* Zeitschrift der Physik B **95**, 143 (1994)
- Dominik Marx & Michele Parrinello, *Ab initio path integral molecular dynamics: Basic ideas,* Journal of Chemical Physics **104**, 4077 (1996)
- Dietrich Menzel, Comment on Feibelman *et al* (1994), Surface Science **318**, 437 (1994)
- Dietrich Menzel, *Adsorbate-Induced Global and Local Expansions and Contractions of a Close-Packed Transition Metal Surface,* Surface Review and Letters **4**, 1283 (1997)
- N D Mermin, Physical Review **137** A1441 (1965)
- A Messiah, *Quantum Mechanics, Volume 1,* (North-Holland, Amsterdam, 1974)
- M Methfessel, D Hennig & M Scheffler, *Trends of the surface relaxations, surface energies and work functions of the 4d transition metals,* Physical Review B **46**, 4816 (1992)
- M Methfessel & A T Paxton, *High-precision sampling for Brillouin-zone integration in metals,* Physical Rev B **40**, 3616 (1989)
- G Michalk, W Moritz, H Pfnür & D Menzel, *A LEED determination of the structures of Ru(001) and of CO/Ru(001)-* $\sqrt{3} \times \sqrt{3}R30^\circ$, Surface Science **129**, 92 (1983)
- Lubos Mitas, *Electronic structure by quantum Monte Carlo: atoms, molecules and solids,* Computer Physics Communications **96**, 107 (1996)
- H J Monkhorst & J D Pack, Physical Review B **13**, 5188 (1976)
- B Montanari, P Ballone & R O Jones, *Density functional study of molecular crystals: Polyethylene and a crystalline analog of bisphenol-A polycarbonate,* Journal of Chemical Physics **108**, 6947 (1998)
- Sam Dylan Moré, *Untersuchungen von Absorbaten auf Einkristalloberflächen mittels Beugung niederenergetischer Elektronen,* Doktorarbeit (PhD Thesis), Freie Universität Berlin (1998): `http://darwin.inf.fu-berlin.de/1998/14/index.h`
- Jens Jørgen Mortensen, *A theoretical study of adsorption and dissociation on metal surfaces,* PhD thesis, Technical University of Denmark (1998)
- Jens Jørgen Mortensen, Bjørk Hammer & Jens K Nørskov, *Alkali promotion of N_2 dissociation over Ru(0001),* Physical Review Letters **80**, 4333 (1998)
- J J Mortensen, Y Morikawa, B Hammer & J K Nørskov, *Density functional calculations of N_2 adsorption and dissociation on a Ru(0001) surface,* Journal of Catalysis **169**, 85 (1997)
- V L Moruzzi, J F Janak & A R Williams, *Calculated Electronic Properties of Metals,* Pergamon, New York (1978)
- J E Müller, *Theory of the co-adsorption of H_2O and CO with K on the Pt(111) surface,* in *Physics and Chemistry of Alkali Metal Adsorption,* Editors H P Bonzel, A M Bradshaw & G Ertl, Elsevier Science Publishers B V (1989); J E Müller, *Theory of the co-adsorption of H_2O and CO with K on the Pt(111) surface,* in *The Chemical Physics of Solid Surfaces and Heterogeneous Catalysis,* volume 6 page 29, Elsevier, Amsterdam (1993)
- F D Murnaghan, Proceedings of the National Academy of Sciences of United States of America **30**, 244 (1944)
- C Nagl, R Schuster, S Renisch & G Ertl, *Regular mixing in a two-dimensional lattice system: The Co-adsorption of N and O on Ru(0001),* Physical Review Letters **81**, 3483 (1998)
- B Narloch, G Held & D Menzel, Surface Science **317**, 131 (1994)
- B Narloch, G Held & D Menzel, Surface Science **340**, 159 (1995)
- Björn Narloch & Dietrich Menzel, *Structural evidence for chemical contributions in the bonding of the heavy rare gases on a close-packed transition metal surface: Xe and Kr on Ru(001),* Chemical Physics Letters **270**, 163 (1997)
- J S Nelson, S J Plimpton & M P Sears, *Plane wave electronic structure calculations on a parallel supercomputer,* Physical Review B **47**, 1765 (1993)
- Jörg Neugebauer & Matthias Scheffler, *Adsorbate-substrate and adsorbate-adsorbate interactions of Na and K adlayers on Al(111),* Physical Review B **46**, 16 067 (1992)
- Ralf Neumann & Nicholas C Handy, *Higher-order gradient corrections for exchange-correlation functionals,* Chemical Physics Letters **266**, 16 (1997)

- A Nilsson, N Wassdahl, M Weinelt, O Karis, T Wiell, P Bennich, J Hasselström, A Föhlisch, J Stöhr & M Samant, *Local probing of the surface chemical bond using X-ray emission spectroscopy,* Applied Physics A **65**, 147 (1997); A Nilsson, M Weinelt, T Wiell, P Bennich, O Karis, N Wassdahl, J Stöhr & M G Samant, *An atom-specific look at the surface chemical bond,* Physical Review Letters **78**, 2847 (1997)
- P Nozieres & D Pines, *The Theory of Quantum Liquids. I,* Benjamin, New York 1966
- W Oed, B Dötsch, L Hammer, K Heinz & K Müller, Surface Science **375**, 91 (1997)
- G L Oliver & J P Perdew, Physical Review A **32**, 2010 (1985)
- G Ortiz & P Ballone, *Pseudo potentials for non-local-density functionals,* Physical Review B **43**, 6376 (1991)
- Herbert Over, *Crystallographic study of interaction between ad-species on metal surfaces,* Progress in Surface Science **58**, 249 (1998)
- H Over, H Bludau, M Gierer & G Ertl, *Structural Properties of Alkali-Metal Atoms Adsorbed on Ru(0001),* Surface Review and Letters **2**, 409 (1995a)
- H Over, H Bludau, R Kose & G Ertl, *Cs and CO co-adsorbed on Ru(0001): low-energy electron diffraction analysis,* Surface Science **331-333**, 62 (1995b)
- H Over, H Bludau, R Kose & G Ertl, *Structural analyses of Cs+CO Co-adsorbed on Ru(0001),* Physical Review B **51**, 4661 (1995c)
- H Over, H Bludau, R Kose, S Schwegmann & G Ertl, in preparation (1999)
- H Over, H Bludau, M Skottke-Klein, G Ertl, W Moritz & C T Campbell, *Low-energy electron-diffraction analysis of the structure of a Cs-O/Ru(0001) co-adsorbate phase,* Physical Review B **46**, 4360 (1992a)
- H Over, H Bludau, M Skottke-Klein, G Ertl, W Moritz & C T Campbell, *Coverage dependence of adsorption-site geometry in the Cs/Ru(0001) system: A low-energy electron-diffraction analysis,* Physical Review B **45**, 8538 (1992b)
- H Over, M Gierer, H Bludau & G Ertl, *Anisotropic thermal displacements of adsorbed atoms and molecules on surfaces studied by low-energy electron diffraction,* Physical Review B **52**, 16 812 (1995d)
- H Over, W Moritz & G Ertl, *Anisotropic Atomic Motions in Structural Analysis by Low Energy Electron Diffraction,* Physical Review Letters **70**, 315 (1993)
- Z Paál, G Ertl & S B Lee, Applied Surface Science **8**, 231 (1981)
- Gianfranco Pacchioni, Sai-Cheong Chung, Sven Krüger & Notker Rösch, *Is CO Chemisorbed on Pt anomalous compared with Ni and Pd? An example of surface chemistry dominated by relativistic effects,* Surface Science **392**, 173 (1997)
- James D Pack & Hendrik J Monkhorst, *"Special points for Brillouin-zone integrations" – a reply,* Physical Review B **16**, 1748 (1977)
- R A de Paola, F M Hoffmann, D Heskett & E W Plummer, *Adsorption of molecular nitrogen on clean and modified Ru(0001) surfaces: The role of σ bonding,* Physical Review B **35**, 4236 (1987)
- Robert G Parr & Weitao Yang, *Density-Functional Theory of Atoms and Molecules,* Oxford University Press, Oxford 1989
- S H Payne, H A McKay, H J Kreuzer, M Gierer, H Bludau, H Over & G Ertl, *Multilayer adsorption and desorption: Cs and Li on Ru(0001),* Physical Review B **54**, 5073 (1996)
- S H Payne, Jun Zhang & H J Kreuzer, *Lattice gas with multiple interactions: isosteric heat and thermal desorption,* Surface Science **264**, 185 (1992)
- M C Payne, J D Joannopoulos, D C Allan, M P Teter & D H Vanderbilt, *Molecular dynamics and ab initio total energy calculations,* Physical Review Letters **56**, 2656 (1986)
- Charles H F Peden, *Carbon monoxide Oxide Oxidation on Model Single-Crystal Catalysts,* in *Surface Science of Catalysis: In Situ Probes and Reaction Kinetics*, edited by D J Dwyer and F M Hoffman (American Chemical Society, Washington DC, 1992)
- J P Perdew, *Unified theory of exchange and correlation beyond the local density approximation,* in *Electronic Structure of Solids '91,* Editors P Ziesche & H Eschrig, Akademie Verlag, Berlin (1991)
- John P Perdew, Kieron Burke & Matthias Ernzerhof, *Generalised Gradient Approximation Made Simple,* Physical Review Letters **77**, 3865 (1996); Erratum **78**, 1396 (1997); Reply to Comment **80**, 891 (1998)
- John P Perdew, Kieron Burke & Yue Wang, *Generalised gradient approximation for the exchange-correlation hole of a many-electron system,* Physical Review B **54**, 16 533 (1996)
- J P Perdew, J A Chevary, S H Vosko, K A Jackson, M R Pederson, D J Singh & C Fiolhais, *Atoms, molecules, solids and surfaces: Applications of the generalised gradient approximation for exchange and correlation,* Physical Review B **46**, 6671 (1992)
- John P Perdew, Stefan Kurth, Ales Zupan & Peter Blaha, *Accurate Density Functional with Correct Formal Properties: A Step Beyond the Generalised Gradient Approximation,* Physical Review Letters **82**, 2544 (1999); Erratum, **82**, 5179 (1999)
- John P Perdew, Robert G Parr, Mel Levy & Jose L Balduz Jr, Physical Review Letters **49**, 1691 (1982)
- J P Perdew & Y Wang, Physical Review B **33**, 8800 (1986)
- John P Perdew & Yue Wang, *Accurate and simple analytic representation of the electron-gas correlation energy,* Physical Review B **45**, 13 244 (1992a)
- J P Perdew & A Zunger, Physical Review B **23**, 5048 (1981)
- José M Pérez-Jordá & A D Becke, *A density-functional study of van der Waals forces: rare gas diatomics,* Chemical Physics Letters **233**, 134 (1995)
- H Pfnür, P Feulner & D Menzel, *The Influence of Adsorbate Interactions on Kinetics and Equilibrium for CO on Ru(001) II. Desorption Kinetics and Equilibrium,* Journal of Chemical Physics **79**, 4613 (1983)

- H Pfnür & D Menzel, *The Influence of Adsorbate Interactions on Kinetics and Equilibrium for CO on Ru(0001). I. Adsorption Kinetics,* Journal of Chemical Physics (1983)
- H Pfnür, D Menzel, F M Hoffmann, A Ortega & A M Bradshaw, *High resolution vibrational spectroscopy of CO on Ru(001): The importance of lateral interactions,* Surface Science **93**, 431 (1980)
- Warren E Pickett, *Pseudo potential methods in condensed matter applications,* Computer Physics Reports **9**, 115 (1989)
- E I Proynov, A Vela & D R Salahub, *Nonlocal Correlation Functional Involving the Laplacian of the Density,* Chemical Physics Letters **230**, 419 (1994); Erratum **234**, 462 (1995)
- P Pulay, Molecular Physics **17**, 197 (1969)
- Péter Pulay, *Convergence Acceleration of Iterative Sequences. The Case of SCF Iteration,* Chemical Physics Letters **73**, 393 (1980)
- A M Rappe, K M Rabe, E Kaxiras & J D Joannopoulos, *Optimised pseudo potentials,* Physical Review B **41**, 1227 (1990); Erratum **44**, 13 175 (1991)
- D K Remler & P A Madden, *Molecular dynamics without effective potentials via the Car-Parrinello approach,* Molecular Physics **70**, 921 (1990)
- S Renisch, R Schuster, J Wintterlin & G Ertl, *Dynamics of adatom motion under the influence of mutual interactions: O/Ru(0001),* Physical Review Letters **82**, 3839 (1999)
- José A Rodriguez & D Wayne Goodman, Science **257**, 897 (1992)
- José A Rodriguez & D Wayne Goodman, *High-pressure catalytic reactions over sing-crystal metal surfaces,* Surface Science Reports **14**, 1 (1991)
- A Schiffer, P Jakob & D Menzel, Surface Science **389**, 116 (1997)
- K-M Schindler, Ph Hofmann, K-U Weiss, R Dippel, P Gardner, V Fritzsche, A M Bradshaw, D P Woodruff, M E Davila, M C Asensio, J C Conesa & A R Gonzàlez-Elipe, Journal of Electron Spectroscopy and Related Phenomena **64/65**, 75 (1993)
- K E Schmidt & M H Kalos, in *Monte Carlo Methods in Statistical Physics II,* Topics in Current Physics **36**, Editor K Binder, Springer, Berlin, Heidelberg (1984)
- Rolf Schuster, Peter J Eng & Ian K Robinson, *Anomalous coverage behaviour of the Cs-Ag distance on Cs/Ag(110),* Surface Science **326**, L477 (1995)
- K Schwarz, Chemical Physics Letters **57**, 605 (1978)
- S Schwegmann, A P Seitsonen, H Dietrich, H Bludau, H Over, K Jacobi & G Ertl, *The adsorption of atomic nitrogen on Ru(0001): Geometry and energetics,* Chemical Physics Letters **264**, 680 (1997)
- S Schwegmann, A P Seitsonen, V De Renzi, H Dietrich, H Bludau, M Gierer, H Over, K Jacobi, M Scheffler & G Ertl, *Oxygen adsorption on the Ru(10$\bar{1}$0) surface: Anomalous coverage dependence,* Physical Review B **57**, 15 487 (1998)
- Alexander Seidl, *Elektronische Struktur von Halbleitern im Rahmen einer verallgemeinerten Kohn-Sham-Theorie,* Doktorarbeit (PhD Thesis), Technische Universität München (1995)
- A Seidl, A Görling, P Vogl, J A Majewski & M Levy, *Generalised Kohn-Sham schemes and the band-gap problem,* Physical Review B **53**, 3764 (1996)
- F Sette, J Stöhr, E B Kollin, D J Dwyer, J L Gland, J L Robbins & A L Johnson, *Na-Induced Bonding and Bond-Length Changes for CO on Pt(111): A Near-Edge X-Ray-Absorption Fine-Structure Study,* Physical Review Letters **54**, 935 (1985)
- L J Sham *Approximations of the exchange and correlation potentials,* in *Computational Methods in Bond Theory*, Editors P J Marcus, J F Janak & A R Williams, Plenum, New York 1971
- H B Shore, J H Rose & E Zaremba, Physical Review B **15**, 2858 (1977)
- David J Singh, *Weighted density approximation ground state studies of solids,* Physical Review B **48**, 14 099 (1993)
- David J Singh, *Plane waves, pseudo potentials and the LAPW method,* Kluwer Academic (1994)
- C Stampfl, S Schwegmann, H Over, M Scheffler & G Ertl, *Structure and stability of a high-coverage (*1 × 1*) oxygen phase on Ru(0001),* Physical Review Letters **77**, 3371 (1996)
- C Stampfl, H J Kreuzer, S H Payne, H Pfnür & M Scheffler, Physical Review Letters **83**, 3991 (1999)
- P Stoltze & J K Nørskov, *Bridging the "pressure gap" between ultrahigh-vacuum surface physics and high-pressure catalysis,* Physical Review Letters **55**, 2502 (1985)
- F Strisland, A Beutler, A J Jaworowski, R Nyholm, B Stelik, D Heskett & J N Andersen, *Adsorption sites in co-adsorption systems determined by photoemission spectroscopy: K and CO co-adsorbed on Rh(111),* Surface Science **410**, 330 (1998)
- Roland Stumpf, *Gesamtenergierechnungen zu Adsorption, Diffusion und Wachstum auf Al-Oberflächen,* Doktorarbeit (PhD Thesis), Technische Universität Berlin, 1993
- R Stumpf, X Gonze & M Scheffler, *A list of separable, norm-conserving, ab initio pseudo potentials,* Research Report of the Fritz-Haber-Institut (1990)
- R Stumpf & M Scheffler, *Simultaneous calculation of the equilibrium atomic structure and its electronic ground state using density-functional theory,* Computer Physics Communications **79**, 447 (1994)
- L Surnev, in *Physics and Chemistry of Alkali Metal Adsorption,* Editors H P Bonzel, A M Bradshaw and G Ertl, Elsevier, Amsterdam (1989), page 173
- A Szabo & N S Ostlund, *Modern Quantum Chemistry,* (McGraw-Hill, New York, 1989) and citations therein
- J D Talman & W F Shadwick, Physical Review A **14**, 36 (1976)
- F Tassone, F Mauri & R Car, *Acceleration schemes for ab initio molecular dynamics simulations and electronic structure calculations,* Physical Review B **50**, 10 561 (1994)
- J Tersoff & D R Hamann, *Theory of the scanning tunnelling microscope,* Physical Review B **31**, 805 (1985)

- Michael Teter, *Additional condition for transferability in pseudo potentials,* Physical Review B **48**, 5031 (1993)
- G E Thomas & W H Weinberg, Nederlands Tijdschrift voor Vakuumtechniek **16**, 57 (1978)
- G E Thomas & W H Weinberg, *The vibrational spectrum and adsorption site of CO on the Ru(001) surface,* Journal of Chemical Physics **70**, 1437 (1979)
- Michael Tinkham, *Group Theory and Quantum Mechanics,* McGraw-Hill, New York (1964)
- B Y Tong & L J Sham, Physical Review **144**, 1 (1966)
- Johannes Trost, *Über die Wechselwirkung zwischen adsorbierten Teilchen und deren mikroskopische Verteilung: Untersuchungen mittels Rastertunnelmikroskopie an den Systemen N/Ru(0001), Cs+O/Ru(0001) und O/Al(111),* Doktorarbeit (PhD Thesis), Freie Universität Berlin (1995)
- J Trost, J Wintterlin & G Ertl, *Atomic scale imaging of a 2D fluid-solid equilibrium for Cs and O co-adsorbed on a Ru(0001) surface,* Surface Science **329**, L583 (1995)
- N Troullier & J L Martins, *Efficient pseudo potentials for plane wave calculations,* Physical Review B **43**, 1993 (1991)
- Mark E Tuckerman, Dominik Marx, Michael L Klein & Michele Parrinello, *Efficient and general algorithms for path integral Car-Parrinello molecular dynamics,* Journal of Chemical Physics **104**, 5579 (1996)
- Mark E Tuckerman & Michele Parrinello, *Integrating the Car-Parrinello equations. I. Basic integration techniques,* Journal of Chemical Physics **101**, 1302 (1994)
- Mark E Tuckerman & Michele Parrinello, *Integrating the Car-Parrinello equations. II. Multiple time scale techniques,* Journal of Chemical Physics **101**, 1316 (1994)
- C Umrigar, *Accelerated Metropolis Method,* Physical Review Letters **71**, 408 (1993)
- C Umrigar, M P Nightingale & K J Runge, *A diffusion Monte Carlo algorithm with very small time-step errors,* Journal of Chemical Physics **99**, 2865 (1993)
- D Vanderbilt, *Optimally smooth norm-conserving pseudo potentials,* Physical Review B **32**, 8412 (1985)
- D Vanderbilt, *Soft self-consistent pseudo potentials in a generalised eigenvalue formalism,* Physical Review B **41**, 7892 (1990)
- S H Vosko, L Wilk & M Nusair, Canadian Journal of Physics **58**, 1200 (1980)
- K Wandelt, in Thin Metal Films and Gas Chemisorption, edited by P Wissmann, Elsevier, Amsterdam (1987); K Wandelt, in Chemistry and Physics of Solid Surfaces VIII, edited by R Vanselow and R Howe, Springer Series in Surface Science Volume 22, Springer, Berlin (1990), page 289
- Y Wang & J P Perdew, Physical Review B **43**, 8911 (1991)
- H Wedler, M A Mendez, P Bayer, U Löffler, K Heinz, V Fritzsche & J B Pendry, *Coverage-dependent DLEED analysis of the adsorption structure of K on Ni(100),* Surface Science **293**, 47 (1993)
- D H Wei, D C Skelton & S D Kevan, *Desorption and molecular interactions on surfaces: CO/Rh(110), CO/Rh(100) and CO/Rh(111),* Surface Science **381**, 49 (1997)
- J J Weimer, E Umbach & D Menzel, *The Properties of K and Co-adsorbed CO/K on Ru(0001),* Surface Science **159**, 83 (1985)
- M Weinert & R E Watson, *Core-level shifts in bulk alloys and surface ad-layers,* Physical Review B **51**, 17 168 (1995)
- J A White & D M Bird, *Implementation of gradient-corrected exchange-correlation potentials in Car-Parrinello total-energy calculations,* Physical Review B **50**, 4954 (1994)
- E P Wigner, Physical Review **46**, 1002 (1934)
- Steffen Wilke, Morrel H Cohen & Matthias Scheffler, *Local iso-electronic reactivity of solid surfaces,* Physical Review Letters **77** 1560 (1996)
- Ellen D Williams & W H Weinberg, *The geometric structure of carbon monoxide chemisorbed on the ruthenium (001) surface at low temperatures,* Surface Science **82**, 93 (1979)
- A Williams & J Soler, Bulletin of the American Physical Society **32**, 562 (1987)
- E Wimmer, A J Freeman, J R Hiskes & A M Karo, *All-electron local-density theory of alkali-metal bonding on transition-metal surfaces: Cs on W(001),* Physical Review B **28**, 3074 (1983)
- J Wintterlin, J Trost, S Renisch, R Schuster, T Zambelli & G. Ertl, *Real-time STM observations of atomic equilibrium fluctuations in an adsorbate system: O/Ru(0001),* Surface Science **394**, 159 (1997)
- D M Wood & Alex Zunger, *A new method for diagonalising large matrices,* Journal of Physics A: Math Gen **18**, 1343 (1985)
- B Woratschek, W Sesselmann, J Küppers, G Ertl & H Haberland, *Singlet to triplet conversion of meta-stable He atoms during de-excitation at a Cs-covered surface,* Physical Review Letters **55**, 611 (1985); G Ertl & J Küppers, *Low Energy Electron and Surface Chemistry,* VCH, Weinheim (1985)
- Yingkai Zhang, Wei Pan & Weitao Yang, *Describing van der Waals Interaction in diatomic molecules with generalised gradient approximations: The role of the exchange functional,* Journal of Chemical Physics **107**, 7921 (1997)
- Y Zhang & W Yang, Comment on Perdew, Burke & Ernzerhof (1996), Physical Review Letters **80**, 890 (1998)

Appendix A

Methodological aspects

A.1 k point generation schemes

Here we shall elaborate on the different **k** point generation schemes and how to estimate the accuracy provided by different sets. Then we shall explain the new **k** point sets which were found by the author to extend the scheme of Cunningham (1974) to the case of two-dimensional hexagonal unit cells.

The quality of a given **k** point set is determined by the amount of error caused in the discrete integration Equation 2.35. We can analyse this error (Chadi & Cohen, 1973) by first expanding the periodic function $f(\mathbf{r})$ to be integrated as a Fourier series

$$f(\mathbf{k}) = f_0 + \sum_{m=1}^{\infty} f_m A_m(\mathbf{k}) \ , \tag{A.1}$$

where f_n, $n = 0, \ldots$ are the expansion coefficients and $A_m(\mathbf{k})$ are

$$A_m(\mathbf{k}) = \sum_{\mathbf{R}_m} e^{i\mathbf{k}\cdot\mathbf{R}_m} \ . \tag{A.2}$$

$\mathbf{R}_m$ contains the real space lattice vectors which are related with the symmetry operations T_i of the symmetry group T, and the subsequent "shells" are ordered so that $0 < |\mathbf{R}_m| \leq |\mathbf{R}_{m+1}|$. The $A_m(\mathbf{k})$ are real-valued and satisfy the following relations:

$$\begin{aligned}
\frac{\Omega}{(2\pi)^3} \int_{\mathrm{BZ}} A_m(\mathbf{k}) \, d\mathbf{k} &= 0 \ , \ m = 1, 2, \ldots \\
\frac{\Omega}{(2\pi)^3} \int_{\mathrm{BZ}} A_m(\mathbf{k}) \, A_n(\mathbf{k}) \, d\mathbf{k} &= N_m \delta_{mn} \\
A_m(\mathbf{k} + \mathbf{G}) &= A_m(\mathbf{k}) \\
A_m(T_i\mathbf{k}) &= A_m(\mathbf{k}) \\
A_m(\mathbf{k}) \, A_n(\mathbf{k}) &= \sum_j a_j(m,n) \, A_j(\mathbf{k}) \ ,
\end{aligned} \tag{A.3}$$

where Ω is the volume of the real space primitive cell, N_m is the number of lattice vectors in the shell $\mathbf{R}_m$ and $\mathbf{G}$ is any reciprocal lattice vector.

The value we want is the integral over the first Brillouin zone,

$$\bar{f} = \frac{\Omega}{(2\pi)^3} \int_{\mathrm{BZ}} f(\mathbf{k}) \, d\mathbf{k} \ . \tag{A.4}$$

By inspection of the Equations A.1 and A.4 one immediately notices that

$$\bar{f} = f_0 \ , \tag{A.5}$$

i.e. the "average" value is just the $R_m = 0$ like always in Fourier transforms and series.

The result of the integral over the set of discrete **k** points 2.35 would be exact if the conditions A.3 would be fulfilled also in the case of the finite **k** point set. This is, however, in general not possible and one has to make a convenient choice of the **k** points. It was shown by Chadi and Cohen that in general the error in integration rapidly decreases with increasing R_m and thus it's best to choose a set which gives zero from as many of the first – *i.e.* shortest – R_m shells as possible. This implies the following condition for the **k** points and their weights:

$$\sum_{\mathbf{k}_i} w_{\mathbf{k}_i} A_m(\mathbf{k}_i) = 0 \ , \quad m = 1, \ldots, N \ . \tag{A.6}$$

As this requirement cannot be fulfilled with a finite number of points there remains error in the sum 2.35 whose magnitude can be obtained from the Equation A.1 multiplying with $w_{\mathbf{k}_i}$ and summing over the k-points:

$$\begin{aligned} \sum_{\mathbf{k}_i} i w_{\mathbf{k}_i} f_0 &= \sum_{\mathbf{k}_i} w_{\mathbf{k}_i} f(\mathbf{k}_i) - \sum_m f_m \sum_{\mathbf{k}_i} w_{\mathbf{k}_i} A_m(\mathbf{k}_i) \\ \Leftrightarrow f_0 &= \sum_{\mathbf{k}_i} w_{\mathbf{k}_i} f(\mathbf{k}_i) - \sum_m{}' f_m \sum_{\mathbf{k}_i} w_{\mathbf{k}_i} A_m(\mathbf{k}_i) \ , \end{aligned} \tag{A.7}$$

where the prime denotes that terms for which the Equation A.6 holds are excluded from the sum. For smooth functions the expansion coefficients decrease rapidly in magnitude and thus by choosing the number of k-points large enough the error can be made negligibly small. Then the sum in the Equation 2.35 becomes a good estimate for the continuous integral,

$$\bar{f} \approx \sum_{\mathbf{k}_i} w_{\mathbf{k}_i} f\left(\mathbf{k}_i\right) \ . \tag{A.8}$$

Chadi and Cohen then continued to show that their points for the face centred cubic cell give an error

$$\epsilon \simeq \sum_m{}' \frac{S_m}{\left|\mathbf{R}_m\right|^3} \ , \tag{A.9}$$

where $S_m = \sum_{\mathbf{k}_i} w_{\mathbf{k}_i} A_m(\mathbf{k}_i)/N_m = \pm 1$. This form has also been used to evaluate the effectiveness of k-point set in the present work:

$$\epsilon \simeq \sum_m \frac{\sum_{\mathbf{k}_i} w_{\mathbf{k}_i} A_m(\mathbf{k}_i)}{N_m \left|\mathbf{R}_m\right|^3} \ . \tag{A.10}$$

As the magnitude of the terms included in the sum decreases rapidly due to the denominator one can terminate the series after rather a small number of shells.

The general procedure to assign the weights w_i on the $\mathbf{k}$ points is first to give an equivalent weight on all the points in the full Brillouin zone. The lattice symmetry operations, including the inversion,[1] are then applied to find the irreducible part of the Brillouin zone and the $\mathbf{k}$ points related by a symmetry operation. The weight of a $\mathbf{k}$ point in the irreducible part of the Brillouin zone is then the number of points related to the current point by the symmetry operations divided by the total number of $\mathbf{k}$ points in the whole Brillouin zone. For clarifying examples please see below.

A.1.1 Monkhorst–Pack construction of k points

The most straight-forward approach to arrange an integration over a function whose general shape is unknown is to arrange an equidistance grid with a constant distance between the points. Monkhorst and Pack (1976) introduced a simple algorithm to obtain the $\mathbf{k}$ point sets: The points in three dimensions are linear combinations of the reciprocal lattice vectors $\mathbf{b}_1$, $\mathbf{b}_2$ and $\mathbf{b}_3$:

$$\mathbf{k} = n_1\mathbf{b}_1 + n_2\mathbf{b}_2 + n_3\mathbf{b}_3 \ . \tag{A.11}$$

The coefficients n_1, n_2 and n_3 are given by

$$n_i = \frac{2p_i - q_i - 1}{2q_i} \ , \ p_i = 1, \ \ldots, \ 2q_i \ . \tag{A.12}$$

The integers q_i are the number of divisions in the three directions. Please note that the Γ point (0,0,0) is contained in the $\mathbf{k}$ point set only if all q_i's are odd because $\mathbf{b}_1$, $\mathbf{b}_2$ and $\mathbf{b}_3$ are linearly independent and thus n_1, n_2 and n_3 must all simultaneously be equal to zero. Examples of these sets will be given below as their illustration is easier in two dimensions.

Fehlner and Vosko (1977) generalised the Monkhorst-Pack point sets by adding a constant vector $\mathbf{k}_0$ to all the $\mathbf{k}$ points:

$$\mathbf{k} = n_1\mathbf{b}_1 + n_2\mathbf{b}_2 + n_3\mathbf{b}_3 + \mathbf{k}_0 \ . \tag{A.13}$$

It is easy to verify that these points zero exactly the same cells in the Equation A.6 as the original Monkhorst-Pack points, *i.e.* when $\mathbf{k}_0 = \mathbf{0}$. The advantage of this generalisation becomes obvious when discussing the $\mathbf{k}$ point sets for the hexagonal cells.

A.1.2 Chadi–Cohen construction of k points

Chadi and Cohen (1973) also gave a practical formula for generating $\mathbf{k}$ point sets. It is based on using the so-called generating $\mathbf{k}$ points $\mathbf{k}_1$ and $\mathbf{k}_2$ from which the set is generated by

$$\mathbf{k}_i = \mathbf{k}_1 + \mathrm{T}_i\mathbf{k}_2 \ , \tag{A.14}$$

[1] The inversion symmetry in $\mathbf{k}$ points is always present due to the time-inversion symmetry (Tinkham, 1964)

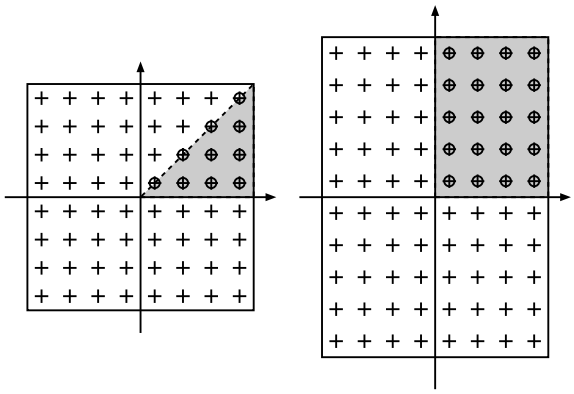

Figure A.1: **k** point sets for two dimensional square and rectangular lattices; the shaded area is the irreducible wedge of the Brillouin zone and the circles the **k** points in it. The division is $q_1 = q_2 = 8$ for the square and $q_1 = 8$, $q_2 = 10$ for the rectangular lattice

where T_i is the symmetry operation of the lattice symmetry group. One can straight-forwardly show that if $\mathbf{k}_1$ satisfies the Equation A.6 for shells C_{m_1} and $\mathbf{k}_2$ for shells C_{m_2} then the new points $\mathbf{k}_i$ satisfy it for both C_{m_1} and C_{m_2}. Thus Chadi and Cohen suggested to choose $\mathbf{k}_1$ so as to zero as many shells as possible and to take $\mathbf{k}_2$ which zeroes further as many of the first non-zero shells of $\mathbf{k}_1$ as possible. Note that in the point sets of Chadi and Cohen the generating points or Γ point do not occur in the final sets. Cunningham (1974) applied the Chadi-Cohen procedure to obtain **k** point sets for two dimensional lattices; the case of the hexagonal lattice will be discussed in detail below.

A.1.3 Two-dimensional hexagonal k point sets

In the case of hexagonal super cell there has been an ongoing debate about the relative merits of different **k** point sets (Chadi, 1977; Pack & Monkhorst, 1977; MacDonald, 1978). The problem arose because the original Monkhorst-Pack **k** point sets can not be reduced with the lattice symmetry operations to the smallest possible irreducible part of the Brillouin zone, and since the number of points in subsequent Cunningham sets increases rapidly, thus providing little flexibility in the choice of the set to be used. The addition of a constant "shift" vector to the Monkhorst-Pack points – please see above – enabled the reduction of the Brillouin zone with the full lattice symmetry group but Γ and other extreme points are then included, and below we shall discuss the generalisation of the Cunningham point sets which provides a vast number of new sets between those originally introduced by Cunningham.

Monkhorst-Pack k point sets

We first show the **k** point sets for the square and rectangular cells in the Figure A.1. The square lattice corresponds to a fcc(100) or bcc(100) face and the rectangular to a fcc(110) or bcc(110) face. The division parameters q_1 and q_2 are equal to eight in the square and eight and ten in the rectangular lattice. The regularity of the grid and the avoidance of $\bar{\Gamma} = (0, 0)$ are clearly visible. The latter aspect is why we do not use any constant shift in the set, *i.e.* $\mathbf{k}_0 = \mathbf{0}$, because this way we avoid having any of the corner points in the set.

It is easy to illustrate the problem with the original Monkhorst-Pack points in the hexagonal cells; let us consider the set with $q_1 = q_2 = 4$. Then $n_1 = \pm\frac{1}{8}, \pm\frac{3}{8}$, $n_2 = \pm\frac{1}{8}, \pm\frac{3}{8}$. We show these points in the Figure A.2, and it becomes immediately obvious that the points can have only the symmetry operations identity, inversion, a mirror plane and a two-fold rotation.[2] There the wedge, which can be obtained by reducing using only the symmetries of the **k** set, of the Brillouin zone remains larger than what is possible and more **k** points are needed compared to a set which can be fully reduced in order to obtain the same accuracy.

Adding a constant **k** vector $\mathbf{k}_0$ which shifts one of the points to the origin $\bar{\Gamma}$ removes this shortcoming and fulfils the whole lattice symmetry group – please see the Figure A.3; thus the irreducible part is only one twelfth of the whole Brillouin zone due to the six lattice symmetry operations[3] plus inversion, altogether twelve separate operations. There appear points also at the outer boundary of the Brillouin zone; this is a general feature of those sets, and has to be taken into account when assigning the weights on the **k** points.

These "shifted Monkhorst-Pack sets" can be easily generated in practise by first drawing an hexagonal equidistance mesh of points centred at $\bar{\Gamma}$. Subsequent sets are then obtained by moving a line – the border of the Brillouin zone – perpendicular to the boundary of the Brillouin zone; whenever the line constitutes a mirror plane an acceptable set is obtained.[4] Note that there are two different ways to form a set depending whether the boundary of the Brillouin zone is perpendicular to $\mathbf{u}_1$ or $\mathbf{u}_2$. Only one of them is given by the shifted Monkhorst-Pack construction; it turns out that they give a better efficiency than the other sets, "30° rotated"

[2] The two-fold rotation is missing in the real-space lattice symmetry operations of the fcc and hcp lattices due to the stacking

[3] If the symmetry group is C_{3v} as it is for the fcc(111) and hcp(0001) surfaces. The operations T_i are identity operation, two rotations by $2\pi/3$ and three mirror planes

[4] The mirror plane guarantees the continuation of the translational symmetry of the grid to the next Brillouin zone

Figure A.2: The **k** point set by the original Monkhorst-Pack scheme obtained with $q_1 = q_2 = 4$; the smmallest wedge of the Brillouin zone which is obtained applying the symmetries of the **k** points is shaded. The arrows show the directions of the reciprocal lattice vectors

Figure A.3: The **k** point set by the modified Monkhorst-Pack scheme obtained with $q_1 = q_2 = 4$ when k_0 is chosen to have $\bar{\Gamma}$ in the resulting set

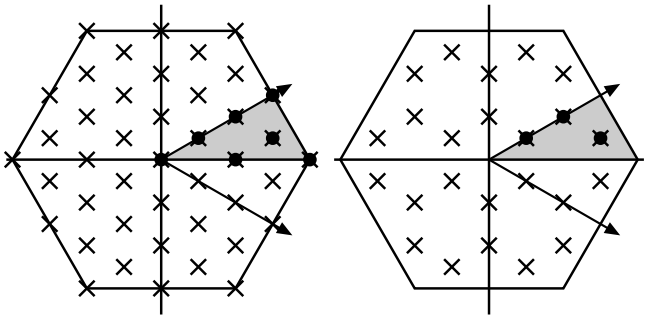

Figure A.4: Examples of the shifted Monkhorst-Pack – *left* – and Cunningham – *right* – **k** point sets

sets; the latter will be denoted by a sign $\angle$ below. However, the rotated sets are needed to give equivalent folding of sets in some cells, especially in the hcp $(\sqrt{3} \times \sqrt{3})$R30° cell.

Cunningham (two-dimensional Chadi-Cohen) k point sets

Cunningham applied the procedure of Chadi and Cohen to the six two-dimensional Bravais lattices. For the square and rectangular the Cunningham sets form a subset of the Monkhorst-Pack **k** point sets like in the three-dimensional case. On the other hand, the Cunningham sets in the hexagonal lattice are visibly different from the shifted Monkhorst-Pack points – please see the Figure A.4: whereas the shifted Monkhorst-Pack points are arranged on a regular grid the Cunningham points contain "holes", *i.e.* points, which are included in the shifted Monkhorst-Pack sets, are missing. These "holes" are exactly the generating points from the previous smaller set; Cunningham furthermore proposed a two-point set which is not related to the subsequent sets with this "rule", but Chadi later proposed a more efficient two-point set. As it turns out below the **k** point mesh does not have to be uniform in order to zero the shells in the Equation A.6, but these points give even a better efficiency than the shifted Monkhorst-Pack points in sets containing a few points. Moreover, the $\bar{\Gamma}$ and other corner points are avoided in these sets, if this property is regarded as essential.

Extended Cunningham k-point sets

As mentioned above the shortcoming of the Cunningham point sets is that the number of points in subsequent sets increases rapidly whereas the shifted Monkhorst-Pack sets provide sets for almost any number of points. However, by folding the original Cunningham points between different Brillouin zones we found out that there exist many other sets – here called the extended Cunningham point sets – which look exactly like the Cunningham point sets, *i.e.* they contain a "missing point" at the centre of each hexagon; please see the Figure A.4. Like for the shifted Monkhorst-Pack sets we were able to find two groups of different sets, the others being 30° rotated with respect to the others; actually the original Cunningham point sets belong to these two groups alternatingly, for example the six-point set belongs to the "rotated" sets, the 18-point set to the original or un-rotated sets, the 45-point set again to the rotated ones *etc*.

We haven't thought of any "mathematically correct" way how to obtain the extended Cunningham point sets,

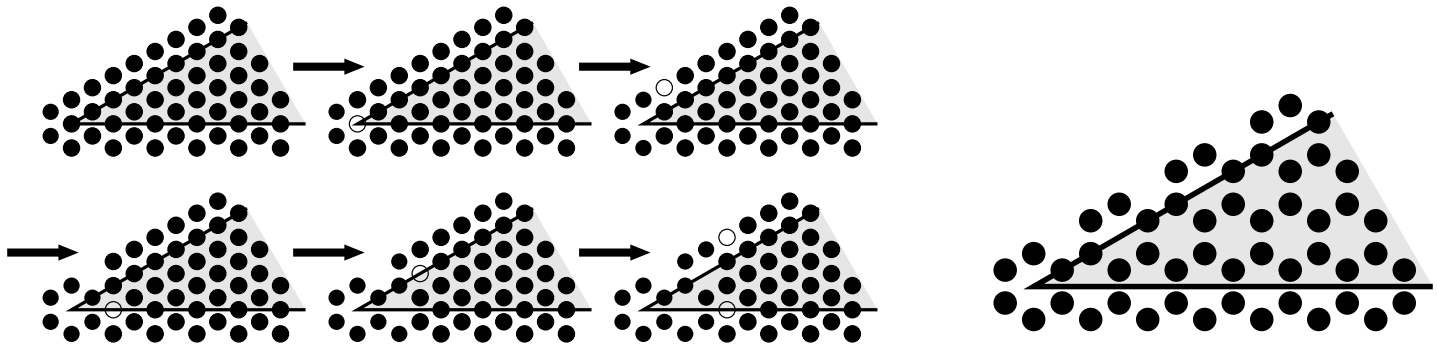

Figure A.5: The procedure to progressively extract the points not belonging to the extended Cunningham sets from the shifted Monkhorst-Pack points

Figure A.6: The grid of the **k** points belonging to the extended Cunningham point sets; the shaded area belongs to the irreducible wedge of the Brillouin zone

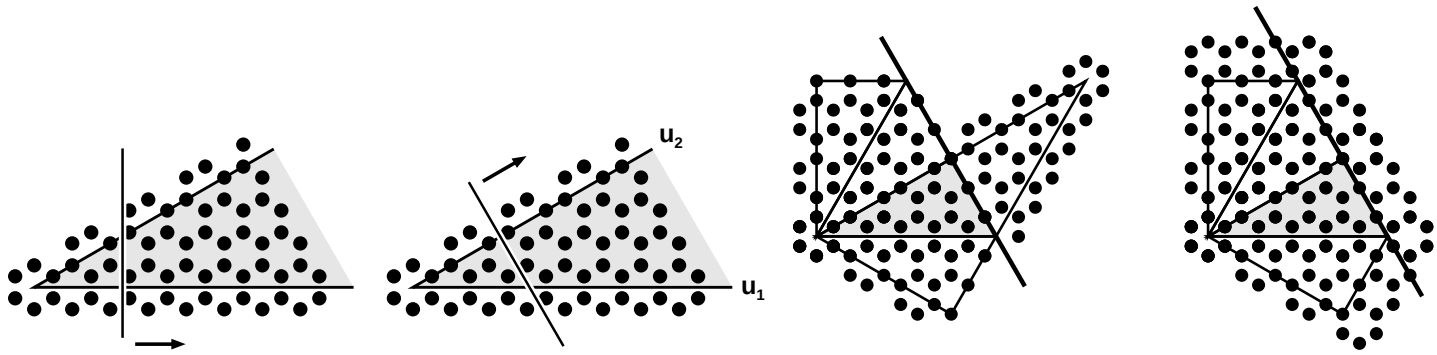

Figure A.7: The procedure to select the extended Cunningham **k** point sets: the line is moved along u_1 or u_2 until some of the valid sets is found. These are obtained when there is a mirror plane perpendicular to $\mathbf{u}_1$ or $\mathbf{u}_2$. The latter leads to the rotated sets $\angle$

Figure A.8: An example of an invalid set generated with the method of the extended Cunningham sets: the pattern is not continuous – *left* – and there is no mirror plane at the Brillouin zone boundary – *right*

except naturally choosing the generating points correctly.[5] However, in practise it is trivial to obtain the point sets using the construction scheme given above for the shifted Monkhorst-Pack points: one starts with the equidistance mesh, first removes $\bar{\Gamma}$ from the set as in the Figure A.5, next the point at the centre of the hexagon neighbouring the hexagon around $\bar{\Gamma}$ and continues removing the points at the centres of the neighbouring hexagons. This results into the grid of points in the Figure A.6; the acceptable sets are again obtained by moving a line perpendicular to the vector $\mathbf{u}_1$ or $\mathbf{u}_2$, at the position where the line acts as a mirror plane for the sets inside and outside the first Brillouin zone. Note that the symmetry requirement is now more restrictive than for the shifted Monkhorst-Pack points due to the "holes"; please see the Figure A.8 for examples of rejected sets.

The sets obtained from the scheme above are listed in the Table A.1 and some of them are shown in the Figure A.9. Please note that these sets include all the original Cunningham sets, and also sets with points at the boundary of the Brillouin zone, *e.g.* the set $\angle 9$. The efficiency, defined as the number of shells zeroed in the Equation A.6 divided by the number of points in the set, of the extended sets is also given and it is compared to the efficiency of the shifted Monkhorst-Pack sets in the Figure A.10 and the Table A.1. The few-point sets seem to be better in the extended Cunningham point sets, but for the larger number of points the shifted Monkhorst-Pack point sets give a smaller error in the purely mathematical analysis of the error; the physical function to be integrated – the density over the Brillouin zone – often contains the most striking features like surface states at and near the corners of the Brillouin zone. Therefore it remains a matter of importance of these states whether the **k** point set should contain points at these points – shifted Monkhorst-Pack points – or not – extended Cunningham points; in the first case the effects from the $\bar{\Gamma}$ and other corner points might be over-emphasised whereas in the second case a larger number of points is needed before the details at the corners are sampled sufficiently accurately.

[5] Since the extended sets appear exactly like the original Cunningham sets and the subsequent set is obtained by choosing $\mathbf{k}_1$ in the Equation A.14 to be the points in the current set, the extended sets must result from a suitable choice of the initial, one- or few-point set

Table A.1: The efficiency of the shifted Monkhorst-Pack and extended Cunningham **k** point sets. Γ, C, E and I show the number of Γ, corner, edge and interior points, respectively, and they have a degeneracy of 1, 3, 6 and 12 when counting the weights of the **k** points if the symmetry group is C_{3v}. $\#k_{BZ}$ is the number of points in the whole two dimensional Brillouin zone, #0 the number of shells zeroed in the Equation A.6 and the last column shows the error estimate of Chadi and Cohen. ∠ indicates that the set is rotated by 30° compared to the unrotated sets; please note that the rotated sets perform worse in the quality

Extended Cunningham

	Γ	C	E	I	$\#k_{BZ}$	#0	CC error
1	0	0	1	0	6	1	4.4290
∠1	0	1	0	0	3	0	—
∠2	0	1	1	0	8	2	2.8687
3	0	0	2	1	24	5	0.5437
∠3	0	0	3	0	18	4	0.8410
∠5	0	1	3	1	32	7	0.3511
6	0	0	3	3	54	11	0.1578
∠7	0	1	4	2	50	10	0.1773
∠9	0	0	6	3	72	14	0.1017
10	0	0	4	6	96	18	0.0654
∠12	0	1	6	5	98	19	0.0631
15	0	0	5	10	150	28	0.0324
∠15	0	1	7	7	128	25	0.0418
∠18	0	0	9	9	162	31	0.0289
21	0	0	6	15	216	39	0.0184
∠22	0	1	9	12	200	37	0.0207

Shifted Monkhorst-Pack

	Γ	C	E	I	$\#k_{BZ}$	#0	CC error
1	1	0	0	0	1	0	—
2	1	1	0	0	4	2	4.8221
∠2	1	1	0	0	3	1	7.4424
3	1	1	1	0	10	4	1.4156
4	1	1	2	0	16	7	0.5916
∠4	1	2	1	0	12	5	0.9154
5	1	0	4	0	25	10	0.2995
∠6	1	1	4	0	27	11	0.2665
7	1	2	3	1	37	14	0.1720
8	1	0	6	1	49	19	0.1070
∠9	1	2	5	1	48	18	0.1106
10	1	1	6	2	64	25	0.0710
12	1	1	7	3	82	31	0.0491
∠12	1	1	8	2	75	28	0.0551
14	1	1	8	4	100	37	0.0353
16	1	0	10	5	121	44	0.0262
∠16	1	2	9	4	108	39	0.0314
19	1	2	9	7	145	51	0.0202
∠20	1	1	12	6	145	52	0.0193
21	1	0	12	8	169	60	0.0154
24	1	1	12	10	196	70	0.0123
∠25	1	2	13	9	192	67	0.0127

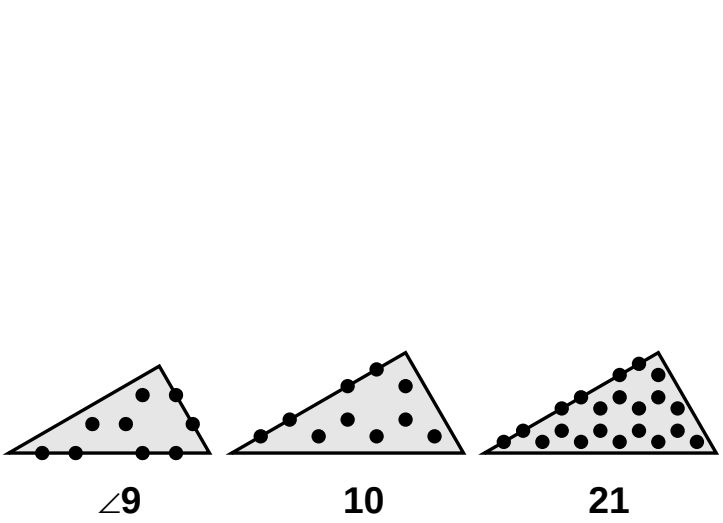

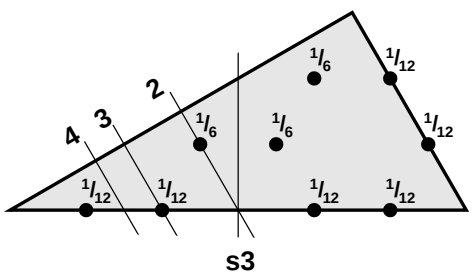

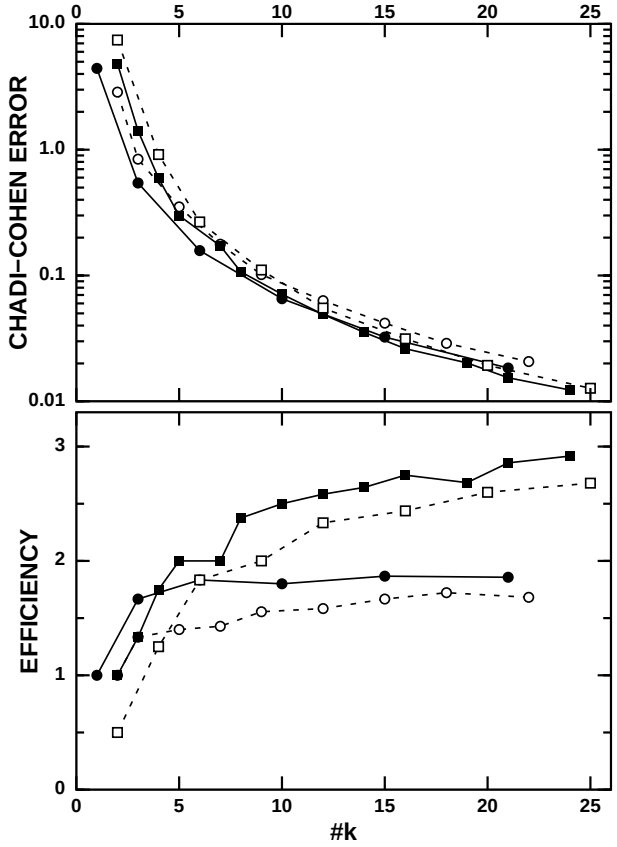

Figure A.9: Examples of the extended Cunningham **k** point sets with ∠9, 10 and 21 points not included in the original work of Cunningham. The lower part shows for the ∠9 point set – used in most of the calculations for ruthenium in the present work – the **k** point weights w_i and folding into $(\sqrt{3}\times\sqrt{3})$R30°, (2×2), (3×3) and (4×4) super-cells. Also folding into at least (2×1), c(2×4) and $(2\sqrt{3}\times2\sqrt{3})$ is possible

Figure A.10: The error estimate of Chadi and Cohen – upper panel – and the efficiency E – lower panel – for the smallest shifted Monkhorst-Pack – squares – and extended Cunningham – spheres **k** point sets. The dashed lines and empty symbols correspond to the rotated **k** sets. The efficiency is defined as the number of shells zeroed in the Equation A.6 divided by the number of points in the set

A.2 Parallelisation of a plane wave code

Although the computational algorithms and computational power have progressed enormously within the last twenty years the amount of calculations is still huge – all computational capacity can be exceeded at least by growing the system size – and time-consuming; thus although there is no direct way of cutting the amount of computation the through-put time can be reduced by employing parallel processing, *i.e.* splitting the problem to several processors which solve each a part of the task simultaneously. The parallel computer architectures have in recent years developed towards massively parallel processing, with up to thousands of processors; parallelising in such platforms requires large efforts in adapting the traditionally serial programs to efficiently performing parallel codes, and not everyone can afford such large, dedicated machines. Also the parallel execution of a program usually increases the total time of computing compared to several independently running serial programs so parallel processing should be used cautiously and only when it is necessary due to the otherwise too long an execution time or other limitations, *e.g.* disc or memory space.

The plane wave pseudo potential method contains mostly large number of almost independent elements and is thus rather straight-forward to parallelise; there are four different approaches (Clarke, Štich & Payne, 1992) at which level to parallelise the method:

- task-parallel: run the same serial code on several processors; very efficient as long as the machines carry enough of memory. This approach is the easiest and cheapest in terms of programming and there is no requirement for inter-processor communication

- **k**-parallel: each node has a part of the **k** points and since the **k** points are almost independent – the density needs to be summed up from all the nodes, furthermore only a couple of trivial operations like determining the occupation numbers; this is the case for the mostly used exchange-correlation functionals, which depend only on the density and not the individual orbitals. The inter-processor communication may be slow, and the amount of additional programming is minimal; however, especially in large systems the number of **k** points is small and this approach can be used only for a couple of processors and hardly ever with more than 8-16 processors. The calculation not explicitly dependent on the **k** points like the density and potential consumes usually only a minor part of the total execution time and thus does not need to be parallelised

- state-parallel: the electronic states are divided to the processors, and they are almost as independent as the **k** points but during the ortho-normalisation of the orbitals – usually with the Gram-Schmidt algorithm – all the orbitals at a **k** point need to be communicated. This causes a lot of simultaneous traffic and thus sets a higher requirement for the network speed and band-width

- plane wave-parallel: as there are lots of plane waves which are independent and operate all the same way the plane wave method is rather easy to parallelise by distributing the calculation at different **g** vectors to the nodes. However, during the three-dimensional fast Fourier transforms all the **g** vectors are needed and a very high demand on the communication speed is set; indeed only few massively parallel architectures – like the Cray T3E (`http://www.cray.com/`) – are suited for this approach, but it offers the advantage not available in the aforementioned schemes that also the fast Fourier transform arrays can be split among the nodes; the calculation of the local potential can and must also be easily parallelised since when going to a high number of processors the relative time in its calculation increases. Although this approach is very critical to achieve a good parallel efficiency even over-linear scaling can been achieved because the total amount of the fast cache memory is increased and arrays can now be stored in the memory instead of recalculating thanks to the increased total memory

The different approaches can be combined, *e.g.* the **G**vectors of a **k** are given to a set of processors like shown in the Figure A.11. The best parallel efficiency can be achieved by such groupings, keeping the **G** vector groups as rather small within the limitations from the memory.

The most difficult part in the parallelisation over the plane waves is the three-dimensional fast Fourier transform; however, like mentioned in the Section 2.4.1 it is composed of three subsequent one-dimensional transforms so that the result on one point is not connected to all the other data simultaneously but only the rows with the same $\mathbf{G}_i$ are connected like was discussed in the Section 2.4.1. Therefore a good strategy to minimise the data communication is to divide the **G** vectors to the processors so that all the vectors on one row in one of the directions are on the same processor, and in the real space the grid points are distributed into groups of planes so that after the inverse transform in the third direction the data does not need to be communicated again as shown in the Figure A.12; the forward transform from real to reciprocal space is just the opposite of the backward transform.

For the wave function a further reduction in the size of data needed to be communicated is achieved by sending only the non-zero data which was described above in the Section 2.4.1.

The parallelisation of the plane wave method is nowadays a standard task and has been documented in the literature; please see *e.g.* Clarke, Štich and Payne (1992), Nelson, Plimpton and Sears (1993) and Brommer *et al* (1993). For example the codes CASTEP/CETEP (Cambridge and Edinburgh/UK), CPMD (Stuttgart/Germany, Zürich/Switzerland), `fhi94md` (Berlin/Germany), FINGER (Helsinki/Finland) and VASP (Vienna/Austria) and the codes used in Lausanne/Switzerland and Trieste/Italy have been parallelised over the **G** vectors.

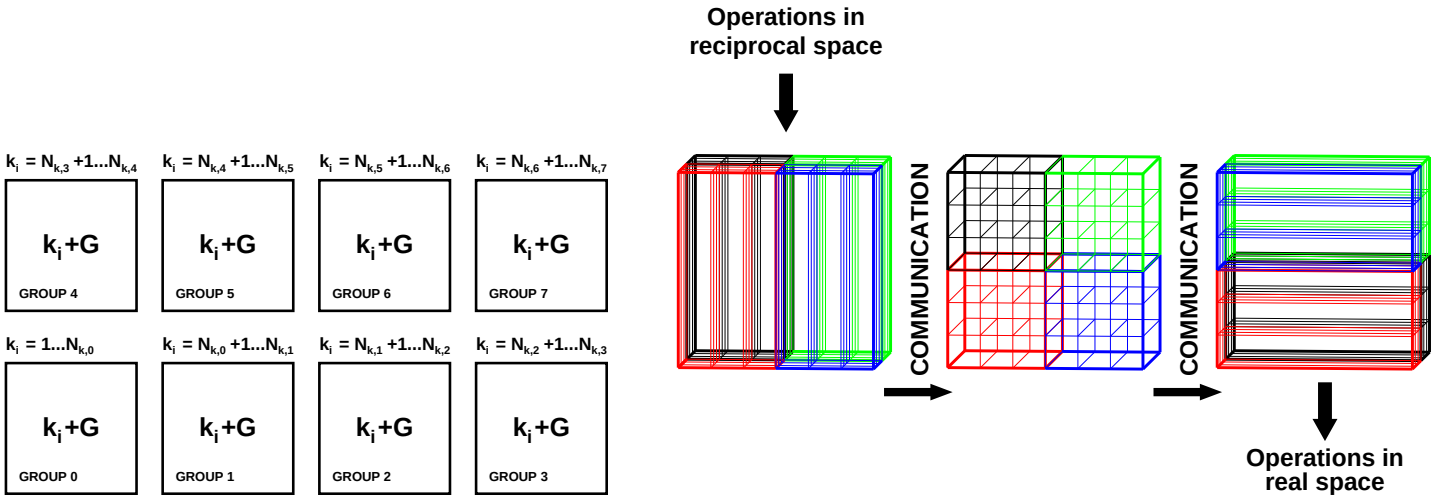

Figure A.11: The grouping of **k** and **G** vectors into two-layer parallelism; in this case the 32 nodes divide the **k** points to the eight groups, and the nodes inside a group further divide the **G** vectors among themselves

Figure A.12: The distribution of elements in reciprocal and real spaces in order to minimise the communications in the three-dimensional fast Fourier transform; the two operations when changing the direction of the transform correspond to a matrix transpose and a communication both. The columns with different colours belong to the different processors, four in our example

A.3 Evaluation of exchange-correlation energy and potential on a discrete grid

The exchange-correlation functional of the homogeneous electron gas is a smooth function and thus the calculations within the local density approximation converge generally easily. However, the functionals of gradient approximations are faster oscillating and therefore more sensitive to the quality of the basis set and numerical algorithms used. Furthermore, since the exchange-correlation term is evaluated on the real space grid it is not invariant of the atomic positions like illustrated in the Figure A.13; even at a cut-off energy of 50 Ry the distance between the grid points is about 0.18 Å and 0.4 Å at 10 Ry cut-off energy. The error does not only affect the energy and potential but also via the self-consistency and, when employing the non-linear core-valence exchange-correlation scheme directly, the forces. While no real solution to this problem has appeared White and Bird (1994) proposed a method which ought to improve the stability and, in some cases, improve the accuracy. Their method will be discussed in a while. Overall the difficulties due to the discrete grid have been studied very little, as the errors from other origins – like the local density approximation, finite basis set, pseudo potentials – have traditionally been much larger than the discretisation error but now, when the calculations are getting more accurate due to the improved computational power, more transferable pseudo potentials *etc* and due to the more frequent use of the gradient approximation, the relative magnitude of this error is emphasised and in our opinion needs special attention.

The problems due to the grid underlying the exchange-correlation energy and potential can arise in various ways:

- The total energy is not constant upon a rigid shift of all atoms in the same direction, without changing the symmetry operations.
- The forces are not zero in a symmetric bulk structure, or they change upon a constant shift of all atoms

It is usually easy to test for the existence and magnitude of the grid effects if their presence is suspected:

- The atoms are set to the original positions, preferably all to the grid points if possible; it has to be recognised here that the symmetries might be broken in the further steps and choose the symmetry operations so that they do not have to be changed later
- All the atoms are shifted by Δz along one axis – here chosen as z – where Δz is the distance of grid points along that axis and the electronic structure is calculated
- All the atoms are shifted by $\Delta z/2$ in the same direction
- All the atoms are shifted by $\Delta z/4$ in the same direction

If the energy and forces on the atoms are the same in the first two cases but different in the others then the grid affects the results; if furthermore all the atoms were originally on the grid points in the third case there are no artificial forces but the energy different from the first two cases, and in the final case even the forces should be asymmetric.

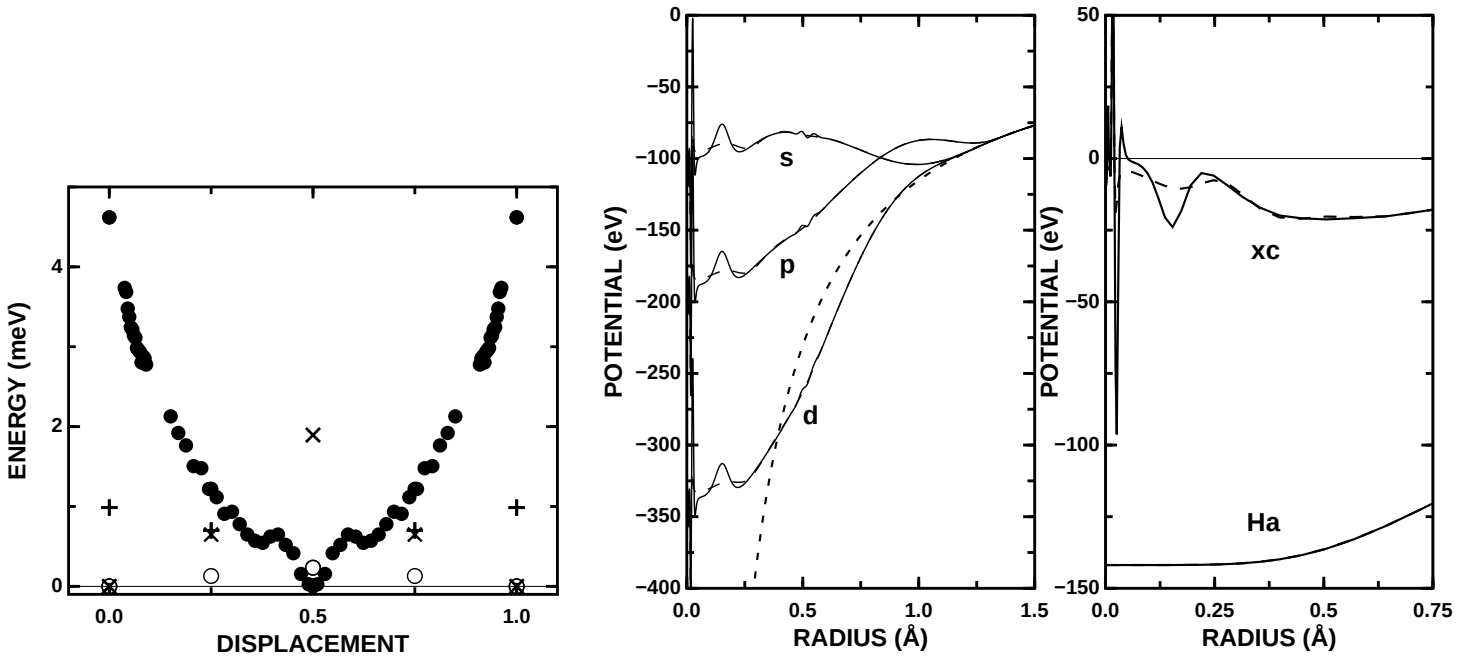

Figure A.13: The error arising from the discrete grid in the evaluation of the exchange-correlation energy and potential: An oxygen atom is moved along one axis between two real-space grid points. The Perdew-Wang'91 functional, a cut-off of 40 Ry for the plane wave basis and duelling 3.2 – filled circles –, 50 Ry/3.85 – crosses –, 70 Ry/4.0 – plus'es – and Perdew-Burke-Ernzerhof functional with 50 Ry/3.85 – empty spheres – were used, the displacement is in units of the grid spacing Δz in the direction of the move and the energy is normalised to its minimum value – at the mid-point between the grid points. Please notice that ideally the line should be zero

Figure A.14: The wiggles in the pseudo potentials for ruthenium generated with the generalised gradient approximation arising from the un-screening procedure. The left panel shows the ionic pseudo potentials generated using the functional of Perdew-Wang 1991 (Perdew, 1991; Perdew *et al*, 1992; Perdew, Burke & Wang, 1996) – solid lines – and Perdew, Burke and Ernzerhof (1996) – long-dashed lines and the -Z_v/r potential. The right panel shows the un-screening exchange-correlation and Hartree potentials

The functionals with gradients cause a further problem in the un-screening step: at the extrema of the density, where the gradient goes to zero, the functionals become unstable; this leads to rapid oscillations in the unscreened, ionic pseudo potentials like shown in the Figure A.14, and at the origin, or the nucleus, the potential diverges. This is, however, generally not significant because the volume of that point in the integrations is infinitely small and in radial integrals for the Fourier transform of the potentials the integrand is multiplied with r^2 and the origin is not weighted if the divergence is of lower order than squared. Please note that the un-screening Hartree potential is totally smooth and that the newer functional of Perdew, Burke and Ernzerhof (1996) behaves much smoother, and the wiggles at about 0.04 Å from the origin have almost disappeared. Since the discovery of this problem – which now has been recognised to be a consequence of the gradient functionals and not a numerical error (Fuchs, personal communication) – the wiggles were tried to be smoothed out by Ortiz and Ballone (1991) and Juan and Kaxiras (1994), but now it is believed they do not disturb the calculation and thus can be present (Fuchs & Scheffler, submitted).

White and Bird (1994) considered the practical implementation of gradient-augmented functional; they showed how one can implement the potential instead of the straight-forward form

$$\frac{df}{dn} = \frac{\partial f}{\partial n} - \nabla \cdot \frac{\partial f}{\partial (\nabla n)} = \frac{\partial f}{\partial n} - \sum_i \frac{\partial}{\partial x_i} \left[\frac{\partial f}{\partial (\partial n / \partial x_i)} \right] , \tag{A.15}$$

where f is the exchange-correlation energy per volume, making use of the fast Fourier transforms as

$$\frac{df}{dn} = \frac{\partial f}{\partial n} - \mathtt{FFT}^{-1} \left\{ \mathtt{i}\mathbf{G} \cdot \mathtt{FFT} \left[\frac{\nabla n}{|\nabla n|} \frac{\partial f}{\partial |\nabla n|} \right] \right\} . \tag{A.16}$$

Thus instead of having to calculate the partial derivatives and to operate to it with the gradient operator $\frac{\partial}{\partial x_i} \left[\frac{\partial f}{\partial (\partial n / \partial x_i)} \right]$ only the partial derivative $\frac{\partial f}{\partial |\nabla n|}$ is needed. The goal of White and Bird was, however, to obtain a numerically efficient and accurate form for the exchange-correlation potential, as they had noticed that if the term

$$\nabla n \cdot \nabla |\nabla n| \tag{A.17}$$

is evaluated as written here using the fast Fourier transform the result contains wave lengths shorter than what the discrete grid, set by the cut-off energy, can contain; thus the exchange-correlation energy and potential are not consistent with each other.

Table A.2: The convergence of the lattice constant a, bulk modulus B and the first derivative B' of the bulk modulus with respect to the pressure of bulk ruthenium in the face-centred cubic cell; the values in the parenthesis are differences in per cent from the value at 80 Ry. Also the total energy relative to the value at 80 Ry is shown

$E_{cut-off}$ (Ry)	a (Å)	B (MBar)	B'	ΔE (meV)
35	3.879 (−0.21)	2.947 (+1.15)	4.721 (+4.27)	511
40	3.888 (+0.04)	2.838 (−2.60)	4.648 (+2.66)	102
45	3.887 (−0.00)	2.924 (+0.36)	4.500 (−0.62)	16
50	3.887 (−0.00)	2.915 (+0.04)	4.522 (−0.12)	8
60	3.887 (+0.00)	2.916 (+0.06)	4.528 (−0.01)	6
70	3.887 (−0.00)	2.912 (−0.05)	4.535 (+0.15)	3
80	3.887 (≡ 0)	2.914 (≡ 0)	4.528 (≡ 0)	≡ 0

However, according to our current understanding (Martin Fuchs, personal communication) this shortcoming can be avoided also by using a different form of the term above:

$$\nabla n \cdot \nabla \left|\nabla n\right| = \nabla n \frac{\nabla n \cdot \nabla \nabla n}{\left|\nabla\right|} \,. \tag{A.18}$$

Although the right hand side looks even more complex than the previous form it can be calculated without a need for Fourier transforming any products of already transformed terms, and thus the exchange-correlation energy and potential are consistent. Yet the form which was suggested by White and Bird is easier to implement for a new gradient functional, and it also can be used (Martin Fuchs, personal communication) to evaluate the potential with the knowledge of the energy only by using finite differences of the energy to calculate the gradient in this form:

$$\frac{\partial f}{\partial \left|\nabla n\right|} \approx \frac{f\left(n; \left|\nabla n\right| + \delta \left|\nabla n\right|\right) - \partial f\left(n; \left|\nabla n\right|\right)}{\delta \left|\nabla n\right|} \tag{A.19}$$

and similarly for the term $\partial f / \partial n$; here we use for δ a small, positive value. In our tests the resulting potential is insensitive for values $\delta = 10^{-2} \ldots 10^{-7}$.

A.4 Test calculations

We have performed a plenty of test calculations for the transition metals and the atoms and molecules which were adsorbed on the surfaces. All the calculations performed make use of the generalised gradient approximation proposed by Perdew and co-workers (Perdew, 1991; Perdew *et al*, 1992; Perdew, Burke & Wang, 1996), but the newer functional of Perdew Burke and Ernzerhof (1996) yields very similar results.

A.4.1 Ruthenium

The pseudo potential which we used for the ruthenium was of the Troullier-Martins type since the electrons in the 4*d* valence shell are very tightly bound and thus would require an extensive plane wave basis set if the Bachelet-Hamann-Schlüter scheme would be used to construct the pseudo potential. The core radii were taken (Catherine Stampfl, personal communication) as $r_{c,l=sd} = 2.48$ Bohr, $r_{c,l=d} = 2.78$ Bohr and were not refined during the work; this pseudo potential has been seen to work well in our previous calculations *e.g.* for the nitrogen adsorption (Schwegmann *et al*, 1997) on the Ru(0001) or oxygen (Schwegmann *et al*, 1998) on the Ru$(10\bar{1}0)$ surface. The *s* component was used as the local component of the pseudo potential.

Cut-off energy

We first studied the size of the basis set needed to present the ruthenium well; since the convergence is rather insensitive to the environment we used the face-centred cubic bulk lattice as the test system rather than the real lattice of ruthenium, hexagonal close-packed, since in this there are two atoms per unit cell and the number of symmetry operations is lower than in the face-centred cubic lattice. We monitored the lattice constant, bulk modulus, the derivative of the bulk modulus with respect to the pressure and the total energy as a function of the cut-off energy; the results are collected in the Table A.2 and it is evident that already a basis set with a cut-off of 45 Ry would give a good convergence.

k point sampling

Next we checked the **k** point sampling required to approximate the integrals over the Brillouin zone accurately. The calculation of the equilibrium lattice structure in the hexagonal close-packed lattice is time consuming since there are two independent lattice parameters a and c whose values need to be resolved. We performed this by a two-dimensional grid of points over several values, typically $\approx 9 \times 8$, of a and c and fitting then a polynomial of the type

$$E(a,c) = f_0 + f_1 a + f_2 c + f_3 a^2 + f_4 ac + f_5 c^2 + f_6 a^3 + f_7 a^2 c + f_8 a c^2 + f_9 c^3 \tag{A.20}$$

Table A.3: The optimised lattice parameter a and the c/a ratio, and the total energy of bulk ruthenium in the close-packed hexagonal lattice. Cut-off energy was 60 Ry; although the total energy is not yet fully converged with the largest **k** sets the energies ΔE are given relative to the set 9×4

Set	Sampling	a (Å)	c/a	ΔE (meV)
Cunningham	3×4	2.742	1.623	−417
	6×2	2.774	1.583	−69
	6×4	2.776	1.580	−53
	9×2	2.774	1.585	−14
	9×4	2.780	1.576	—
Monkhorst-Pack	$4 \times 4 \times 8$	2.796	1.548	−89
	$5 \times 5 \times 8$	2.758	1.609	−92
	$6 \times 6 \times 8$	2.786	1.567	+16
	$8 \times 8 \times 8$	2.777	1.581	−25
Experimental		2.70	1.584	

Table A.4: Convergence tests for the thickness of the slab of Ru(0001) and the vacuum region with varying number of atomic N_{slab} and vacuum N_{vacuum} layers; given are the total energy per atom, the energy difference E(N)-E(N-1) which eventually would converge to the energy of an atom in bulk, and the work function. The calculations were done on ideal, non-relaxed slab; the relaxation of the outer-most atomic layer did not change the results noticeably

N_{slab}	N_{vacuum}	E(N)/N (eV)	E(N)-E(N-1) (eV)	ϕ (eV)
1	6	−440.812	—	5.807
2	6	−442.229	−443.646	5.179
3	6	−442.602	−443.349	4.995
4	6	−442.755	−443.211	5.177
5	6	−442.869	−443.325	5.157
6	6	−442.938	−443.285	5.143
4	1	−442.784		—
4	2	−442.753		—
4	3	−442.755		5.171
4	4	−442.755		5.172
4	5	−442.755		5.168
4	6	−442.755		5.177

where the f_i, $i = 1, \ldots, 9$ are the fitting parameters. The **k** point sets are referred to as $N_{\mathbf{k}_\parallel} \times N_{\mathbf{k}_c}$ for the Cunningham sets, where $N_{\mathbf{k}_\parallel} \times N_{\mathbf{k}_c}$ is the number of **k** points along the plane in the irreducible wedge of the Brillouin zone which is perpendicular to the c axis and $N_{\mathbf{k}_c}$ is the number of points in the upper space $\mathbf{k}_c > 0$; in the case of the Monkhorst-Pack sets the notation $N_{\mathbf{k}_1} \times N_{\mathbf{k}_3} \times N_{\mathbf{k}_3}$ is used where the $N_{\mathbf{k}_i}$ are the partitions in each direction i in the full Brillouin zone; the point sets were shifted so that perpendicular to the c axis $\mathbf{k}_{xy} = 0$ was included in the set in order to preserve the same symmetry as discussed in the Section A.1.3. The results collected are in the Table A.3 and they show that in the lattice parameters are reasonably well converged when going from the 6×4 to the 9×4 or from the $6 \times 6 \times 8$ to the $8 \times 8 \times 8$ sets. In the main body of the calculations in the present work we used from the set 9×4 the nine points parallel to the two-dimensional Brillouin zone in the slab calculations; the points are shown in the Figure A.9.

Thickness of slab and vacuum

When the slab geometry is used it is necessary to confirm that the slab is thick enough *i.e.* it has enough substrate layers so that the properties inside the slab approach those of the real bulk, and that the two surfaces do not interact via the slab or the vacuum; the latter is easy to notice if the asymptotic densities from the two surfaces overlap considerably. In the Table A.4 we show the results of a systematic study of the energy and work function as a function of the number of layers in the substrate and the equivalent in vacuum. We can conclude that beyond three to four layers of the substrate the results converge, and already three layers of vacuum, corresponding to about 6,5 Å, is enough to give well converged results. To be on the safe side we employed a five layer slab throughout the calculations of the present work unless otherwise mentioned, and we had about 15 Å of vacuum separating the slab from its own replicas; this distance was mainly dictated by the slow asymptotic decay of the density of the alkali metal cesium.

A.4.2 Oxygen

It turns out that the most stringent requirement for the basis set size is set by the oxygen; thus to have a consistent description of all the systems in the present work we must find a suitable compromise between the accuracy and the size of basis set. We search for this optimum by investigating the properties of the oxygen dimer, namely the bond length, vibrational frequency and binding energy of the oxygen dimer compared to two isolated oxygen atoms. The ground state of the atom and of the oxygen dimer are spin polarised but by the time we were doing these calculations we did not have access to a plane wave code with the spin polarisation implemented, although it is straight-forward to program; also the Kohn-Sham scheme, being based on a single

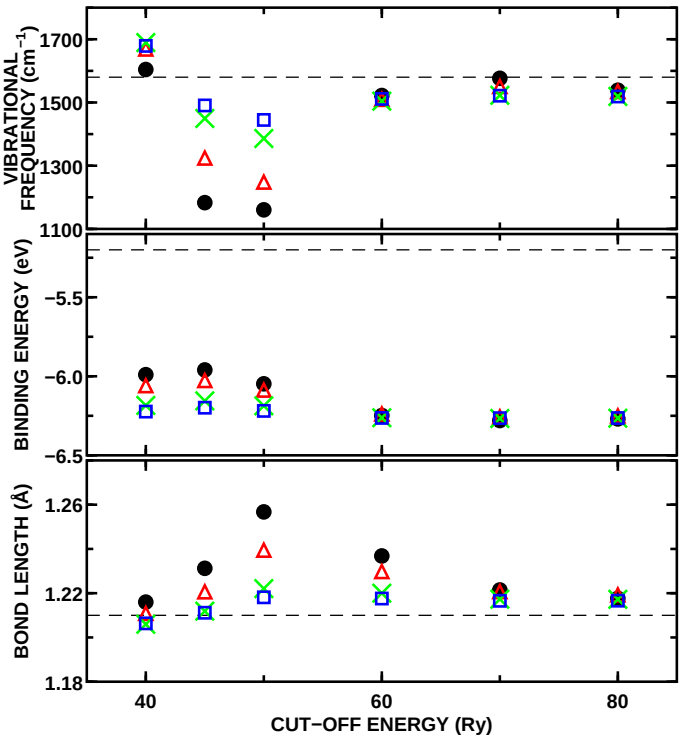

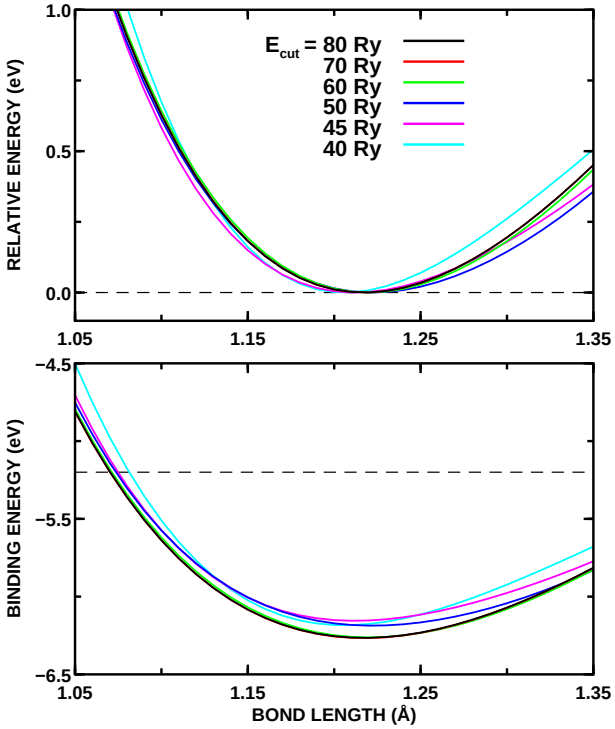

Figure A.15: Convergence test of the molecular properties of an oxygen dimer as a function of the cut-off energy used in the expansion of the Kohn-Sham orbitals in a basis of plane waves. The panels are from bottom to top the bond length in Ångströms, the binding or atomisation energy of the dimer to two isolated atoms and the frequency of the stretching mode vibration of the molecule in inverse centi metres. The horizontal dashed lines are the experimental values. The different markers are for different core radii of the *s* and *p* pseudo potentials – the radius of the *d* potential is irrelevant if it is included – and the markers are for $r_{c,l=sp} = 1.2$ Bohr – filled circles – 1.3 Bohr – triangles – 1.4 Bohr – crosses – and 1.5 Bohr – empty squares

Figure A.16: The energy versus bond length of an oxygen dimer calculated with different values of the cut-off energy; the core radii $r_{c,l=sp} = 1.4$ Bohr. Lower panel: the binding energy of the oxygen dimer, with the experimental value as the horizontal line. Upper panel: the same curves but with normalised to the minimum

determinant for the many bode wave function, gives the ground state of atoms with an open shell as non-spherical (Kutzler & Painter, 1987). The latter is difficult to achieve due to rapid oscillation in the occupation of the states which in principle are degenerate and thus close in the energy. Therefore we obtained the spin energies of the O_2 molecule and the energy difference between a spherical and non-spherical oxygen atom from a calculation employing a cluster program with the same exchange-correlation functional as in our calculations, and the spin energies of the atoms were kindly provided to us by Martin Fuchs (personal communication).

Size of unit cell

First we shall discuss the size of the unit cell necessary to isolate the molecules from each other; the Table A.5 shows the binding energy as a function of the length of the edges of a cubic cell; there remains interaction even beyond a separation of 9 Å, but we estimate the accuracy to be sufficient in a cell of 8-9 Å. Please notice that the unit cell size could probably be somewhat reduced by using a small set of special **k** points instead of the Γ point only like we have done; at the limit of no overlap between the periodically repeated molecules these should be identical but when there remains a small overlap the few **k** points located as to give an average of the weak interaction over the Brillouin zone converge faster than when Γ point only is used since the slightly dispersed bands have extremal values at the Γ point.

Cut-off energy and radii

For the studies aiming at finding a suitable pseudo potential and a sufficient cut-off energy we performed calculations for the oxygen dimer with slightly varying pseudo potential radii and the cut-off energy. The results are collected into the Figure A.15; we see that especially the vibrational frequency does not converge to a reasonably constant value until a cut-off of about 60-80 Ry. Although the value at 40 Ry is closer to the value from experiments and converged calculations it is accidental as is seen from the Figure A.16, which shows the binding energy and the energy adjusted to a common minimum. Clearly the calculations performed at 40 Ry deviate more from the converged results than the results from calculations with an inter-mediate value for the energy cut-off. The error at the low and inter-mediate cut-off energies is at its largest when using the pseudo potentials with the smallest core radii as expected, but the results converge to almost identical values at the

Table A.5: The binding energy of the oxygen dimer as a function of the cubic cell length in our super cell calculation; the values in parenthesis is the deviation in milli electron volts from the result in the largest cell

Unit cell (Bohr)	$E_B(O_2)$ (eV)
10	−6.276 (−84)
11	−6.222 (−30)
12	−6.209 (−17)
13	−6.199 (−7)
14	−6.191 (+1)
15	−6.187 (+4)
16	−6.183 (+9)
17	−6.192 (≡ 0)

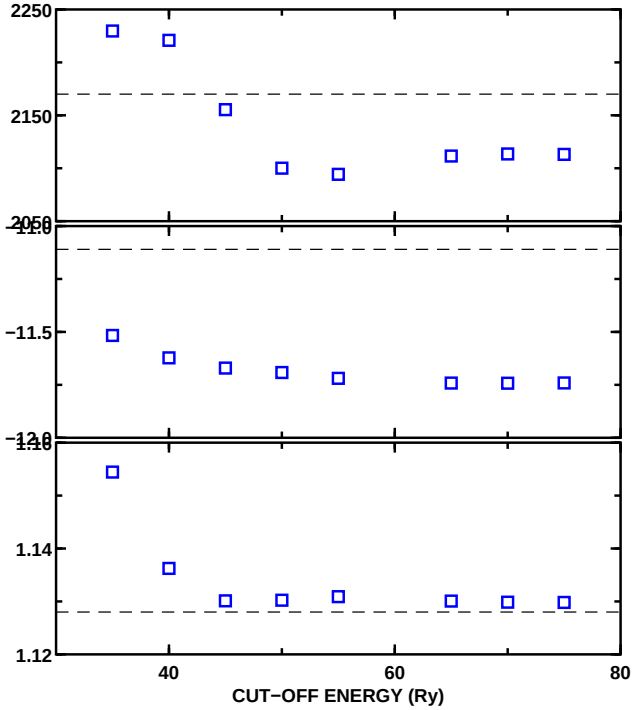

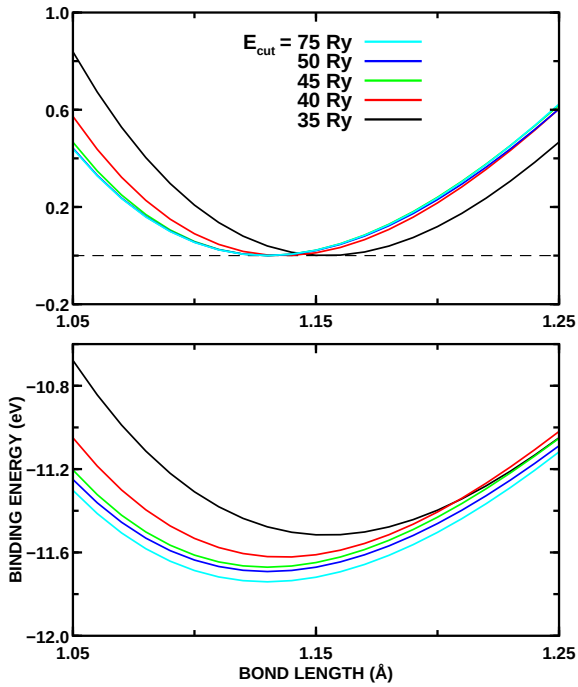

Figure A.17: Convergence test of the molecular properties of an carbon monoxide dimer as a function of the cut-off energy used in the expansion of the Kohn-Sham orbitals in a basis of plane waves. The panels are from bottom to top the bond length in Ångströms, the binding or atomisation energy of the dimer to two isolated atoms and the frequency of the stretching mode vibration of the molecule in inverse centi metres. The horizontal dashed lines denote the experimental values

Figure A.18: The energy versus bond length of a carbon monoxide dimer calculated with different values of the cut-off energy. Lower panel: the binding energy of the dimer, with the experimental value as the horizontal line. Upper panel: the same curves but with normalised to the minimum

high cut-off energy; thus a large core radius would be justified but it is important that this is only a test for one system. As a compromise between between the accuracy and a reasonable cut-off energy we chose to use 50 Ry with cut-off radii 1.4 Bohr; this settles then the cut-off energy for the system studied in the present work.

A.4.3 Carbon monoxide

To investigate the properties of the carbon monoxide we use basically the same parameters and pseudo potentials as were used for the oxygen as the carbon monoxide are relatively similar molecules.

Cut-off energy

The characteristic properties of the carbon monoxide dimer in the Figure A.17 as the function of the cut-off energy show that these converge slightly earlier, at 40-45 Ry, than the corresponding ones of the oxygen dimer; the core radii of the pseudo potentials of the carbon and oxygen atom are $r^{\mathrm{C}}_{c,l=sp} = 1.35$ Bohr and $r^{\mathrm{O}}_{c,l=sp} = 1.4$ Bohr. The Figure A.18 further proves that the one-dimensional potential energy surface for stretching the C-O bond length is very well converged already the cut-off energy of 50 Ry.

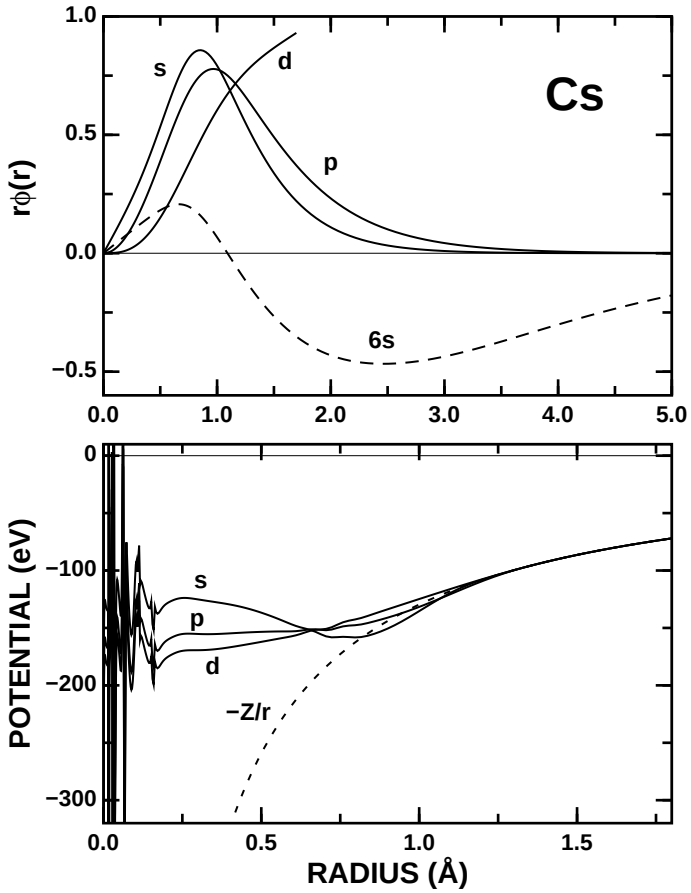

Figure A.19: The pseudo potentials – lower panel – and the pseudo orbitals of the potential used in the present work for cesium; the wave functions have been multiplied with the radius. Please notice that the 5*s* state is node-less but its first excited state, describing the 6*s* state, has a radial node

A.4.4 Cesium

To describe the cesium traditionally a pseudo potential with only the 6*s* in the valence is used; however in this case the pseudo potential must be generated with a largely ionised configuration, thus in the spirit of the Bachelet-Hamann-Schlüter scheme, in order to obtain a transferable pseudo potential. This has probably a justification *a posteriori* not only due to the popular concept of the ionicity of the cesium and especially its 6*s* orbital in different chemical environments but also since the 5*d* and 4*s* are un-bound in the neutral atom but often become also somewhat occupied upon changing to a different surrounding, and these states are lowered and bound when the atom is ionised when part of the charge on the 6*s* is removed.

However since the next orbital, 5*p*, is only 13 eV lower in energy than the eigenvalue of the 6*s* state it can, although fully occupied, at least polarise in different environments and in some cases we have seen that this these and even the 5*s* states lie energetically close to the semi-core molecular hybrids of the carbon monoxide. Thus we chose to include the 5*p* as the valence state of the *p* character in the pseudo potential; however then we had difficulties in finding a pseudo potential without ghost states and we were forced to include the 5*s* state as the valence state with the *s* character since we had not implemented a scheme to treat different radial states with the same *l* quantum number in the pseudo potential. Thus the 6*s* is obtained as the first excited state of the pseudo potential constructed for the 5*s* state; please see the Figure A.19 where the electronic pseudo orbitals and the orbital obtained for the 6*s* are shown. In this construction the quality and transferability of the pseudo potential largely relies on how the pseudo potential constructed from the 5*s* state describes the relevant changes in the energy region of the 6*s* eigenvalue. A further alternative to insure the transferability and good description of the 6*s* state would be the use of several projectors at different energies in the pseudo potential like present *e.g.* in the Vanderbilt ultra-soft pseudo potentials. The core radii were chosen (Martin Fuchs, personal communication) as r_c = 2.3, 2.6 and 3.2 Bohr for the 5*s*, 5*p* and 5*d* channel respectively.

Cut-off energy

We tested the required cut-off and the quality of the pseudo potential in the body centred cubic lattice of bulk cesium; we also did some calculations in cesium chloride and face centred cubic lattice of cesium but these calculations shall not be discussed here. The Table A.6 shows the convergence of the relevant lattice properties with an increasing cut-off energy. The lattice constant is almost four per cent larger than in the experiments – and we haven't even included the zero-point corrections to our results – and thus slightly more than the usual 1. . . 3 %; however all the properties of the lattice converge well already below 50 Ry and are reasonably close to

Table A.6: The convergence of the lattice constant a, bulk modulus B, the first derivative B' of the bulk modulus with respect to the pressure, the total energy, and the cohesive energy of bulk cesium in the body centred cubic cell; the values in the parenthesis are differences in per cent from the value at 80 Ry

$E_{cut-off}$ (Ry)	a (Å)	B (MBar)	B'	ΔE (meV)	E_{coh} (eV)
35	6.283 (−0.04)	0.021 (+18.66)	1.393 (+62.80)	580	0.61
40	6.289 (+0.05)	0.018 (+1.27)	3.845 (+2.69)	275	0.62
45	6.287 (+0.02)	0.018 (+0.83)	3.749 (+0.15)	154	0.61
50	6.286 (+0.00)	0.018 (+0.11)	3.823 (+2.12)	129	—
60	6.286 (+0.01)	0.018 (+0.44)	3.688 (−1.50)	106	0.62
80	6.286 (≡ 0)	0.018 (≡ 0)	3.744 (≡ 0)	≡ 0	—
Expr.	6.05	0.020		—	0.80

the experiments, giving reliability to our pseudo potential and the numerical method in general. The cohesive energy was extracted using the energy of the cesium atom in a simple cubic super cell with the edge length of 35 Bohr; this was found to be sufficient to converge the energy to within milli electron volts, but such a large cell is required due to tell very large extent of the weakly bound 6s orbital. The spin energy of 0.12 eV within the generalised gradient approximation of Perdew *et al* (1991) of the cesium atom was again obtained from Martin Fuchs (personal communication).

ELECTROPOSITIVITY - ELECTRONEGATIVITY

HYDROGEN 1.0079 0.089 **H** 1 $1s^1$ 3.75 HEX 1.731																	HELIUM 4.0026 0.179 **He** 2 $1s^2$ 3.57 HEX 1.633
LITHIUM 6.941 0.53 **Li** 3 $1s^2 2s^1$ 3.49 BCC	BERYLLIUM 9.0122 1.85 **Be** 4 $1s^2 2s^2$ 2.29 HEX 1.567											BORON 10.81 2.34 **B** 5 $1s^2 2s^2 2p^1$ 8.73 TET 0.576	CARBON 12.01 2.26 **C** 6 $1s^2 2s^2 2p^2$ 3.57 DIA	NITROGEN 14.007 1.03 **N** 7 $1s^2 2s^2 2p^3$ 4.039 HEX 1.651	OXYGEN 15.999 1.43 **O** 8 $1s^2 2s^2 2p^4$ 6.83 CUB	FLUORINE 18.998 1.97 **F** 9 $1s^2 2s^2 2p^5$ MCL	NEON 20.18 1.56 **Ne** 10 $1s^2 2s^2 2p^6$ 4.43 FCC
SODIUM 22.9898 0.97 **Na** 11 [Ne]$3s^1$ 4.23 BCC	MAGNESIUM 24.305 1.74 **Mg** 12 [Ne]$3s^2$ 3.21 HEX 1.624											ALUMINIUM 26.982 2.70 **Al** 13 [Ne]$3s^2 3p^1$ 4.05 FCC	SILICON 28.086 2.33 **Si** 14 [Ne]$3s^2 3p^2$ 5.43 DIA	PHOSPHORUS 30.974 1.82 **P** 15 [Ne]$3s^2 3p^3$ 7.17 CUB	SULPHUR 32.064 2.07 **S** 16 [Ne]$3s^2 3p^4$ 10.47 ORC 2.339 1.229	CHLORINE 35.453 2.09 **Cl** 17 [Ne]$3s^2 3p^5$ 6.24 ORC 1.324 0.718	ARGON 39.948 1.78 **Ar** 18 [Ne]$3s^2 3p^6$ 5.26 FCC
POTASSIUM 39.09 0.86 **K** 19 [Ar]$4s^1$ 5.23 BCC	CALCIUM 40.08 1.54 **Ca** 20 [Ar]$4s^2$ 5.58 FCC	SCANDIUM 44.956 2.99 **Sc** 21 [Ar]$3d^1 4s^2$ 3.31 HEX 1.594	TITANIUM 47.90 4.51 **Ti** 22 [Ar]$3d^2 4s^2$ 2.95 HEX 1.588	VANADIUM 50.942 6.1 **V** 23 [Ar]$3d^3 4s^2$ 3.02 BCC	CHROMIUM 52.00 7.19 **Cr** 24 [Ar]$3d^5 4s^1$ 2.88 BCC	MANGANESE 54.938 7.43 **Mn** 25 [Ar]$3d^5 4s^2$ 8.89 CUB	IRON 55.85 7.86 **Fe** 26 [Ar]$3d^6 4s^2$ 2.87 BCC	COBALT 58.93 8.9 **Co** 27 [Ar]$3d^7 4s^2$ 2.51 HEX 1.622	NICKEL 58.71 8.9 **Ni** 28 [Ar]$3d^8 4s^2$ 3.52 FCC	COPPER 63.55 8.96 **Cu** 29 [Ar]$3d^{10} 4s^1$ 3.61 FCC	ZINC 65.38 7.14 **Zn** 30 [Ar]$3d^{10} 4s^2$ 2.66 HEX 1.856	GALLIUM 69.72 5.91 **Ga** 31 [Ar]$3d^{10} 4s^2 4p^1$ 4.51 ORC 1.695 1.001	GERMANIUM 72.59 5.32 **Ge** 32 [Ar]$3d^{10} 4s^2 4p^2$ 5.66 DIA	ARSENIC 74.922 5.72 **As** 33 [Ar]$3d^{10} 4s^2 4p^3$ 4.13 RHL 54°10'	SELENIUM 78.96 4.79 **Se** 34 [Ar]$3d^{10} 4s^2 4p^4$ 4.36 HEX 1.136	BROMINE 79.91 4.10 **Br** 35 [Ar]$3d^{10} 4s^2 4p^5$ 6.67 ORC 1.307 0.672	KRYPTON 83.80 3.07 **Kr** 36 [Ar]$3d^{10} 4s^2 4p^6$ 5.72 FCC
RUBIDIUM 85.47 1.53 **Rb** 37 [Kr]$5s^1$ 5.59 BCC	STRONTIUM 87.62 2.60 **Sr** 38 [Kr]$5s^2$ 6.08 FCC	YTTRIUM 88.91 4.46 **Y** 39 [Kr]$4d^1 5s^2$ 3.65 HEX 1.571	ZIRCONIUM 91.22 6.49 **Zr** 40 [Kr]$4d^2 5s^2$ 3.23 HEX 1.593	NIOBIUM 92.91 8.4 **Nb** 41 [Kr]$4d^4 5s^1$ 3.30 BCC	MOLYBDENUM 95.94 10.2 **Mo** 42 [Kr]$4d^5 5s^1$ 3.15 BCC	TECHNETIUM 98.91 11.5 **Tc** 43 [Kr]$4d^5 5s^2$ 2.74 HEX 1.604	RUTHENIUM 101.07 12.2 **Ru** 44 [Kr]$4d^7 5s^1$ 2.70 HEX 1.584	RHODIUM 102.90 12.4 **Rh** 45 [Kr]$4d^8 5s^1$ 3.80 FCC	PALLADIUM 106.40 12.0 **Pd** 46 [Kr]$4d^{10} 5s^0$ 3.89 FCC	SILVER 107.87 10.5 **Ag** 47 [Kr]$4d^{10} 5s^1$ 4.09 FCC	CADMIUM 112.40 8.65 **Cd** 48 [Kr]$4d^{10} 5s^2$ 2.98 HEX 1.886	INDIUM 114.82 7.31 **In** 49 [Kr]$4d^{10} 5s^2 5p^1$ 4.59 TET 1.076	TIN 118.69 7.30 **Sn** 50 [Kr]$4d^{10} 5s^2 5p^2$ 5.82 TET 0.546	ANTIMONY 121.75 6.62 **Sb** 51 [Kr]$4d^{10} 5s^2 5p^3$ 4.51 RHL 57°6'	TELLURIUM 127.60 6.24 **Te** 52 [Kr]$4d^{10} 5s^2 5p^4$ 4.45 HEX 1.330	IODINE 126.90 4.94 **I** 53 [Kr]$4d^{10} 5s^2 5p^5$ 7.27 ORC 1.347 0.659	XENON 131.30 3.77 **Xe** 54 [Kr]$4d^{10} 5s^2 5p^6$ 6.20 FCC
CESIUM 132.91 1.90 **Cs** 55 [Xe]$6s^1$ 6.05 BCC	BARIUM 137.34 3.5 **Ba** 56 [Xe]$6s^2$ 5.02 BCC	LANTHANUM 138.91 6.17 **La** 57 [Xe]$5d^1 6s^2$ 3.75 HEX 1.619	HAFNIUM 178.49 13.1 **Hf** 72 [Xe]$4f^{14} 5d^2 6s^2$ 3.20 HEX 1.582	TANTALUM 180.95 16.6 **Ta** 73 [Xe]$4f^{14} 5d^3 6s^2$ 3.31 BCC	TUNGSTEN 183.85 19.3 **W** 74 [Xe]$4f^{14} 5d^4 6s^2$ 3.16 BCC	RHENIUM 186.2 21.0 **Re** 75 [Xe]$4f^{14} 5d^5 6s^2$ 2.76 HEX 1.615	OSMIUM 190.20 22.6 **Os** 76 [Xe]$4f^{14} 5d^6 6s^2$ 2.74 HEX 1.579	IRIDIUM 192.22 22.5 **Ir** 77 [Xe]$4f^{14} 5d^7 6s^2$ 3.84 FCC	PLATINUM 195.09 21.4 **Pt** 78 [Xe]$4f^{14} 5d^9 6s^0$ 3.92 FCC	GOLD 196.97 19.3 **Au** 79 [Xe]$4f^{14} 5d^{10} 6s^1$ 4.08 FCC	MERCURY 200.59 13.6 **Hg** 80 [Xe]$4f^{14} 5d^{10} 6s^2$ 2.99 RHL 70°45'	THALLIUM 204.37 11.85 **Tl** 81 [Xe]$4f^{14} 5d^{10} 6s^2 6p^1$ 3.46 HEX 1.599	LEAD 207.19 11.4 **Pb** 82 [Xe]$4f^{14} 5d^{10} 6s^2 6p^1$ 4.95 FCC	BISMUTH 208.98 9.8 **Bi** 83 [Xe]$4f^{14} 5d^{10} 6s^2 6p^1$ 4.75 RHL 57°14'	POLONIUM 210 9.4 **Po** 84 [Xe]$4f^{14} 5d^{10} 6s^2 6p^1$ 3.35 SC	ASTATINE 210 **At** 85	RADON 222 (4.4) **Rn** 86 [Xe]$4f^{14} 5d^{10} 6s^2 6p^1$ (FCC)
FRANCIUM 223 **Fr** 87 [Rn]$7s^1$ (BCC)	RADIUM 226 (5.0) **Ra** 88 [Rn]$7s^2$	ACTINIUM 227 10.1 **Ac** 89 [Rn]$6d^1 7s^2$ 5.31 FCC															

CERIUM 140.12 6.77 **Ce** 58 [Xe]$4f^2 5d^0 6s^2$ 5.16 FCC	PRASEODYMIUM 140.91 6.77 **Pr** 59 [Xe]$4f^3 5d^0 6s^2$ 3.67 HEX 1.614	NEODYMIUM 144.24 7.00 **Nd** 60 [Xe]$4f^4 5d^0 6s^2$ 3.66 HEX 1.614	PROMETHIUM 145 **Pm** 61 [Xe]$4f^5 5d^0 6s^2$	SAMARIUM 150.35 7.54 **Sm** 62 [Xe]$4f^6 5d^0 6s^2$ 9.00 RHL 23°13'	EUROPIUM 151.96 7.90 **Eu** 63 [Xe]$4f^7 5d^0 6s^2$ 4.61 BCC	GADOLINIUM 157.25 8.23 **Gd** 64 [Xe]$4f^7 5d^1 6s^2$ 3.64 HEX 1.588	TERBIUM 158.92 8.54 **Tb** 65 [Xe]$4f^9 5d^0 6s^2$ 3.60 HEX 1.581	DYSPROSIUM 162.50 8.78 **Dy** 66 [Xe]$4f^{10} 5d^0 6s^2$ 3.59 HEX 1.573	HOLMIUM 164.93 9.05 **Ho** 67 [Xe]$4f^{11} 5d^0 6s^2$ 3.58 HEX 1.570	ERBIUM 167.26 9.37 **Er** 68 [Xe]$4f^{12} 5d^0 6s^2$ 3.56 HEX 1.570	THULIUM 168.93 9.31 **Tm** 69 [Xe]$4f^{13} 5d^0 6s^2$ 3.54 HEX 1.570	YTTERBIUM 173.04 6.97 **Yb** 70 [Xe]$4f^{14} 5d^0 6s^2$ 5.49 FCC	LUTETIUM 174.97 9.84 **Lu** 71 [Xe]$4f^{14} 5d^1 6s^2$ 3.51 HEX 1.585
THORIUM 232.04 11.7 **Th** 90 [Rn]$6d^2 7s^2$ 5.08 FCC	PROTACTINIUM 231 15.4 **Pa** 91 [Rn]$5f^2 6d^1 7s^2$ 3.92 TET 0.825	URANIUM 238.03 19.07 **U** 92 [Rn]$5f^3 6d^1 7s^2$ 2.85 ORC 2.056 1.736	NEPTUNIUM 237.05 23.05 **Np** 93 [Rn]$5f^5 6d^0 7s^2$ 4.72 ORC 1.411 1.035	PLUTONIUM 244 19.8 **Pu** 94 [Rn]$5f^6 6d^0 7s^2$ MCL	AMERICIUM 243 11.8 **Am** 95 [Rn]$5f^7 6d^0 7s^2$	CURIUM 247 **Cm** 96 [Rn]$5f^7 6d^1 7s^2$	BERKELIUM 247 **Bk** 97 [Rn]$5f^9 6d^0 7s^2$	CALIFORNIUM 251 **Cf** 98 [Rn]$5f^{10} 6d^0 7s^2$	EINSTEINIUM 254 **Es** 99	FERMIUM 257 **Fm** 100	MENDELEVIUM 256 **Md** 101	NOBELIUM 254 **No** 102	LAWRENCIUM 257 **Lw** 103

M. Sc. Ari Paavo Seitsonen

Theoretical Investigations into Adsorption and Co-adsorption on Transition-Metal Surfaces as Models to Heterogeneous Catalysis

Zusammenfassung

Eines der Standbeine der Oberflächenforschung in der physikalischen Chemie ist die Untersuchung von heterogen-katalysierten Reaktionen. Dabei müssen zuerst beide Reaktanden auf der katalytisch aktiven Oberfläche adsorbieren, bevor sie miteinder zum Produkt reagieren. Eine Schlüsselrolle für ein tieferes Verständnis auf mikroskopischer Ebene spielen daher Untersuchungen von Adsorbat- und Koadsorbatsystemen auf Metalloberflächen. Die Komplexität realer Katalysatoren erfordert die Einschränkung auf Modellsysteme und Modellreaktionen, wie sie etwa durch Metalleinkristalloberflächen und der CO Oxidationsreaktion realisiert sind.

In der vorliegenden Arbeit wurde die Dichtefunktionaltheorie zur Berechnung der elektronischen und atomaren Struktur von O, CO, Cs und deren Koadsorbatsysteme auf Ru(0001) benutzt. Technische Einzelheiten der Weiterentwicklung des verwendeten Programmes sind in einem Anhang beschrieben. Die Untersuchung von Cs und dessen Wechselwirkung mit CO und Sauerstoff ergeben detaillierte Informationen zur Alkalimetall-promotierten CO Oxidation.

Das Cäsium wird durch die Adsorption auf Ru(0001) deutlich polarisiert, was mit einem starken lokalen elektrischen Feld (senkrecht zur Oberfläche) von etwa $1\,\mathrm{V/Å}$ einhergeht. Diese hohe Feldstärke verändert maßgeblich die Elektronendichteverteilung in Koadsorbaten (Promotorwirkung) und im Substrat. Die elektronische Antwort des Substrates auf die Adsorption von Cs konnte sehr gut mit einem äusseren elektrischen Feld modelliert werden.

Die Adsorption von CO (Kohlenmonoxid) auf Metalloberflächen wird traditionell im Rahmen des Blyholdermodells, einem Donator-Akzeptormodell, beschrieben: Das CO 5σ Orbital (HOMO) gibt Ladung an das unterliegende Substrat ab und erhält im Gegenzug Ladung von der Metallunterlage in das $2\pi^*$ CO Orbital (LUMO). Andere Molekülorbitale von CO sind nach diesem Modell an der Bindung nicht beteiligt. Die hier vorgestellten DFT Rechungen zeigen deutlich, daß dieses Modell zu einfach ist und daß neben dem CO 5σ und $2\pi^*$ Orbitalen eine starke und für die Bindung entscheidende Mischung mit dem CO-4σ Orbital auftritt. Das isoelektronische Molekül N_2 verhält sich hinsichtlich seiner Bindung zu Ru(0001) ähnlich wie CO. DFT Rechungen der CO Chemisorption auf anderen Übergangsmetalloberflächen, wie Cu(111) und Pt(111), ergaben von Experimenten abweichende Adsorptionsplätze. Dies mag auf zu grobe Näherungen in der GGA (*engl.* Generalized Gradient Approximation) hinweisen.

Die Wechselwirkung zwischen Cs und Sauerstoff oder CO ist attraktiv, wie es auch experimentell gefunden worden ist und wie man es aufgrund der unterschiedlichen Elektronegativitäten erwarten sollte. Die atomaren Geometrien der Koadsorbatstrukturen, wie sie mit DFT gefunden wurden, stimmen ausgezeichnet mit experimentellen Werten überein. Das CO Molekül polarisiert in Gegenwart des koadsorbierten Cs Atoms aufgrund des hohen Cs-induzierten elektrischen Feldes. Die gefundene Verlängerung des CO Bindungsabstandes wird durch Adsorption, Platzwechsel von on-top auf einen dreifachkoordinierten Platz und der Antwort von CO auf das hohe Cs-induzierte elektrische Feld erklärt.

Die hier vorgestellten DFT Rechnungen ergeben atomare und elektronische Strukturen, die mit experimentellen Befunden sehr gut in Einklang sind. Die verwendeten Näherungen in DFT-GGA erlauben also eine zuverlässige Beschreibung der Adsorbat- und Koadsorbatphasen auf Ru(0001) und stellen daher einen guten Startpunkt für weitere DFT Rechnungen der katalytischen Aktivität und der mikroskopischen Reaktionsschritte dar.

Lebenslauf

Ari Paavo Seitsonen

Geboren:	am 17. April AD 1968 in Janakkala, Finnland	
Staatsangehörigkeit:	Finnisch	
Eltern:	Seija Sinikka Seitsonen (geb. Kiuru), Hausfrau, und Eino Erkki Seitsonen, Landwirt	
Geschwister:	Mika Eerik Seitsonen	
Schule:	1975-1984:	Tervakoski Grundschule, Finnland
	1984-1987:	Tervakoski Gymnasium, Finnland
	1987:	Abitur an der Tervakoski Gymnasium, Finnland
	1987-1988:	Militärdienst (Artillerie); nachher Offizier der Reserve
Studium:	1988-1993:	Studium an der Technischen Universität Helsinki
	Oktober 1993:	Beginn der vorliegenden Dissertation am Fritz-Haber-Institut der Max-Planck-Institut, Berlin

Berlin, 17. April AD 2001